IN-SITU ONLINE MEASUREMENT OF RADON (^{222}Rn) DATA AND DEVELOPING ITS CORRELATION WITH GEOPHYSICAL PHENOMENA IN SEISMICALLY ACTIVE REGIONS: A CASE STUDY OF MAT FAULT AT ZAWLPUI, SERCHHIP DISTRICT, MIZORAM

A THESIS SUBMITTED IN PARTIAL FULFILLMENT OF THE REQUIREMENTS FOR THE DEGREE OF DOCTOR OF PHILOSOPHY

T THUAMTHANSANGA
MZU REGISTRATION NO.: 72 of 2014
PH.D. REGISTRATION NO. : MZU/Ph.D./1099 of 24.04.2018

DEPARTMENT OF PHYSICS
SCHOOL OF PHYSICAL SCIENCES
DECEMBER, 2022

IN-SITU ONLINE MEASUREMENT OF RADON (^{222}Rn) DATA AND DEVELOPING ITS CORRELATION WITH GEOPHYSICAL PHENOMENA IN SEISMICALLY ACTIVE REGIONS: A CASE STUDY OF MAT FAULT AT ZAWLPUI, SERCHHIP DISTRICT, MIZORAM

By

T Thuamthansanga

Department of Physics

Name of Supervisor: Prof. R.C. Tiwari

Name of Joint Supervisor: Prof. R.P. Tiwari

Submitted

in partial fulfillment of the requirement

of the Degree of Doctor of Philosophy in Physics of Mizoram University, Aizawl

MIZORAM UNIVERSITY

DEPARTMENT OF PHYSICS

Aizawl - 796004, MIZORAM, India

(A Central University Established by an Act of Parliament of India)

Prof. R. C. Tiwari
Supervisor

Ph:+91-389-2330522(O) +91-9862300514 (M) & Fax: +91-389-2330435
Email: ramesh_mzu@rediffmail.com

Date:

Certificate

This is to certify that the thesis entitled *"In-situ online measurement of radon (^{222} Rn) data and developing its correlation with geophysical phenomena in seismically active regions: A case study of Mat fault at Zawlpui, Serchhip District, Mizoram."* submitted by Shri T Thuamthansanga, for the degree of Doctor of Philosophy in Physics, of the Mizoram University: Aizawl, India, embodies the record of original investigations carried out by him under my supervision. He has been duly registered and the thesis presented is worthy of being considered for the award of Ph.D. degree. This research work has not been submitted for any degree of any other university.

(Prof. Raghavendra Prasad Tiwari)
Joint Supervisor

(Prof. Ramesh Chandra Tiwari)
Supervisor

Declaration of the Candidate

Mizoram University

December, 2022

I, T Thuamthansanga, hereby declare that the subject matter of this thesis is the record of work done by me, that the contents of this thesis did not form basis of the award of any previous degree to me or to do the best of my knowledge to anybody else, and that the thesis has not been submitted by me for any research degree in any other University/Institute.

This is being submitted to the Mizoram University for the degree of Doctor of Philosophy in Physics.

(T THUAMTHANSANGA)

Candidate

(Prof. ZAITHANZAUVA PACHUAU) (Prof. RAMESH CHANDRA TIWARI)

Head Supervisor

Acknowledgement

First and foremost, I would like to express my sincere gratitude to my Supervisor Prof. R.C Tiwari for his valuable guidance, high spirit encouragement and supervision during my entire period of study. I would also like to thank my Joint Supervisor Prof. R.P. Tiwari for introducing me to basic geology which has been utilized fruitfully in the entire work.

My special thanks go to Dr. B.K. Sahoo for helping me in designing field studies, statistical analysis and for his endless idea during the project work. I would also like to thank his team at BARC, Mumbai (India) for their enlightening instructions for the project works and for their hospitality during our stay in Mumbai.

I express my heartfelt thanks to Prof. Diwakar Tiwari, Dean, School of Physical Sciences for his support in the completion of my work. Without him it would have been difficult for me to solve the administrative problem on my own. I would also like to thank the Head, Department of Physics and all the faculty members, teaching as well as non-teaching . Without the help and support I received from them this study would not have been possible. Also, I want to thank all the research scholars in the department for the friendship and the productive intellectual atmosphere that I have enjoyed all these years.

I gratefully acknowledge the DAE-BRNS, BARC, Mumbai, India for financial grants to carry out the research work.

I am grateful to U Mathua and family, Pu Saphranga and family of Serchhip and Pa Chhana and family of Zotlang for their kind and warm hospitality during my entire field studies.

Indeed I am in depth to my family and lucky to have such a wonderful family. I can never give enough thanks to my parents, brothers and sister. It is their love, affection, endless support of all kind that makes this work possible. Above all, I thank the Lord Almighty for being with me throughout these years and keeping me in good health to complete this work.

Date: (**T THUAMTHANSANGA**)

Contents

List of Figures

List of Tables

Dedication

To my parents, brothers and sister

1

Introduction

1.1 Background

Radon is a radioactive noble gas discovered by German scientist Frederick Dorn in 1900 (George, 2008) soon after the discovery of radium by Curies in 1898 (Kolthoff *et al*., 1966). The Curies noticed that when radium is in contact with an air medium the medium conducts electricity which later was explained by Dorn as a phenomenon due to emanation from radium. Rutherford coined this gaseous element from radium 'emanation' and marked it with the symbol '*Em*' which later in 1923 was given the official name 'Radon' by the International Committee on Chemical Elements. Radon has three naturally occurring isotopes radon (^{222}Rn: $T_{1/2}$, 3.825 d, decay series of ^{238}U), thoron (^{220}Rn: $T_{1/2}$, 55.6 s, decay series of ^{232}Th) and actinon (^{219}Rn: $T_{1/2}$, 3.6 s, decay series of ^{235}U). Due to its extremely small half-life (3.6s) and low activity concentrations in the environment relative to its two isotopes actinon has often been neglected in most practical studies as well as in this thesis. The radon isotopes naturally originated from the earth's crust and as well from anthropogenic activities. The natural sources include emissions from rocks, soil and ore bodies in the earth's crust and building materials like bricks, cement, tiles etc (Nazaroff and Nero, 1988; UNSCEAR, 2000). These natural sources were also called Naturally Occurring Radioactive Materials (NORMs). Sources due to anthropogenic activities constitute waste products of uranium mines and milling facilities, zircon plants, coal and phospho-gypsum industries etc. This arising source from anthropogenic activity is also known as Technologically Enhanced Natural Occurring Radioactive Materials (TENORMs). In this thesis, we will be focusing only on radon and thoron gases emitted from natural sources in the earth's crust. Being originated in the earth's crust and gaseous elements, the isotope pair diffuses easily in the pore space of the earth's crust and exhales into the atmosphere. They tend to build up in enclosed spaces like underground mines or houses and are found to be omnipresent indoor air pollutants. In the early 1900s, exposure to radioactivity was considered to enhance good health

and people were reported to drink radon-rich water for that purpose (Ball *et al*., 1991). It was not until the 1970s that a quantitative risk estimate for lung cancer could be established among underground miners, after diagnosing an overwhelming number of lung cancers among them (Swedjemark, 2004). Uranium mining became intensified during the 1940s-1960s in countries like Africa, Canada and the United States of America, where radon serves as a useful pathfinder to its parent nuclei (Ball *et al*., 1991; Khattak *et al*., 2011; Swedjemark, 2004). In India, it was started in 1948 and in north-eastern India (NE India) in particular in 1950 (Gupta and Sarangi, 2005). No economic concentration was found in northeast India except in Meghalaya state (Gupta and Sarangi, 2005). Besides as a tracer to uranium deposit, some other discipline where radon has been studied includes earthquake prediction (Igarashi and Wakita, 1990; Jaishi *et al*., 2013; King, 1986; Shapiro *et al*., 1981; Vaupotič *et al*., 2010; Yasuoka and Shinogi, 1997; Zmazek *et al*., 2002), tracer to a hidden fault (Nalukudiparambil *et al*., 2021; Singh *et al*., 2014), health hazard (Auvinen *et al*., 1996; Baysson *et al*., 2004) etc. In addition, the recorded radon anomaly in a Russian well before the Tashkent earthquake in 1966 was regarded by many authors as the first official report where radon anomaly was correlated with geophysical phenomena (Ulomov and Mavashev, 1967).

1.2 Mechanism of emission and transportation of radon and thoron in soil

The main sources of radon and thoron in soil and air are their parent nuclei radium and thorium in the earth's crust respectively. The isotope pair concentration varies with time and space and their concentrations in the air are the main significant contributor to radiation exposure to that in water and soil. The isotope pair concentration level in air and water depends on four factors viz. nature of the sources, emanating power, transportation from the sources and their ultimate spreading. The physical mechanism by which radon and thoron gases are released from the rocks matrix is not yet fully understood. Despite its higher activity exhalation rate (about 100 times than that of radon) the total global thoron activity inventory in the atmosphere is much less that of radon (about 100 times less), primarily because of the shorter half-life of thoron (Harley, 1973). Only a fraction of radon or thoron atoms generated in the soil escapes from the solid grains and makes

their way into the pore of the medium. The isotope pair passes through different processes in the earth's crust till they get emitted to the atmosphere viz. emanation by recoil process, transportation by diffusion or advection process or both and then ultimately gets emitted to the atmosphere.

Emanation/Recoil effect: In the earth's crust radon isotope pairs are produced by the process of 'recoil effect' due to decay of their parent nuclei (Bossus, 1984; Parekh, 1990; Sasaki *et al*., 2005; Semkow, 1990; Semkow, 1991; Semkow and Sasaki, 2004). The mechanism was proposed by Tanner (1980) (Fig. 1.1). He expressed that radon/thoron atom after recoil from its parent nuclei seldom gets mobilized through the soil matrix. In fact, only a fraction of them whose recoil path terminated in the liquid or gas phase were available for transportation toward the surface. During the recoil process, majority of radon/thoron atoms get stuck within the same grain or get embedded in the adjacent grain based on their recoil path and position of their parent nuclei in the soil grain. In case the radium atom is located at the edge of the grain away from the pores space the recoil path will terminate within the same grain and hence will not be available for transportation. On the other hand, if the radium atom is located near the surface adjacent to the pore space, the recoil path may terminate inside the adjacent soil grain which disabled it for transportation. Hence only that fraction whose recoil path gets terminated within the soil pore or liquid will be available for transportation through the matrix. The process by which radon and thoron atoms were produced by *recoil effect* in radium-bearing soil grain is known as *emanation*. The fraction of radon or thoron atoms released into the pore space or rock from the radium-bearing grain is termed as radon or thoron *emanation coefficients*. The recoil energy of radon and thoron atom is 86 KeV and 103 KeV respectively (Bossus, 1984). The recoil range of radon in common minerals, water and air are 0.02-0.07 μm, 0.1 μm and 63 μm respectively while the recoil range of thoron in the air is 83 μm (Tanner, 1980).

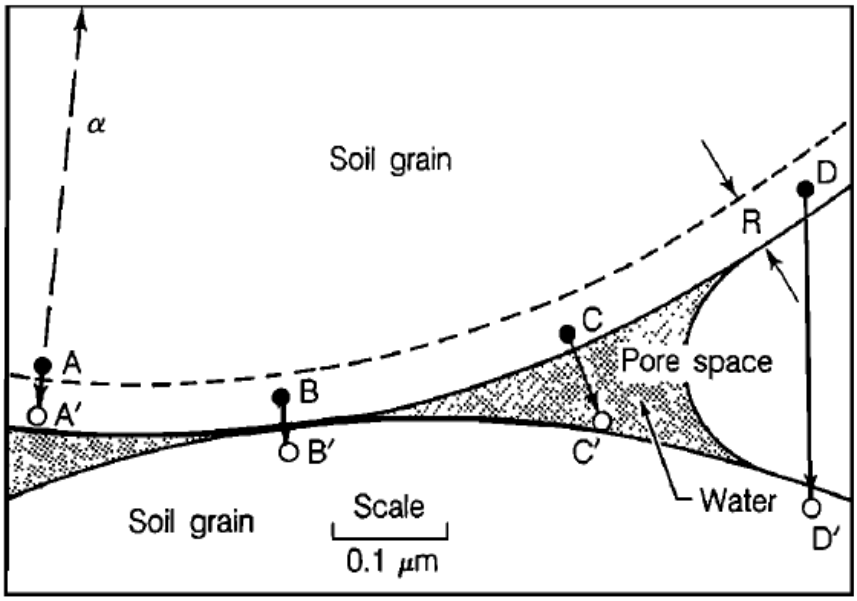

Fig. 1.1: Schematic sketch of the possible emanation scenarios in a solid-water-air system. Radium atom, indicated by solid circles, decay, producing an alpha particle and a recoiling radon atom which may end its recoil at the point indicated by the open circle; R=recoil range; case A-A') ^{222}Rn remains inside the grain; case B-B') ^{222}Rn reaches the adjacent grain; case C-C') ^{222}Rn atom reaches the water-filled pore space, possibly reaching the air-filled pore space by diffusion; case D-D') recoil energy is large, ^{222}Rn crosses the air-filled pore space and penetrates into the adjacent grain (after Tanner, 1980).

An increase in humidity or the presence of water in the soil pore reduced recoil energy and tends to terminate the recoil path of radon atom within the pore space and hence enhancing the emanation coefficient. Hence humidity was reported to raise the radon/thoron *emanation* while the effect of temperature was found to be negligible by some authors (Bossew, 2003; Moore, 1984; Sakoda, *et al*., 2010; Strong and Levins, 1982). It has been also reported that the presence of humidity up to 15-17% by weight (optimum level) (Stranden *et al*., 1984) in the soil enhanced ^{222}Rn emanation by absorbing its recoil energy which prevent it from burying in the adjacent soil grain (Asher-Bolinder *et al*., 1991). In the case of dry soil, the release of radon or thoron atom is attenuated by re-adsorption of the atoms in the pores and fractures in the solid. Megumi and Mamuro (1974) also suggested that radon and

thoron emanation gets enhanced if the soil grain is slightly moist and beyond that, it gets reduced due to a lower diffusion rate in water-filled pores. Besides soil humidity, grain size and temperature effects have also been reported in contrast to some reports who found it to be negligible as mentioned above. The radon and thoron emanation tends to increase with decrease in grain size (Markkanen and Arvela, 1992; Morawska and Jeffris, 1994). Megumi and Mamuro (1974) stated that the smaller the grain size, the larger the surface area which is available for Ra-226 adsorption and hence increases in emanation coefficient. Stranden *et al*. (1984) found that with the increase of temperature from 5 to 50 °C, the radon exhalation rate for a soil sample increases by 55%.

Transportation by diffusion process: The radon and thoron atoms which get terminated in the pore space are now transported toward the surface mainly by two mechanisms namely diffusion and advective process or both (Fig.1.2). Transportation due to diffusion arises due to difference in the spatial distribution of radon and thoron concentrations in the earth crust. The radon concentration was relatively low at the surface and increases with depth and attains an asymptotic value at around 1m from the surface (Friedmann, 2012; Sahoo and Gaware, 2016). This existing concentration gradient is the reason why radon and thoron gases diffuse toward the ground surface. The diffusion coefficient of radon in air, the surface of the water and soil is about 0.1 $cm^2\ s^{-1}$, $10^{-5}\ cm^2\ s^{-1}$ and $10^{-2}\ cm^2\ s^{-1}$ or less respectively (Tanner, 1964). The radon and thoron diffusion length in typical soil was found to be 1 m and 1 cm respectively (Nazaroff, 1992). Hence it was speculated that only radium at 1 m and 1 cm depths may contribute to the isotopes pair gases at the surface. The notion of radon and thoron data within 1 m depth from the ground surface is important as it is the proposed sampling depth for this thesis. The diffusion process for the radon isotope pair through soil pores can be expressed by equation (1.1) (Andrews *et al*., 1986).

$$C_x = C_o \exp\left[-x/L\right] \tag{1.1}$$

where C_x is the radon or thoron concentration at a distance x in water or air from the surface, C_o is the concentration at the surface, $L = D/\lambda$ where D is the diffusion coefficient and λ the decay constant.

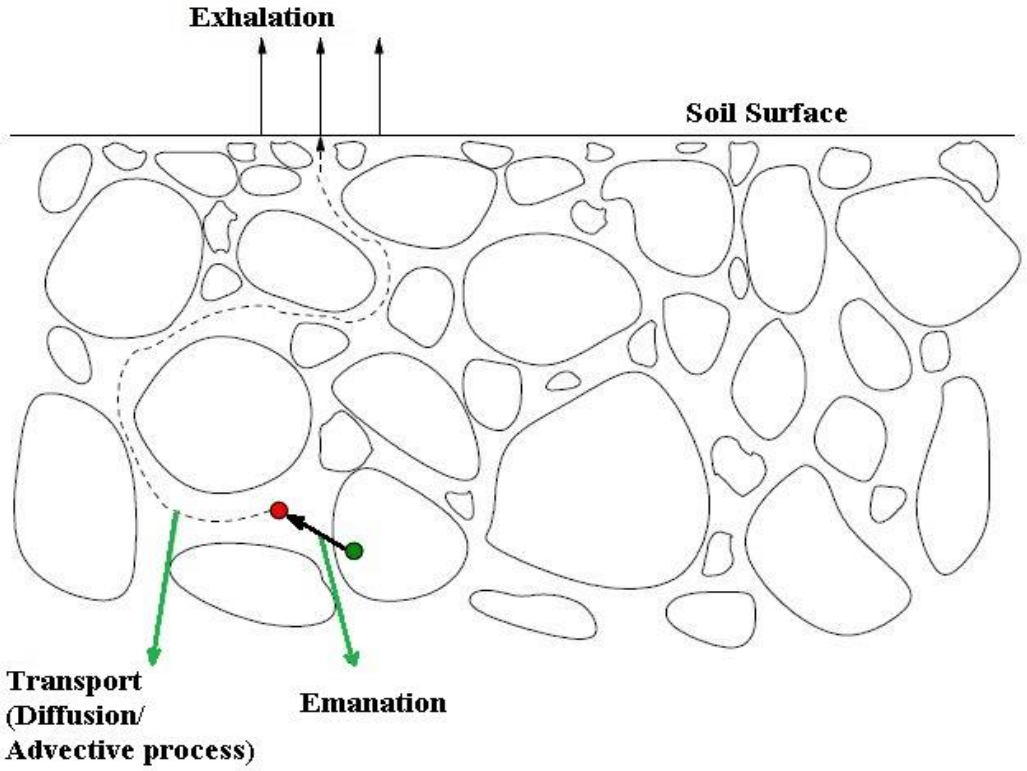

Fig. 1.2: Process of radon/thoron emission from soil matrix to atmosphere.

Transportation by advective process: The radon isotope pair also gets mobilized through the soil matrix by the flow of air known as advective transport. The advection of radon and thoron gases through the soil matrix arises due to the presence of a pressure gradient in the pore air. The process is not limited to an exchange of air in open space but also to that of porous media having a pressure gradient which is governed by a law called Darcy's law. The advective velocity depends not only on the magnitude of the pressure gradient but also on the hydraulic conductivity (permeability/air viscosity $\approx 10^{-6} m^2 kg^{-1}$) of the soil which further depends on the permeability of the soil ($1.5\times10^{-11} ms^{-1}$). In the advective process, the isotope pair atoms are escorted toward the surface by the microscopic flow of gases such as CH_4, CO_2, N_2 etc. with transport velocity 'v'. Taking into account of this

transport velocity (v), Grammakov (1936) estimated the concentration of radon at a distance 'x' from the surface ($C_{o)}$ by the following equation (1.2),

$$C_x = C_o \exp\left[\left\{\left(\frac{v}{2D}\right) - \left(\frac{v^2}{4D^2} + \frac{\lambda}{D}\right)^{1/2}\right\} x\right] \tag{1.2}$$

It must be noted that in an open-ground surface fluctuation in atmospheric pressure can induce a fluctuating pressure pulse in the soil which travels with a diffusion coefficient of $0.1 m^2 s^{-1}$. The diffusion coefficient of this induced pressure pulse was much higher than that of the molecular diffusion coefficient of radon ($10^{-5} m^2 s^{-1}$) in soil. The induced pressure difference nullifies the existing pressured gradient between the soil and atmosphere for a considerable amount of time as it travels rapidly into the soil. Hence for radon exhalation study in the open atmosphere, the Darcian-induced advective transport often gets neglected in comparison to the diffusive transport. But in the case of monitoring in a close environment such as inside a building, radon monitoring station etc. the advective process is the main mechanism by which radon gets emitted from soil. Because meteorologically the environment inside the building is stable and a sustainable pressure gradient has been achieved between the soil and atmosphere above. Such that radon gases enter the room through cracks in the floor and wall. The advective process has been more visible in countries which have cold climates because living rooms were generally warmer than the outside air. In the present thesis, both the transport mechanisms have been considered as the measurements were carried out in an open atmosphere and a closed environment as well.

Once radon and thoron atoms are transported to the surface by either diffusion or advective process or both they get emitted to the atmosphere. The flow chart diagram showing the generation of radon in the soil till it gets emitted to the atmosphere is shown in Fig. 1.3.

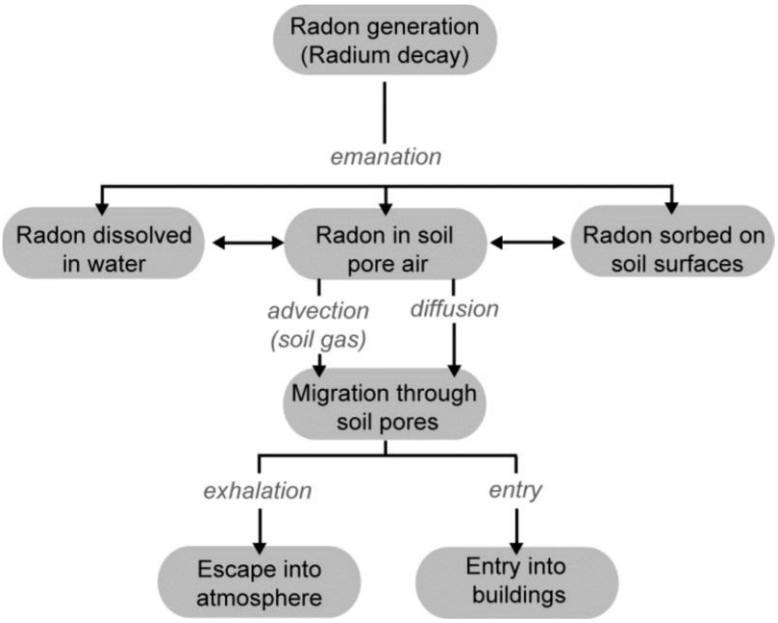

Fig. 1.3: Schematic representation of radon generation and migration in the soil and its entry into the atmosphere or buildings (after Nazaroff *et al*., 1992).

1.3 Factors affecting radon/thoron exhalation

Considering the influence of external factors is a must when the aim is to develop a causal relationship between radon and geophysical phenomena as the exhalation process is also significantly affected by other parameters. One such major factor and the most important is meteorological factors. Besides the meteorological factors, the radon exhalation process is also affected by the physiochemical feature of the soil (such as grain size, density, porosity, permeability, mineral content, presence of radioactive elements (uranium, thorium etc.) underneath the soil) and geophysical factors (such as morphology, present of a geological fault, movement of ground-water and nature of aquifer). Having failed to remove components of such effect from the radon data will mask its genuine real geophysical characteristics and may result in false prediction (Ramola *et al*., 2008; Walia *et al*., 2003). As far as the study is confined to observing geophysical properties of radon data the effect due to physiochemical features of the soil and geophysical factors can be neglected if the monitoring station and region are pre-surveyed. It must be confirmed that the monitoring station is free from or minimally affected by such factors before starting continuous monitoring. In the present thesis, the monitoring station is pre-surveyed

by carrying out mass exhalation rate measurement at a different selected location in a fault region. The location having the highest and most stable mass exhalation rate after several measurements were selected for the monitoring station. It affirmed that the location was hardly affected by physiochemical features and geophysical factors but probably by geophysical phenomena and meteorological factors.

The meteorological factor of air temperature caused soil-gas radon to expand and thereby enhancing its exhalation (Segovia *et al*., 1987; Singh *et al*., 1988; Virk *et al*., 2000). Hence air temperature has a positive correlation with radon. The barometric pressure exhibits a pumping effect on soil radon data, that is, with the rise in pressure poor air radon gets pushed into the soil and hence diluting its concentration (Gingrich, 1984; King, 1984). Rainfall exhibits a capping effect on radon exhalation, heavy rainfall clogged soil pore and prevent soil radon from escaping to the atmosphere hence reducing its exhalation (King, 1984; Virk *et al*., 2000). Presence of humidity up to 15-17% by weight (optimum level) (Stranden *et al*., 1984) in the soil enhanced ^{222}Rn emanation by absorbing its recoil energy which prevent it from burying in the adjacent soil grain (Asher-Bolinder *et al*., 1991). The speeding wind was found to remove radon gas from the upper surface of the soil and hence reducing its concentration (Gingrich, 1984; Virk *et al*., 2000; Walia *et al*., 2005). The influence of these meteorological factors and that of tidal forces appears as a periodic or quasi-periodic component in the time series radon/thoron data due to their diurnal, semi-diurnal, seasonal and monthly variation. Removal of periodicities in the radon/thoron time series data was failed so far by many researchers, especially of this region who used linear analysis techniques. Since radon/thoron data are non-linear in nature application of linear technique leave uncertainties in the result. In this thesis, a non-linear analysis technique has been used to remove periodicities in the time series radon/thorn data hence any observed anomalies in the time series data may be regarded solely due to geophysical phenomena of the region.

1.4 Mechanism of the geophysical process (earthquake) and radon

Several premonitory signs have been observed before an earthquake from an early time. Such indicator includes observation of animal behaviour, pattern recognition,

recurrence intervals, crustal movement, anomalous changes in phenomena such as tilt, fluid pressure, electric and magnetic fields, radon emission, frequency of occurrence of small local earthquakes, ratio of the number of small to large shocks etc (Scholz *et al*., 1973). But scientists of the time from USSR and Japan were sceptical and uncertain about the validity and practical reality of these effects. Because many of the above-mentioned premonitory effects though able to describe the location and size of a future earthquake were not able to predict the time of the event. Such that a meaningful earthquake prediction must consist of (1) the time of occurrence with small uncertainty (2) the location and magnitude with small uncertainty (3) statistical investigation based significant information about the occurrence of the earthquake. Based on the time span prediction may also be categorized into (1) long-term (many years) (2) midterm (months to 1 year) (3) short-term (days to weeks) and (4) immediate (hours to one day). During the 1960s and 1970s premonitory changes in the ratio of seismic compressional velocity to seismic shear velocity (v_P/v_S) was observed by seismologist in Garm region of USSR, Adirondack region of New York State and San Fernando California. To assess the prediction time, place and magnitude of an earthquake Scholz *et al*. (1973) emphasized the necessity of an observation program, reduced data and research. They (Scholz *et al*., 1973) also suggested that the mechanism of premonitory changes that lead to prediction seems deterministic rather than probabilistic. To explain the above-mentioned premonitory ratio (v_P/v_S) changes a model called Dilatancy model has been proposed (Friedmann, 2012). The theory is developed between 1970 and 1985 and is based on a Laboratory fracture study and states that rock undergoes inelastic volumetric changes prior to failure. Literally, Dilatancy means an elastic increase in volume under stress as shown in Fig. 1.4.

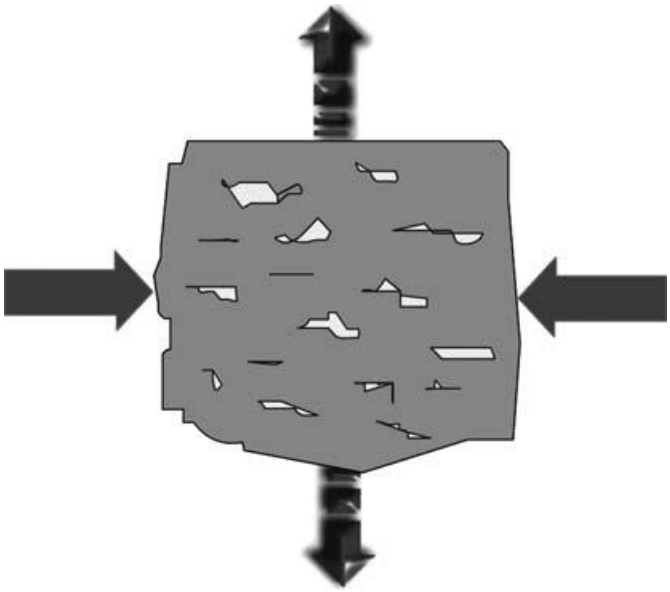

Fig. 1.4: Dilatancy: increasing stress causes cracks in the rock, which enlarges the material perpendicular to the main axis of stress. This causes an effective increase in volume (after Friedmann, 2012).

The Dilatancy theory states that increasing stress results in cracks in the rock materials which in turn cause the material to expand perpendicular to the main axis of stress. The theory consists of two other sub-theories namely the Dilatancy-diffusion theory and the Dilatancy-instability theory. According to the Dilatancy-diffusion theory, there is an additional grease effect by water and/or gases penetrating into the open crack in the last stage of preparation before an earthquake. The Dilatancy-instability theory on the other hand suggested exponential fracturing above a certain stress level at the last stage of preparation before stress release. As mentioned elsewhere, in an undisturbed borehole the radon concentration is a function of depth and is close to zero at the surface. It acts as an indicator for changes in gas streams in the earth's crust and the most suitable depth for detecting such changes is between 0.5 and 1 m depth (Friedmann, 2012). According to the Dilatancy theory due to substantial changes in the rock properties shortly prior to the earthquake either Dilatancy-diffusion or Dilatancy-instability processes or both processes will take place. In both processes, a significant amount of masses were moved resulting in the movement of the subsurface toward the ground surface.

Consequently, opening of new cracks, widening or closing of old cracks or redistribution of open and closed cracks can happen. In dry rocks, opening or closing of cracks will lead to significant changes of the diffusion coefficient of radon. Volumetric changes in the rock will also lead to a subsurface gas flow and therefore to additional radon transport. In case the new open cracks get filled with water the increased water-rock interface leads to an increase in radon emanation from the rock matrix to the water. On the other hand, if the water-filled cracks get close, the water will be compressed to another subsurface volume where the emanation from the rock to the water may be different. All these processes lead to pressure and water level variations in the relevant aquifer. It may also result in changes in the mixing ratios for the water which can be observed at the earth's surface. Finally, Imme and Morelli (2012) mentioned that gas flows can also result in the movement of some groundwater hence all previously discussed mechanisms which are consequences of the redistribution of water in the earth's crust can take into effect. The main drawback of this theory is that it is confined to a small volume surrounding the impending earthquake and is not applicable to far locations where other geochemical anomalies occur. Another drawback of this theory is the influence of the environment especially meteorological factors when the considered gas is radon in particular. Fluctuations in air temperature and pressure will disturb the radon concentration near the ground surface while precipitation and humidity may change the permeability of the soil which may affect soil gas radon concentration.

Anderson and Grew (1977) and Atkinson (1984) proposed more realistic explanations for rock fracturing in the study of stress corrosion cracking and subcritical crack growth respectively. These studies have shown that moisture content can influence crack propagation and under moderate to high-level humidity influence crack growth can take place at very low strain rates. The phenomena were suggested to be useful for many of the ground gas anomalies monitored as the substantial distance from impending earthquakes by Thomas (1988). Because the observed radon anomalies are due to slow crack growth controlled by stress corrosion in a rock matrix saturated by ground waters. Again another form of radon gas emission method known as the compression mechanism was proposed by King

(1978). The mechanism suggested that anomalies in the radon emission may be due to the crustal compression before an impending earthquake that squeezes out soil gas into the atmosphere at an increasing rate. Despite the proposal of several models for geochemical precursors and their relation with earthquakes, probably all of them are associated with one of the following mechanisms (Thomas, 1988).

- Physico-Chemical release by ultrasonic vibration (UV model).
- Chemical release due to pressure-sensitive solubility (PSS model).
- Physical release by pore collapse (PC model).
- Chemical release by increased loss from, or reaction with, freshly created rock surfaces (IRSA model).
- Physical mixing due to aquifer breaching/fluid mixing (AB/FM model).

Numerous empirical relations between radon anomaly and earthquake parameters have been proposed in the past. Some notable relations are described as follows. The relation between precursor time (*T*) and earthquake magnitude (*M*) was proposed by Rikitake (1976) as given in equation 1.3.

$$\log T = 0.76M - 1.83 \tag{1.3}$$

Sultankhodzhayev (1984) proposed a relation between earthquake magnitude (*M*), precursor time (*T*) and the epicenter distance (*R*) based on the radon data in a seismically active zone of Central Asia as,

$$\log RT = 0.63 \pm 0.15 \tag{1.4}$$

Dobrovolsky *et al.* (1979) and Fleischer (1981) proposed empirical relation within which the earthquake preparation zone may be manifested by considering the strain field model as.

$$R = 10 \exp 0.43M \qquad \text{(Dobrovolsky } et\ al.\text{, 1979)} \tag{1.5}$$

$$R = \left(10 \exp 0.48M\right)/1.66 \text{ for } M>3 \qquad \text{(Fleischer, 1981)} \tag{1.6}$$

Where R is the epicenter distance in km and M is the magnitude of the earthquake on Richter scale. Virk (1996) further modified the above relations by considering 142 case studies in N-W Himalayas, India as

$$R = \left.\begin{array}{l} 10\exp 0.32M \ \ (10 < R < 50) \\ 10\exp 0.43M \ \ (50 < R < 100) \\ 10\exp 0.56M \ \ (100 < R < 500) \\ 10\exp 0.63M \ \ (500 < R < 1250) \end{array}\right\} \tag{1.7}$$

1.5 Mechanism of earthquakes

The geophysical processes particularly earthquakes predominantly occur along the active fault zones. Variation of radon along such zone is higher and acts as a useful indicator in earthquake precursory studies (Vaupotic *et al*., 2010). The mechanism and background of earthquakes can be explained on the basis of plate tectonics which starts from deep within the earth. The earth is comprised of three distinct layers namely the crust, the mantle and the core. The crust has an average thickness of 5 km and forms the outermost layer of the earth exposed to the atmosphere. The next layer just below the crust is the mantle whose brittle solid upper part with the crust constitutes the *lithosphere*. Again the *lithosphere* is bounded by the atmosphere above and *asthenosphere* below which is partially molten parts of the mantle. The *asthenosphere* contains partially molten rocks which are ductile (folds, stretch, compress and flow without fracturing) and experience aseismic slip. On the other hand, the lithosphere is rocky, brittle and able to sustain tremendous shear stress and can undergo fracture and seismic slip. It is the upper 10 km of the lithosphere which practically is the crust where earthquakes occur due to tectonic movement. As mentioned above the lithosphere is brittle and breaks into thick moving slabs called tectonic plates. Now, these different tectonic plates float over the asthenosphere which is in the molten state. These freely floating plates collide and interlock each other resulting in shear stress by definite yet unseen forces. The release of this build-up stress is how an earthquake happens in the lithosphere. The mobile rock beneath the rigid plates is being heated by the radioactive decay of naturally occurring chemical elements (such as uranium, thorium and potassium) and by the gravitational

energy left over from the formation of the earth (residual heat). There is a huge temperature difference between the upper and lower layer of the mantle which is about 1315.6 ^{0}C. This temperature difference results in a convective flow of molten rock in the mantle like asphalt under heavy weight. Again this moving mantle results in the fracture of the above brittle lithosphere and leads to the formation of tectonic plates and consequently to an earthquake. Just below the mantle is the core of the earth having a temperature of about 5500 ^{0}C. It is further divided into a liquid outer layer and a metallic solid inner core. A geologic map showing different tectonic plates of the earth is shown in Fig. 1.5.

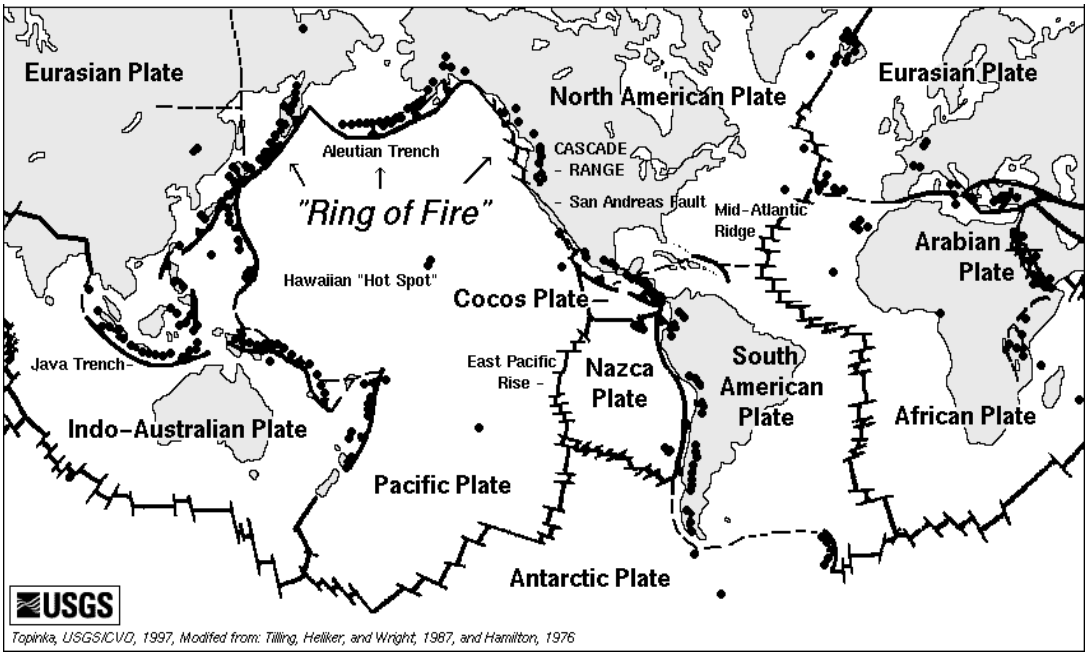

Fig. 1.5: A map of tectonic plates which make up the earth's crust.

1.5.1 Forces on the earth's crust

Rocks of the lithosphere (crust and upper mantle) were constantly subjected to forces produced by plate tectonics due to their mutual gradual movement. Those rocks located along the boundaries of any two plates of the crust often resist movements. When tectonic plate slide past each other the relative constant gradual slip accumulate a relative motion at rates of the order of millimetres per year. On some other occasions, the accumulated strain is released with slip rates of the order of

meters per second as an earthquake (Kanamori and Brodsky, 2004). As a result of resistance by the rocks, stress builds up along the fault plane until it reaches the breaking strength of the rock. After attaining the breaking strength an earthquake occurs, the stress is relaxed and a new cycle begins. Stress is defined as the force per unit area developed when two tectonic plates collide or press each other. Depending on how the edges of the tectonic plate meet and direction of their motion different types of stress may act on earth's rocks as depicted in Fig. 1.6.

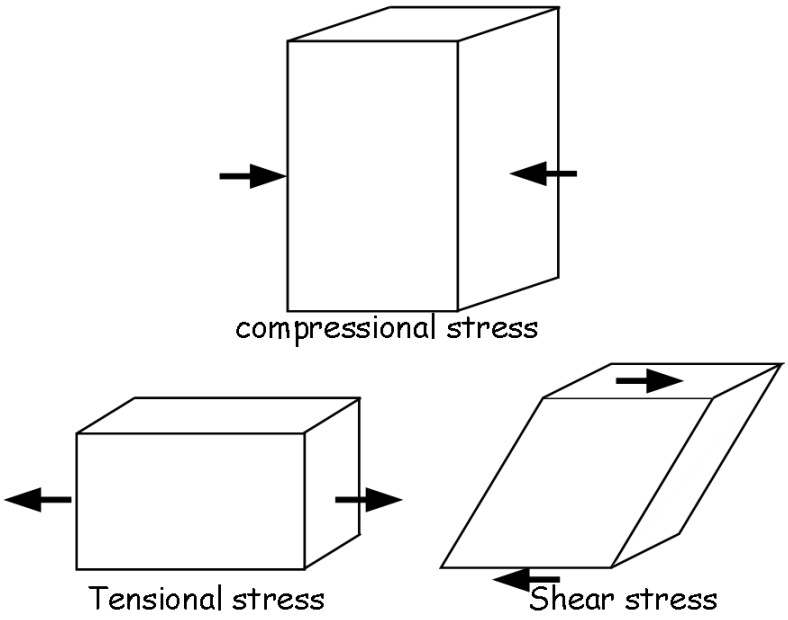

Fig. 1.6: Types of stresses acting on a material.

When the stress due to tectonic plate movement squeezes the rock and causes decrease in the volume of the material it is called compressional stress. But when the stress stretches the rock it is called tensional stress and when the stress results in slippage and translation it is called shear stress. The mentioned changes in shape, size and volume were referred to as strain. The strain is mostly expressed in percentage without any attached metric unit such as per cent change in length, volume or shape etc. When stress is experienced by a rock, it undergoes several successive segments of deformation as shown in Fig. 1.7.

- Elastic deformation: Elastic deformation takes place when the experience stress is low and the strain is reversible.

- Plastic deformation: This type of deformation occurs when the applied strain is greater than the strength of the rock. The strain is irreversible as the applied stress rapture the rock and causes permanent deformation even when stress is reduced to zero. The point of rapture is called the failure and is designated by the 'X' on the graph.

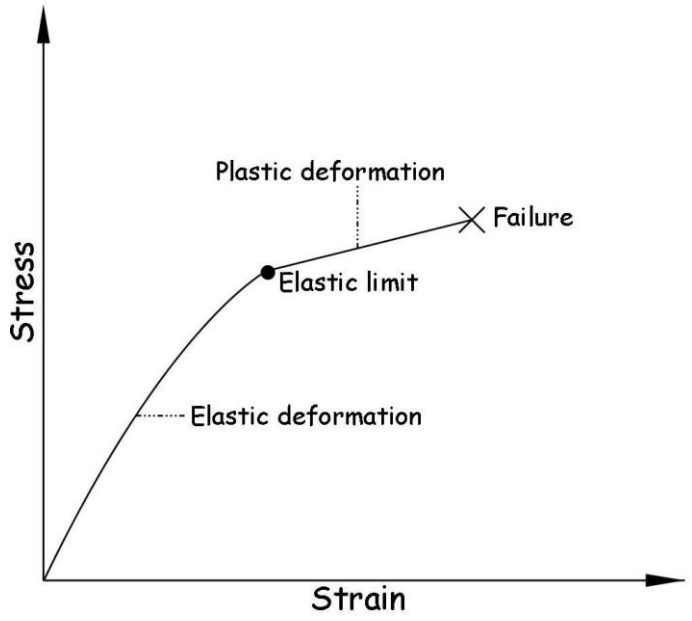

Fig. 1.7: A typical stress-strain curve.

1.5.2 Faults

A fault is characterized by a region constituting fractured materials, gouges and fluids. It is also identified as a least strength zones capable of impacting geochemical anomalies. The active tectonic region has a causal relationship with instabilities in the crustal fluid resulting in fluid flow which in turn impact faulting as they influence the strength of the fault (Bernard *et al*., 1996). Most earthquakes are due to stress release caused by sudden slippage along a fault. In other words "stick-slip" frictional instability along pre-existing faults is responsible for a slip of fault resulting in earthquakes (Brace and Byerlee, 1966). Due to its loose soil formation fault gouge offers a suitable path for gas leakage which is enhanced by soil permeability. King *et al*. (1996) suggested that the presence of fault gouge leads to low permeability zone when measured radon is soil across a creeping fault. At the

same time, Wood *et al*. (1994) suggested that soil gas anomalies depend on the types of fault (such as reverse or normal faults). King (1986) also mentioned that if the former stress with abundant pore fluid in pre-existing faults reaches near the critical level amplification of gas anomalies may be observed. The exact point inside the earth where the fault rapture takes place is called the focus or hypocenter. The point on the surface, directly above the focus is called the epicenter. Depending on the direction of relative displacement or slip faults can be classified into three different types (Fig. 1.8). The fault which arises due to horizontal and vertical compression is called a reverse fault. This type of fault pushed up the rock on one side of the fault relative to the other side and squeezes it which leads to the shortening of the crust. In case of normal fault associated movement is partly horizontal and partly vertical. The horizontal movement pulls the rock apart and stretches the crust resulting in relative downward movement of rocks of the other fault. Strike-slip faults on the other hand are caused by horizontal shear. The associated movement of this fault is mainly horizontal and in opposite directions.

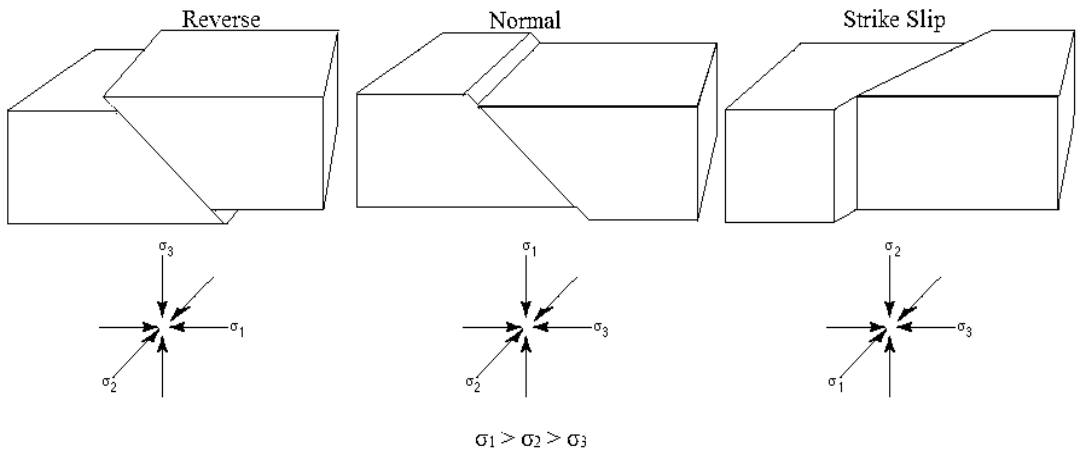

Fig. 1.8: Schematic of the orientation of the principal stresses and the corresponding type of faulting.

1.5.3 Energy generated during faulting

The forces generated in the earth's crust are typically described in terms of the shear stress and the shear strain. The movement of fault during an earthquake can

be viewed as a frictional sliding on a fault plane. The friction changes as a function of slip of two sides of the fault plane, velocity and history of contact. For the occurrence of an earthquake, the friction must decreases rapidly with the slip, which is referred to as slip-weakening (Kanamori and Brodsky, 2001). Hence the existing forces within the earth's crust can typically be described in terms of shear stress and shear strain. An illustration of the simplified geometry of a slab of crustal rock is shown in Fig 1.9. At the plane's boundary of the slab, equal and opposite forces act tangentially. From the top figure of Figure 1.9 it can be seen that one plane is displaced downward by a distance 'y' relative to the other. The separation distance of the two planes is 'x'. Hence the strain in the slab is y/x. Consequently, the ratio of stress to strain is called the rigidity of the slab material (μ). In the earth's crust, there are planes that can support only relatively low stresses before rupturing called fault planes.

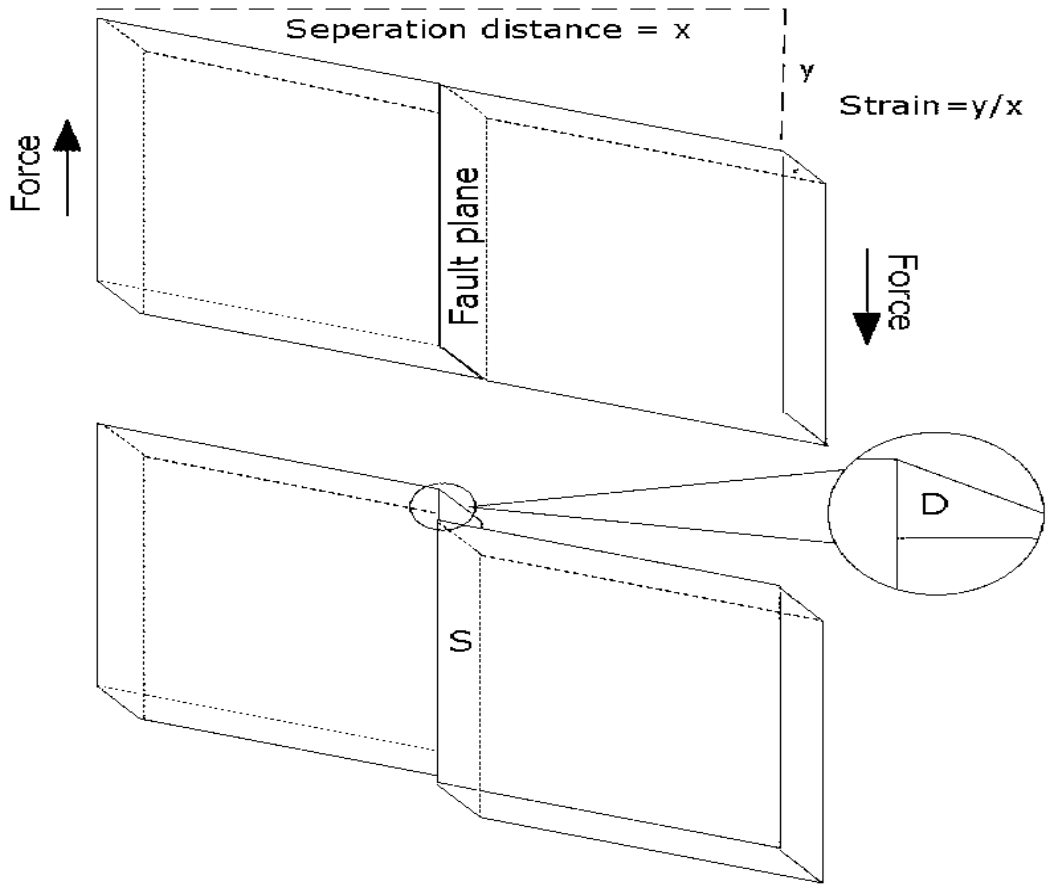

Fig. 1.9: A slab of crustal rock with two equal and opposite forces acting tangentially (after Kanamori and Brodsky, 2001).

Consider a simple and uncomplicated stress-release model (Kanamori and Heaton, 2000). Plot showing stress on the fault plane as a function of slip is shown in Figure 1.10. An earthquake happens when the static frictional stress (shear stress), σ_o is exceeded by the stress on the fault plane. As shown in Figure 1.9 tectonic plates on either side of the fault experience a relative slip (D over an area S). At the start of an earthquake, the initial shear stress σ_o drops to a constant dynamic friction σ_f. In the end, the stress on the fault plane is σ_1 (final stress) and the average slip offset is D. In Fig. 1.10a, it is represented as $\sigma_f = \sigma_1$. The dynamic stress drop, $\Delta\sigma_d = \sigma_o - \sigma_f$, initially drives the sliding. The sliding stops when the shear stress drops below a final frictional stress, σ_1. A variety of mechanisms can stop sliding, such as geometric and compositional heterogeneity, dynamically changing velocity or history-dependent friction and so σ_1 is not necessarily equal to σ_f (Kanamori and Brodsky, 2001). The difference between the initial and the final frictional stresses is the static stress drop, $\Delta\sigma_s = \sigma_o - \sigma_1$.

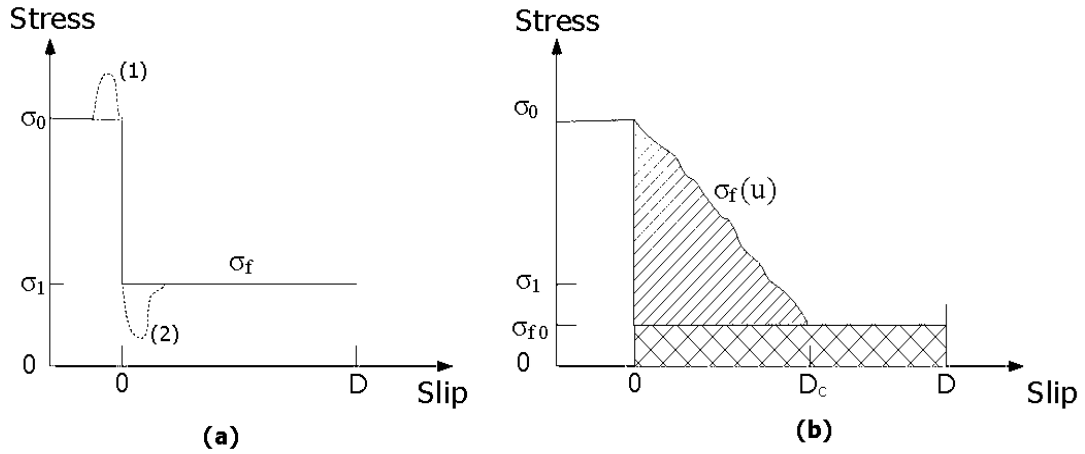

Fig. 1.10: Illustration of simple stress release pattern during faulting. (a) Simple case. (b) Slip-weakening model. Hatched and cross-hatched areas indicate fracture energy and frictional energy loss.

The overall size of the earthquake is the seismic moment defined by $M_o = \mu SD$. The seismic moment is measured in energy units, but it does not directly represent the energy released by an earthquake. The magnitude *M*, of an earthquake, is given in terms of the seismic moment (Kanamori and Brodsky, 2001),

$$M = \left(\log M_o - 9.1\right)/1.5 \; (M_o \; in \; Nm) \tag{1.8}$$

During the process of an earthquake, the potential energy (strain energy plus gravitational energy) of the system, *W*, drops to $W - \Delta W$ where ΔW is the strain energy drop and the seismic wave is radiated carrying energy E_R. Then the energy budget can be written as (Kanamori and Heaton, 2000),

$$\Delta W = E_R + E_F + E_G \tag{1.9}$$

where $E_F = \sigma_f DS$ is the frictional energy loss, E_G is the fracture energy, and $\Delta W = \left(\sigma_o - \sigma_1\right)/2$ (Knopoff, 1958; Dahlen, 1977). Therefore, Eq. (1.9) becomes,

$$E_R = \left(\sigma_o + \sigma_1\right) DS/2 - \sigma_f DS - E_G = \frac{1}{2}\left(2\Delta\sigma_d - \Delta\sigma_s\right) DS - E_G$$

$$= M_o \left(2\Delta\sigma_d - \Delta\sigma_s\right)/2\mu - E_G \tag{1.10}$$

For large and shallow earthquakes E_G can be ignored (Heaton, 1990), and Eq. (1.10) can be written as,

$$E_R = M_o \left(2\Delta\sigma_d - \Delta\sigma_s\right)/2\mu \tag{1.11}$$

Stress variation during faulting can be more complex than as shown in Fig. 1.10a. It may increase at the beginning of the slip motion (curve (1) in Fig. 1.10a) because of loading caused by advancing rapture or of the state-rate dependent friction law (Dieterich, 1979). Also, the friction may not be constant during faulting. It may drop drastically in the beginning and later resume a larger value (curve (2) in Fig. 1.10a) or, it may decrease gradually to a constant level (Fig. 1.10b). If the friction is not constant, σ_f drops to a constant value σ_{fo} until the slip becomes D_c. The final stress σ_1

can be different from σ_{fo}. Then the average friction $\bar{\sigma}_f$ is given by (Kanamori and Heaton, 2000),

$$\bar{\sigma}_f = \frac{1}{D}\int_0^D \sigma_f(u)\,du \tag{1.12}$$

where u is the slip (offset) of the fault plane. Then Eq. (1.11) can be written as,

$$E_R = M_o\left(2\Delta\bar{\sigma}_d - \Delta\sigma_s\right)/2\mu \tag{1.13}$$

where, $\Delta\bar{\sigma}_d = \sigma_o - \bar{\sigma}_f$.

1.6 Models

Several discrete models explaining the critical state of the earthquake preparation process have been proposed. Some of such proposed models were discussed below.

1.6.1 The IPE model

The IPE model was first put forward at the Institute of Physics of the Earth by Moscow Soviet scientists. It is based on the concept of fracture mechanism and briefly summarized by Mjachkin *et al*. (1975) as follows:

- Fractures of statistically heterogeneous materials are caused by the increase in the number and size of crack-like defects.
- The defects may develop in time under approximately constant stress and the rate of their formation increases with the increase of stress.
- The total deformation consists of intrinsic elastic deformation and deformation caused by the mutual displacement of crack edges.
- Macro facture (development of the main fault) is the result of avalanche-like growth and resulting instability which occurs on reaching a certain density of cracks.
- Formation of the main fault results in the decrease of stress level in the surrounding volume; as a result, the growth of new defects stops and the number of active cracks is decreased.

- The fracture process does not depend strongly on a scale.

Taking into account the above mentioned points earthquake preparation process can be elaborated as follows. Inherently randomly distributed defects called micro-cracks are always present in rocks. The number and size of such defects with desirable orientation slowly multiply under the influence of tectonic shear stress. Formation of cracks takes place for the entire volume in case the media is statistically homogenous. This uniformity in cracking is also known as quasi-homogenous and corresponds to the formation of stable tension cracks at the end of shear stress (Brace and Bombolakis, 1963). At this stage changes in medium properties were expected such as effective modulus of elasticity and anisotropy. The deformation process through different stages of the earthquake preparation zone is shown in figure 1.11. In figure 1.11, stage I is identified by uniform cracking and no indicatory precursors is yet developed. Stage II occurs when most of the medium volume attained a certain critical average density of cracks. These cracks interact among themselves and cause stage II to accelerate (or avalanche) (Finkel, 1970). The accelerating cracks in stage II lead to a sharp increase in the rate of total deformation and also to sudden changes in the physical characteristics of the medium. In case the processes in this stage result in an earthquake then it is by definition, unstable. It means that the further increase of deformation is accompanied by a decrease in stress. The medium being heterogeneous, unstable deformation is restricted to a narrow zone where several relatively large cracks are formed. At this moment the material literally divides into two parts as shown in Fig. 1. 1.12. In narrow zone A, The process of unstable deformation occurs within a narrow zone (A) while the loads drop in the surrounding zone (B). Development of cracks in zone B ceased due to a general decrease of stresses in stage III. The deformation rate of the whole zone is slowed down during this stage of instability.

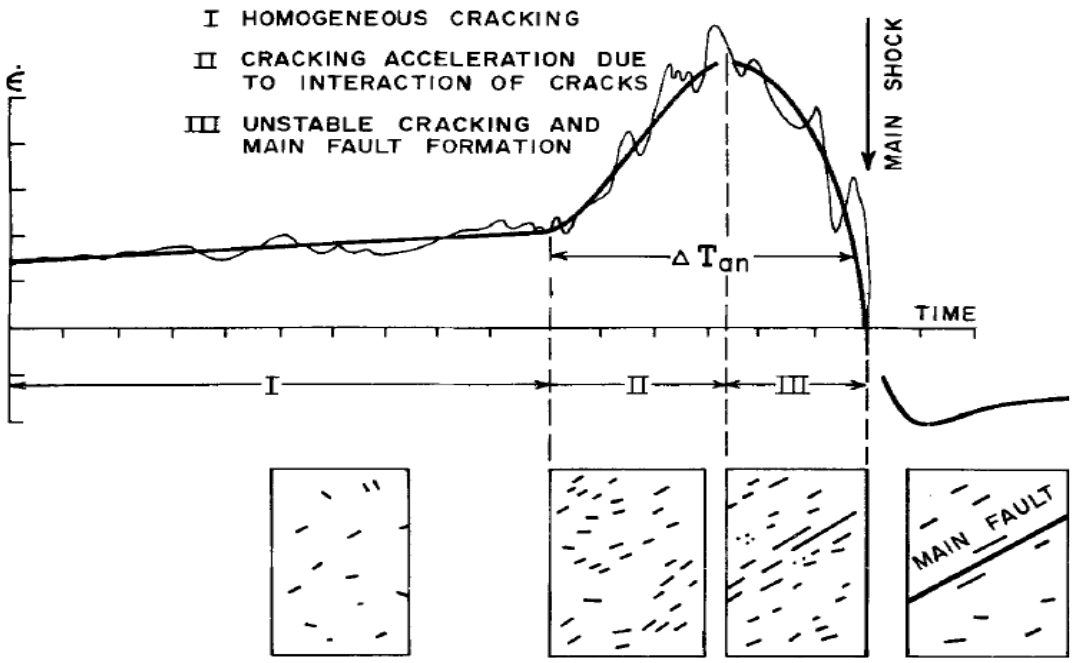

Fig. 1.11: Change of average deformation velocity during the seismic cycle (from Mjachkin *et al*., 1975).

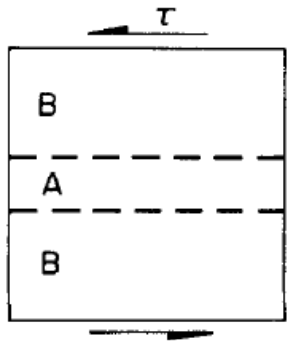

Fig. 1.12: An ideal scheme of formation of the zones of unstable deformation. A-zone of unstable deformation, B-zone of unloading (from Mjachkin *et al*. 1975).

At the same time restoration of many original characteristics of the rock takes place. Zone A is also characterized by an increased concentration of small faults parallel to the future main fault. It is assumed that during an earthquake collapse of solid materials between the small faults formed the main fault. Qualitatively it can be speculated that the growth or extension of small cracks in stages II and III is analogous to the formation of the main fault. Hence all of those small events, too,

must be preceded by a short-term, small-amplitude change of deformation velocity. Such indicatory fluctuations might appear as foreshocks to the main event and acts as a short-term precursor (Mjachkin *et al*., 1975) represented by the thin line in Fig. 1.11. The amount of cracking of rocks is related to increased radon content, increased flow of spring etc. which sharply increased at stage II and flatten out at III. The fall of such a process can be expected before an earthquake when small cracks become closed.

1.6.2 The Dilatancy-Diffusion Model

Enormous effort has been devoted to explain earthquake precursors based on Dilatancy and fluid flow model since 1971 by U.S geophysicists. The term Dilatancy stands for a non-elastic increase in volume under stress. Change in the dilatants volume in soils is characterized by void space between the grains whereas in rocks it takes the form of new cracks which open up between the grains (Mjachkin *et al*., 1975). It is in accordance with the laboratory experiments by Brace *et al*. (1966) which show that the rock uniaxial compression undergoes a volume expansion just prior to fracture. In the case of rock masses there can be two types of dilatant cracks- firstly a large-scale version of the micro-crack having the same relation to the principal stresses as dilatant micro-cracks. Secondly, a large-scale version of a dilatants crack might be along those joints, fault oriented in the appropriate direction relative to maximum compression. Nur and Simmons (1969) highlighted that cracks in dry rocks have significant effects on seismic velocities. Formation of new cracks and/or the enlargement of old cracks might cause decrease in velocity and V_P/V_S ratio prior to thrust-type earthquakes (Nur, 1972; Whitcomb *et al*., 1973). Presence of water or a mixture of water and /or air vapour in the dilatant cracks might strongly influence the effect of dilatancy on velocity (Nur, 1972). Thus changes in V_P/V_S ratio should be reversed in both the two cases.

Different steps for understanding the model as a whole were put forward by Scholz *et al*. (1973) as follows and depicted in Fig. 1.13.

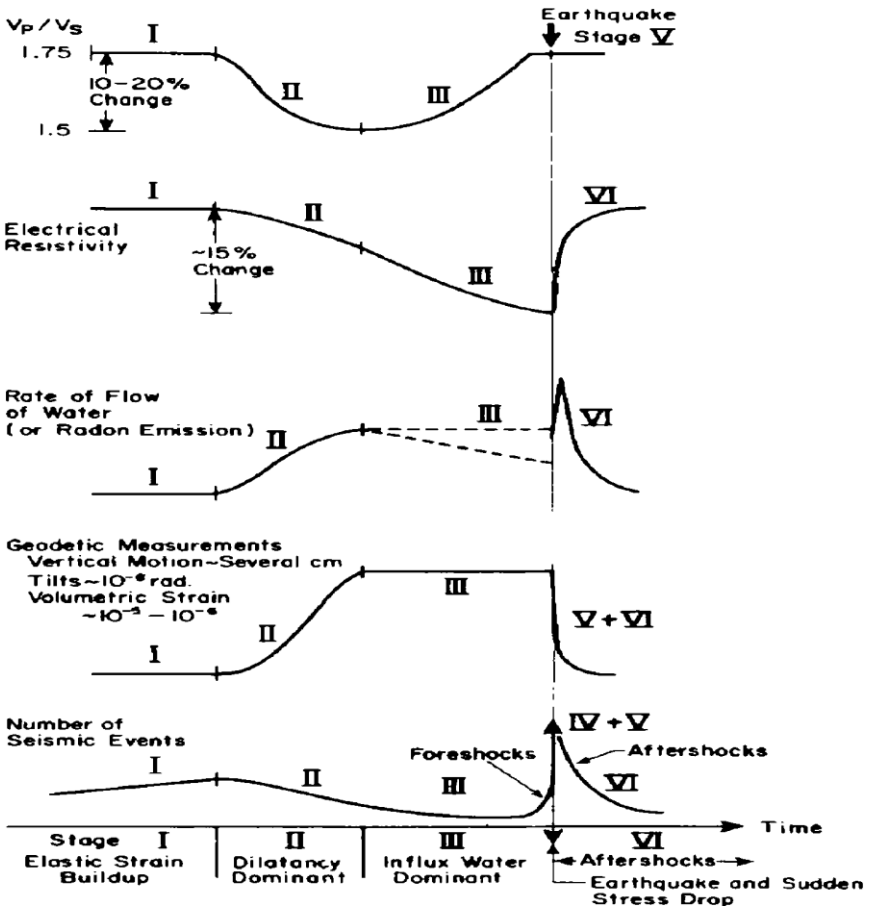

Fig. 1.13: Predicted Changes in various physical parameters as a function in time during the earthquake cycle for the dilatancy model (from Scholz *et al*., 1973).

At stage I no dilatants cracks have been formed or begun to open despite the increasing stress. In stage II the dilatants cracks began to form and become under-saturated. Several changes in physical properties such as velocity and resistivity take place at this stage. In stage III the physical properties return to their initial level as water re-enters the dilatants rocks. The re-entering of water as well as the rise in the pore pressure lowers the effective confining pressure. This phenomenon accelerates the fracture and frictional sliding resulting in an earthquake at the end of stage III. Anderson and Whitcomb, (1973) presented the detailed effect of pore fluid on seismic velocities as shown in Fig. 1.14.

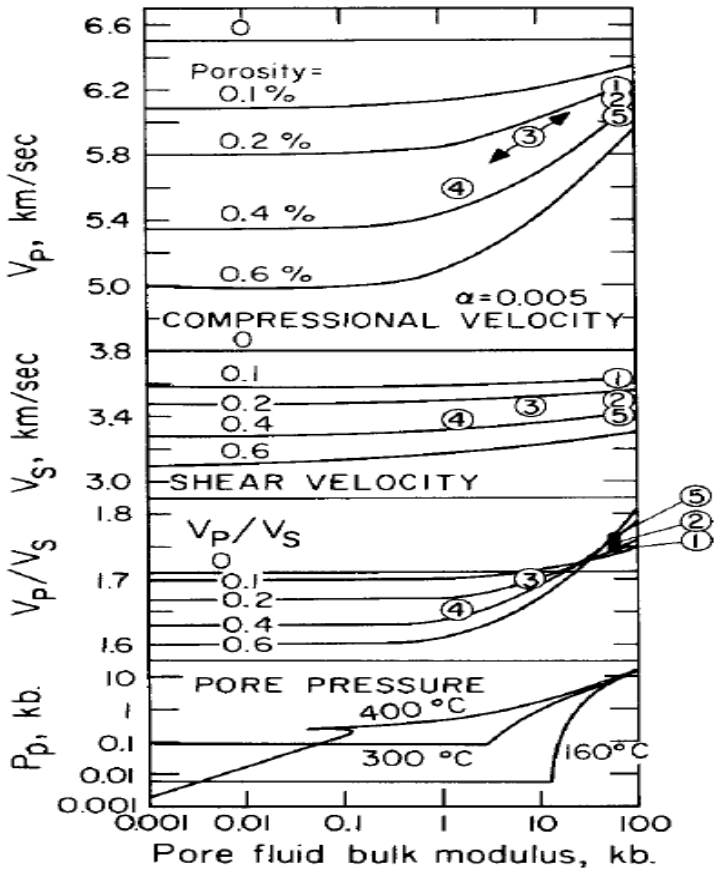

Fig. 1.14: Compression velocity (V_P), shear velocity (V_S) and V_P/V_S as a function of pore fluid bulk modulus and porosity. The lower panel gives the pore fluid bulk modulus as a function of pore pressure (P_P) and temperature. Circled numbers refer to successive stages from the onset of dilatancy 1 to fracture 5 with initial porosity of 0.2% (after Anderson and Whitcomb, 1973).

In figure 1.14 the different stages during dilatancy are represented by different curves with numbers. The initial stage of dilatancy is represented by stages 1 and 2 where the porosity increases slowly with time so that there is no change in the pore pressure. The velocity gradually increases and hence V_P/V_S increases slightly. The porosity increases during the accelerated dilatancy period such that the pore fluid bulk modulus decreases and the velocity drop rapidly to stage 3 and subsequently down to stage 4. The region between stages 4 and 5 is the region of anomalous seismic velocity where the rock's deformation strengthens due to lower pore pressure and higher effective pressure. Despite continuous increase in porosity, the velocity

will increase until fluid flow into the anomalous region. Then after attaining the critical value of the pore pressure the fracture/slipping of rocks takes place.

Mjachkin *et al*. (1975) give a brief comparison between the IPE and DD models which includes the following points-

- According to the IPE model, the earthquake occurs as a fault is formed; it involves fracture of intact rock on a large scale comparable with the dimensions of the main rapture. This might involve either new faulting, the extension of an old fault into new rock, or the re-fracture of a healed fault. According to the DD model, an earthquake can result from motion on a pre-existing fault; it does not require large-scale fracture.
- In the IPE model, the earthquake occurs after a stress drop having a duration of approximately half the anomaly time. The main earthquake occurs at significantly less than the maximum stress prior to the earthquake. By contrast, the earthquake in the DD model occurs near the peak stress.
- In both models, cracks develop uniformly at first over some volume of rock adjacent to the future rapture surface. In the IPE model cracks of a different orientation form in a zone near the fractured fault (zone A in Fig. 1.12) just before the earthquake, even in the central part of a long fracture fault. No such zone is required according to the DD model; cracks may enlarge prior to the earthquake but orientation should remain the same throughout the anomalous period.
- Pore fluids play a central role in the DD model whereas they are not required in the IPE model.
- In the IPE model, the cracks which form in response to stress have an orientation parallel to the main fault prior to the earthquake. In the DD model cracks are parallel to the plane of the least compression and thus inclined to the main fault.

1.6.3 Slider-Block Model

The sliding-Block model was first proposed by Burridge and Knopoff (1967). It is a spring block model having the most direct relevance to the behaviour and

understanding of earthquake faults. It is a relatively simple deterministic model consisting of massive blocks of the same size and the masses connected to each other by springs with spring constant k_C. The entire mass-spring system is attached to a rigid plate and connected to the slider plate (with constant velocity V) via springs with spring constant k_L as shown in Fig. 1.15.

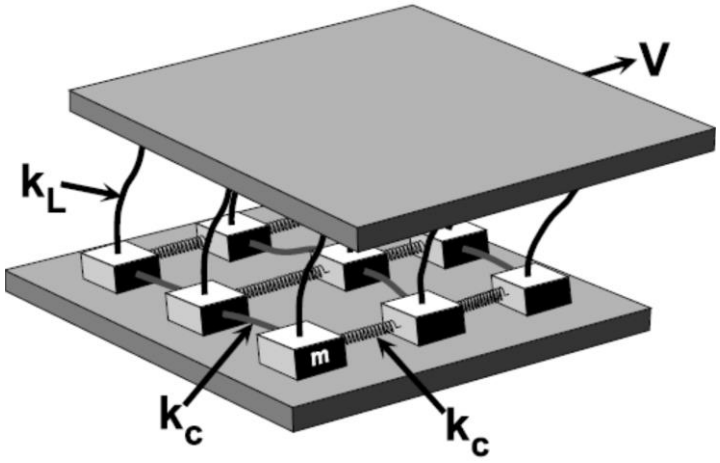

Fig. 1.15: Illustration of the two-dimensional slider block model (after Rundle *et al*., 2003).

When the mass-spring system is dragged on the fixed rigid plate by the driving plate, some blocks slip at regular intervals of time. The slip of a single block is interpreted as a small earthquake with the release of some potential energy. Sometimes, the slip of a single block will redefine the forces on its nearest neighbours and triggers the slip of adjacent blocks causing a large earthquake with larger amount of potential energy released (Kanamori and Brodsky, 2004).

A differential equation describing an interaction between the blocks can be developed by taking into account the spring stiffness, mass and friction. To derive the differential equation, consider a block of mass m dragged over a surface by a spring constant k_L attached to a driver plate with constant velocity V. Let's further consider a one-dimensional chain of slider blocks for the sake of simplicity (Fig. 1.16).

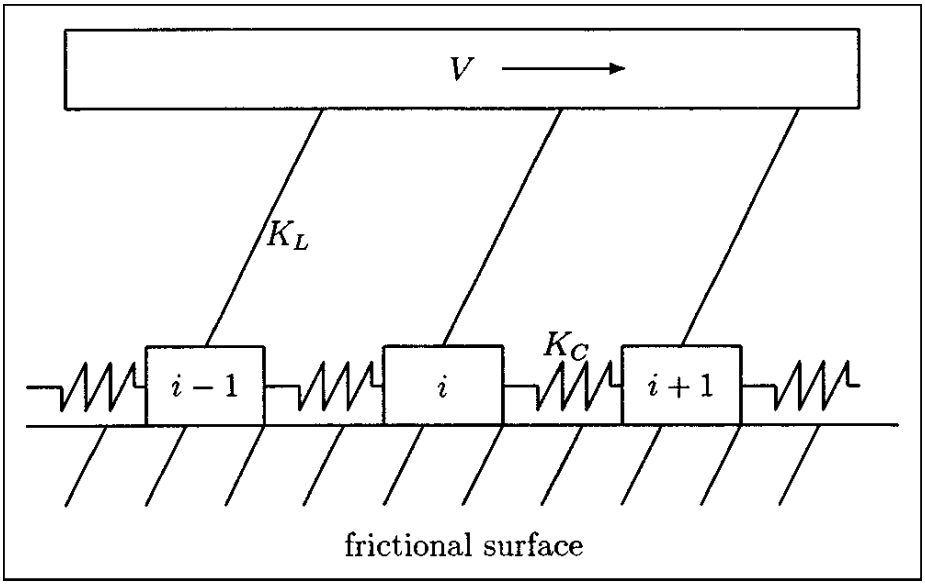

Fig. 1.16: Schematic of a simple one-dimensional slider block model.

The constraint imposed by the spring simplifies the dynamics by restricting the blocks to move along or opposite to the plate's motion. The velocity-dependent frictional force must decrease with an increase in the sliding block's velocity for the production of dynamic instability (Ferguson *et al*., 1998).

The total force acting on the i^{th} block is given by,

$$F_i = F_C + F_L - \Phi \tag{1.14}$$

where F_C is the force arising from the springs connected to the neighbouring blocks, F_L is the force due to the spring which connects the block to the driver plate and Φ is the velocity-dependent friction force acting on the block (Olami *et al*., 1992). According to Newton's second law of motion, the equation of motion for block *i* is,

$$F_i = m\ddot{X} \tag{1.15}$$

Now,

$$F_C = F_{i-1} + F_{i+1}$$

$$\Rightarrow F_C = k_C\left(X_{i-1} - X_i\right) + k_C\left(X_{i+1} - X_i\right)$$

$$\Rightarrow F_C = k_C\left(X_{i+1} - 2X_i + X_{i-1}\right) \tag{1.16}$$

And,

$$F_L = k_L\left(Vt' - X_i\right) \tag{1.17}$$

where X_i is the displacement of the block from the initial position and t' is the time. Substituting, Eq. (1.15), (1.16) and (1.17) in Eq. (1.14) we have the equation of motion as follows

$$m\ddot{X}_i = k_L\left(Vt' - X_i\right) + k_C\left(X_{i+1} - 2X_i + X_{i-1}\right) - \Phi\left(\dot{X}_i\right) \tag{1.18}$$

In order to make the equation dimensionless, the time t' is measured in units of characteristics frequency, $\omega = \sqrt{k_L/m}$ and the displacement X_i in units of length $L = \Phi(0)/k_L$, $\Phi(0)$ being the reference value of the friction force. The dimensional quantities can be written as follows (Kawamura *et al*., 2012),

- Dimensionless time: $t = t'\omega \quad \Rightarrow t' = t/\omega$
- Dimensionless displacement: $x_i = X_i / L \qquad \Rightarrow X_i = Lx_i = \dfrac{\Phi(0)}{k_L} x_i$
- Dimensionless stiffness parameter: $l = \sqrt{k_C / k_L}$
- Dimensionless loading rate: $v = V/\left(L\omega\right)$
- Dimensionless friction force: $\phi\left(\dot{x}_i\right) = \Phi\left(\dot{X}_i\right)/\Phi\left(0\right)$

Substituting these new quantities in Eq. (1.18) we get the dimensional equation of motion as,

$$\ddot{x}_i = vt - x_i + l^2\left(x_{i+1} - 2x_i + x_{i-1}\right) - \phi\left(\dot{x}_i\right) \tag{1.19}$$

The dimensionless friction force is given by (Carlson *et al*., 1991),

$$\phi\left(\dot{x}\right) = \begin{cases} \left(-\infty, 1\right], \text{ for } \dot{x}_i \le 0, \\ \dfrac{1-\sigma}{1 + 2\alpha\dot{x}_i/\left(1-\sigma\right)}, \text{ for } \dot{x}_i \ge 0 \end{cases} \tag{1.20}$$

The friction force is determined by two parameters, σ and α. σ indicates an instantaneous drop of the friction force and α represents the rate at which the friction force decreases as the sliding velocity increases. It is assumed that the loading rate v is infinitesimally small ($v = 0$) during an earthquake event (Mori and Kawamura, 2005).

1.7 Seismicity and geology of the Study Area

Northeast India and Mizoram in particular is one of the six most seismically active regions of the world along with Mexico, Taiwan, California, Japan and Turkey. The region is located at the junction of the Himalayan arc to the north and the Burmese arc to the east (Tiwari, 2002). According to BIS, (2002) Northeast India lies at zone V (the highest seismic level); the seismic zone map of India is shown in Fig. 1.17a. The collision tectonics between the Eurasian plate and Indian plate at the north and subduction tectonics at the east attributes seismicity of the region and is one of the most dynamic sectors of the present-day crust (Dewey and Bird, 1970; Kayal, 1996; Sarmah, 1999). The region belongs to the Surma basin which is part of the greater Bengal Basin. The basin is an area of folded sediment which is wider to the north and narrower to the south with many NE-SW and NW-SE trending lineaments/faults. The region is also characterized by westerly convex, sinuous structural ridges and valleys. The tectonic map of Northeast India and some major active faults are shown Fig. 1.17b. Based on the distribution of its epicentres, fault plane solutions and geotectonic features the NE-India was divided into five seismotectonic zones (Fig. 1.18) (Jaishi *et al*., 2014). They are as follows, (i) Eastern Himalayan collision zone (zone A) (ii) Indo-Myanmar subduction zone (zone B), (iii) Syntaxis zone of Himalayan arc and Burmese arc (Mishmi Hills, zone C) (iv) Plate boundary zone of the Shillong plateau and Assam valley (zone D) and (v) Bengal basin and plate boundary zone of Tripura-Mizoram fold belt (zone E).

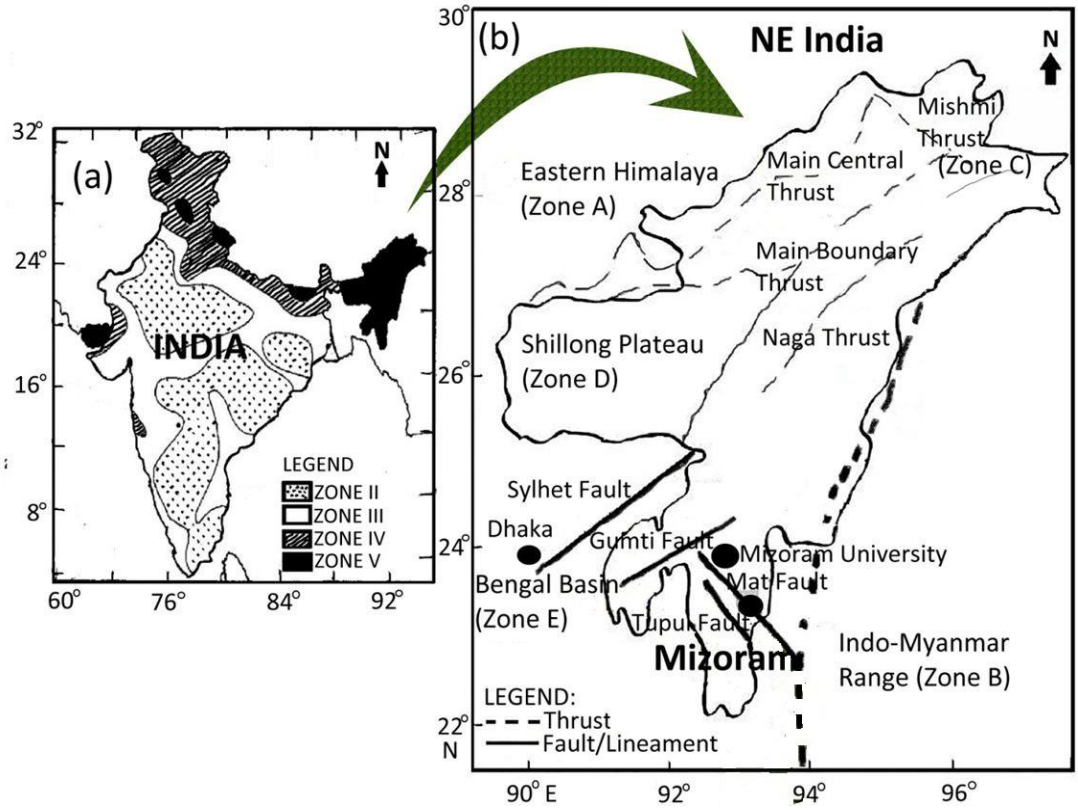

Fig. 1.17: (a) Seismic zone map of India and (b) northeastern India showing its different seismotectonic zones with major fault.

The NE-SW Syllhet fault running from near Dhaka (Bangladesh) demarcates the northwestern boundary of the Surma basin while the Gumti fault cut across the basin. There are many such NE lineaments/faults in the southern part of the Surma basin (Mizoram) which show strike-slip displacement of the fold axes along them. Among the NW-SE trending faults, Mat fault and Tuipui fault lies within Mizoram at the southern part of the basin. Mat fault obliquely cuts across the general north-south trend of the Indo-Burmese arc as shown in Fig. 1.17b. It trends NW-SE and is traceable across the entire Mizoram on the satellite as well as on the geological maps. Hence, this part has been selected for monitoring Radon and Thoron anomalies and their possible correlation with geophysical phenomena.

In addition to the Mat fault, the study was extended to the Chite fault located within Aizawl town, Mizoram India. The geomorphologic map of Aizawl city consisting Chite fault may be outlined as follows. The geomorphology is part of a

meridional ridge (i.e. anticlines ridges and Tlawng synclines) and narrow valley (i.e. often controlled by faults). The town and its area are characterized by tertiary sedimentary rocks belonging to the Surma group of rocks of the Oligocene-Miocene age. Rocks of this group have been further subdivided into Middle Bhuban, upper Bhuban and Bokabil formations. The core of the Aizawl anticline is occupied by the middle bhuban formation and the lithological characteristics of this region are underlain by thinly bedded sandstones-siltstones/shale in 50:50 ratios with mudstone associated mainly with sandstones. Generally, the rock beds strike $N15^0E$-$S15^0W$ with moderate to steep dips either toward the east or west. The trend of the Aizawl anticline is N-S near Aizawl town and changes to NNE-SSE in the south where Tlawng syncline trend NNW-SSE. The anticline and syncline both plunge toward the north (G.S.I., 1988). The area is infested by several faults which were longitudinal, transverse and oblique in deposition with varying magnitude. Imprints of those longitudinal faults are visible along Chite river and Muthi river. The major transverse fault runs along Siphui river dissecting the ridge axis along the E-W segment of Tlawng river. It also dissects diagonal faults parallel to Sele river, Kurung river along the NE-SW segment of Tlawng. Our area of interest is along Chite valley located in the east of Aizawl anticline ridge. Flowing between Aizawl and Zemabawk Chite river creates a broad valley as shown in Fig. 1.18. The valley is approximately 600m in length and 45-60 m in width with 1.5-2.5 m thick saturated sand and gravel. Both the study areas (Mat and Chite faults) are mostly mountainous and hilly whose ranges traverse in the north-south direction separated by north-south flowing rivers and valleys. Their vicinities are divided into a high structural hill, medium structural hill, low structural hill and valley hill based on their relative heights with reference to the mean sea level and nature of the topography. It has been observed that the areas located within the vicinity of fault zones are more vulnerable to landslides. Being a sloping valley in orientation, the area experiences constant erosion by streams due to its soft nature of lithology. The geomorphologic features surrounding the fault region are shown in Fig. 1.19.

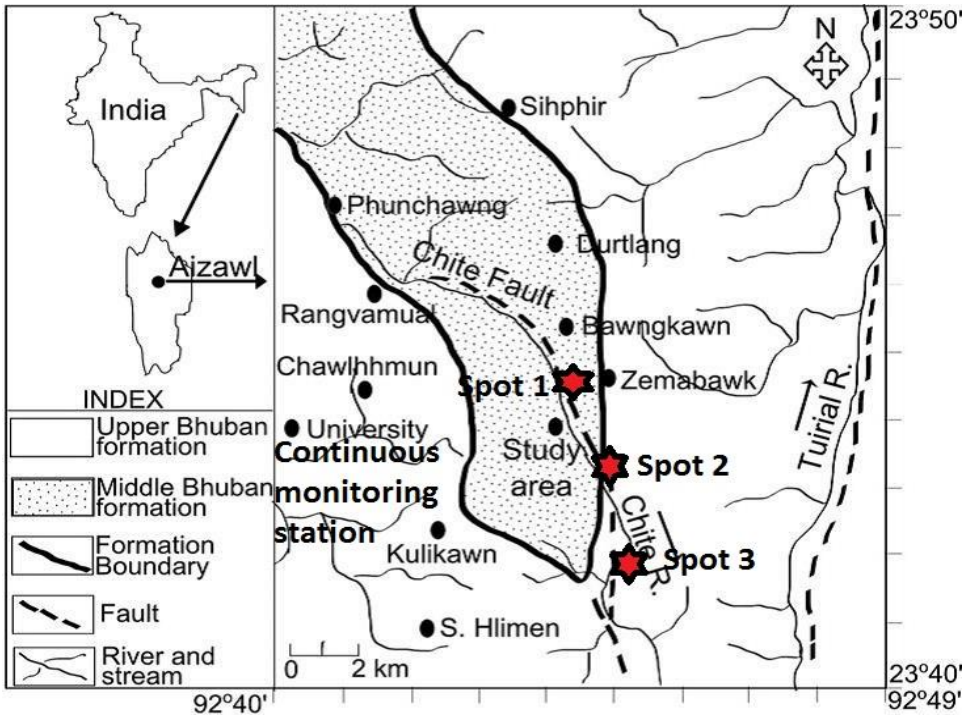

Fig. 1.18: Location map of the study area at Chite fault showing the three sampling spots (spot 1, spot 2 and spot 3), the continuous radon monitoring station at Mizoram University and the geology of the region (after Singh *et al*., 2014).

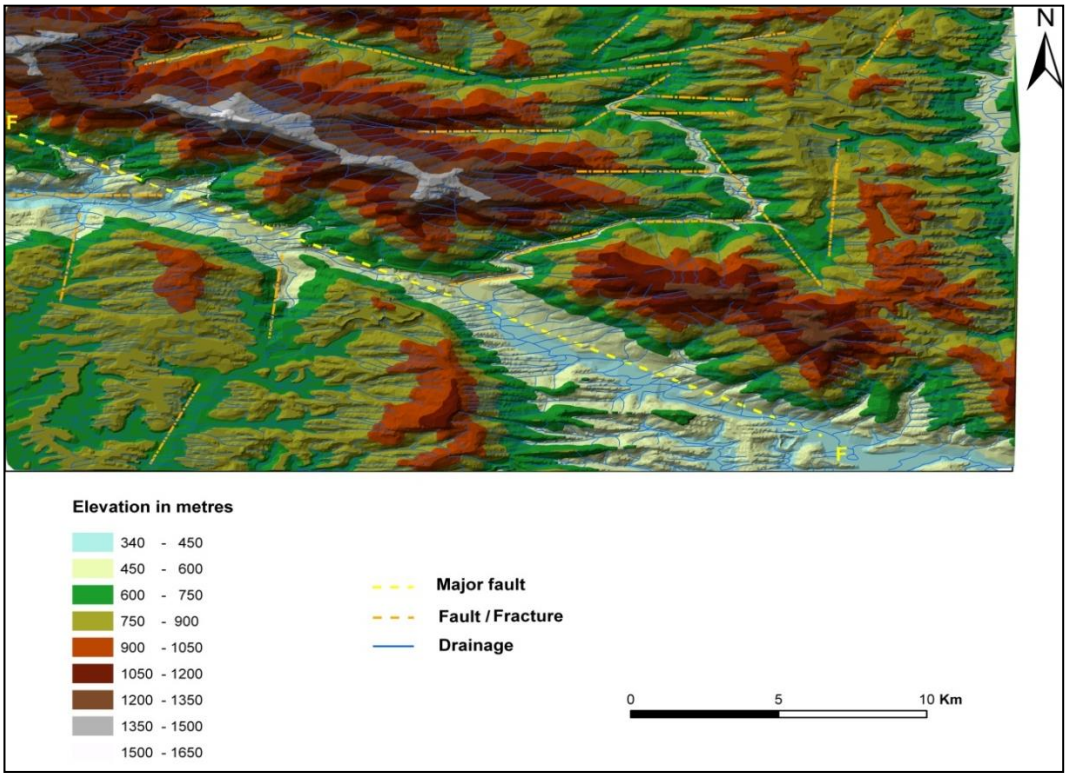

Fig. 1.19: Triangulated irregular network showing an oblique view of the prominent Mat fault (thick yellow line), other minor faults and geomorphologic features. F represents the Mat Fault (after Jaishi *et al*., 2014).

1.8 Motivation, Scope and objectives of the present study

As mentioned elsewhere the geological and tectonic processes induce earthquakes as a result of movement along the fault line. Earthquakes of all-natural calamities still imposed a disastrous threat to mankind as they affect large areas causing death, casualties and destruction of physical resources on a massive scale. Over the past decade, earthquakes become a major topic which draws the attention of many researchers around the world due to their devastating nature. Yet no concrete theory or technique has been established till date in predicting earthquakes exactly. However, anomalies of gases like CO_2, *He*, H_2, *Rn*, CH_4 and N_2 and highly volatile metals such as *Hg*, *Sb* and *As* are qualitatively noticed before several earthquakes. Such anomalies are pronounced along fault lines as it provided an easy pathway for them due to their loose soil formation. Hence monitoring the variation of such gases and metals at a suitable fault region could possibly be used to predict earthquakes. Of all these, monitoring of radon (*Rn*) concentration along the active fault region is the most widely used as a possible precursor to earthquakes. Such an officially recorded anomaly was in 1966 before the Tashkent earthquakes in a Russian well (Ulomov and Mavashev, 1967). The observation ignites optimistic motivation for many researchers and was instantly followed up by researchers from China, Japan and USA in the year 1973, 1975 and 1978, respectively (Dubinchuk, 1993). Since then this observation motivates researchers around the globe to pursue radon monitoring for earthquake prediction (Igarashi and Wakita, 1990; Jaishi *et al*., 2013; King, 1986; Shapiro *et al*., 1981; Vaupotič *et al*., 2010; Yasuoka and Shinogi, 1997; Zmazek *et al*., 2002). In India, the radon monitoring for uranium prospecting began in 1948 and later in 1950 in northeast India (NE-India) (Gupta and Sarangi, 2005) where no economic concentration was found in NE-India except at Meghalaya state. On the other hand, monitoring of radon data for earthquake studies in NE-India and Mizoram state, in particular, was started by Jaishi *et al*. (2013, 2014, 2014a, 2014b, 2015) and Singh *et al*. (2014, 2016, 2017) in 2011 at Mat and Chite faults. Both the

studies concluded that the region was seismically active and the radon and earthquake data generated at Mat fault and Chite fault correlated with a success rate of 60%. Despite the optimistic outcome both the studies made by Jaishi *et al*. (2013, 2014, 2014a, 2014b, 2015) and Singh *et al*. (2014, 2016, 2017) lacks behind the real-time nature of radon variation as they were generated with a frequency of 15 days and 7 days respectively. Besides, both studies fail to remove intermittencies in the radon data due to meteorological effects leaving huge uncertainties in the result. As radon emissions are not only influenced by geophysical phenomena but also by several factors such as meteorological factors (temperature, pressure, rainfall, humidity and wind speed), physicochemical features of the soil (such as grain size, density, porosity, permeability etc) and geophysical factors (morphology and movement of groundwater and nature of aquifers) (Chowdhury *et al*., 2017; Sahoo *et al*., 2020). If the radon data are corrupted with variation due to the above-mentioned external factors it will lead to uncertainties in the result and ultimately to a failed prediction. Hence removal of intermittency in the radon data due to external factors rather than geophysical phenomena is a must to have prediction with high accuracy and avoid false prediction. At the same time regarding the human population of the study region, there is a phenomenal increase in the population density and development programmes in northeast India. Such phenomenal increases in population density are common in state capital like Aizawl City and its nearby town. Besides, over the past two decades, the region had witnessed a mushrooming growth of unplanned urban centres. This further worsens the vulnerability and risk of the human population and physical structures of the region to impending earthquakes. Hence the realistic approach to understanding and assessing the status of seismicity of the region is an unavoidable necessity. Moreover, the vulnerability and alarming condition of the region call for an urgent and sustainable mitigation effort. Subsequently, hunting for all possible means and efforts that may assist in reducing the seismic risk of the region is of vital importance. One such possible candidate may be monitoring radon concentration variation in a seismically active region. However, it was noticed that earthquakes are not always preceded by radon anomaly and vice-versa despite the enormous reports that the technique has been successfully used in several seismic areas. But considering the desperate and alarming situation of the

region, understanding the behaviour and precursory effort of impending geophysical phenomena with any available technique is an option.

Motivated by the above consideration, we started monitoring *in-situ* online soil radon and thoron data along Mat fault which is the most prominent fault in the hilly region of Mizoram state, India. At the same time, a 15 min cycle online data of the isotope pair was continuously monitored at the department of Physics, Mizoram University, Aizawl, Mizoram (India). Both data from the two locations were cross-analyzed to reveal their geophysical characteristics. The study was extended to Chite fault located in the vicinity of the continuous monitoring station at Mizoram University. The study overcomes setbacks of many researchers especially those of Jaishi *et al*. (2013, 2014, 2014a, 2014b, 2015) and Singh *et al*. (2014, 2016, 2017) who fails to generate real-time online data in the same region. It was also the first study where online data with such high frequency (15 min cycles) has been accomplished at one of the highest seismicity of the world i.e. at the vicinity of the Indo-Burman subduction line and at the junction of the Himalayan arc and Burmese arc. In this study intermittency in the isotope pair data due to meteorological factors has been removed using non-linear statistical analysis. At the same time, effects due to physicochemical features of the soil and geophysical factors were minimized by pre-surveying the radon isotope pair exhalation rate and designing the monitoring station to nullify such effect. Hence any observed anomalies in the isotope pair concentrations under such monitoring station may solely be taken as due to geophysical phenomena as all the others influencing factors were discarded or minimized. Keeping in view the necessity for a sustainable earthquake mitigation programme in this seismically active region (Seismic Zone V) the above mentioned progression/advancement in the measuring and statistical analysis technique may depict the importance of this study. The present work is an attempt to generate *in-situ* online radon and thoron databases and try to understand their correlation with geophysical phenomena of the region in real-time with real-time data. However, to confirm such obligation long-term data recording and analysis may be required. In addition, radon and thoron profiles of the region, estimation of their parent nuclei, their comparison with worldwide averages and critical values given by UNSCEAR (2000, 1982) and IAEA (2004, 2013) were also presented.

The main objectives of the study are as follows-

- To generate *in-situ* online radon (^{222}Rn) data at Mat Fault.
- To develop correlation between the *in-situ* online generated radon (^{222}Rn) data at Mat fault and geophysical phenomena.

2

Review of Literature

Exposure to radioactivity has been considered to enhance good health in the early 1900s and people were reported to drink radon-rich water for that purpose (Ball *et al*., 1991). A quantitative risk estimate for lung cancer could be established among underground miners only by the 1970s, after diagnosing an overwhelming number of lung cancers among them (Swedjemark, 2004). During the 1940s-1960s, uranium mining became intensified in countries like Africa, Canada and the United States of America, where radon serve as a useful pathfinder to its parent nuclei (Ball *et al*., 1991; Khattak *et al*., 2011; Swedjemark, 2004). In India and particularly in north-eastern India (NE India) it was started in 1948 and 1950 respectively (Gupta and Sarangi, 2005). But no economic concentration was found in northeast India except in Meghalaya state (Gupta and Sarangi, 2005). A few years later its possible application as a premonitory gas to earthquakes came into light as its anomalies were reported to precede geophysical phenomena such as earthquake and volcanic activities. Soon monitoring of radon anomalies for earthquake prediction become a global phenomenon. Enormous work has been done over the past three decades with a proposed active and passive method and statistical technique for explaining and analysis of experimental field data.

In 1953 Z. Hatuda measured soil radon data in an active fault zone of Japan for 2 years and observed significant radon concentration anomaly before the Tonankai earthquake of M8.0 (Hatuda, 1953). S. Okabe observed that radon in the atmosphere near the ground surface significantly increase before local seismicity in Tottori, Japan and also suggested that soil gas is enriched in radon in the fault zone (Okabe, 1956). In 1959 Tanner noticed that soil radon measurement is highly influenced by meteorological factors (Tanner, 1959). A few years later in 1964, he proposed that radon could be used as an indicator for uranium deposits and as well as a premonitory gas to earthquakes (Tanner, 1964). The first officially recorded radon

anomaly in groundwater was observed in a Russian well before the Tashkent earthquake (M=5.3) (Ulomov and Mahashev, 1967). Before this earthquake radon concentration in the well started to increase at least for one year. After this observation in the Russian well radon anomalies in soil and groundwater before seismic activity become a well-known fact. The following paragraph presented some important studies relating to soil radon and geophysical phenomena (specifically earthquakes).

In his 1978 report, C. Y. King observed radon anomalies during two earthquakes (M=4.3 and 4.0) along the San Andreas and Hayward-Calaveras faults (King, 1978). By installing 60 more monitoring network stations he extended the work since 1975 along a 380 km section of the San Andreas Fault system between Santa Rosa and Cholame in central California (King, 1980). The monitoring networks deployed the Track Etch method and continuously measured sub-surface soil radon gas in an attempt to find any indicatory signal of an earthquake. Several events have been recorded by these network stations long but limited some fault segments (~100 km). Some of the events lasted several weeks to months and the radon concentrations during this period increased by a factor of 2 above the average approximately. Also, no systematic relation was observed between radon and meteorological conditions despite some events happening in different seasons. On the other hand, they coincided reasonably well in time and space with larger local earthquakes above a threshold magnitude of about 4.0. These episodic radon changes were presumed by King (1980) as a result of fluctuation in the gassing out rate in the fault zones in response to some episodic strain changes, which incidentally caused the earthquakes.

Between 1981-1983 Fleischer and Mogro-Campero studied the correlation between radon concentration and earthquake occurrence near Sand Point, Alaska (Fleischer and Mogro-Campero, 1985). They observed anomalies in radon concentration 6 weeks prior to the M=6.3 earthquake occurring at 180 km from the monitoring stations. They also observed both a raise and fall in radon concentration during seismic events in the Yakataga region. For example, radon minimum and maximum were recorded during the quake events of May 2, 1982, and June-July 1980 respectively. They determined the relative dislocation strain intensity (RSI)

value and concluded that quake events with large magnitude are identifiable by radon. While quakes with smaller magnitudes are identifiable only if the magnitude of quakes is close to the maximum allowed by the uncertainty. No significant correlation was observed between radon and meteorological factors (such as rainfall, snow accumulation, temperature, etc.)

Rastogi *et al*. (1986) observed an increase in radon concentration between March-April, 1984 during high seismicity. Their observation came after a major earthquake happens in the region, that is, Bhatsa dam, Maharashtra, India, during August 1983-July 1984. In their later report, Rastogi *et al*. (1987) observed precursory phenomena of radon in earthquake sequence at the Osmansagar reservoir, Hyderabad, India during January-February, 1982.

In Spain, the radon concentration in soil gas was studied by Duenas and Fernandez (1988). They found both pre and post-anomalies as well as 'no' radon anomaly for earthquakes with a magnitude of 2-4 at 90 km distance from the measuring site. In the same year, Friedmann *et al*. (1988) observed an increase in soil radon concentration during the strong earthquake (M=5.7) of July 5, 1983. The observation was made from a network of five monitoring sites along 200 km at the North Anatolian Fault Zone, Bolu, Turkey. Hirotaka *et al*. (1988) observed radon anomaly before the Nagano Prefecture earthquake (M=6.8) of September 14, 1984, at 65 km away from the epicenter at the Atotsugawa fault. They noticed a remarkable increase in radon concentration 2 weeks before the earthquakes while a gradual increase three months before the quake.

Between 1984 and 1987 a daily monitoring of soil gas radon was carried out by Singh *et al*. (1991) in Amritsar (India). Several radon anomalies were recorded during the observation period as follows: March 23, 1984 (M=5.0); July 29, 1985 (M=6.8); April 21, 1986 (M=5.7); July 10, 1986 (M=3.8); March 17, 1987 (M=4.3); and May 1, 1987 (M=5). The precursory time for these observed radon anomalies ranges from 3 to 10 days with an epicentral distance of 100-400 km. Monnin and Seidel (1991) reported a finding on the characteristics of radon in soil air during the earthquake in Mexico. They suggest that deeper fluid motion results in near-surface radon fluctuation. According to the theory, deeper fluid motion supports the Pore Collapse (PC) model creating an upward motion of pore fluids that acts as radon

carriers. Based on this theoretical model they suggested that a large quantity of radon is expected to show during a short duration prior to a quake.

Segovia *et al*. (1995a, 1995b) surveyed soil gas radon and short-lived daughter concentration using SSNTD along the Guerrero coastal zone near Laguna Verde, Mexico. During 1990-1991 they observed weak radon anomalies before the M=4.7 and M=5.5 earthquakes at the Acapulco stations. They also observed a significant radon anomaly during 1992-1994 earthquakes. Alekseev *et al*. (1995) deployed SSNTD to measure continuous radon data in soil with a frequency of 5-7 days at the Ashkhabad and Kum-Dang regions in Turkmenistan. A simultaneous anomaly in radon concentration was observed during the devastating earthquake that occurred on 14 March, 1983.

In Northern Thailand, Wattananikorn *et al*. (1998) performed a study on radon measurement in soil gas using LR-115 solid state detector at a depth of 50 cm and 100 cm below the ground surface. During their observation period of 40 days, they correlated several earthquakes with radon anomalies. Garavaglia *et al*. (1998) performed radon measurements in a cave in Villanova, which is one of the most seismically active regions of the Alps in NE Italy. Variation in the radon concentration was observed during the local seismicity of M=2.5-4.2 between December 1996 and March 1997. Besides the effect of seismic events fluctuation in radon concentration due to pressure and temperature was also observed.

A generalized idea to remove noise components from measured radon data in order to have a genuine residual component that reflects solely geodynamic processes was described by Finkelstein *et al.* (1998). By taking into account numerous regular and irregular parameters they derived the actual variation in radon concentration. The parameters taken into account were radon emanation from the soil, variation of radon due to vertical warm convection arising shortly after sunrise, variation of radon due to rain and radon dissolved in underground water, variation due to fluctuation in air pressure, variation due to air movement, variation related to deep geodynamics, due to strong geodynamic storms in periods of solar chromo spherical bursts, and variation caused by the settling of aerosols following dust storms. The approach was demonstrated using data gathered in Israel at the time of the October 12, 1992, Giza earthquake in Egypt. A significant increase in radon

concentration was observed 4 days before the earthquake. They emphasized that the observed anomaly was associated with the geodynamic process preceding the earthquake.

Virk *et al*. (2001) study and proposed the applicability of the conceptual helium/radon ratio model as a predictive tool for earthquakes in N-W Himalaya, India. At Palampur they observed concentration anomalies of radon, helium and their ratio on 24, 27 and 20 March 1999, respectively before the Chamoli earthquake (M=6.5) of 29 March 1999 approximately 393 km away. They suggested that the helium/radon ratio is not sensitive to microearthquakes as the aftershock at Chamoli was not identifiable in the form of helium/radon anomalies. In Croatia, Planinić *et al*. (2001) performed radon concentration measurements in the soil at Osijek for two years between 1998 and 2000 using LR-115 nuclear track film. During this period parameters like temporal radon variations, barometric pressure, precipitation and temperature were recorded. They observed a reversed correlation between soil radon concentration and barometric pressure. At the same time, six earthquakes (M=2.7-3.8) located at 70-320 km from the measuring site were recorded during this period. Out of the six earthquakes two of them (M=2.8 and 2.7) were correlated with radon anomalies. In both cases the radon anomalies appeared one month prior to the earthquakes.

Negarestani *et al*. (2002) performed a soil radon survey in Thailand and used a Layered Neural Network to estimate radon concentration in soil related to environmental parameters. With this technique, they were able to differentiate fluctuation in radon concentration due to environmental parameters from those arising from geophysical phenomena on the earth. Taking into account environmental parameters which may have a non-linear effect on soil radon data they suggested that the proposed technique can give a better estimation of radon variations in soil.

Richon *et al*. (2003) continuously monitored soil gas radon concentration at Taal volcano, Luzon Island, Philippines between June 1993 and November 1996. A single earthquake (M=7.1) was recorded during this period on November 15, 1994, between Luzon and Mindoro, 48 km south of the volcano. An anomalous increase in soil radon (peak to background ratio = 6) unique in the whole time series was

observed 22 days before the earthquake. In Egypt, a soil radon survey was carried out by Moussa and El Arabi (2003) during 2001-2002 by using ALPHA GUARD along the fault line of the Qena-Safaga fault. In the active fault zone, they observed high anomalous radon peaks (5-10 times greater than the background value) on different dates. In Slovenia, soil radon concentration was collected from three stations in the Krsko basin by Zmazek *et al*. (2003). They adopted a new analysis technique called decision trees for their radon data in earthquake prediction studies. Analyses from the three stations indicate that the model outperforms other previously used regression methods in predicting soil radon concentration. The regression methods are based on environmental factors to predict radon concentration in soil gas. Such environmental data are barometric pressure, soil temperature, air temperature and rainfall. Taking into account that the radon concentration was influenced only by environmental parameters they developed a model which predicts radon concentration with a correlation of 0.8. The correlation was found to be much lower in periods with seismic activity. The decrease in predictive accuracy appears 1-7 days before earthquakes with a local magnitude of 0.8-3.3.

In Poland Swakon *et al*. (2004) study soil radon and thoron concentrations as well as radioactive natural isotopes of radium, thorium and potassium in the vicinity of geologic fault zones within the Krakow region. For radon and thoron measurement AlphaGUARD PQ2000 PRO and diffusion chambers with CR-39 detectors were used while Gamma-ray spectrometry was used for radioactive isotope measurements. In contrast to those earlier surveys elevated levels of radon and thoron concentration in soil gas were observed in the study area. Burton *et al*. (2004) performed a series of discrete measurements of soil radon concentrations with a high spatial resolution (~5-100 m) in the Santa Venerina area of Mt. Etna, Italy. The measurement was carried out between July 2002 and May 2003 and revealed well-defined linear anomalies. These anomalies were interpreted as being caused by active faults whose higher porosity than surrounding soils enabled increased CO_2 flux carrying radon from beneath. They also indicated that high spatial resolution of sampling is required to correctly map the radon anomalies. A series of earthquakes shook the region in October 2002 resulting in localized damage and soil fractures along the geometry of active faults which strengthened their hypothesis that the radon anomalies are

localized along active faults. They also observed that the spatial distribution of thoron emission was different and in contrast to that of radon probably due to its short half-life.

An automatic soil gas monitoring station was set up by Yang *et al*. (2005) in an active fault zone of SW Taiwan. During continuous measurement of more than a year, some spike-like anomalous high radon and thoron concentrations were observed. Only 100 m away a similar soil radon spectrum was also obtained from an independent monitoring station. These observed anomalous peaks usually precede earthquakes ($M \geq 4.5$) by a few days or weeks. They concluded that particularly at a fault zone soil radon and thoron can serve as useful tools for earthquake surveillance. Using solid-state nuclear track detectors Nevinsky and Tsvetkova (2005) developed a simple automatic detector for soil radon on the mud volcano and in the cave in the Krasnodar territory (Russia). A cylinder reel of LR-115 connected with clockwork having a revolutionary time period of 2 weeks was dug in the soil along with its containing pipe for assessing daily soil radon data. They observed that areas of high concentration of soil radon move to that side where the earthquake occurs. Walia *et al*. (2005a) performed radon monitoring at Palampur and Dalhousie stations in the Kangra valley of Himachal Pradesh (India) from June 1996 to September 1999. They used the emanometry technique and recorded discrete radon concentrations in soil gas and groundwater at both stations. The influence of meteorological factors on radon concentration was also evaluated. The radon exhalation exhibits a positive correlation with temperature, rainfall, and relative humidity but a negative correlation with wind velocity. Both positive and negative radon anomalies were recorded.

Crockett *et al*. (2006) performed short-term (two-hourly) measurements of real-time radon data at two separate locations (2.25 km apart) in Northampton, in the English East Midlands (UK). The measurement was simultaneously carried out at the two locations for 25 weeks from June to December 2002 during which the Dudley earthquake (magnitude=5.0) and smaller aftershocks occurred in the English West Midlands, UK. Prior to the main Dudley earthquake, they observed two simultaneous in-phase short-term (6-9 h) radon anomalies. Their further study shows that a similar

period occurred prior to another smaller but recorded earthquake in the English Channel.

Ghosh *et al*. (2007) measured radon concentration in soil gas at Kolkata, India using CR-39 solid-state nuclear track detector (SSNTD). Correlation of radon anomaly with earthquakes of $M \geq 4$ occurred within 1000 km radius from the measuring site were observed between November 2005 and October 2006. At the same time, they also observed seasonal variation of radon concentration which was abruptly high during June-July when the mean total rainfall was also quite high. Giammanco *et al*. (2007) performed a study of ^{220}Rn and ^{222}Rn activity and of CO_2 flux in soil and fumaroles on Mount Etna volcano during 2005-2006, both in its summit area and along active faults on its flanks. They observed an empirical relationship between the isotope pair ratio ($^{220}Rn/^{222}Rn$) and CO_2 efflux which is an inverse relationship.

At the National Pingtung University of Science and Technology (NPUST) campus in southern Taiwan, a systematical analysis of soil-gas compositions was performed by Fu *et al*. (2008) at the National Pingtung University of Science and Technology (NPUST) campus in southern Taiwan. They systematically collected soil-gas samples from a grid of 200-300 m spacing and about 1.2×2.3 km^2 area. A 130 cm length hollow steel probe with 3 cm in diameter was inserted to 100 cm depth to collect the soil sample. For detecting helium, radon and CO_2 a helium leak detector (ASM100HDS, Alcatel), radon detector (RTM 2100, SARAD) and micro gas chromatography (CP4900, Varian) were used respectively. During the observation period the effect of rainfall on the variation of soil He, Rn and CO_2 were found to be minor. Their observed strong correlation (0.8753) between Rn and CO_2 suggested that CO_2 could serve as a carrier gas for soil radon at the measuring site. During a consecutive measurement for several months, anomalously high concentrations appeared to be spike-like a few hours to a few days before the earthquakes. They suggested that the variations in soil-gas compositions along the Chaochou Fault may reflect the regional crustal stress/strain changes prior to earthquakes.

İnan *et al.* (2008) studies the physical and chemical properties of warm and hot spring waters as well as soil radon concentrations in the Marmara region for 3

years; following the İzmit earthquake of 17 August 1999 (M=7.4). Daily bottled spring water from the springs was collected monthly during site visits and 30 daily samples from each spring were brought to the laboratory where they were analyzed for anions and cations using Ion Chromatography instruments (Dionex DX600). Weekly samples from all spring monitoring sites were also analyzed for O and D isotopes by EA-IRMS system (Micromass UK). Soil radon was measured continuously with 15 min cycle using alpha particle detectors (model 611 Alpha-Meter). Optimistic and encouraging ground radon emanation anomalies have been identified and found to be related to earthquakes with M>4 of the region. But, no systematic and consistent anomalies have been identified in the physical and/or chemical properties of the spring waters related to earthquakes occurring in the observation period. They observed that in absence of seismic activity the radon data showed Rayleigh-type probability density function (PDF). However, at the time of earthquake build-up processes, the data showed deviations from Rayleigh-type PDF.

Giammanco *et al*. (2009) continued the systematic radon investigation in Italy at the Pernicana Fault (Mount Etna). The radon concentrations were sampled by three methods viz. passive, spot and continuous methods. It was observed that higher radon values were generally recorded on the upthrown side of the fault and the lowest values occurred generally close to the main fault plane. In contrast, higher CO_2 emissions were recorded on the fault plane. This characteristic can be explained by the in-soil gas transport mechanism. For example along the main fault plane, advective transport of deep gases (CO_2, Rn) occurs because of the high-ground fracturing and permeability. However, at the surface, dilution of radon by CO_2 prevails, hence producing lower radon values. A non-linear based radon prediction technique called Artificial Neural Network (ANN) was employed by Külahci *et al*. (2009) to study earthquakes in the East Anatolian Fault System (EAFS), Turkey. The ANN system has an individual training strategy with fixed-weight and supervised models leading to radon estimations. The average relative error between the magnitudes of the earthquakes acquired by ANN and measured data was about 2.3%. The relative error between the test and earthquake data varies between 0% and 12%.

They also suggested that the ANN approach is a potential alternative to other models with complex mathematical operations.

Vaupotič *et al*. (2010) continuously (1 h cycle) measured soil radon activity concentration at 80 cm depth from the ground surface at Cazzaso (Friuli) in northeast Italy, using a Barasol probe. At the same time, environmental parameters (air and soil temperature, barometric pressure) were also recorded. Barometric pressure was found to have a correlation with radon concentration. The radon anomalies were defined by the 2σ/gradient criterion and have been observed prior to some earthquakes with the most visible peak being the one prior to the M=5.1 earthquake. Reddy *et al.* (2010) performed continuous (1 h cycle) monitoring of soil gas radon at two sites around the Warna reservoir, India during 2005-2007. Eleven seismic events (including two aftershocks) with a magnitude range of M=4 to M=4.8 were recorded during the study period. For most of the recorded events, precursory anomalies in the radon concentration were observed. However, for some of the given earthquakes, the radon precursory anomalies were observed at one of the two sites only. They also observed that multiple depth probes exhibit contrast behaviour in recording temporal radon variation. The reason behind the non-concurrence in radon data of the sites and probes, including the combined effect of site heterogeneity, focal depth, epicentral distance, earthquake magnitude, faults responsible for the earthquake, etc, were discussed.

Torkar *et al.* (2010) simulated radon content in soil gas by employing artificial neural networks (ANN) from three boreholes at the Orlica fault in the Krško basin, Slovenia. The radon data were categorized into seismically active (SA) and non-seismically active (NSA) periods data for differentiating anomalies due to environmental parameters to that of resulting solely by seismic activity. Firstly, the SA data from the dataset was eliminated and then the ANN with 5 inputs for environmental parameters and a single output (radon concentration) was trained with the standard back-propagation technique. This predicted radon concentration (C_p) was then compared to measurements (C_m) and three types of anomalies (CA-correct anomaly, FA-false anomaly and NA-no anomaly) have been detected in the signal $|C_m/C_p-1|$ by varying five parameters describing an anomaly within predefined

intervals. Based on this technique they were able to correctly predict 10 seismic events out of 13 within the 2-year period.

Neri *et al*. (2011) performed measurements of radon and thoron emissions from the soil on the eastern flank of Mt. Etna which is a zone characterized by the presence of numerous seismogenic and aseismic faults. Statistical analysis was performed on the soil radon and thoron data for determining the distribution trends, recognizing anomaly threshold value and producing distribution maps that highlighted a significant spatial correlation between soil gas anomalies and tectonic lineaments. They suggested that both the isotope pair anomalies were confined in areas affected by relatively deep (5-10 km depth) seismic activity. However, a less evident correlation was found between soil gas anomalies and the released seismic energy. They finally concluded that hidden faults buried by recent soil cover or faults that are not visible at the surface can be revealed by mapping the distribution of radon and thoron in soil gas. They also suggested that the knowledge of the correlation between soil gas data, earthquake depth and intensity may give hints on the source of gas and/or fault dynamics.

In Romania, the temporal variation of radon concentration was investigated by Zoran *et al*. (2012) in Vrancea active region. The study was carried out in air near the ground and in-ground air by employing solid-state nuclear track detectors CR-39 and LR-115 at two seismic stations Vrancioaia (VRI) and Plostina (PLOR). Correlation of radon concentration variation with earthquake ($2.0 \leq M \leq 4.9$) was observed at 1 m height above the ground surface during the period of November, 2010-October, 2011. Radon anomalies at both the stations have been recorded during the monitoring period. They have found that greater times between the start of the anomaly, and the earthquake as well as longer durations of the radon anomalies appear to be associated with larger earthquake magnitudes. They concluded that the knowledge of air-ground-gas radon variation is very important for seismic indicatory assessment as well as for a precise pointer of geologic active faults. Chaudhuri *et al.* (2012) investigated variations in gas discharge from the Baratang mud volcano (Middle Andaman). In this study besides radon; helium, methane and carbon dioxide were continuously monitored to observe the regional pre-seismic activity. They have

deployed three different types of monitoring instruments; (i) For monitoring of He, O_2 + Ar, N_2, CH_4 and CO_2 a programmable micro gas chromatograph (type Agilent/Varian CP 490) was used. (ii) For recording radon concentrations and gamma activity levels instruments such as Alpha Guard PQ 2000 PRO and Saphymo/Genitron were used. (iii) For recording the concentration of ^{222}Rn daughter products (^{218}Po and ^{214}Po) Doseman Pro and Sarad were used. Between January 19-20, 2010 a sharp dip in radon concentration (> 2σ) was recorded prior to the 4.7 M earthquakes of February 2, 2010 at epicentral distance of 170 km. However, they have observed a high concentration of CH_4 and CO_2 and affirmed it to be unequivocal evidence of a close link with gas hydrate formations.

Padilla *et al*. (2013) continuously measured soil gas radon and thoron activities at El Hierro, Canary Islands (Spain) during the period (2011-2012) of volcanic unrest. The measurement was carried out at two different monitoring stations, namely HIE02 and HIE03. In both the station's radon and radon-thoron ratios anomalies were noticed prior to the submarine eruption onset and the strongest earthquake (M=4.6) of November 11, 2011. They concluded that the observed radon anomalies were in correlation with rock fracturing processes (seismic activity) and the increased magmatic CO_2 outflow. Walia *et al.* (2013) measured soil-gases compositions at continuous earthquake monitoring stations along Hsincheng and Hsinhua faults in Hsinchu and Tainan areas, respectively. They performed soil-gas surveys before selecting the monitoring site by investigating the occurrence of deeper gas emanation to check the seismic sensitivity of the sites. They concluded that the stress/strain transmission for a particular earthquake was hindered by different tectonic settings of the region under study.

Jaishi *et al*. (2013) performed continuous measurements of soil gas radon and thoron concentration along Mat Fault in Mizoram (India) with an aim to establish a correlation between their anomalies with the seismic activity of the region. According to the earthquake zonation map of India, the region lies at Zone V (Highest seismic level) and is one of the six most seismically active regions of the world (BIS, 2002). Geologically it is located at the junction of the Himalayan Arc and Burmese Arc. The measurement was performed between July 2011 and Feb 2013 using LR-115 Type II solid-state nuclear track detectors. They observed

anomalous behaviour in radon and thoron concentrations prior to some earthquakes. Besides positive peaks, a sharp fall in radon concentration was also noticed prior to the large earthquake of M=6.8. However, in the case of thoron data, only a positive correlation was observed with seismic activity.

In central Europe Briestensky´ *et al.* (2014) monitored fault displacement in the Bohemian Massif. It was supplemented by radon and CO_2 monitoring at the Mladeč Caves and Zbrašov Aragonite Caves respectively. The changes in fault displacement trends and anomalous radon and carbon dioxide concentrations during 2011 indicated that there was a significant period of tectonic instability. This period of tectonic instability was in coincidence with the catastrophic M=9.0 Tōhoku Earthquake of March 11, 2011. The observed Tōhoku Earthquake in the Pacific Ocean and the unusual amount of geodynamic activity recorded in the Bohemian Massif and Western Carpathians within the same period reflect that global tectonic changes are contemporaneous. H.P. Jaishi and group extended their measurement at Mat Bridge to Tuichang but along the same fault (Mat fault) (Jaishi *et al*., 2014a, 2014b). They presented the meteorological influences on radon and thoron data in detail. At Mat Bridge, radon data exhibits a moderate positive correlation with relative humidity but no specific correlations were found with air temperature and rainfall. However, at Tuichang inverse correlation coefficient was obtained between radon/thoron concentration and the meteorological parameters except in one case (thoron and relative humidity) which showed a weak positive correlation. The standard deviation method was employed in order to differentiate those anomalies which are solely caused by seismic events and not by meteorological parameters. A positive correlation was found between radon/thoron data and the earthquakes that occurred during the observation period. Several spike-like radon and thoron anomalies were observed preceding the earthquakes. Five events within the range M5.2 to M6.7 occurred during the observation period. Two radon anomalies were correlated with the event of M6.0 and M6.7 and one thoron anomaly to the event of M6.7. The precursor time for the entire correlated event was found to be the same (i.e., after 16-31 days of LR-115 exposure period), and both of these events occurred along the Indo-Myanmar ranges. They suggested that the study area is active to the seismic event generated along the Indo-Burma subduction tectonics. High and low

radon/thoron ratios were observed in the investigation area which provides useful information about deep and shallow gas source mixing.

Piersanti *et al*. (2015) measured real-time radon data at Pietralunga, Italian region Umbria, northern Italian Apennines during the period of 2010-2013. They aim to systematically characterize the short-term and long-term pattern of temporal variation of soil radon data in a seismically active region. They observed a significant correlation pattern between radon emanation and Spatio-temporal variation of release seismic moment. However, no significant correlation was observed between radon and small-magnitude earthquakes characterizing local seismicity. Oh and Kim, (2015) performed dual monitoring of radon and thoron for seismic precursory studies at Seongryu Cave (limestone cave), Korea during the period of May 18, 2010-June 17, 2011. They claim it to be the first of its kind where radon and thoron were coupled measured for earthquake prediction. They suggested that radon anomaly can also occur due to diffusive inputs over its lifetime (3.6 days) hence thoron which has a short half-life (55.6s) and free from environmental effects in a cave is necessary to be measured in coupled. Thoron and radon anomalies were observed in February 2011 before the Tohoku-Oki earthquake (M_w9.0) of Japan. Radon anomaly was also observed during summer but they considered the one observed along with thoron in February to be valid. They concluded that the combined isotope pair method could give a new approach in seismic precursory studies had the method been used extensively worldwide.

Barman *et al*. (2016) continuously monitor radon concentrations at Bakreswar Geochemical Monitoring Laboratory, West Bengal, India for a period of one year. Radon monitoring instrument called BARASOL BMC2 was deployed for recording radon data and has an adjustable measuring time window of 1 to 240 min. Periodicities in the time series radon data as a result of external factors particularly due to meteorological factors were identified and discarded by applying a non-linear analysis technique called Empirical Mode decomposition based Hilbert-Huang Transform (EMD-HHT). Hence the data was free from corruption due to external factors and any observed anomalies were solely due to seismic activity within the considered epicentral distance of 500 km from the monitoring site. During the observation period, five radon spikes have been correlated with five earthquakes

within the considered region. They suggested that EMD-HHT may be a suitable technique for extracting genuine seismic-related data from the time series radon data.

Chowdhury *et al*. (2017) generated continuous radon data at Ravangla, Sikkim, India during the period of October 2015-May 2016 using BARASOL BMC2 (Algade, France). Embedded periodicities of the time series radon data were deleted using the EMD-HHT technique. Two radon anomalies were observed and no spurious signals have been observed. The observed radon anomalies were correlated with earthquakes of November 19, 2015 and April 5, 2016 within 500 km radius from the monitoring site. At the same time, they considered only those earthquakes with M≥5 which were disastrous to mankind. Fu *et al*. (2017) monitor radon data at Dong-hua soil-gas station located in the northern part of Longitudinal Valley Fault, Eastern Taiwan. They synchronized the radon variation with CO_2 variation as it was the companion gas for radon in soil. A significant radon anomaly was observed 2 weeks before the Rueisuei earthquake (M_w6.4) of October 31, 2013. A recurrent anomaly was also observed 3 weeks before the Fanglin earthquake (M_w5.9) of May 21, 2014. They suggested that longer periods of soil gas anomaly were positively correlated with impending earthquakes of larger magnitude.

Kuo *et al*. (2018) performed monitoring of groundwater radon in southwest Taiwan since November 2009 at Paihe spring. The study also highlighted the validity of limestone aquifers as strain meters. Groundwater radon anomalies (declined in concentration) have been observed before the Jiasian (M_w6.3) and Meinong (M_w6.4) earthquakes of March 4, 2010 and February 5, 2016 respectively. The radon concentrations at Paihe spring specifically drop from their background level of 144±7 and 137±8 pCi/L to 104±8 and 97±9 pCi/L respectively prior to the Jiasian and Meinong quakes. They also put forward that limestone aquifer can acts as a strain meter for seismic activity by using radon as a tracer. They concluded that long-term continuous monitoring of groundwater radon at a suitable geological site is necessary and may provide vital data for forecasting disastrous local earthquakes. Deb *et al*. (2018) monitored radon data at two sites 200 m apart at Jadavpur University, Kolkata, West Bengal (India). The measurement was done using a solid-state nuclear track detector CR-39 during the period of August 2012-December 2013. Radon anomalies have been correlated with seven earthquakes occurring during the

measuring period, out of which anomalies of two quakes were observed at the two sites simultaneously. The absence of anomalies for some earthquakes and comparison with other studies has been discussed in detail.

Tareen *et al*. (2019) performed radon monitoring at Muzaffarabad in northern Pakistan and applied three types of computational intelligence (CI) techniques on the time series radon data. The three CI techniques were Feed Forward Neural Network (FFNN), Support Vector Regression (SVR) and Recurrent Neural Networks (RNN). The region experienced a devastating earthquake of 7.6 Richter scale on October 8, 2005 (8:50 am local time) taking 87, 350 lives, injuring approximately 138,000 people and causing 3.5 million people homeless according to Pakistani officials. The three CI models correlated the February 20, 2017 radon anomalies with March 5, 2017 earthquake. They also found that the measured radon data and the one predicted by the CI models were in close agreement. However, when observed for short-term periods their asymmetry may clearly be seen. They concluded that the FFNN outperform the RNN and supports SVR in estimating radon concentration using meteorological parameters. Ambrosino *et al*. (2019) monitored radon concentration variation in three Slovak and Czech caves for 1 year between July 1, 2016 and June 30, 2017. Besides radon data meteorological factors affecting radon gas emission were also continuously measured. Seasonal variation of radon concentrations was observed and found to be maximum during summer. To identify radon anomalies in the time series data multiple linear regression, empirical mode decomposition and support regression vector techniques were employed. The observed radon anomalies were correlated with earthquakes occurring in Europe.

Zhang *et al*. (2020) performed an analysis of 38 years' worth of groundwater radon data in an attempt to find pre-seismic anomalies. The radon data belongs to a period of 1977-2015 and was generated from Banglazhang geothermal field, China. Wavelet coherence analysis was applied to remove meteorological effects on the time series radon data. Radon data within the period of 1980-2008 were further selected for analysis using a decision tree. The decision tree identified 15 radon anomalies for the 24 selected earthquakes. They also speculated that the anomalous increase in radon concentration was due to continuous compensation from the newly formed internal surface of the cracks to the aquifer system. On the other hand, the

anomalous decrease in radon concentration was due to radon partitioning into the gas phase and the change of mixing ratio of shallow and deep water. Sahoo *et al*. (2020) generated continuous radon data with 10 min cycle at Badargadh station in Kutch region of Gujarat (India) during January 1, 2017-December 31, 2017. Besides radon data, meteorological parameters were also recorded simultaneously. Diurnally the radon concentration was found to be maximum in the afternoon when the intensity of sunlight is maximum. Seasonally the radon concentration was maximum during the rainy season. The meteorological influence on radon data was identified by applying Fast Fourier Transform. Periodicities in the time series radon data and anomalies due to geophysical phenomena were identified by applying EMD-HHT. The observed radon anomalies were correlated with four earthquakes occurring during the study period.

Haider *et al*. (2021) measured radon data as well as meteorological parameters (temperature, pressure and humidity) in northern Pakistan from July 24, 2014-April 31, 2015. They explored the efficiency of different intelligence algorithms such as artificial neural network (ANN), multiple linear regression (MLR) and decision trees (DT) in identifying anomalies in a time series radon data. They divided the radon data into seismically active (SA) and non-seismically active (NSA) data using time window periods of ±7 around the time of the earthquake. The NSA data were used for training the intelligent algorithm with three inputs (meteorological parameters) and one output (Radon). The predicted radon was then cross-analyzed with the measured radon data near the SA period. The study shows that the entire employed intelligent algorithm shows a significant deviation of Q value around the time of earthquakes where Q is the discrepancy between the simulated and measured data. They also mentioned that ANN performs better than the other techniques in predicting radon data. Muto *et al*. (2021) observed a fall in atmospheric radon concentration during the quiescence of seismic activity before the 2018 northern Osaka earthquake. The atmospheric radon concentration was continuously monitored at Osaka Medical and Pharmaceutical University (OMPU). They suggested that the deep-seated sedimentary layer of the Osaka basin which might be the main source of radon gets less damaged and fractured during seismic quiescence. Reduction in

damage to the sedimentary layer leads to a decrease in radon emanation rate and consequently to its exhalation rate into the atmosphere.

Jin *et al*. (2022) obtained the data series of residual radon concentration (C_{Rr}) from the long-term data series (C_{Rn}) to exclude interference from environmental factors. The distribution of C_{Rn} and C_{Rr} was tested and was found that they deviated from the traditional default normal distribution. Such that the box plots of non-normally distributed were used to redefine the anomaly threshold. From the temporal and spatial analysis of C_{Rn} and C_{Rr} they observed short-term pattern anomaly before the Wenchuan, Lushan and Jiuzhaigou earthquakes. Chowdhury *et al*. (2022) generated radon data from a network of three monitoring stations in Eastern India. The monitoring stations are located in Ravangla and Diphu in the eastern Himalayan region and Tantloi in the geothermal region. The non-linear time series radon data was analyzed by EMD-HHT methods to extract genuine earthquake-related anomalies. Radon anomalies have been correlated with an earthquake of M_w5.0 occurring within 500 km radius from the monitoring site. Simultaneous radon anomalies were also observed from the three monitoring stations prior to the earthquake of the common region. They suggested that monitoring of radon anomalies from networks of monitoring stations might be promising steps in understating the earthquake generating process. Bose *et al*. (2022) monitored variation in radon content, ionospheric scintillation and total electron content (TEC) of the soil and ionosphere respectively in an attempt to understand the April-May, 2015 Nepal earthquakes. The radon content was recorded using a solid state nuclear track detector (SSNTD) while the TEC and ionospheric scintillation by Global Positioning System (GPS) satellite of L1 frequency during summer and April-May, 2015 respectively. The measurement was carried out at Kolkata city, West Bengal, India. Anomalies in TEC and weak to intense fluctuation in some link GPS were observed prior to some earthquakes although 2015 is a low-to-medium solar activity year. Approximately simultaneous and prominent anomalies were observed from radon, TEC and ionospheric scintillation prior to Mw>7.0 devastating 2015 Nepal earthquake. They presented the effectiveness of analyzing two different types of seismic precursors and claimed it to be the first of its kind in the Nepal Himalayan

region where ionospheric scintillation and TEC have been simultaneously studied with radon data for seismic precursor research.

3

Materials and Methods

3.1 Radon and thoron Measurement Method

Monitoring technique of radon isotope pair and their decay products has evolved greatly. The monitoring techniques are mainly based on the detection of alpha, beta and gamma radiation emitted by the radioisotope pair independently or in combination. Based on the sampling methods the radon monitoring instruments can be divided into three types namely grab (or instantaneous), integrating and continuous types. At the same time, the instrument can either be active or passive. The three types of monitoring instruments/methods were briefly discussed as follows.

Scintillation Cell Grab Sampling Method: The method is based on pumping the sampling gas into the scintillation cell through a progeny filter. The interior of the scintillation cell is coated with zinc sulfide phosphor and intact with the photomultiplier tube (PMT) by its glass window. The light pulses in the cell as a result of interaction between alpha disintegrations from the air sample and the zinc sulfide are recorded by the PMT and are proportional to the radon concentration. In this method, the sampling host is kept short so as to draw room air into the cell and the filter is used as long as it remains undamaged and functional. The cell must be evacuated at least five times at 10 torr before sampling through the filter. To measure the radon concentration the alpha count of the cell was taken for 500 s after post sampling delay of about 180 min to achieve equilibrium between radon and its decay products ^{218}Po and ^{214}Po. Then the radon concentration was estimated by the relation given in equation (3.1).

$$C_{Rn222}(Bqcm^{-3}) = \frac{C}{3EV\exp(-\lambda t)} \tag{3.1}$$

where C is the net count rate (s^{-1}), E is the efficiency of counting (fraction), V is the volume of the sampler (cm^3), λ is the decay constant of radon (s^{-1}), t is the time delay

post-sampling (*s*) and *3* represents the three alphas from ^{222}Rn, ^{218}Po and ^{214}Po decay.

After measurement, to assured quality, the cell must be flushed with aged air or nitrogen and left overnight before reuse. The cell must be periodically recalibrated at a radon level similar to those found in the tested sited and checked for leakage. The scalar, detector and high voltage supply of the cell counting system must be calibrated in a radon calibration chamber before being used. The background of the cells should also be assessed routinely and should be subtracted from the observed counts.

Double-Filtered Method: In this method, air is drawn through a cylinder (0.5-1000 L) fitted with a high-efficiency filter at each end to trap the progeny for about 5 to 30 min. The inlet filter blocked the short-lived progeny from the sampled air while the exit filter collects the progeny formed inside the cylinder during the time of transit from one end to the other. By measuring the activity collected on the exit filter information about radon/thoron concentration can be obtained. The system must be leaked proof, the pump should have a uniform flow rate and sampling must continue until enough progeny activity is collected in the ext filter paper. The required sampling time depends on the airflow rate and size of the cylinder. The radon progeny activity on the second filter is proportional to the radon concentration in the sampled air. If C_{Rn} is the concentration of radon in air (Bqm^{-3}), C is the counts measured between t_1 and t_2 reckoned from the end of sampling for time T, and f is the fraction of radon progeny reaching the exit filter and V is the cylinder volume between the filters, then the radon concentration is estimated as given in equation 3.2.

$$C_{Rn}(Bqm^{-3}) = \frac{C}{EVf(t_1, t_2)} \tag{3.2}$$

Where E is the counting efficiency of the set-up deployed, Z is the theoretical counts depending on the radioactive build-up in the cylinder. Cylinder with a large volume can have a sensitivity of 0.7 Bqm^{-3} and thus can be used for environmental sampling. To establish the correction factors samples should be taken from different humidities and temperatures. To verify the acceptable limits calibration should be carried out at

several flow rates and exposure times. Calibration factors must be established with the identical gamma counting system and counting geometry used in sampling.

Continuous Radon Monitors: Based on the types of detection online radon monitors can be categorized into several types. Among them, the three widely used online radon monitors are briefly discussed.

The first type of online radon monitor operates as an ionization chamber. Radon of the ambient air diffuses into the chamber through a filtered area so that the radon concentration in the chamber follows the radon concentration in the ambient air with some small time lag. Inside the chamber, the alpha particles emitted during the decay of radon atoms produce bursts of ions. This was then recorded as an individual electrical pulse corresponding to each disintegration. AlphaGuard is the most popular commercially available radon detector of this type.

The second type of online radon monitor is based on solid-state silicon detectors. In this type, ambient air is allowed to flow through a filter into a detection chamber where radon undergoes decay. The decay products are collected using an electric field onto a solid-state silicon detector like PIN diode where the alphas emitted by the decay of these products are detected. The RAD7 and RTM-2200 are popular instruments of this type. However, these detectors are prone to interference due to the presence of humidity and trace gas.

The third type of radon monitor is based on the scintillation of alpha particles from the decay of radon gas within the cell. Ambient air is sampled through a progeny filter and alpha particles due to initial and subsequent radon decay are detected by the scintillation cell and a photomultiplier. It uses either a flow-through cell or a periodic-fill cell to draw the sample air. In the flow-through cell, the sample air is drawn continuously into the cell by a small pump. However, in the periodic-fill cell, the sample air is drawn into the cell by a pre-selected time interval; then the scintillations are counted and the cycle is repeated. A third variation operates by radon diffusion through a filter area with the radon concentration in the cell varying with the radon concentration in the ambient air, after a small diffusion time lag. Combination of grab sampling and continuous radon monitor methods has been

applied in this thesis for generating radon data at the faults and continuous monitoring station respectively.

3.2 Scintillation based Smart Radon Thoron Monitor (SMARTRnDuo)

The SMARTRnDuo is a ZnS (Ag) based alpha scintillation counter developed and calibrated by Bhabha Atomic Research Centre, Mumbai, India (Gaware *et al*., 2011, 2011a, 2013). The monitor is adopted and employed in the present thesis. It is a technologically advanced portable dual radon and thoron monitor capable of *in-situ* field studies and continuous online measurement. The photo and schematic diagram of the microprocessor-based radon monitor are shown in Fig. 3.1a and Fig. 3.1b respectively. The technical specification of SMARTRnDuo is also given in Table 3.1. To measure radon, the sample gas is collected in a scintillation cell of 150 cm^3 by a diffusion process. During this process, the sampled gas passes through a "progeny filter" and "thoron discriminator" which eliminates progenies of the isotope pair and thoron gas respectively. The thoron discriminator based on "diffusion-time delay" does not allow the short-lived thoron (half-life 55.6 s) to pass through.

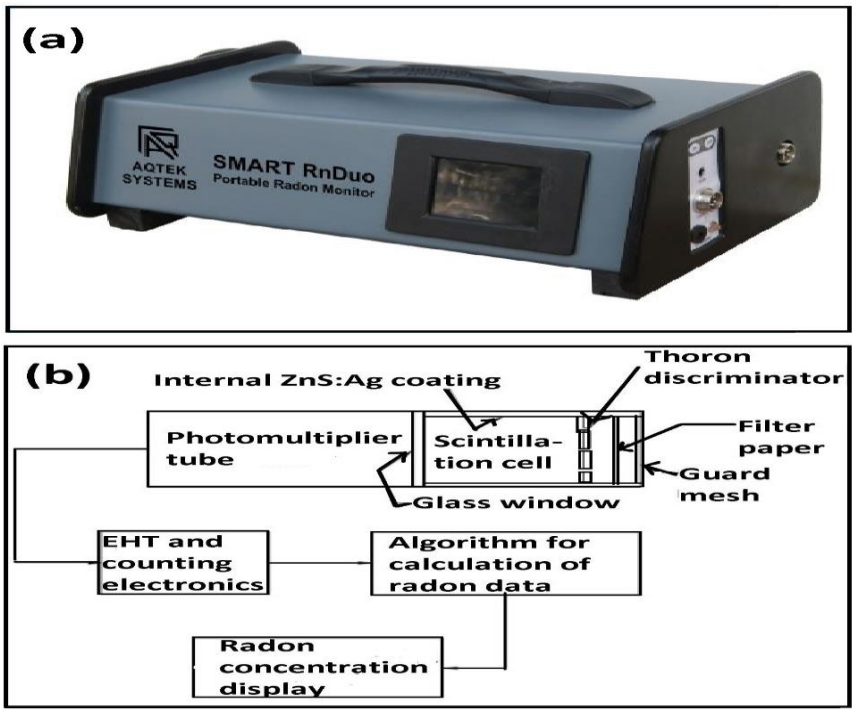

Fig. 3.1: (a) Photo of SMARTRnDuo along with its sampling components (b) Schematic of the radon measurement process in SMARTRnDuo.

Table 3.1: Technical specification of SMARTRnDuo.

Detector type	**Scintillation cell**
Scintillation coating	Internally coated ZnS (Ag)
Scintillation cell active volume	153 cm^{-3}
Radon sensitivity	1.2 CPH$(Bqm^{-3})^{-1}$/ 44.5 CPH$(pCiL^{-1})^{-1}$ *CPH=counts per hour*
Thoron sensitivity	0.8 CPH$(Bqm^{-3})^{-1}$/ 30 CPH$(pCiL^{-1})^{-1}$
Sampling type	Diffusion mode or Flow mode
Sampling flow rate	0.5-0.7 Litre per min with an in-built pump
Measurement cycle time	15 / 30 / 60 min
Response time	15 minutes for attaining 95% of radon or thoron
Minimum detection limit	Radon: 8 Bqm^{-3} at 1 σ and 1 hrs cycle Thoron: 15 Bqm^{-3} at 1 σ and 1 hrs cycle
Upper detection limit	50 $MBqm^{-3}$
Effect of sample humidity and trace gases on sensitivity	Practically nil until the humidity is not condensed on scintillator surface.
Thoron interference	< 5% with sniffing mode of sampling
Power	External 110- 240 V AC 50/60 Hz , Internal 6 V DC Battery
Dimension	37 cm x 20 cm x 12 cm

Hence alpha activity was recorded only for radon and its decay products formed inside the scintillation cell volume. The alpha scintillations from radon and its decay products formed inside the cell are continuously counted by the PMT and the associated counting electronics. The automated continuous monitoring of radon was not possible without reckoning its decay product activities as their buildup and decay

activities inside the cell are complicated and never attain equilibrium with radon. However, the SMARTRnDuo was equipped with an algorithm which enabled the successful deployment of scintillation technology to continuously measure radon concentration. The algorithm takes into account the theoretical decay and growth of decay products of radon during the ongoing measurement cycle and from the radon concentration in history. The alpha counts obtained are processed by the microprocessor unit as per the developed algorithm to display the radon concentration (Gaware *et al*., 2011, 2011a, 2013).

To measure thoron, the sample gas is drawn into the scintillation cell (150 cm^3) by the inbuilt pump by flow mode. In flow mode, the sampling gas passes through a "progeny filter" which eliminates radon and thoron progenies but fails to differentiate them. Such that, the initial part of each measurement cycle gives counts of total alpha particles from the isotope pair and their long-lived decay products. The next 5 minutes were delayed in counting alpha particles so that the short-lived (55.6s) thoron may decay out. After that, the monitor automatically resumes counting the persistent activity in the cell, namely the radon and background activity. The thoron concentration is obtained by subtracting the last interval alpha counts from the initial interval counts (Gaware *et al*., 2011, 2011a, 2013).

3.3 Protocol for Measurement of Radon Isotope Pair at Mat Fault

Formation of Grid: First and foremost a survey was made along Mat fault to locate and select an ideal place for monitoring the radon isotope pair and collecting samples. For this, a wide open area situated along Serchhip-Thenzawl road called Zawlpui area (23.3^0N, 92.9^0E) was selected. The area was passing through by Mat fault and is the most pronounced part of the fault (Malsawma et al., 2010). After selecting the location a rectangular grid of 9 spots covering an area of 1000×400 m was developed with three spots within the fault line (Fig. 3.2). The first 6 spots form a sub-rectangular grid (400×200 m), where three of them lie within and along the fault line while the other three lie at a distance of 200 m from the fault line adjacent to the first three spots. The last three 200 m apart spots lie at a distance of 1 km from

the fault line adjacent to the first two groups as shown in Fig. 3.2. Every radon and thoron data at Mat fault were retrieved from those six spots.

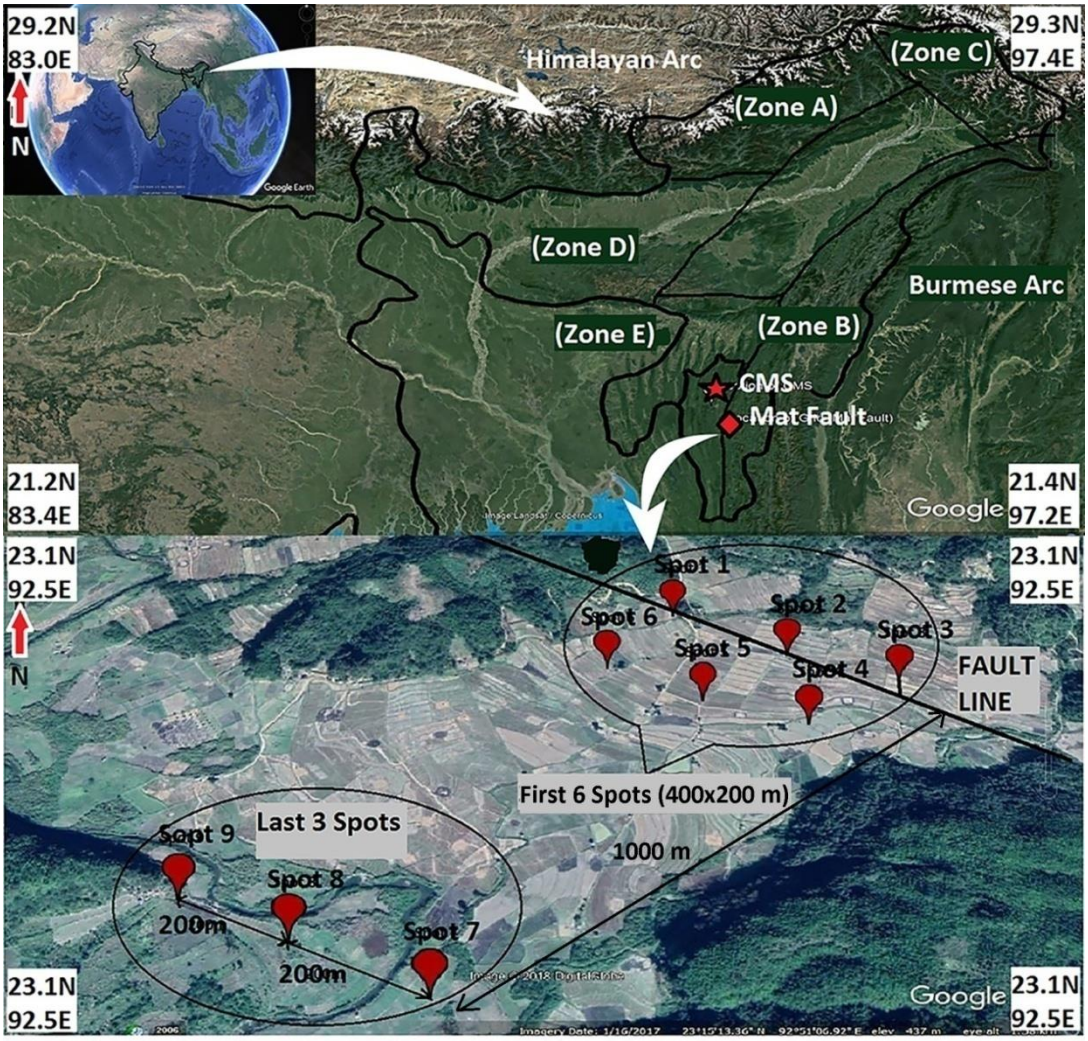

Fig. 3.2: Map showing location of Mat fault and formation of the rectangular grid (1000×400 m) at Zawlpui.

Radon and Thoron data: To measure *in-situ* data of the isotope pair at different sampling depths the following procedure has been followed. Firstly, for measurement at the soil-air interface radon exhalation chamber (Accumulator chamber=3.3×10^{-3} m^3) was placed at spot 1 by immersing its opening edge at 2 cm depth into the soil. Precaution was taken in such a way that the accumulator-soil interface was airtight to avoid interference by atmospheric air. The sample outlet of the accumulator chamber was connected with the sample inlet of the scintillation cell

of the SMARTRnDuo through a progeny filter using a rubber tube (Fig. 3.3). The cell outlet was then connected to the pump inlet but whose outlet was kept open for releasing the counted sample gas into the atmosphere. At the same time, the sample inlet of the accumulator chamber was closed to avoid atmospheric air. After completion of the connection between the accumulator chamber and the SMARTRnDuo/monitor, it was turned ON in thoron mode with 15 minutes cycle. By turning *ON* the monitor, the inbuilt pump draws in the accumulated sample gas of the accumulator chamber through a progeny filter into the scintillation cell of the monitor. At the same time, it draws out all the gases which were already counted in the scintillation cell volume through the tube connecting the sample outlet and pump inlet of the instrument and releases them to the atmosphere through the opening pump outlet. Progenies of the isotope pair and trace gases were eliminated by the progeny filter before entering the scintillation cell. Of the 15 min cycle, the initial 5 min was utilized for pumping in the sample gas and counting alpha particles simultaneously. Hence alpha counts of this first 5 min interval were attributed to both radon and thoron concentrations in the sample gas. Automatically the inbuilt pump switches OFF after the first 5 min and counting of alpha particles was also delayed for the following 5 min to ensure that short-live thoron may decay out. Again the monitor automatically starts counting alpha particles in the last 5 min interval of the 15 min cycle which attributes to the radon concentration of the initial 5 min sampling gas. Finally, the thoron concentration was obtained by subtracting the last 5 min interval counts (radon counts) from the initial 5 min counts (sum of radon and thoron counts) of the 15 min cycle. After acquiring the isotope pair data at the soil-air interface the accumulator chamber was replaced by a soil probe of 1 m length for assessing deeper sampling depths. As shown in Fig. 3.4 the soil probe was hammered down to the desired sampling depth which is 5 cm depth just after the soil-air interface. The connection of the soil probe and the monitor was done in such a way that the sample outlet of the soil probe was connected to the scintillator inlet of the monitor through a progeny filter. Like in case of the accumulator the sample inlet of the soil probe was closed to avoid atmospheric air and the pump outlet was open for releasing of counted gas. All other connections and methods of operation of the monitor for retrieving the isotope pair data were exactly the same as that of the soil-

air interface mentioned above. After 15 min cycle that is after acquiring radon isotope pair data at 5 cm depth the soil probe was further hammered down at 50 cm depth to obtain data of this depth. The connection and method of operation of the monitor remain the same as that of 5 cm depth. Again after another 15 min, the soil probe was further hammered down to 1 m depth and by operating in the same manner the isotope pair data of this depth was recorded by the monitor. In this way, the isotope pair data of four different sampling depths at spot 1 was obtained. Now it was proceeded to spot 2 and the same method and operation manual has been repeated to obtain the isotope pair data of the four sampling depths. The procedure keeps on repeating until spot 9 was reached and a total of 1 hour was spent at each spot for acquiring the four sampling depths. In this manner, the isotope pair data of four different sampling depths were monitored with one-month frequency from those 9 spots at Mat fault (Zawlpui) in an attempt to find their geophysical properties.

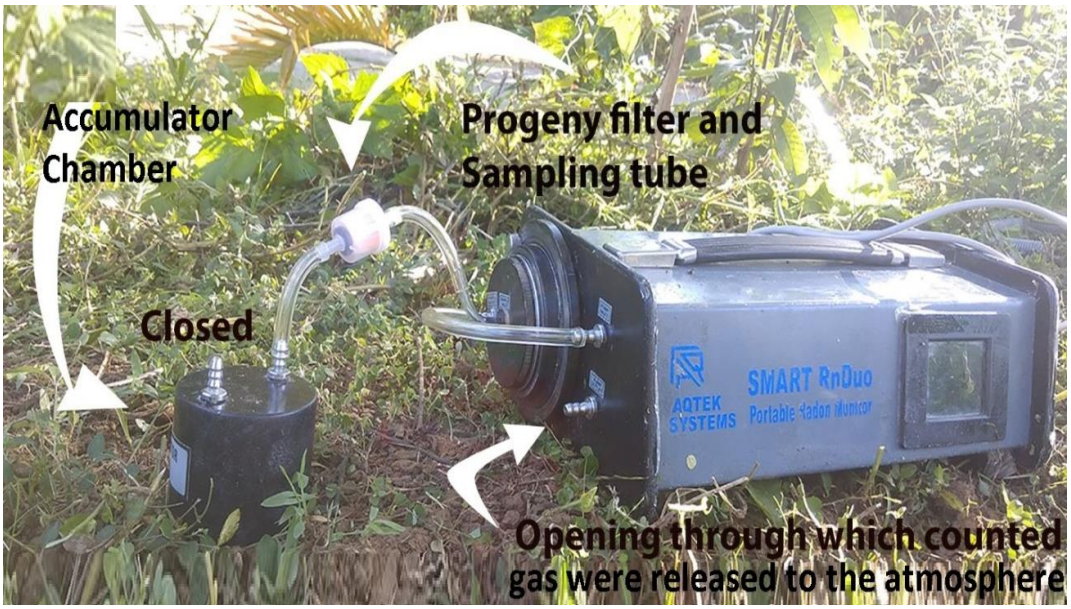

Fig. 3.3: Photo showing the arrangement of an accumulator chamber (3.3×10^{-3} m^3) and SMARTRnDuo for measurement of radon isotope pair at the soil-air interface.

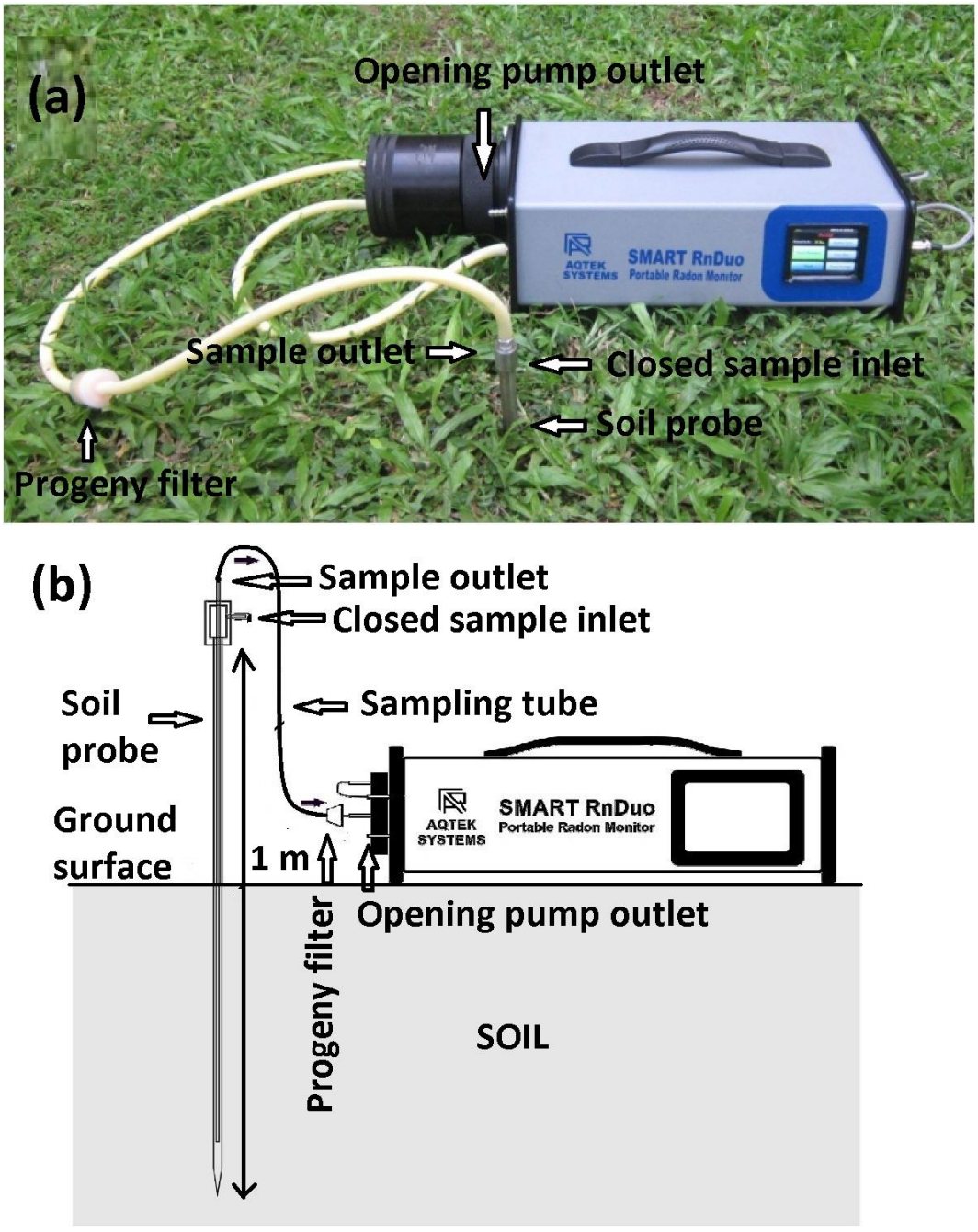

Fig. 3.4: (a) Photo showing the arrangement of SMARTRnDuo and a soil probe (1 m) for measurement of the isotope pair data at different soil depths (b) Schematic diagram depicting measurement of soil radon and thoron data using soil probe of 1 m length and SMARTRnDuo.

Radon Mass exhalation rate: Every time the field was visited with a frequency of once a month, soil samples were simultaneously collected from each of the 9 spots. Each collected soil sample approximately weight 0.5 kg and was packed in air-tight plastic bags such that the isotope pair may not escape. They were then brought back to the Laboratory and emptied into a radon mass exhalation chamber (5.0×10^{-4} m^3). The detector probe of the monitor was then removed and mounted on it using the provided slide-tight mechanism which prevents it from leakage (Fig. 3.5). After finishing the connection between the monitor and the mass exhalation chamber, it was operated in radon mode with 60 min cycle for 24 hours. In radon mode entry of thoron into the scintillation cell was hindered by the thoron discriminator placed in front of the cell hence only radon data was recorded. Since the scintillation cell is fixed with the mass exhalation chamber for 24 hours the radon concentration is expected to increase or build-up after every 60 min by the time it was recorded and displayed on the monitor screen. After 24 hours the recorded radon concentration data was downloaded and least fitted to obtain the radon build-up rate *C(t)*. The build-up rate was then subsequently substituted into equation (3.3) to obtain the radon mass exhalation rate of the region.

$$C(t) = \left(\frac{J_m M}{V} \right) t + C_\circ \tag{3.3}$$

where J_m is the radon mass exhalation rate ($Bqkg^{-1}s^{-1}$), M is the mass of the soil sample (kg), V is the volume of the mass exhalation chamber (m^3) and C_0 is the radon concentration at $t=0$.

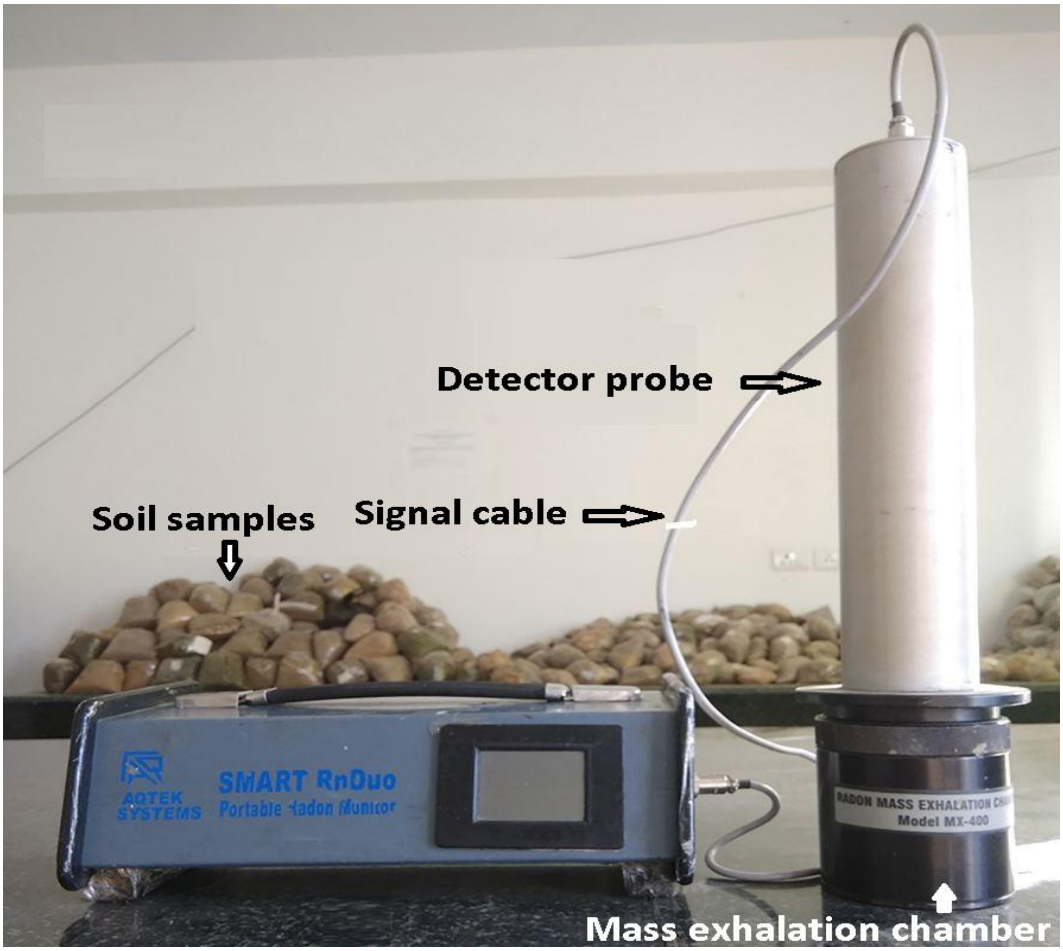

Fig. 3.5: Photo of collected soil samples and arrangement of SMARTRnDuo for performing radon mass exhalation.

Radon isotope pair data in water: For measuring radon and thoron data from water, all water sources near the vicinity of the above 9 sampling spots were located. A total of 5 such water spots were selected for sampling spots. Similar to those of soils the water samples were collected with one month frequency from these selected spots. Starting from the first spot water samples were collected in a leak-tight sampling glass bottle of 2.2×10^{-4} m^3. The sampling bottle was connected to the monitor using a bubbler having a sampling outlet and bubbling pipe (Fig. 3.6). The sample outlet of the bubbler was connected to the sampling inlet of the monitor through a progeny filter while the pump outlet of the monitor to the bubbling pipe. After finishing the necessary connection the pump was turned ON for 3 min such that it may cause bubbling in the sample water through the bubbler. These actions

will push most of the dissolves radon gas in water into the scintillation cell through the progeny filter. Now, the monitor was run in radon mode for 1 hour with 15 min cycle. And this counting of alpha particles must be done within 4-5 hours after sampling. The first reading was discarded to avoid corruption in the data. Averages of the last three readings were taken as radon concentrations of the sample water. The exact same procedure was followed for retrieving thoron concentration in water except that the monitor was operated in thoron mode. In this way, radon and thoron concentrations of all five sampling spots were assessed by moving from one spot to another till the last spot was reached.

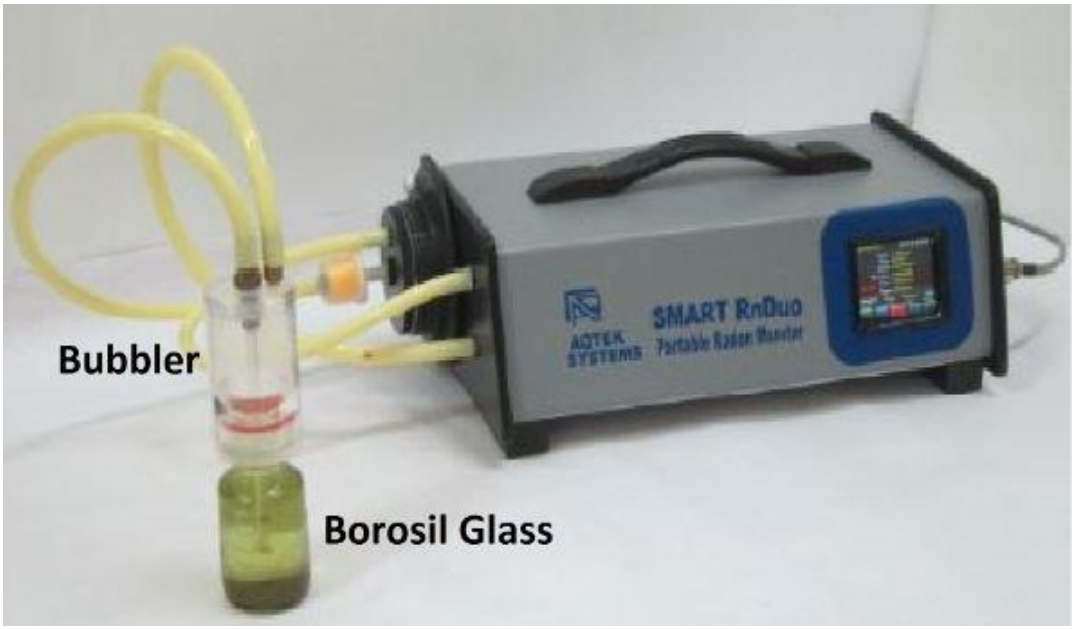

Fig. 3.6: Photo showing the arrangement of SMARTRnDuo and collected water sample in a glass bottle (2.2×10^{-4} m^3) for measurement of the isotope pair data in water.

3.4 Protocol for Measurement of Radon Isotope Pair at Chite Fault

Formation of sampling spots: Chite fault lies at the heart of Aizawl city and the formation of grid with large coverage was not possible due to hindrance by the congested building structure. Such that instead of a rectangular grid three sampling spots situated along the fault line were selected for generating the radon isotope pair

data (23.7^0N, 92.7^0E) (Fig. 3.7). At the same time, the distance between the three sampling spots was approximately 500 m from each other.

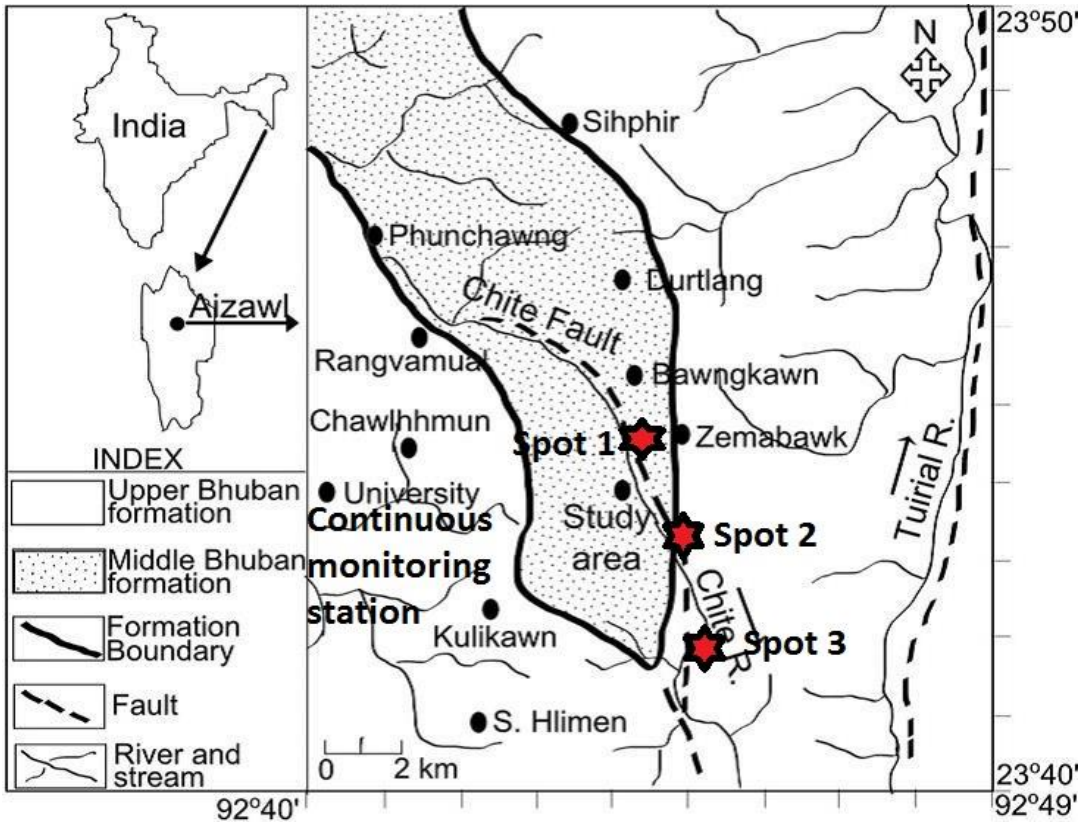

Fig. 3.7: Geological set-up of the study area showing Chite fault and the three measuring spots (Modified after Singh et al., 2014).

The method of acquiring the *in-situ* isotope pair data of the four sampling depths (soil-air interface, 5 cm, 50 cm and 1 m depths), radon mass exhalation rate, the isotope pair data in water and procedure in operating the monitor is exactly the same as that of Mat fault. The only difference to that of Mat fault is that the number of sampling spots gets reduced to 3 from 9.

3.5 Protocol for online monitoring of radon isotope pair

Before setting up the monitoring station a survey was made such that the selected location is suitable for such a setup. The main desired feature for such a location is that it should be at least 1 m away from a concrete building wall; it shouldn't be near any water source or drainage and shouldn't have any hidden concrete object which can hinder upward degassing. It should also be verified that the location has a normal

radon mass exhalation rate by comparing it with other locations. Based on the preliminary investigation the Department of Physics, Mizoram University, Aizawl, Mizoram was selected for continuous monitoring station (23.4^0N, 92.3^0E). After selecting a suitable location the next task is to set up a monitoring station with a stable environment such that meteorological influence on the isotope pair data may be minimized. For that, a monitoring station with dimensions of 2 m × 2 m × 1.5 m was set up at the above selected location (Fig. 3.8a). The dimension of the monitoring station was selected in such a way that it takes care of the 1 m diffusion length of radon in soil. Since the station was shaded from all sides, the exchange of meteorological factors from outside to inside was prevented and vice versa. Under such conditions, external influences especially due to meteorological factors on the exhalation process of radon gas were assumed to be extremely minimized. Such that to a certain level any observed radon anomalies monitored under such conditions may be taken as only due to geophysical phenomena of the region. An accumulator chamber of 5.0×10^{-4} m^3 was placed at the centre of the station and connected to the monitor via two rubber tubes, one for sampling (inlet tube) and the other for releasing it (outlet tube) (Fig. 3.8b). The monitor was then operated in thoron mode with 15 min cycle. During the first 5 min interval, the accumulated sample gas of the accumulator chamber was brought into the scintillation cell through the inlet tube by the pump. At the same time counted sampled gas inside the scintillation cell was released back to the accumulator chamber through the outlet tube. All alpha particles and trace gases of the sampling gas were filtered out by the progeny filter attached to the inlet tube (Fig. 3.8b) and hence only radon and thoron gases make it into the scintillation cell. During this period the monitor not only sampled but simultaneously counts alpha particles from the isotope pairs. Since the progeny filter and the monitor were unable to differentiate alpha particles of the isotope pair, hence alpha counts of the first 5 min interval were attributed to both radon and thoron. The next 5 min was delayed in counting to ensure that the short lives (55.6s) thoron decayed off. Counting of alpha particles was resumed during the last 5 min interval which attributed to the radon concentration of the sampling gas. After that, the inbuilt pump automatically turns ON for another 15 min cycle of sampling and counting and so on for 24 hours during the whole measuring period.

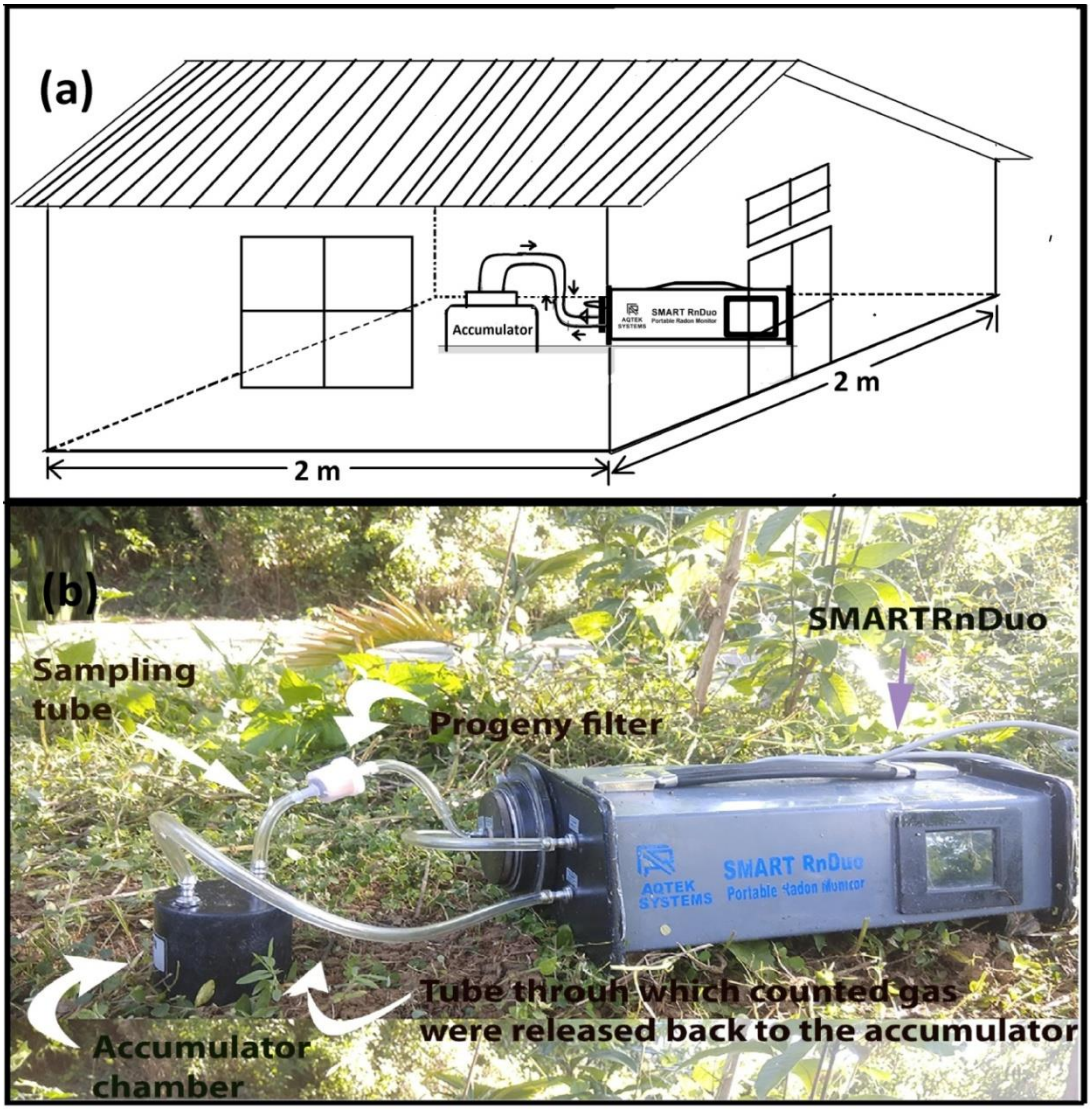

Fig. 3.8: (a) Schematic diagram showing the set-up of the continuous monitoring station (Geostation) at the Department of Physics, Mizoram University (b) Photo of the SMARTRnDuo and its complete arrangement for continuous monitoring of the isotope pair data.

3.6 Meteorological Influence on the Radon Isotope Pair Data

Pearson correlation analysis: To observe the meteorological influence on the isotope pair data a Pearson correlation analysis was performed between the two data in SPSS statistical package. To test the significance of the correlation analysis a two-tail t-test at 95% confidence level (α=0.05) was further performed. Hence any

correlation analysis having a significance p-value less than 0.05 is considered significant or otherwise non-significant.

Multiple Linear Regression (MLR): For observing the most influencing meteorological factors on the isotope pair data a backward MLR was performed through different models in SPSS statistical package. In the first model, the dependent variable (Radon) was regressed with all the predictor variables (air temperature, pressure, rainfall, humidity and wind speed). In the next model variables with the highest p-value was excluded to improve the model. The exclusion of variables in the succeeded model was completely based on the p-value being the highest in the previous model regardless of whether it is significant or not. And the process was repeated until no candidate variable was available. The raw score multiple linear regression was given by equation (3.4) (Jaishi et al., 2014b; Singh et al., 2017) and facilitates the study of several independent variables for a given independent variable.

$$Y' = a + b_1X_1 + b_2X_2 + b_3X_3 + ... + b_nX_n \quad (3.4)$$

where Y' is the predicted value of the dependent variable, a is the constant term, b_1, b_2, ..., b_n are the regression coefficient and X_1, X_2, ..., X_n are the independent variables. But the regression coefficient of equation (3.4) depends on the unit of the independent variable; hence it was not appropriate to compare the independent variables amongst themselves to find out the most influencing independent variables on the dependent variables. To overcome this problem both the coefficient and variables were standardised using equation (3.5) (Jaishi et al., 2014b) which facilitate direct comparison among the predictors.

$$Z_Y' = \beta_1Z_{X1} + \beta_2Z_{X2} + ... + \beta_nZ_{Xn} \quad (3.5)$$

where β's and Z's are the standardised coefficient and Z-scores, respectively.

3.7 Methods for identifying radon and thoron anomalies

Until now no definite criterion has been defined for assigning anomalies in the time series radon isotope pair data; hence every author defines it as appropriate to its own

data (Igarashi and Wakita, 1990). For example, anomalies of atmospheric radon data 5 m above the ground surface at Kobe Pharmaceutical University was observed at 3σ (σ = standard deviation) from the mean (Iwata et al., 2018; Kawada et al., 2007; Omori et al., 2007; Yasuoka et al., 2009). On the other hand, several authors (Deb et al., 2018; Ghosh et al., 2007; Jaishi et al., 2014, 2014a; Ramola et al., 2008; Singh et al., 2014, 2016, 2017; Vaupotič et al., 2010) monitoring soil radon data adopt the mean plus 'n' times standard deviation (SD) criterion (n = 1, 2, 3,.....). All of them including authors (Jaishi et al., 2014, 2014a; Singh et al., 2014, 2016, 2017) who had monitors at the present study area by passive sampling reports radon anomalies at 2σ, 1.5σ as well as at 1σ prior to earthquakes. Recently, Sahoo et al. (2020) reports fluctuation in the Instantaneous Energy of time series radon data above 2σ and 1σ before some local earthquakes at Kutch, Gujarat, India. All these reports, specifically of radon data in soil signify that accumulated strain at a local distance from the monitoring station resulted in an increase of radon concentration above 1σ from its mean or more. Hence, any fluctuation above 1σ was confidently taken as a radon anomaly due to local geophysical phenomena in this thesis as well.

3.8 Non-linear based statistical technique for identifying radon and thoron anomalies (Empirical Mode Decomposition based Hilbert-Huang Transform)

Radon and thoron data are non-linear data as their exhalation process are affected by many external factors and meteorological factors being the most popular one. The effect of such external factors on the time series radon isotope pair data is embedded in the form of periodicities with different frequencies. Hence identification of the isotope pair anomalies directly from the raw data or application of linear or traditional analysis techniques such as Fourier transform, wavelet transform etc. is ambiguous and may lead to a false result. Hence a non-linear analysis technique called empirical mode decomposition based Hilbert Huang Transform (EMD-HHT) has been utilized for identifying the isotope pair anomalies in this thesis. The EMD-HHT is a two-step statistical analysis method for non-linear data. It is developed by Huang *et al*. (1998) and focused on the drawbacks of traditional methods like Fourier transform, wavelet transform etc. which were limited to linear systems only. Identifying abrupt changes in the frequency of non-linear data was the main

limitation of those traditional techniques, hence applying it to non-linear soil radon data is incompatible and ambiguous. The EMD-HHT technique facilitates all the inadequacy of those linear methods and is capable of identifying abrupt changes in the frequency of the non-linear data such as time series radon data (Huang et al., 1998a). Since time series radon data are influenced by periodic oscillations, direct application of Hilbert transform to the raw data may not be suitable as it is corrupted with noise, low-frequency trends, offsets, etc. (Shekel, 1953; Boashash, 1992; Cohen, 1995). Unless the raw data satisfied some restrictive global condition, the definition of some statistical parameters obtained from the transformation becomes ambiguous, especially the instantaneous frequency. Such problems are overcome by applying EMD to the raw data before feeding it to the HHT. The EMD completely breakdown the raw data into different oscillatory modes known as intrinsic mode function (IMF) which facilitates extracting all periodic oscillations embedded in the raw data. After that, only the significant IMFs are fed to the HHT to produce a consistent and meaningful frequency-time domain spectrum known as the Hilbert-Huang (HH) spectrum. The HH-spectrum provides various statistical properties of the raw radon data and intermittencies in the radon energy due to geophysical phenomena are also derived from it. The EMD-HHT was executed to the radon data by the following steps:

According to Huang *et al*. (1998a), a function designated as an intrinsic mode function (IMF) must satisfy the following two criteria: (1) for the whole raw dataset, the number of extrema and zero-crossing must be equal or else differ at most by one and (2) at any point along the data, the mean value of the envelopes defined by the local extrema must be zero. To facilitate the EMD the input signal (raw data) must also satisfy two criteria (1) that it must contain at least one minima and maxima i.e. a minimum of two extrema (2) the time-lapse between extrema defined by the characteristic time scale. Now all minima and maxima of the entire data are identified and connected using a cubic spline forming an envelope. The line connecting the maxima forms the upper envelope while that connecting the minima forms the lower envelope. This envelope is now utilized by the EMD to decompose the raw data into different oscillatory modes. All the dataset are now confined within

the envelope and has a mean of m1. The difference between the raw data X(t) and the mean m1 is taken and designated as the first component h1.

$$X(t) - m1 = h1 \tag{3.6}$$

The first component h1 is taken as the raw data and its mean m11 is subtracted from it to obtain the second component h11. The iteration continues k times until the wave is completely symmetric and the above mention criteria are achieved. The last component h1k denoted as c1 is the first IMF obtained from the raw data. It is the finest scale of the raw data devoid of riding waves and has the smallest period of all the IMFs. Using this component (c1) all the IMF may be extracted from the raw data.

$$h1 - m11 = h11 \ \ldots\ldots\ldots\ldots \ h1_{(k-1)} - m1k = h1k(c1) \tag{3.7}$$

Now the finest scale of the data c1 obtained from equation (3.7) is subtracted from the raw data X(t) to obtain the first residual r1.

$$X(t) - c1 = r1 \tag{3.8}$$

Again the residue r1 is treated as the raw data and the same subtraction is carried out to obtain the second residue r2 and so on till the signal becomes a monotonic function and no more IMF can be extracted from it.

$$r1 - c2 = r2 \ \ldots\ldots\ldots \ X(t) - \sum_{j=1}^{n} c_j = r_n \tag{3.9}$$

Here c_j is the IMFs and r_n is the monotonic function. In this manner, all the IMFs from the raw data are extracted which now can be analyzed using the Hilbert-Huang transformation. The Hilbert transform produced instantaneous amplitude A(t) and phase θ(t) of the IMFs and exhibit them in a time-frequency domain called the Hilbert-Huang spectrum, H(t, ω). The Hilbert-Huang spectrum is a weighted non-normalized joint amplitude-frequency-time distribution. Consequently time derivative of the phase θ(t), gives the instantaneous frequency (ω) of the IMFs.

$$\omega(t) = \frac{\partial \theta(t)}{\partial t} \tag{3.10}$$

$$H(t,\omega) = \mathrm{Re}\sum_i A_i(t)\exp(j\int \omega_i(t)dt) \tag{3.11}$$

Besides the instantaneous frequency, three other important statistical characteristics of the IMFs are extracted from the HH-spectrum.

Marginal spectrum, h(ω): It represents a measure of the total amplitude (energy) contributed by each frequency value or it is a probabilistic representation of accumulated energy over the entire data span.

$$h(\omega) = \int_0^T H(t,\omega)dt \tag{3.12}$$

Degree of non-stationary, DNS(ω): It is an index representing that the considered raw data is non-stationary data. Physically it is a measure of how much the HH-spectrum deviates from the mean marginal spectrum.

$$DNS(\omega) = \frac{1}{T}\int_0^T \left(1 - \frac{H(t,\omega)}{h(\omega)}\right)^2 dt \tag{3.13}$$

Instantaneous Energy, IE: It is the variation of energy with time from where intermittencies of the data will be observed.

$$IE(t) = \int_\omega H^2(t,\omega)d\omega \tag{3.14}$$

Applications of the EMD-HHT technique in various fields of work were given in detail by Barman et al. (2016), Chowdhury et al. (2017) and Sahoo et al. (2020).

3.9 Method of calculation for estimating Uranium and Thorium from their respective daughter nuclei

The isotope pair data counts of Mat fault, Chite fault and the continuous monitoring station were converted into their respective concentrations using equation (3.15) (IAEA, 2013).

$$C_{Rn} = \frac{C}{3EVe^{-\lambda t}} \tag{3.15}$$

where C is the net count rate (count per second, s^{-1}) of ^{222}Rn or ^{220}Rn, E is the efficiency of counting, V is the volume of the sampler (m^3), λ is the decay constant of ^{222}Rn or ^{220}Rn, t is the time delay post-sampling (s) and 3 represent the three alphas in the respective decay chain of ^{222}Rn and ^{220}Rn.

For acquiring radon flux, the monitor was operated in radon mode with 15 min cycle using an accumulator chamber (2.1×10^{-4} m^3) for 3 hours in each of the desired sampling spots. The arrangement between the monitor and the accumulator chamber was exactly as shown in Fig. 3.8b. The accumulated radon concentration of each spot was least fitted and then averaged out to get the radon concentration built-up rate $C(t)$. It was then subsequently substituted in equation (3.16) to get the radon flux of the region (IAEA, 2013).

$$C(t) = C_0 + k\frac{A}{V}ft \tag{3.16}$$

where C_0 is the initial concentration (Bqm^{-3}), k is the factor by which the initial flux drops while the gas inside the accumulator passes through a state of uniform mixing prior to deployment to the state of diffusive mixing post to deployment, A is the surface area of the opening of the accumulator (m^2), V is the effective volume of the sampling device (m^3), f is the flux of radon ($Bqm^{-2}s^{-1}$) and t is the measurement time (s).

To obtain thoron flux the thoron equilibrium concentration is required in the first step. Using the thoron equilibrium concentration, the thoron flux of the soil-air interface will be estimated. For that, the accumulator chamber was placed in one of the desired sampling spots and connected to the monitor. Now the monitor was operated in thoron mode with 15 minutes cycle for 1 hour at each spot. The average of the last three readings from all the spots was taken as the thoron equilibrium concentration of the region. The first reading of each spot has been neglected to avoid corruption in the data due to external sources. The equilibrium concentration was then substituted in equation (3.17) to estimate the thoron flux of the region (IAEA, 2013).

$$f = \frac{C_{eq}V\lambda}{A} \tag{3.17}$$

where C_{eq} is the ^{220}Rn equilibrium concentration (Bqm^{-3}), V is the effective volume of the sampling device (m^3), λ is the thoron decay constant and A is the surface opening area of the accumulator (m^2).

To estimate the ^{238}U concentration, first, the radon production rate (J_m) was obtained from the soil sample. The method for assessing J_m was already discussed elsewhere in section 3.3. After obtaining the mass exhalation rate it was further substituted into equation (3.18) for retrieving ^{226}Ra content of the soil samples (IAEA, 2013).

$$J_m = R\mathrm{E}\lambda \tag{3.18}$$

where R is ^{226}Rn content of the soil in $Bqkg^{-1}$, E is the emanation coefficient of ^{222}Rn (0.1-0.3 in soil) (IAEA, 2013), λ is the radioactive decay constant of ^{222}Rn .

On the other hand, the ^{232}Th content of the soil was estimated using equation (3.19) after substituting the thoron flux from equation (3.17) (IAEA, 2013).

$$f = \lambda LR\rho E \tag{3.19}$$

where f is the ^{220}Rn flux at the soil-air interface, λ is the ^{220}Rn decay constant, L is the diffusion length of ^{220}Rn in soil (0.013 m) (IAEA, 2013), R is the ^{224}Ra content in the soil, ρ is the density of the soil matrix and E is the emanation coefficient of ^{220}Rn (0.14) (IAEA, 2013).

For estimating the uranium and thorium contents in water the radon and thoron concentrations were first retrieved as discussed in section 3.3. The obtained radon and thoron concentrations were then substituted in equation (3.20) for retrieving ^{238}U and ^{232}Th content of the water respectively (IAEA, 2013).

$$E = \frac{VC}{MR} \tag{3.20}$$

where E is the radon or thoron emanation coefficient, V is the effective volume of the sampling device (m^3), C is the radon or thoron concentrations (Bqm^{-3}), M is the total mass of the sample (kg) and R is the ^{226}Ra or ^{224}Ra content of the sample water

(*Bqkg*$^{-1}$). Since, the ^{226}Ra and ^{224}Ra are in equilibrium concentrations with their parent nuclei, they may be used for depicting ^{238}U and ^{232}Th concentrations of the region respectively.

4

Results and Discussion

4.1 Radon and Thoron data profile of the study region

The radon profile at Mat fault, the continuous monitoring station (Mizoram University) and Chite fault were assessed through different window periods of field studies. All the studies were carried out between 2017 and 2019.

At Mat fault: The radon and thoron concentrations of the soil-air interface at Mat fault were found to be 8143.2±125 Bqm^{-3} and 13822.9±124 Bqm^{-3}, respectively with a ratio of 1.69. The isotope pair concentrations were obtained by substituting their respective average counts in equation (3.1) of the previous chapter. Where their average counts were of six months (May, 2018-October, 2018) period one-month frequency sampling data from 9 location spots. The average radon and thoron concentrations from the three successive sampling depths (5 cm, 50 cm and 1 m) were also found to be 1614.3±114 Bqm^{-3} and 3143.5±140 Bqm^{-3} respectively with a ratio of 1.94. Hence the average radon and thoron concentration of the four sampling depths (soil-air interface, 5 cm, 50 cm and 1 m depths) representing Mat fault was estimated to be 4878.8±117 Bqm^{-3} and 8483.2±132 Bqm^{-3} respectively with a ratio of 1.74.

At the continuous monitoring station (Mizoram University): At Mizoram University the radon and thoron concentrations were found to be 2219±6.2 Bqm^{-3} and 2729±7.2 Bqm^{-3} with a ratio of 1.2. The isotope pair data at Mizoram University was an average of three months period acquired with 15 min cycle from one spot.

At Chite fault: At Chite fault, the isotope pair data was an average of six months period one-month frequency sampled data from 3 location spots. The radon and thoron concentrations at this fault were found to be 5164.6±110 Bqm^{-3} and 8968.1±160 Bqm^{-3} respectively with a ratio of 1.74.

The isotope pair concentrations of the two faults were relatively close and were much higher than that of Mizoram University indicating that fault provides an easy

pathway to migrating gas due to its loose soil formation (Aswal *et al*., 2016; King, 1986). At the same time, the higher thoron concentration of all the three sampling locations revealed that the region has a higher thoron concentration than its isotope. However, when compared to the global average given by IAEA (2013) they were well within the limits of 10^3-10^5 Bqm^{-3} in soil. The standard error of the isotope pair data at MZU was quite low compared to that of at Mat and Chite fault revealing the provided equilibrium environment inside the monitoring station by shading it. The observed high standard error at Mat and Chite fault may be due to the data being generated in open space under the influence of all external factors. Also, they were an average of all data measured in all different seasons for one complete year with one-month frequency.

Radon and thoron depth profile: The radon and thoron depth profile study was performed in two different window periods that is from November, 2017-April, 2018 and May, 2018- October, 2018. Both the studies were carried out at Mat fault whose averages represent the region. To reveal the radon and thoron depths profile all the data were expressed in counts per minute ($Countsm^{-1}$). For the first window period; averages of the monthly generated radon and thoron data $Countsm^{-1}$ of all the four sampling depths were given in Table 4.1. From Table 4.1, it can be seen that except at 1 m depth the thoron counts were higher than radon for the whole observation period. The radon to thoron ratio was 0.8 at the soil-air interface, 0.5 at 5 cm depth, 0.8 at 50 cm depth and 1.4 at 1 m depth respectively. Hence, in general, like their concentrations, the thoron count was higher than radon. The rate by which the two gases changes with depth was obtained by substituting $countsm^{-1}$ data of the two gases in equation (4.1). For this, the radon data at the ground surface was neglected instead the 5 cm data was selected to represent radon at the surface.

$$\frac{C_i - C_n}{n - i} \tag{4.1}$$

where i is the i^{th} sampling depth in *cm*, n is the n^{th} sampling depth in *cm* successive to the i^{th} sampling depth, C_i the observed $Countsm^{-1}$ of ^{222}Rn or ^{220}Rn data at the i^{th} sampling depth and C_n the $Countsm^{-1}$ of ^{222}Rn or ^{220}Rn at the n^{th} sampling depth.

Table 4.1: Details of the isotope pair counts per minute ($countsm^{-1}$) at different sampling depths, their ratio and changes of the $countsm^{-1}$ with depth ($Countsm^{-1}cm^{-1}$) for data generated during November, 2017-April, 2017.

Location/Depth	**Average counts per minute ($Countsm^{-1}$)**		**$^{222}Rn/^{220}Rn$ counts ratio**
	^{222}Rn	**^{220}Rn**	
Soil-Air interface	35.4	41.7	0.8
5 cm depth	113.2	222.0	0.5
50 cm depth	288.5	354.8	0.8
1 m depth	467.9	339.4	1.4

Sample gas	**Average counts per minute per centimetre ($Countsm^{-1}cm^{-1}$)**		
	5 cm-50 cm	**50 cm-1m**	**5 cm-1 m**
^{222}Rn	3.9	3.6	3.7
^{220}Rn	3.0	-0.3	1.3

Using equation (4.1) it was estimated that ^{222}Rn increases with the rate of 3.9 $Countsm^{-1}cm^{-1}$ and 3.6 $Countsm^{-1}cm^{-1}$ from sampling depths of 5 cm-50 cm and 50 cm-1 m respectively with an average of 3.7 $Countsm^{-1}cm^{-1}$ from 5 cm-1 m depth. On the other hand ^{220}Rn changes from a sampling depth of 5 cm-50 cm with the rates of 3.0 $Countsm^{-1}cm^{-1}$ and then changes with the rate of -0.3 $Countsm^{-1}cm^{-1}$ from 50 cm-1 m with an average of 1.3 $Countsm^{-1}cm^{-1}$ from 5cm-1m depth.

For the second study period, after substituting the isotope pair counts per minute ($Countsm^{-1}$) in equation (4.1) their depth profile has been observed as shown in Table 4.2. It has been found that radon changes by the rate of 4.0 $Countsm^{-1}cm^{-1}$ from

5 cm to 50 cm depths and 3.3 *Countsm^{-1}cm^{-1}* from 50 cm to 1 m depths with an average of 3.7 *Countsm^{-1}cm^{-1}* between 5 cm and 1 m sampling depths. However, thoron changes by 0.2 *Countsm^{-1}cm^{-1}* and 0.7 *Countsm^{-1}cm^{-1}* from 5 cm to 50 cm and 50 cm to 1 m, respectively with an average of 0.5 *Countsm^{-1}cm^{-1}* from 5 cm to 1m depths. Hence, the diffusion rate of radon and thoron of the region was approximated to be 3.7 *Countsm^{-1}cm^{-1}* and 0.5 *Countsm^{-1}cm^{-1}* respectively.

Table 4.2: Details of changes of the isotope pair counts per minute (countsm^{-1}) with depth (Countsm^{-1}cm^{-1}) for data generated during May, 2018-October, 2018.

Sample gas	**Average counts per minute per centimetre (Countsm^{-1}cm^{-1})**		
	5 cm-50 cm	**50 cm-1m**	**5 cm-1 m**
^{222}Rn	4.0	3.3	3.7
^{220}Rn	0.2	0.7	0.5

When compared the two study periods, the first period that is November, 2017 to April, 2018 comprised the dry season while the second period May, 2019 to October, 2018 comprised the wet and turbulence season of the region. But when compared the radon data count per minute per centimetre (Countsm^{-1}cm) of the two study periods they exactly have the same value of 3.7 indicating that the radon profile within 1 m from the ground surface remains more or less the same during the whole season. Thoron data other hand has an average of 1.3 Countsm^{-1}cm and 0.5 Countsm^{-1}cm during the first and second study periods respectively with an average of 0.9 Countsm^{-1}cm for the whole season. It means that if we move toward the 1 m depth by a centimetre step and count for 1 minute at each centimetre, the radon counts will be added by 3.7 counts at every extra centimetre depth while 0.9 counts for thoron. This observation indicates that the isotope pair data were minimum at the surface and increases with depth. This is an ideal depth and condition for monitoring radon variation due to geophysical phenomena because at deeper sapling depth (~ 1 m depth and beyond) they attained asymptotic value and their variation due to external source is hard to identify (Sahoo *et al*., 2016).

4.2 Uranium and Thorium content of the region

4.2.1 Radon isotope pair (^{222}Rn and ^{220}Rn) fluxes and their parent nuclei (^{238}U and ^{232}Th) content at Mat Fault

At Mat fault, radon and thoron data of the sub-soil were measured during May, 2018-October, 2018 from 9 sampling spots with one-month frequency. As mentioned above any estimated radon and thorn data was an average of six months period one-month frequency sampled data from 9 locations spots. The isotope pair data were then utilized for estimating their fluxes, production rate in soil, uranium and thorium content. By following the methods detailed in section 3.9 of the previous chapter and utilizing the isotope pair data the following estimation has been made at Mat fault (Table 4.3). The ^{222}Rn and ^{220}Rn fluxes at the soil-air interface at Mat fault were found to be 0.015 $Bqm^{-2}s^{-1}$ and 2.7 $Bqm^{-2}s^{-1}$, respectively. The mass exhalation rate of radon at Mat fault was also found to be 0.030 $Bqkg^{-1}h^{-1}$. The ^{226}Ra and ^{224}Ra content of the soil was estimated to be 16.9 $Bqkg^{-1}$ and 49.7 $Bqkg^{-1}$ respectively. The ^{226}Ra and ^{224}Ra concentrations are in equilibrium with their respective parent nuclei (^{238}U and ^{232}Th) in soil (IAEA, 2013). Hence the ^{238}U and ^{232}Th content of Mat fault may be expressed as 16.9 $Bqkg^{-1}$ and 49.7 $Bqkg^{-1}$, respectively. The ^{220}Rn flux to ^{222}Rn flux and ^{232}Th to ^{238}U content was found to have a ratio of 180 and 2.9 respectively (Table 4.3). It was also already mentioned in the previous section that the radon to thoron ratio was less than one. Hence it was evident that the higher ^{232}Th content reflects in higher concentrations and flux of its daughter nuclei (^{220}Rn) to that of its isotope (^{222}Rn) of ^{238}U decay chain. When compared to that of the worldwide average the ^{222}Rn flux was in close agreement with the one (15-20 $mBqm^{-2}s^{-1}$) given by UNSCEAR (1982) while ^{220}Rn flux surpass the reported range (1-1.9 $Bqm^{-2}s^{-1}$). The activity concentration of ^{238}U and ^{232}Th were found to be respectively lower and higher than their corresponding global average of 35 $Bqkg^{-1}$ and 30 $Bqkg^{-1}$ given by UNSCEAR (2000). At the same time, both the activity concentration of ^{238}U and ^{232}Th were much lower than the critical value of 1000 $Bqkg^{-1}$ set by IAEA (2004). Hence in terms of health hazards, no radiological risk was observed in the study area.

Table 4.3: Details of estimated ^{222}Rn, ^{220}Rn, ^{238}U and ^{232}Th data at Mat fault.

	^{222}Rn	^{220}Rn	Ratio

			(^{220}Rn/^{222}Rn)
Bqm^{-2}s^{-1}	0.015	2.7	180
	^{238}U	**^{232}Th**	**Ratio (^{232}Th/^{238}U)**
Bqkg^{-1}	16.9	49.7	2.9

4.2.2 Radon isotope pair (^{222}Rn and ^{220}Rn) fluxes and their parent nuclei (^{238}U and ^{232}Th) content at Chite Fault

The sampling method for radon and thoron data at Chite fault was exactly the same as that of Mat fault. Instead of 9 sampling spots, three sampling spots 500 m apart along the fault line were considered as mentioned in the previous chapter. The data were assessed between February, 2018 and July, 2018 with one month frequency. Hence just like that of Mat fault, the isotope pair data were an average of six months period one-month frequency sampled data from 3 sampling spots. The methods for obtaining the isotope pair concentrations, fluxes and procedure for estimating their respective parent nuclei are exactly as described in section 3.9 in the previous chapter.

The radon and thoron fluxes at Chite fault were found to be 0.02 *Bqm^{-2}s^{-1}* and 2.4 *Bqm^{-2}s^{-1}*, respectively (Table 4.4). Also, the ^{238}U and ^{232}Th content of Chite fault was estimated to be 32.9 *Bqkg^{-1}* and 44.9 *Bqkg^{-1}* respectively. Again the obtained results were compared with the global average given by organizations like UNSCEAR (1982, 2000) and IAEA (2004, 2013). The reported global averages were as follows: (1) radon flux=15-20 *mBqm^{-2}s^{-1}*; thoron flux=1-1.9 *Bqm^{-2}s^{-1}* (UNSCEAR, 1982) and (2) ^{238}U content of soil=35 *Bqkg^{-1}*; ^{232}Th content of soil=30 *Bqkg^{-1}* (UNSCEAR, 2000). When compared with the global average, radon and uranium content were in agreement with high accuracy. While the thoron flux and thorium content were higher than the global average as that of Mat fault (Table 4.4). At the same time, the thoron flux and thorium content were higher than that of radon flux and radium content respectively. However, when compared to the critical value (1000 *Bqkg^{-1}*)

given by IAEA (2004), the estimated uranium and thorium content were much below it. Hence no radiological risk was observed from the Chite fault area as well.

Table 4.4: Details of estimated ^{222}Rn, ^{220}Rn, ^{238}U and ^{232}Th data at Chite fault.

	^{222}Rn	**^{220}Rn**	**Ratio (^{220}Rn/^{222}Rn)**
Bqm^{-2}s^{-1}	0.02	2.4	120
	^{238}U	**^{232}Th**	**Ratio (^{232}Th/^{238}U)**
Bqkg^{-1}	32.9	44.9	1.4

When compared the estimated values of the two faults, it was evident that the radon flux and uranium content of the region falls within the worldwide average limits. However the thoron flux and thorium content of the region surpass the global average. The higher thorium content reflects the observed higher thoron contents in both the faults. But when compared to the critical value given by IAEA (2004) no radiological risk was observed for the region.

4.3 Radon isotope pair (^{222}Rn and ^{220}Rn) and their parent nuclei (^{238}U and ^{232}Th) concentrations in water and their comparison to that of in soil

To investigate the radon isotope pair data in water, all water sources in the vicinity of the 9 sampling spots at Mat fault were identified as mentioned elsewhere. A total of 5 such water sources were selected for investigation. The radon isotope pair data in water were measured between May, 2018 and October, 2018. At the same time, the isotope pair data in soil was also simultaneously measured at all the 5 selected spots for comparison. Hence any water or soil data in this section is an average of six months period one-month frequency sampling data from 5 sampling spots. It must also be noted that radon isotope pair data of this section were distinct from data reported elsewhere and generated separately for studies in water and its comparison with soil data. Similar to that of the above two sections the calculation methodology was that of given in section 3.9 of the previous chapter. The radon and thoron data in

water were found to be 7557.0 and 12091.2 Bqm^{-3}, respectively (Table 4.5). Also, the uranium and thorium content in water were estimated to be 41.6 and 124.8 $Bqkg^{-1}$, respectively (Table 4.5). On the other hand, radon and thoron concentrations in soil (generated in the vicinity of the 5 water sources) were found to be 5649.4 and 11858.2 Bqm^{-3} respectively (Table 4.5). The radon and thoron fluxes of the soil-air interface were found to be 0.016 and 1.25 $Bqm^{-2}s^{-1}$ respectively with radon mass exhalation rate of 7.36×10^{-6} $Bqkg^{-1}h^{-1}$ (Table 4.5). Finally, the ^{238}U and ^{232}Th content of the soil were estimated to be 17.5 and 22.6 $Bqkg^{-1}$ respectively (Table 4.5).

When compared the radon isotope pair data of the two sampling media i.e. water and soil, their concentration in water was found to be higher than in soil. Their parent nuclei content in water were also higher in water. The radon concentration in water and soil has a ratio of 1.3 while thoron has 1.0 respectively. The uranium content in water and soil also has a ratio of 2.4 while thorium has 5.5 in the two sampling media. Hence it was evident that the radon isotope pair as well as their parent concentrations in water was higher than that of soil in the region. Again when compared the two isotope pairs, in particular, the thoron, as well as thorium concentrations, were higher than radon and uranium concentrations in both the media (i.e. water and soil).

Table 4.5**: Detail estimated value of ^{238}U and ^{232}Th concentrations and fluxes of their daughter nuclei in soil and water at Mat fault.**

	Soil			**Water**			**ratio**	
	^{222}Rn	^{220}Rn	ratio	^{222}Rn	^{220}Rn	ratio	$^{222}Rn_W/^{222}Rn_S$	$^{220}Rn_W/^{220}Rn_S$
Bqm^{-3}	5649.4	11858.2	2.1	7557.0	12091.2	1.6	1.3	1.02
$Bqm^{-2}s^{-1}$	0.016	1.25	79.3					
	Soil			Water			ratio	
	^{238}U	^{232}Th	ratio	^{238}U	^{232}Th	ratio	$^{238}U_W/^{238}U_S$	$^{232}Th_W/^{232}Th_S$
$Bqkg^{-1}$	17.5	22.6	1.3	41.6	124.8	3	2.4	5.5

Finally, when compared the obtained isotope pair data with the global average and critical value set by UNSCEAR (1982, 2000) and IAEA (2004, 2013) the following observations have been made. The obtained isotope pair concentrations in soil and water, fall within the range (10^3-10^5 Bqm^{-3}in soil) given by IAEA (2013). The isotope pair fluxes were also in close agreement with the worldwide average (15-20 $mBqm^{-2}s^{-1}$ for radon and 1-1.9 $Bqm^{-2}s^{-1}$ for thoron) given by UNSCEAR (1982). As for the parent nuclei content, the ^{238}U and ^{232}Th content of the soil was lower than that of the worldwide average (35 and 30 $Bqkg^{-1}$ for ^{238}U and ^{232}Th, respectively) given by UNSCEAR (2000). On the other hand, their concentrations in water were higher than the reported average (UNSCEAR, 2000). The higher ^{232}Th content evinces the observed higher concentrations and fluxes of its daughter nuclei to its isotope in both media. Consequently, when compared to that of the critical value set by IAEA (2004) (1000 $Bqkg^{-1}$) no radiological hazards have been observed from ^{238}U and ^{232}Th in the region.

4.4. Meteorological Factors and the Radon Isotope Pair Data

4.4.1 Diurnal variation of Radon and Thoron Data

In the present investigation, the radon isotope pair data has been monitored with 15 min cycle at Mizoram and no radon data has been generated with such high frequency in the region until now. With such sampling frequency, the real-time nature of the radon isotope pair has been presented. To study the diurnal nature of the isotope pair, data generated during December 2018 has been selected. Data from this period has been selected to avoid extreme meteorological effects on the data. During this period the weather is calm with clear sky sunny days, gentle breeze and no heavy rainfall, hence a suitable season to observe the diurnal variation. From Fig. 4.1a the radon concentrations peaks were mostly observed at an average time of 7:47±1:40 AM in the morning with a range of 2:52-10:30 AM. However, its minimum was observed in the evening at an average of 6:20±1:39 PM with a range of 3:4-9:44 PM. Such that, the radon concentration was maximum in the morning (approximately at around 7:47 AM) and from there on it gradually decreases to its minimum at around 6:20±1:39 PM in the evening and the cycle repeats on. This observation may be

attributed to the location of the monitoring station and that radon varies diurnally under the influence of temperature. The monitoring station lies in the east of the Department of Physics building in contact with it. As soon as the sun rise it was received by the monitoring station and the temperature inside it increased as well. But as the sun goes up the four-storey building and the nearby trees start shadowing the monitoring station and hence reducing temperature of the monitoring station. In the afternoon the sun was located on the other side of the building and the monitoring station was completely cut off from sunlight by the building. From this qualitative analysis, it was evident that radon diurnal variation was peak at around 7:47±1:40 AM in the morning when the monitoring station gets maximum sunlight and minimum at around 6:20±1:39 PM in the evening after sunset. Hence in general it can be stated the radon data at Mizoram University varies diurnally with temperature. The thoron concentration, on the other hand, has no significant response to external factors but remains constant with a certain limit with an average of 3648 Bqm^{-3} (Fig. 4.1b). From the qualitative analysis meteorological influence on thoron concentration remains unknown. The application of statistical analysis techniques in identifying meteorological influence on the thoron data will also be discussed in the upcoming section.

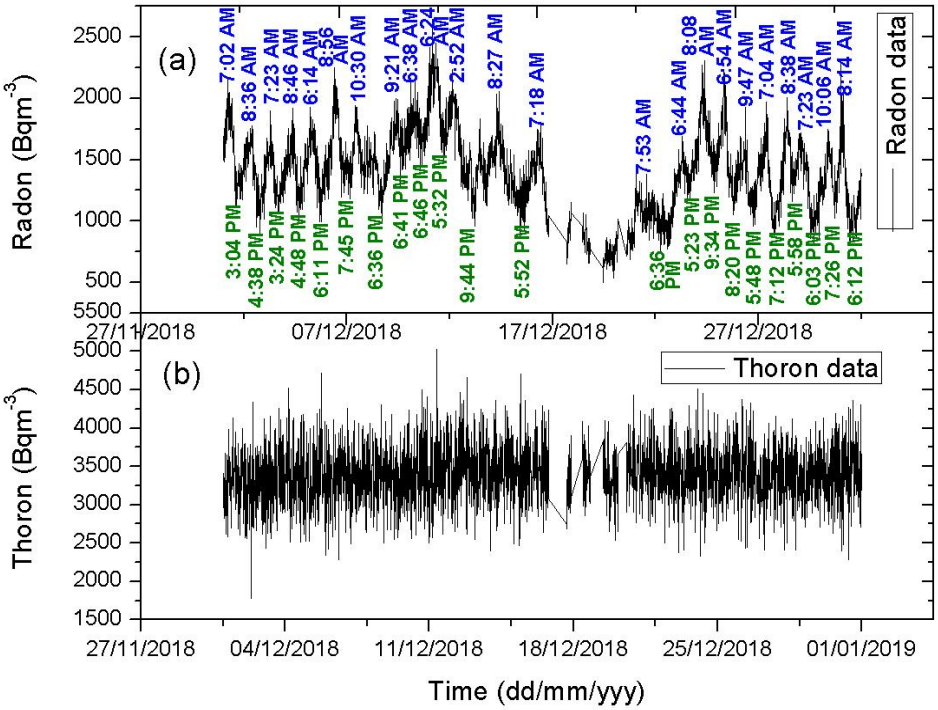

Fig. 4.1: Plot of (a) 15 min cycle radon data at Mizoram University for the period of December 2018 showing its diurnal variation along with its maxima and minima timing (b) 15 min cycle thoron data at Mizoram University for the period of December 2018.

4.4.2 Seasonal variation of Radon and Thoron Data

At Mat Fault: The climate of northeast India Mizoram state in particular can be broadly classified into three seasons (i) summer (rainy) season, (ii) winter (cold) season and (iii) spring (warm) season (Pachuau *et al*., 1994). In general climate of the region is moderate throughout the year. Each season may briefly be described as follows:

Summer (rainy) season: The highest rainfall is observed in this season received from the south-west monsoon. At the same time, it is also the longest of the three seasons starting from the second-half of May and lasting till late October.

Temperature of this season fluctuates with high frequency sometimes as high as the spring season and decreases rapidly during rain and on the onset of monsoon.

Winter (cold) season: The season is characterized by a small amount of rainfall received from northeast known as a retreating monsoon. It starts in November and lasts till February and mists are common in valleys during this period.

Spring (warm) season: The season is identified by high temperatures with bright sunshine and clear blue sky. It starts from March to the first half of May and the highest temperature was observed in this season.

In order to see the seasonal variation of the isotope pair data at Mat fault, *in-situ* online data of the four sampling depths of the entire field work (November, 2017-October, 2018) was considered. The isotope pair data has been divided seasonally and a comparison has been made between each season. From Fig. 4.2a it was evident that in all the sampling depths the radon data was highest during summer followed by winter and minimum during spring. It must be noted that the recorded radon data was maximum in summer when the soil was expected to be wet and minimum in spring when the temperature was the highest. As mentioned above rainfall and high temperature were expected in the summer season. Also rise in soil humidity up to a certain critical level (15-17% by weight) (Stranden *et al*., 1984) has been reported to enhance radon emanation in soil (Asher-Bolinder *et al*., 1991). Gases in the upper surface were also reported to be expanding during raise in temperature thereby increasing radon exhalation (Ramola *et al*., 1990; Segovia *et al*., 1987; Singh *et al*., 1988; Virk *et al*., 2000; Walia *et al*., 2005). Hence increase in soil humidity due to rainfall or raise in temperature or both can be the main reason behind maximum radon concentration during summer season. On the other hand, the minimum radon concentration during the spring season might be due to the masking of temperature effect by other parameters which will be discussed in detail in the upcoming section. The radon concentration of the winter season lies between the other two seasons. It can be speculated that due to the calm weather of this season the radon concentration was less perturbed and more equilibrium in comparison to its value in the other two seasons where the weather is both extreme.

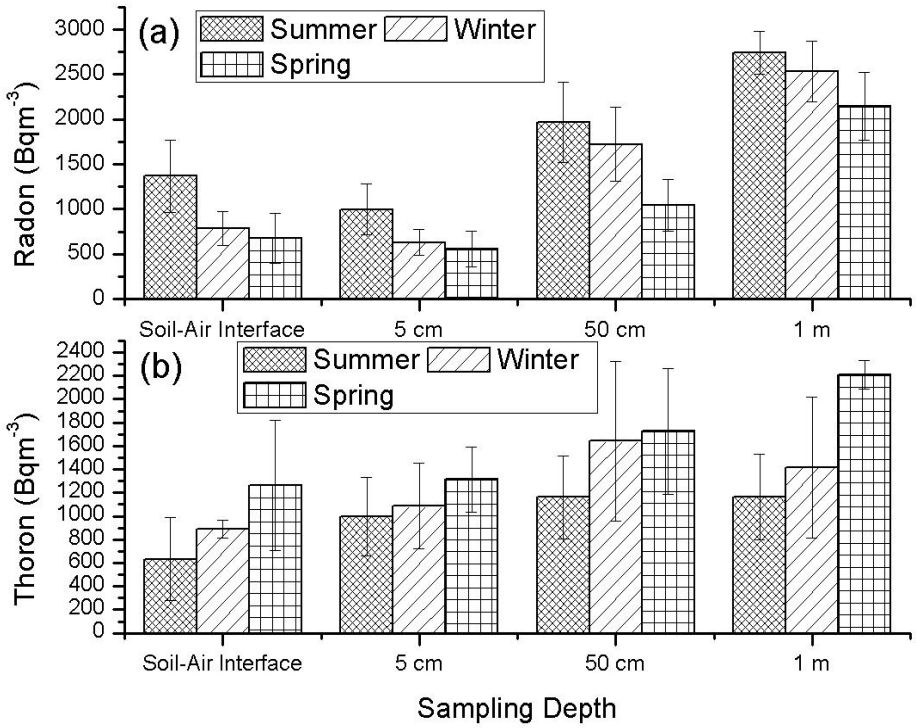

Fig. 4.2: Plot of (a) radon data of four different sampling depths (soil-air interface, 5 cm, 50 cm and 1 m) at Mat fault during the three broadly classified seasons (summer, winter and spring) of the region acquired between November, 2017-October, 2018 (b) thoron data of four different sampling depths (soil-air interface, 5 cm, 50 cm and 1 m) at Mat fault during the three broadly classified seasons (summer, winter and spring) of the region acquired between November, 2017-October, 2018.

In contrast to radon data the thoron data was found to be maximum during spring, followed by the winter season and minimum during summer (Fig. 4.2b). As mentioned above sub-soil radon gas has been found to expand during raise in temperature thereby enhancing its exhalation (Ramola *et al*., 1990; Segovia *et al*., 1987; Singh *et al*., 1988; Virk *et al*., 2000; Walia *et al*., 2005). It has been also mentioned that during rainfall capping effect may occur and hindered the radon gas from exhalation and hence reduced its concentrations (King, 1984; Tanner, 1964, 1980: Virk *et al*., 2000). For thoron, it can be speculated that its high concentration during the spring season positively correlated with the high temperature of the

season. However, its observed low concentration during summer might be due to the capping effect caused by rainfall despite high temperature is also expected in this period. The thoron concentration of the winter season lies between that of the two seasons and the same explanation goes for it as that of radon in winter season.

At Chite Fault: The isotope pair data at Chite fault were acquired during February, 2018-July, 2018. From Fig. 4.3a, the same observation has been made as that of Mat fault. In all the sampling depths the radon concentrations were maximum and minimum during summer and spring respectively. And the same explanation goes as that of radon variation at Mat fault. On the other hand, the seasonal variation of thoron at Chite fault was distinctive from that of Mat fault. At the soil-air interface and 1 m depths it exactly varies as that of radon data, that is, maximum during summer and minimum during spring. But at 5 cm and 50 cm depths the thoron data changes its character and was found to be maximum during winter and minimum during spring (Fig. 4.3b). When compared to that of Mat fault thoron data of the two locations seasonally varies differently while radon data were in phase. Analysis from different sampling depths shows that the thoron maximum of the region (Mat and Chite fault) was observed during spring, summer and winter. At the same time, thoron minimum of the region was observed during summer as well as in spring. Hence for the present study, we are uncertain about the seasonal variation of thoron data. But details correlations of the isotope pair data with meteorological factors will be discussed in detail in the following section.

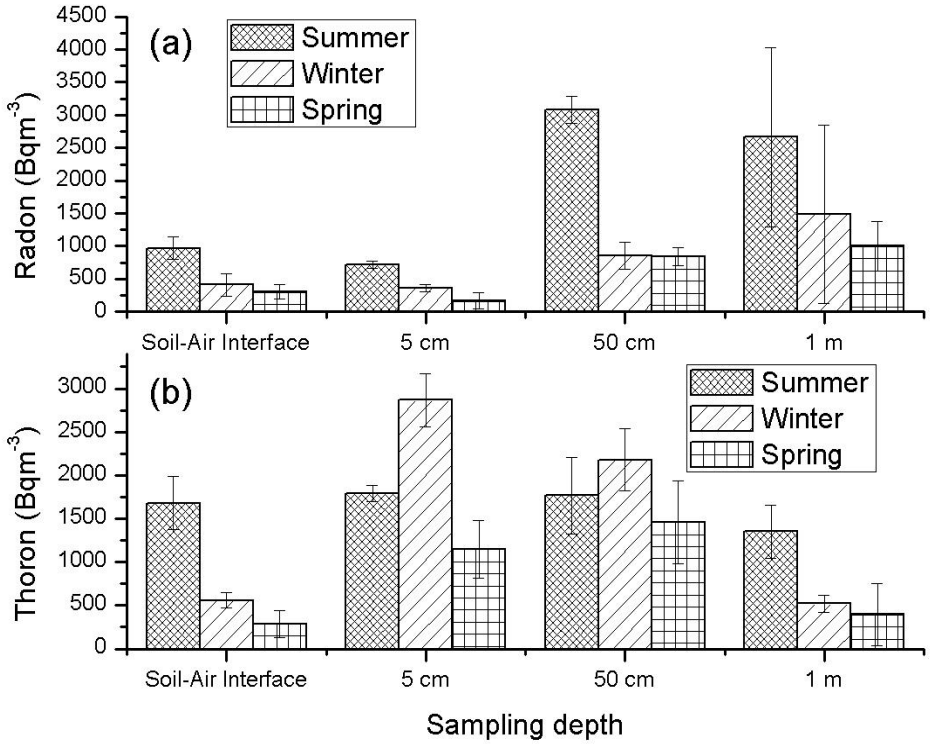

Fig. 4.3: Plot of (a) radon data of four different sampling depths (soil-air interface, 5 cm, 50 cm and 1 m) at Chite fault during the three broadly classified seasons (summer, winter and spring) of the region acquired between February, 2018-July, 2018 (b) thoron data of the four different sampling depths at Chite fault during the three broadly classified seasons (summer, winter and spring) of the region acquired between February, 2018-July, 2018.

4.5 Meteorological Influence on the Radon and Thoron data

4.5.1 The isotope pair data and meteorological factors at Mat fault

The diurnal and seasonal variation studies of the isotope pair in the two previous sections gave us information and trend on how they behave in general. In this section, the one-to-one relationship between the isotope pair and each meteorological factor was presented and the most influencing factor was also identified. The meteorological influence on the radon isotope pair was studied for one complete season in two different window periods. The first window period comprises six

months from November, 2017 to April, 2018. This period comprises the winter and spring seasons of the region as mentioned elsewhere. The period was also characterized by calm weather with no rain and low temperature during winter. But the highest temperature was observed during spring. The second window period was from May, 2018 to October, 2018 and this period was characterized by heavy rainfall with turbulent weather. After performing linear correlation analysis, the following observations have been made between the meteorological and the isotope pair data at Mat fault.

During the first observation period (i.e. between November, 2017 and April, 2018) air temperature was found to have a weak reverse correlation with radon at 5 cm (r=-0.2) and 50 cm (-0.1) depths while a positive correlation at 1 m depth (0.1) (Fig. 4.4 (a-c), Table 4.6). It also exhibits moderate reverse (-0.3) and positive (0.4) correlation with thoron data at 5 cm and 50 cm depths respectively and a strong positive correlation (0.8) at 1 m depth(Fig. 4.4 (a-c), Table 4.6). The same observation, that is, weak and moderate reverse correlation of the isotope pair data with air temperature has been observed by Jaishi *et al*. (2014, 2014a) at 80 cm depths in the same fault. At the same time, Singh *et al*., (2016) who monitored radon data at Chite fault (57 km from Mat fault) and several authors (Segovia *et al*., 1987; Singh *et al*., 1988; Virk *et al*., 2000; Walia *et al*., 2005) also reported that radon has a positive correlation with air temperature. In general, it was concluded that air temperature and the isotope pair has a weak correlation during this period.

Barometric pressure has a moderate positive correlation (0.5, 0.5 and 0.4) with radon data in all the three successive sampling depths respectively (Fig. 4.4 (d-f), Table 4.6). But with thoron the meteorological parameters have weak (-0.1) and strong (-0.6 and -0.8) reverse correlations at the three respective sampling depths (Fig. 4.4 (d-f), Table 4.6). Several reports (Gingrich, 1984; King, 1984; Segovia *et al*., 1987; Singh *et al*., 1988; Virk and Singh, 1993; Wakita *et al*., 1985) and Singh *et al*., (2016) who studied in the same region suggested that due to formation of atmospheric pumping effect during raise in pressure poor air radon was push into the upper region of the soil which dilutes its concentration. When compared it was found that only thoron data was in agreement with the above previously mentioned reports

but radon behaviours were totally out of phase. Hence for the study period, the relationship between radon data and the barometric pressure was uncertain.

Rainfall was observed to have a moderate reverse correlation with radon data in all the three sampling depths (-0.3, -0.4 and -0.3) (Fig. 4.5(a-c), Table 4.6). It also has a weak negative (-0.2), zero and moderate positive (0.3) correlation with thoron data at the three successive sampling depths (Fig. 4.5(a-c), Table 4.6). The finding was in agreement with some reports (Singh *et al*., 1988; Virk and Singh, 1993) and those of the region (Jaishi *et al*., 2014, 2014a, 2015). It has been suggested that beyond the optimum level (Stranden *et al*., 1984) the radon exhalation process to the atmosphere was hindered due to the capping effect and hence decrease its concentration. However, as long as the soil moisture due to rainfall remains below the optimum level (Stranden *et al*., 1984) it enhances the radon emanation and hence its exhalation (Asher-Bolinder *et al*., 1991). Hence based on the optimum level rainfall can have a positive and negative relationship with the isotope pair data which has been observed both in this study period.

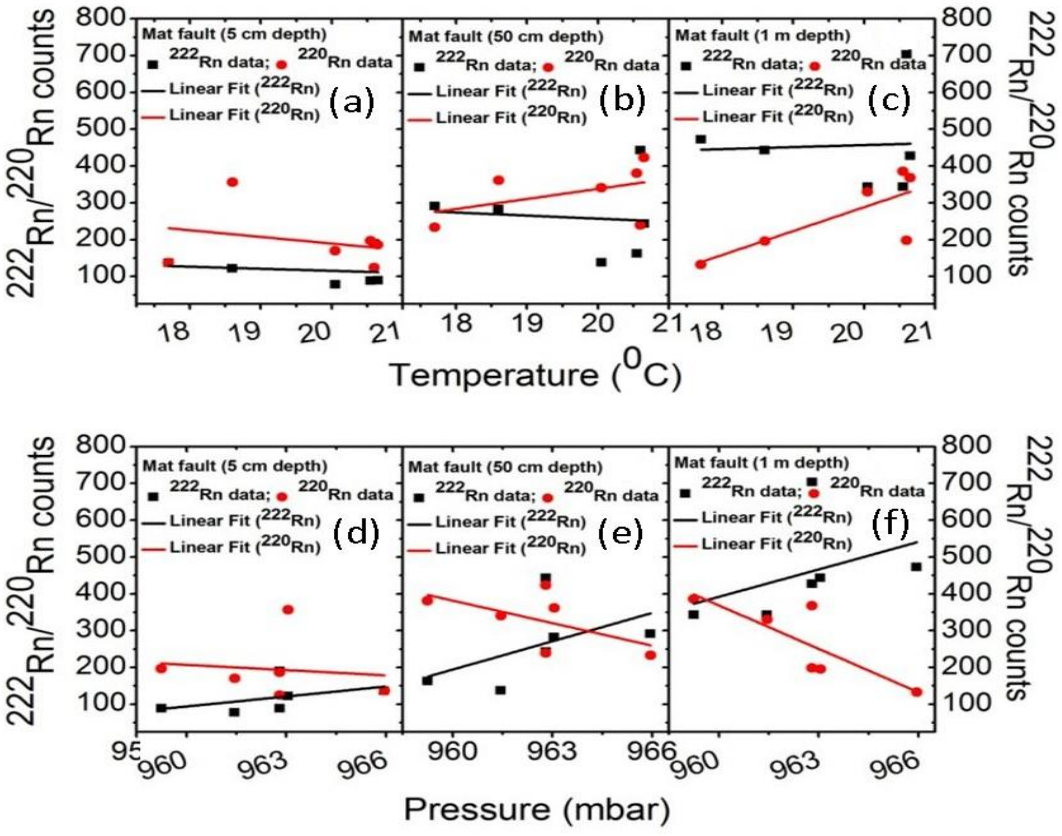

Fig. 4.4: (a-c) Plot of $^{222}Rn/^{220}Rn$ counts versus air temperature at Mat fault generated during November, 2017-April, 2018 at sampling depths of 5 cm, 50 cm and 1 m depths (d-f) Plot of $^{222}Rn/^{220}Rn$ counts versus barometric pressure at Mat fault generated during November, 2017-April, 2018 at sampling depths of 5 cm, 50 cm and 1 m depths.

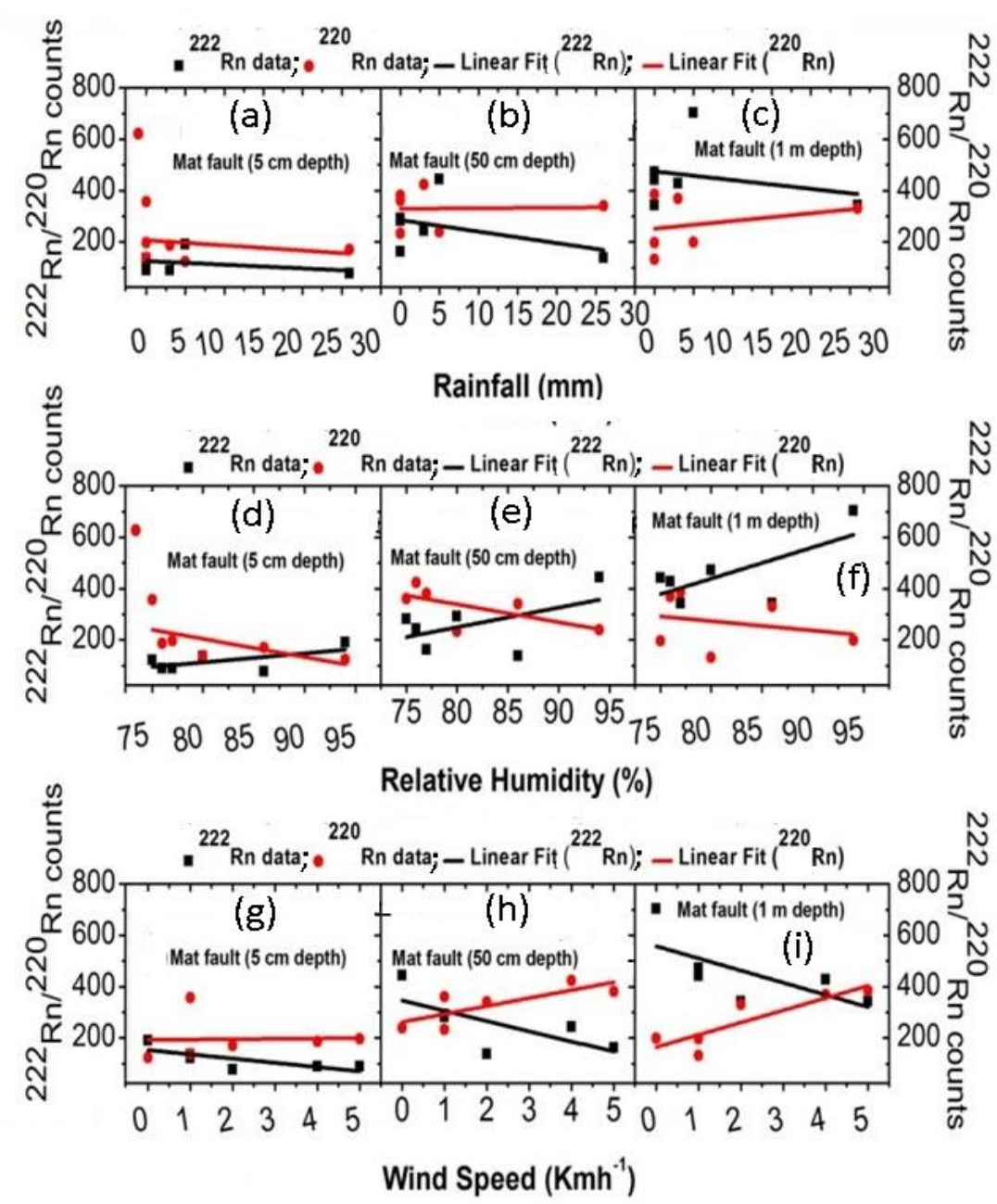

Fig. 4.5: (a-c) Plot of $^{222}Rn/^{220}Rn$ counts versus rainfall at Mat fault generated during November, 2017-April, 2018 at sampling depths of 5 cm, 50 cm and 1 m depths (d-f) Plot of $^{222}Rn/^{220}Rn$ counts versus relative humidity at Mat fault generated during November, 2017-April, 2018 at sampling depths of 5 cm, 50 cm and 1 m depths (g-i) Plot of $^{222}Rn/^{220}Rn$ counts versus wind speed at Mat fault generated during November, 2017-April, 2018 at sampling depths of 5 cm, 50 cm and 1 m depths.

Relative humidity has a positive and reverse correlation with radon and thoron respectively. The correlation coefficient was moderate and strong in both the cases. They were found to be 0.6, 0.5 and 0.7 for radon and -0.6, -0.7 and -0.3 for thoron at the three sampling depths respectively (Fig. 4.5(d-f), Table 4.6). The observed positive correlation between radon and humidity was in agreement with those of Jaishi *et al*., (2014a) and Singh *et al*., (2016) who study in the same region. The observation made for thoron data were also in agreement with that of Guedalia *et al*. (1970) who suggested that an increase in soil moisture suppress thoron emission within 5 cm depth from the ground surface. Rainfall can be considered the main factor that humidity depends on, hence explanation given for rainfall and the isotope pair data in the above paragraph may as well be adopted for humidity and the isotope pair.

Wind speed exhibits a strong reverse correlation with radon data while it has a strong positive correlation with thoron data except at 5 cm depth. The correlation coefficients were -0.8, -0.7 and -0.7 for radon and 0, 0.8 and 0.9 for thoron data at 5 cm, 50 cm and 1 m depths respectively (Fig. 4.5(g-i), Table 4.6). The observed relationship between radon and wind speed was in agreement with several reports (Gingrich, 1984; Virk *et al*., 2000; Walia *et al*., 2005) where speeding wind was found to remove surface radon and hence reducing its concentrations. At the same time, a positive correlation between radon and wind speed has also been reported by some authors (Singh *et al*., 1988; Virk and Singh, 1993). Guedalia *et al*. (1970) also observed no correlation between thoron and a wind speed of 0.02-0.05 ms^{-1} circulated by a pump at the ground surface.

Table 4.6: Details correlation of meteorological parameters with ^{222}Rn and ^{220}Rn data generated at Mat fault during November, 2017-April, 2018.

^{222}Rn						
Meteorological Parameters	**5 cm**		**50 cm**		**1 m**	
	Slope	**r**	**Slope**	**r**	**Slope**	**r**
Temperature (^0C)	-5.6	-0.2	-8.3	-0.1	5.5	0.1
Pressure (mbar)	9.0	0.5	25.7	0.5	24.9	0.4
Rainfall (mm)	-1.4	-0.3	-4.5	-0.4	-3.4	-0.3
Humidity (%)	3.5	0.6	7.7	0.5	12.2	0.7
Wind Velocity (Kmh^{-1})	-16.6	-0.8	-39.7	-0.7	-47.4	-0.7
^{220}Rn						
Meteorological Parameters	**5 cm**		**50 cm**		**1 m**	
	Slope	**r**	**Slope**	**r**	**Slope**	**r**
Temperature (^0C)	-18.1	-0.3	27.4	0.4	65.0	0.8
Pressure (mbar)	-4.8	-0.1	-20.4	-0.6	-39.3	-0.8
Rainfall (mm)	-2.0	-0.2	0.2	0.0	3.0	0.3
Humidity (%)	-7.1	-0.6	-6.9	-0.7	-3.7	-0.3
Wind Velocity (Kmh^{-1})	1.4	0.0	31.0	0.8	47.8	0.9

For the first period of observation, the meteorological influence on the radon isotope pair may be generalized as follows; air temperature shows no significant influence on radon data but on thoron data. Barometric pressure and relative humidity were found to raise radon concentrations while they show a reverse effect on its isotope. Rainfall moderately tends to suppress radon concentration and as well thoron concentration at the surface. Wind speed strongly tries to suppress radon concentration but shows the opposite on thoron concentration.

During the second observation period (i.e. between May, 2018 and October, 2018) the following meteorological influence on the radon isotope pair has been made. From Table 4.7 it can be seen that air temperature and barometric pressure have reverse correlation with radon data at the surface (i.e. at 5 cm and 50 cm depths) and a positive correlation at 1 m depth (Fig. 4.6(a-c), 4.6(d-f)). And when correlate the two parameters with thoron data the exact opposite as that of radon was observed. That is a direct correlation was observed at the surface and a reverse one at greater depth (1 m depth) (Fig. 4.6(a-c), 4.6(d-f)). Again from Table 4.7 rainfall and humidity show a direct correlation with radon data near the surface and a reverse correlation at 1 m sampling depth (Fig. 4.6(g-i), Fig. 4.7(a-c)). On the other hand, the two parameters show a reverse correlation with thoron data at all the sampling depths (Fig. 4.6(g-i), Fig. 4.7(a-c)). Finally wind speed exhibit direct and reverse correlation with radon and thoron data at the surface respectively (Fig. 4.7(d-f)). At the same time, it shows zero correlation with the two isotope pair data at 1 m depth (Fig. 4.7(d-f)). The causal relationship between the radon isotope pair data and the meteorological factors has been explained in detail elsewhere. In this measuring period masking effect of the meteorological factors upon one another and identifying the significant factors were our main focus.

It must be noted that the second study period falls within rainy season of the region during which maximum distortion due to meteorological factors was expected. To minimise the meteorological effect a clear sky sunny day was selected for a field visit at Mat fault. But often the measurement was interrupted by a short duration rainfall (approximately 1 hour) accompanied by cold wind. It was experienced during measurement that the interrupting rainfall was random, unpredictable and the air temperature automatically drops and regains its value during and after the rainfall respectively. It must also be noted that the study region belongs to a tropical region where frequent and heavy rainfall was expected. Sometimes the rainfall lasts for weeks with cloudy skies hindering the sunshine.

Table 4.7: Details correlation of ^{222}rn/^{220}rn data of different sampling depths at mat fault with meteorological parameters and their inter-correlation.

Meteorological/^{222}Rn /^{220}Rn data		Temperature (^{0}C)	Pressure (mbar)	Rainfall (mm)	Humidity (%)	Wind speed (Kmh^{-1})	^{222}Rn at depth of			^{220}Rn at depth of		
							5 cm	*50 cm*	*1 m*	*5 cm*	*50 cm*	*1 m*
Temperature (^{0}C)		1	0.5	-0.6	0.3	-0.8	-0.4	-0.6	0.5	0.4	0.3	-0.3
Pressure (mbar)			1	-0.8	-0.4	-0.6	-0.5	-0.3	0.7	0.4	0.5	-0.3
Rainfall (mm)				1	0.2	0.5	0.5	-0.3	-0.5	-0.3	-0.1	-0.3
Humidity (%)					1	-0.4	0.0	0.5	-0.1	-0.5	-0.6	-0.8
Wind speed (Kmh-1)						1	0.7	0.9	0.0	-0.7	-0.5	0.0
^{222}Rn at depth of	***5 cm***						1	0.5	-0.3	-0.7	-0.4	0.0
	50 cm							1	0.0	-0.7	-0.2	-0.2
	1 m								1	0.6	0.6	0.4
^{220}Rn at depth of	***5 cm***									1	0.6	0.6
	50 cm										1	0.4
	1 m											1

The mentioned climate condition clearly indicates the possible meteorological influences on the isotope pair data as well as masking effects amongst the meteorological factors.

From Table 4.7 the linear correlation analysis shows that rainfall, humidity and wind speed have a positive correlation with radon data at 5 cm and 50 cm sampling depths. The inter-correlation analysis shows that humidity and wind speed exhibit positive relation with rainfall (Table 4.7). It was speculated that humidity and wind speed were the direct result and were accompanied by rainfall. Hence from the inter-linear correlation analysis, their effect on radon exhalation was considered to be masked by rainfall.

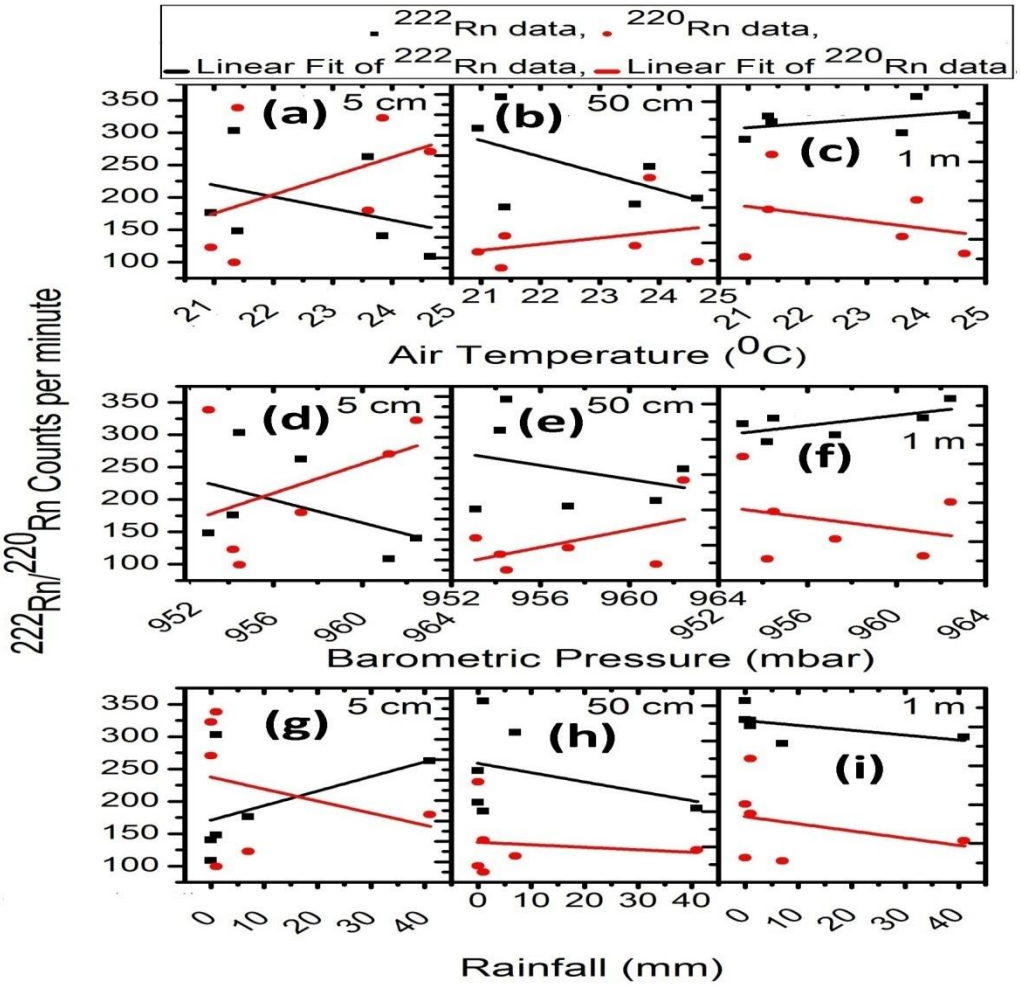

Fig. 4.6: (a-c) Plot of $^{222}Rn/^{220}Rn$ counts versus temperature at Mat fault generated during May, 2018-October, 2018 at sampling depths of 5 cm, 50 cm and 1 m depths

(d-f) Plot of $^{222}Rn/^{220}Rn$ counts versus barometric pressure at Mat fault generated during May, 2018-October, 2018 at sampling depths of 5 cm, 50 cm and 1 m depths (g-i) Plot of $^{222}Rn/^{220}Rn$ counts versus rainfall at Mat fault generated during May, 2018-October, 2018 at sampling depths of 5 cm, 50 cm and 1 m depths.

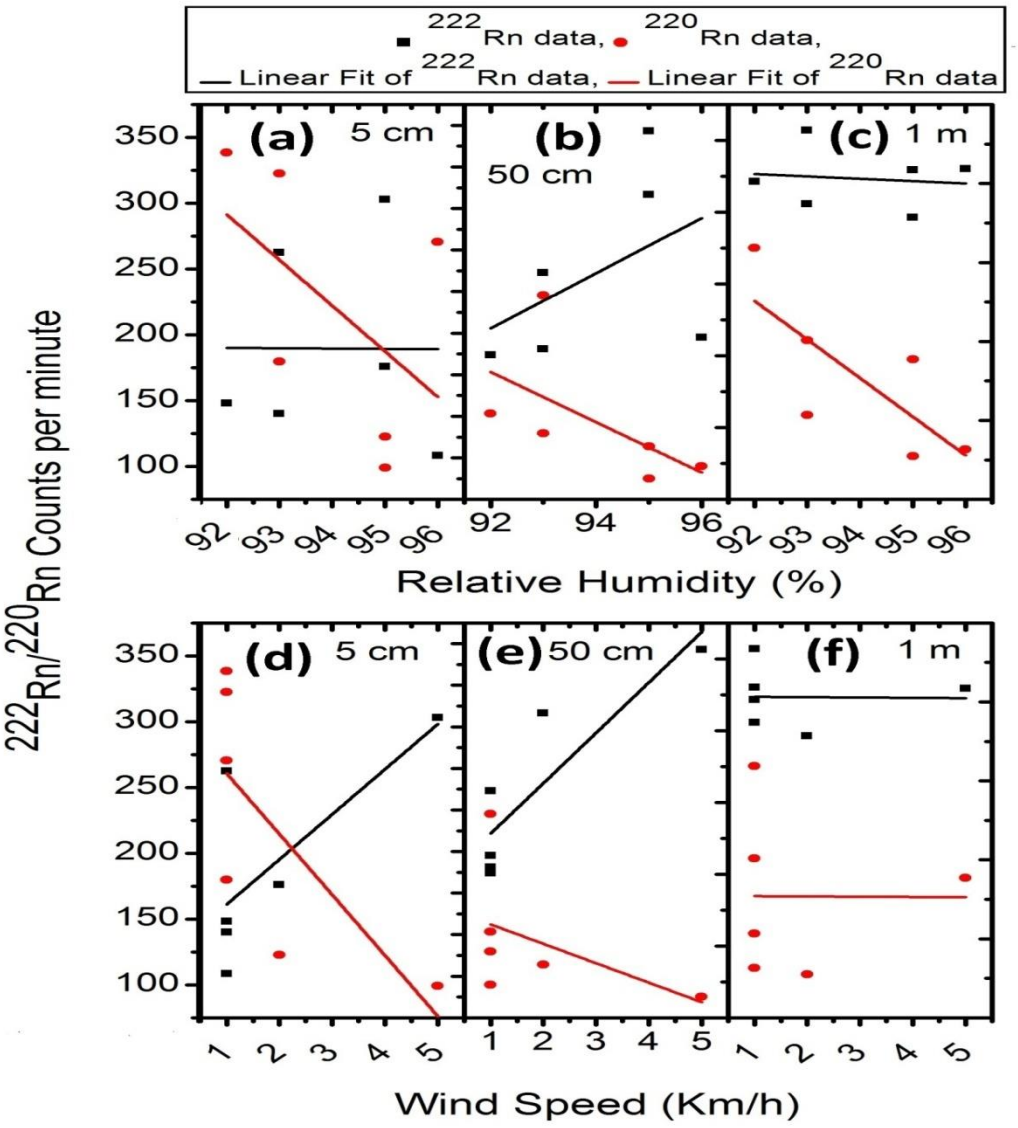

Fig. 4.7: (a-c) Plot of $^{222}Rn/^{220}Rn$ counts versus humidity at Mat fault generated during May, 2018-October, 2018 at sampling depths of 5 cm, 50 cm and 1 m depths (d-f) Plot of $^{222}Rn/^{220}Rn$ counts versus wind speed at Mat fault generated during May, 2018-October, 2018 at sampling depths of 5 cm, 50 cm and 1 m depths.

Masking effect of meteorological factors upon one another was also reported by Asher-Bolinder *et al*. (1991) and Sundal *et al*. (2008). Increase in the moisture content of the soil below the optimum level (15-17% by weight) due to precipitation (Stranden *et al*., 1984) and reduced in barometric pressure at the ground surface due to the accompanying wind during the short rainfall was a favour for ^{222}Rn exhalation. Air temperature and pressure show a reverse correlation with radon data near the ground surface. The reverse correlation between radon and air temperature was against many findings (Segovia *et al*., 1987; Singh *et al*., 1988; Virk *et al*., 2000; Walia *et al*., 2005) where raise in temperature was reported to expand soil gas hence causing absorbed vapour species to escape. Hence it was obvious that the effect of temperature was masked by pressure as the two parameters have a positive correlation. It was evident that during rain fall the effect of air temperature was lowered or masked by rainfall and its accompanied wind speed. But as soon as the rain ceased again the air temperature was masked by pressure. In general, it was concluded that at sampling depths close to the ground surface rainfall and Barometric pressure were the main factors influencing radon exhalation while all other factors get masked either by them. Rainfall tends to enhance radon exhalation while pressure does the reverse.

The radon data at 1 m depth shows a complete opposite character to that of 5 cm and 50 cm depths when correlates with meteorological factors. It has zero correlation with wind speed, positive correlation with air temperature and pressure and negative correlation with rainfall and humidity. Except for wind speed the observation was completely out of phase to that of 5 cm and 50 cm. In other words, the nature of meteorological influence on radon data at 1 m was not aligned with that observed in majority of the sampling depths. Hence the observation made at 1 m depth may be treated as outlier data. But the observed zero correlation between radon and wind speed indicates that at 1 m depth the meteorological influence particularly by wind speed was absent which might as well be the scenario for the other factors. It can be generalized that for the present study period we were uncertain about the meteorological influence at 1 m depth or the meteorological influence at 1 m depth was insignificant. There were also authors (Friedmann, 2012; Jaishi *et al*., 2013;

Singh *et al*., 2014) who selected their sampling depth beyond 80 cm depths to avoid meteorological effects which probably may as well be the scenario observed at 1 m depth in the present study period.

In case of thoron data (Table 4.7), at 5 cm and 50 cm depth, the correlation analysis shows that they exhibit a positive correlation with air temperature and barometric pressure and a negative correlation with rainfall, humidity and wind speed. This observation at 5 cm and 50 cm depth was exactly the same as that of radon data at 1 m depth (Table 4.7). As mentioned elsewhere increase in air temperature tends to enhance radon exhalation while due to pumping effect raise in pressure tends to suppress it. Hence the observed positive relationship between thoron and pressure was absurd and was regarded to be masked by air temperature as the two parameters have a positive correlation (Table 4.7). Also as mentioned elsewhere above, an increase in soil moisture due to precipitation beyond the critical value leads to capping effect hence hindering radon exhalation. This may be the reason behind the observed reverse correlation between thoron and rainfall. Humidity and wind speed were considered to be masked by rainfall as they show positive correlation with it (Table 4.7). At 1 m depth thoron exhibits zero correlation with wind speed and reverse correlation with all the other parameters. As for that of radon data, it was generalized that either the meteorological influence on thoron data at 1 m was insignificant or we are uncertain of it. Hence for the study period, it was found that air temperature tries to enhance thoron exhalation and rainfall tries to suppress it.

When compared to that of the first study period the inter-linear correlation analysis of the second study period clearly reveals which parameters were significant in influencing radon isotope pair data and which parameters get masked. It was found that air temperature, rainfall and barometric pressure were the significant factors while all the other factors get masked. Hence at Mat fault Rainfall tends to raise radon concentration while pressure tends to suppress it. Also, air temperature tends to raise thoron concentration and rainfall tries to suppress it. Like that of observed for their seasonal changes, the isotope pair data seems to respond each meteorological factor differently which may be due to differences in their half-life.

4.5.2 The isotope pair data and meteorological factors at the continuous monitoring station (Mizoram University)

The radon isotope pair data at Mizoram University was monitored with 15 min cycle for 24 hours at the soil-air interface. Hence the isotope pair data at MZU will be presenting their characteristic at the ground surface with meteorological factors in three window periods. The three-time window period were during January, 2017-March, 2017; November, 2017-April, 2018; May, 2018-October, 2018 comprising all seasons of the region.

The first measurement was carried out between January, 2017 and March, 2017 approximately comprising winter season of the region. A statistical t-test (at 95% confidence level) was performed to observe the meteorological effect on the isotope pair data and masking effect among themselves. During this period no significant correlation was observed between radon data and any of the meteorological factors (Table 4.8, Fig. 4.8(a-e)). On the other hand, thoron exhibits a reverse correlation with rainfall (r=-0.35, p=0.0014) and humidity (r=-0.33, p=0.003), positive correlation with pressure (r=0.49, $p=4\times10^{-6}$) and no significant correlation with temperature and wind speed (Table 4.8, Fig. 4.8(f-j)). The inter-linear correlation analysis reveals that masking effect among the meteorological factors was in accordance with that observed in Mat fault. The positive correlation of rainfall data with humidity (r=0.37, p=0.0007) and wind speed (r=0.27, p=0.016) indicates that both parameters were the direct effect of rainfall (Table 4.8). At the same time the reverse correlation between rainfall and thoron may be due to formation of capping effect hindering thoron from escaping to the surface (King, 1984; Tanner, 1964, 1980; Virk *et al*., 2000;). The reverse correlation between rainfall and pressure (r=-0.23, p=0.04) may be due to the accompanying wind suppressing pressure at the ground surface. Also, the reverse correlation between air temperature and humidity may also be regarded as precipitation and wind being its accompanying factors which consequently reduced the air temperature. The positive correlation between thoron and pressure seems ambiguous because radon's poor atmospheric gas is pushed into the upper layer of the earth and hence diluting its concentrations during raise in pressure (Gingrich, 1984; King, 1984; Segovia *et al*., 1987; Wakita *et al*.,

1985). Hence for the study period, no significant correlation was observed between radon and meteorological factors. While for thoron data precipitation tends to suppress it but its enhancing factors were uncertain.

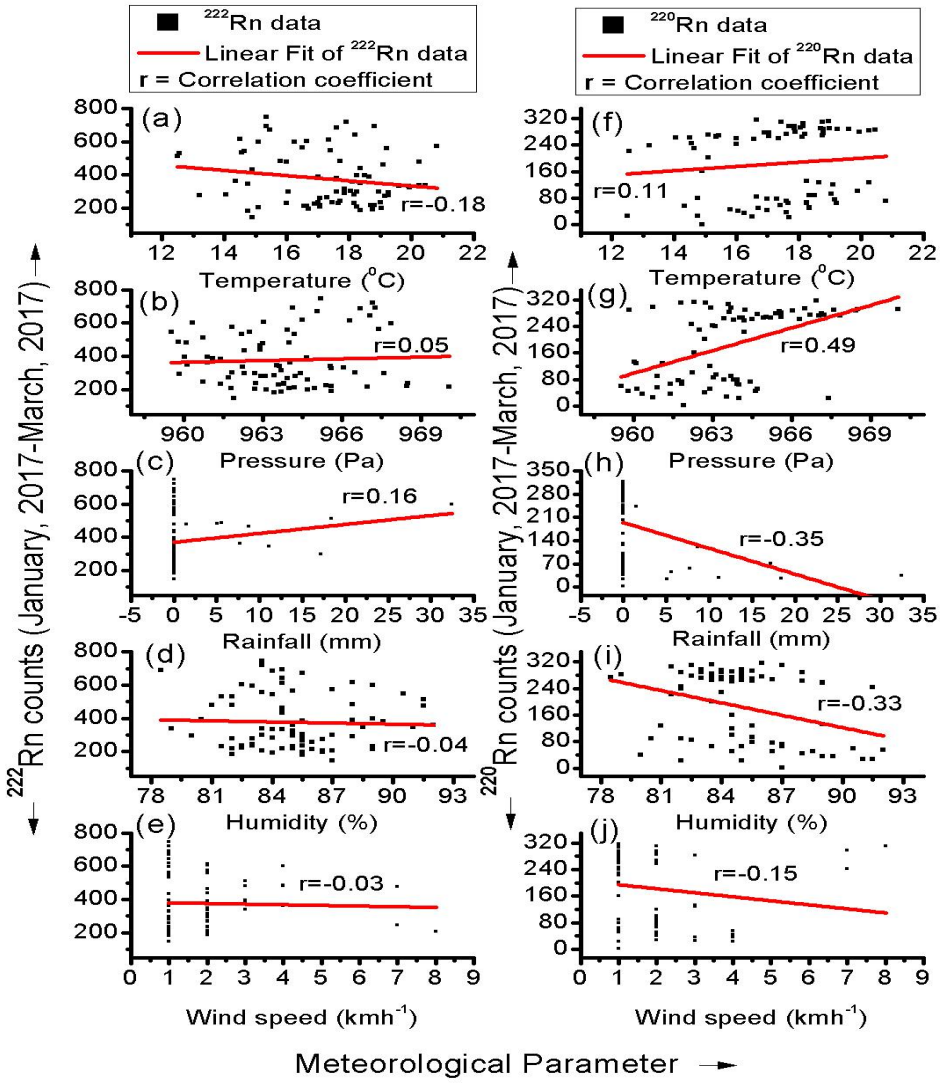

Fig. 4.8: Analysis plot between radon isotopes (radon and thoron) and Meteorological data recorded at Mizoram University, Aizawl (India), showing the extent of meteorological influence on the isotope pair data by displaying the correlation strength r (Pearson's correlation coefficient value) between the isotope pair and each meteorological parameters. Plot of radon data versus (a) temperature (b) pressure (c) rainfall (d) humidity and (e) wind speed. Plot of thoron data versus (f) temperature (g) pressure (h) rainfall (i) humidity and (j) wind speed.

Table 4.8: Details of correlation between meteorological parameters and radon and thoron data at Mizoram University recorded between January, 2017 and March, 2017.

		Temperature (^{0}C)	**Pressure (Pa)**	**Rainfall (mm)**	**Humidity (%)**	**Wind speed (Kmh^{-1})**	**^{222}Rn**	**^{220}Rn**
Temperature	r		0.12	-0.22	-0.26	0.08	-0.18	0.11
(^{0}C)	Sig.		0.30	0.05	0.02	0.46	0.11	0.33
Pressure	r			-0.23	-0.34	-0.44	0.05	0.49
(Pa)	Sig.			0.04	0.002	5.9×10^{-5}	0.66	4×10^{-6}
Rainfall	r				0.37	0.27	0.16	-0.35
(mm)	Sig.				0.0007	0.016	0.15	0.0014
Humidity	r					0.30	-0.04	-0.33
(%)	Sig.					0.008	0.73	0.003
Wind speed	r						-0.03	-0.15
(Kmh^{-1})	Sig.						0.8	0.17
^{222}Rn	r							-0.03
	Sig.							0.8

The second measurement at Mizoram University was carried out between November, 2017 and April, 2018 comprising the winter and spring seasons of the region. During this period the result of Pearson correlation analysis between the radon isotope pair data and meteorological factors was reported. Except for the moderate correlation (-0.3) with humidity radon has no significant correlation with any of the meteorological factors and particularly was zero with wind speed (Table 4.9, Fig. 4.9). Thoron data shows zero correlation with rainfall and a moderate correlation with all the other meteorological factors (Table 4.9).

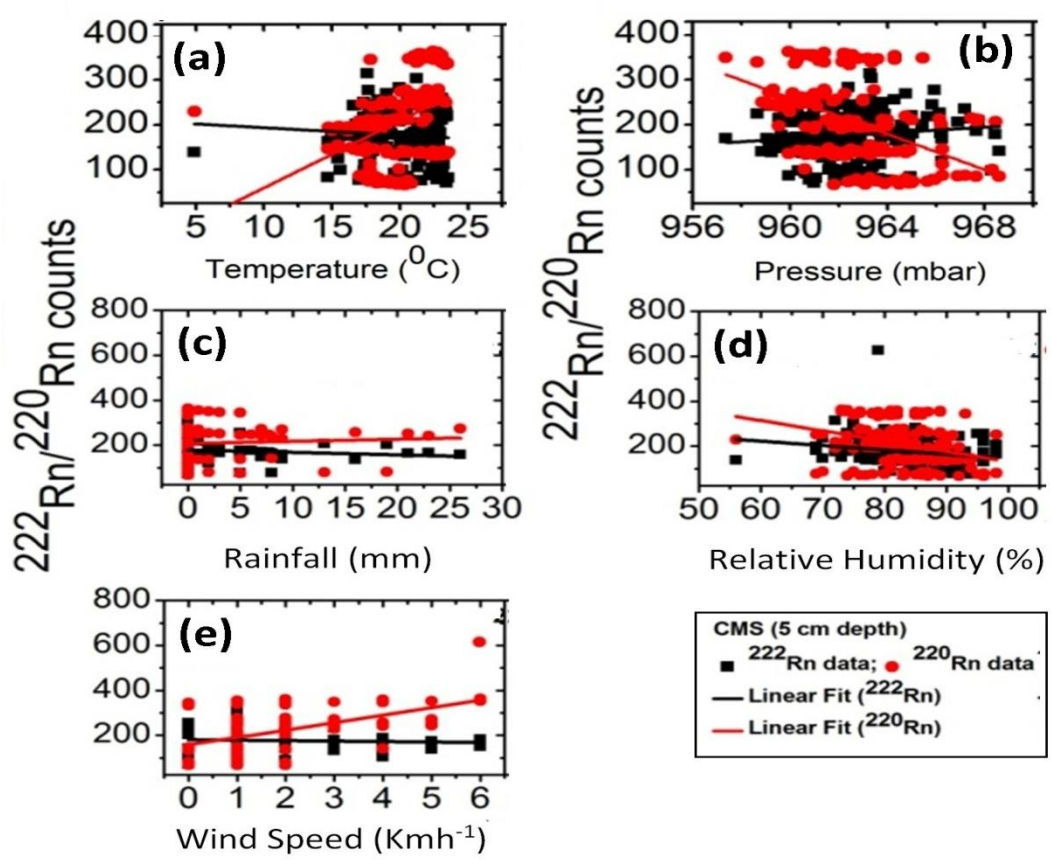

Fig. 4.9: Linear graph of (a) ^{222}Rn/^{220}Rn versus air temperature (^{0}C) (b) ^{222}Rn/^{220}Rn versus barometric pressure (mbar) (c) ^{222}Rn/^{220}Rn versus precipitation (mm) (d) ^{222}Rn/^{220}Rn versus relative humidity (%) and (e) ^{222}Rn/^{220}Rn versus wind speed (Kmh^{-1}) for the period of November, 2017 to April, 2018 at Mizoram University.

Table 4.9: Details correlation of meteorological parameters with ^{222}Rn and ^{220}Rn data generated at Mizoram University during November, 2017-April, 2018.

Meteorological Parameters	**^{222}Rn**		**^{220}Rn**	
	Slope	**r**	**Slope**	**r**
Temperature (^{0}C)	-1.7	-0.1	15	0.4
Pressure (mbar)	3.2	0.1	-19.9	-0.5
Rainfall (mm)	-1.1	-0.1	1	0
Humidity (%)	-2	-0.3	-4.6	-0.3
Wind Velocity (Kmh^{-1})	-2	0	33.4	0.4

The third measurement at Mizoram University was done between May, 2018 and October, 2018 comprising rainy season of the region. The measuring period was characterized by turbulent weather, heavy rainfall and high temperature as that of spring. From Table 4.10 and Fig. 4.10 (a-e) radon has correlation coefficients of -0.3, -0.5, 0.0, 0.3 and 0.0 with air temperature, pressure, rainfall, humidity and wind speed, respectively. Besides the two insignificant ($p>0.05$) zero correlations with rainfall and wind speed no strong correlation were observed between radon and any of the meteorological factors but a moderate one (Table 4.10). Thoron data on the other hand exhibits correlation coefficients of 0.1, 0.1, -0.2, 0.1 and -0.1 with air temperature, pressure, rainfall, humidity and wind speed, respectively (Table 4.10, Fig. 4.10 (a-e)). In case of thoron no significant ($p\leq0.05$) correlation was observed except for rainfall which was a weak correlation (-0.2) (Table 4.10). Hence it was evident that no significant correlation was observed between thoron data at Mizoram University and meteorological factors. In general, for this window time period, no strong and significant correlation was observed between the isotope pair data and meteorological factors.

From the three window periods observation, it was evident that the meteorological influence on radon data slightly change from insignificant to moderate during rainy season. It indicates that during turbulence season radon exhalation does get affected by external factors. At the same time, it was evident from the weak correlation coefficient that the isotope data at MZU was mildly or negligibly affected by meteorological factors. The weak correlation was attributed to the provided shading obstructing the meteorological factors inside the monitoring station. Details construction of the monitoring station was discussed in the materials and methods section. Radon and thoron data monitored under such conditions may only be perturbed by geophysical phenomena as other factors especially meteorological factors have been ruled out. Attaining such conditions was our main objective as our main focus was identifying the nature of the isotope pair data during geophysical phenomena. Since the radon data was highly free from external factors it will be deployed as a reference for the isotope pair data at Mat fault and Chite fault for identifying their geophysical nature.

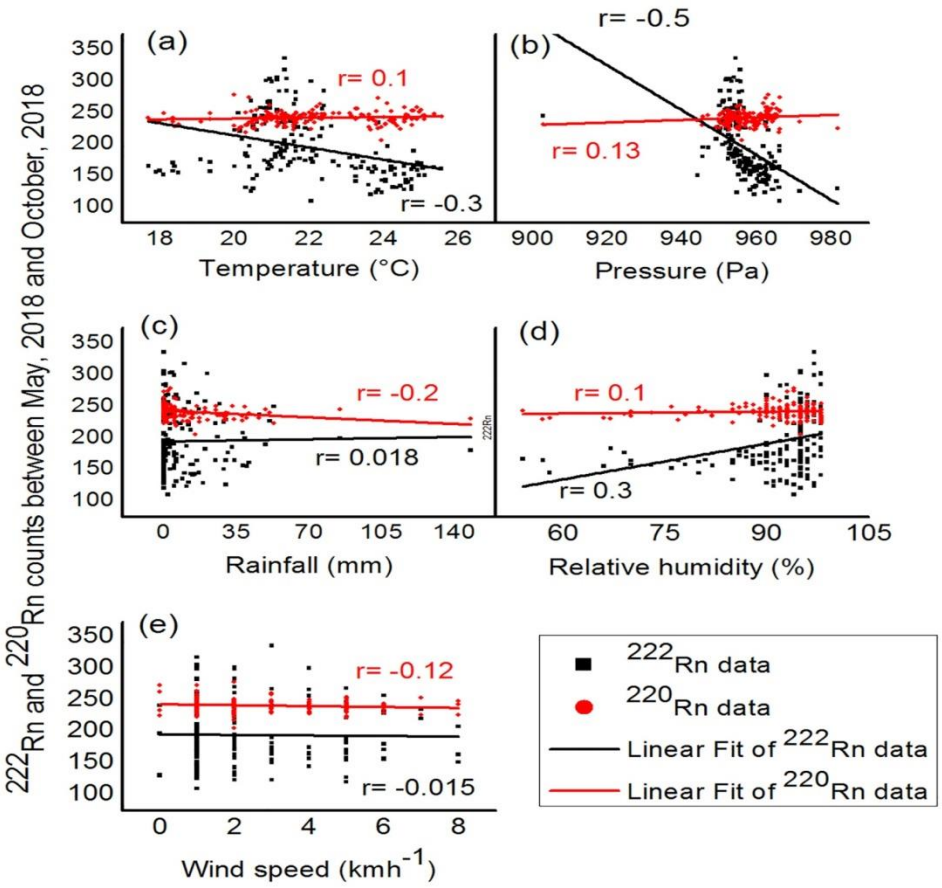

Fig. 4.10: Linear graph of (a) $^{222}Rn/^{220}Rn$ versus air temperature (^{0}C) (b) $^{222}Rn/^{220}Rn$ versus barometric pressure (mbar) (c) $^{222}Rn/^{220}Rn$ versus precipitation (mm) (d) $^{222}Rn/^{220}Rn$ versus relative humidity (%) and (e) $^{222}Rn/^{220}Rn$ versus wind speed (Kmh^{-1}) for the period of May, 2018 to October, 2018 at Mizoram University.

Table 4.10: Details of correlation between ^{222}Rn and ^{220}Rn counts with meteorological parameters (air temperature, pressure, rainfall, humidity and wind speed) using a two-tail t-test at significant level of 0.05 for the period of May, 2018 and October, 2018 at Mizoram University.

		Temperature (^{0}C)	Humidity (%)	Rainfall (mm)	Pressure (mbar)	Wind Speed (Km/h)	^{222}Rn	^{220}Rn
Temperature (^{0}C)	r	1	0.2	-0.3	0.3	-0.5	-0.3	0.1
	p-value		0.0009	0.0004	0.0001	7.4E-12	2.2E-06	0.2
Humidity (%)	r		1	0.04	-0.3	-0.1	0.3	0.1
	p-value			0.6	0.0006	0.2	4.7E-05	0.3
Rainfall (mm)	r			1	-0.2	0.1	0.02	-0.2
	p-value				0.01	0.1	0.8	0.001
Pressure (mbar)	r				1	-0.2	-0.5	0.1
	p-value					0.002	1.1E-11	0.1
Wind Speed (Km/h)	r					1	-0.02	-0.1
	p-value						0.8	0.1
^{222}Rn	r						1	0.1
	p-value							0.1
	No. of data points	180	180	180	180	180	180	180
^{220}Rn	r							1

4.5.3 The isotope pair data and meteorological factors at Chite fault

The radon isotope pair data at Chite fault were generated once a month between February, 2018 and July, 2018. From Table 4.11 and Fig. 4.11(a-d) no strong or significant correlation was observed between radon and temperature in all the four sampling depths (-0.1, -0.2, -0.2, 0.2). However, pressure has a strong reverse correlation (-0.7, -0.7, -0.8, -0.6) with radon data of all the sampling depths (Table 4.11, Fig. 4.11(e-h). Rainfall has a moderate positive correlation (0.2, 0.2, 0.3, 0.3) with radon data at deeper sampling depth while humidity shows a strong positive correlation (0.7, 0.6, 0.7, 0.8) (Table 4.11, Fig. 4.11(i-l), Fig. 4.12(a-d)). Wind speed also shows a strong reverse correlation with radon data of all the sampling depths (-0.5, -0.6, -0.4, -0.4) (Table 4.11, Fig. 4.12(e-h)). As thoroughly discussed elsewhere, due to atmospheric pumping effect radon and pressure were reported to have reverse correlation (Gingrich, 1984; King, 1984; Segovia *et al*., 1987; Wakita *et al*., 1985). The positive correlation between rainfall, humidity and radon may totally be regarded as due to rainfall as humidity has been frequently observed as the direct effect of rainfall. The observed reverse correlation between radon and wind speed indicates that speeding wind was removing radon from the soil surface hence diluting its concentration (Gingrich, 1984; Virk *et al*., 2000; Walia *et al*., 2005). But from the inter-correlation analysis wind speed has been continuously found to be masked by other meteorological factors and hence was neglected as well like humidity at Chite fault. Hence at Chite fault rainfall tends to raise radon concentration while pressure tries to suppress it.

Thoron data on the other hand exhibit strong correlation with temperature at 50 cm depth (0.8) (Table 4.11, Fig. 4.11(a-d)). But in all the other sampling depths temperature has no significant correlation with thoron data (-0.1, 0.2, 0.2) hence the observed correlation at 50 cm depth may be regarded as outlier data. Hence it was assumed that temperature has no significant correlation with thoron. Pressure has no significant correlation with thoron data at 5 cm and 50 cm depths (0.2, 0.2) but a strong reverse correlation at the soil-air interface and 1 m depth (-0.7, -0.6)(Table 4.11, Fig. 4.11(e-h)).

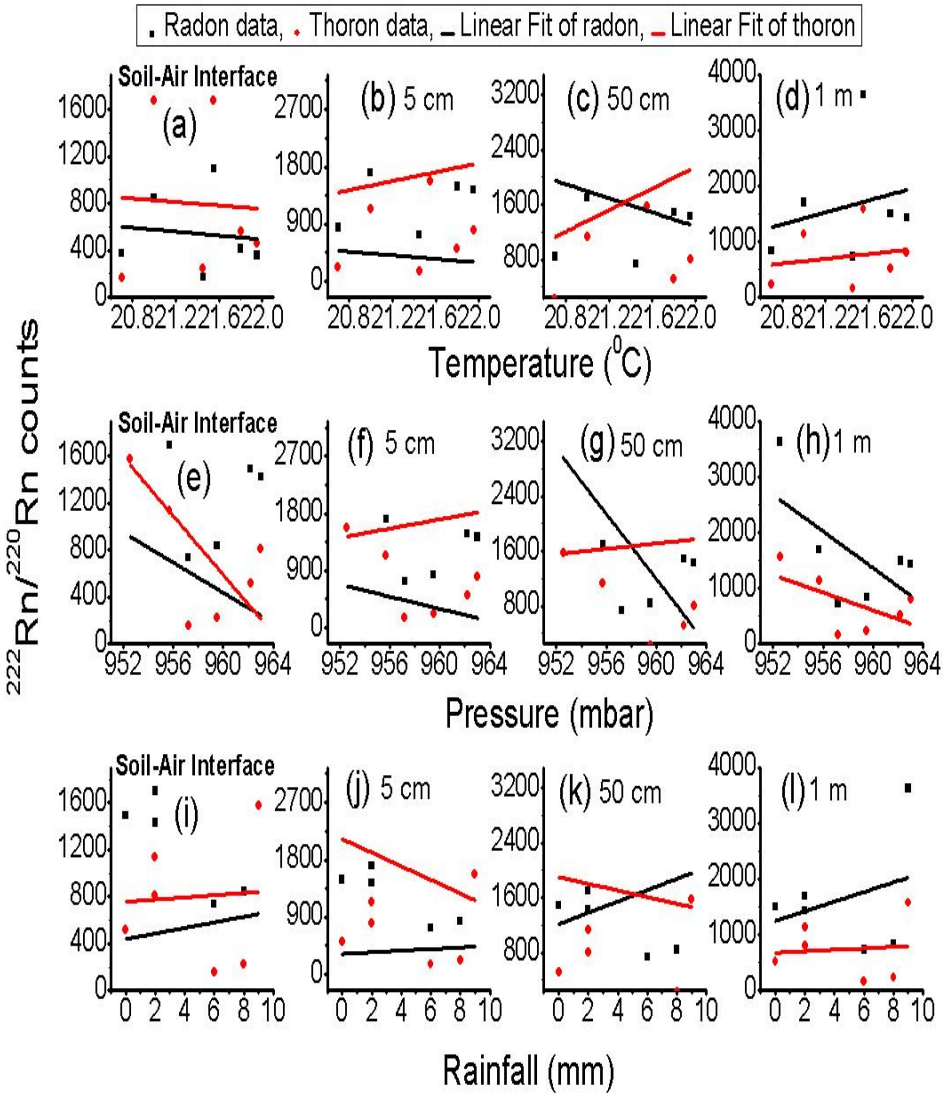

Fig. 4.11: Linear graph of (a-d) $^{222}Rn/^{220}Rn$ versus air temperature (^{0}C) at the soil-air interface, 5 cm, 50 cm and 1 m depths (e-h) $^{222}Rn/^{220}Rn$ versus barometric pressure at the soil-air interface, 5 cm, 50 cm and 1 m depths (mbar) (i-l) $^{222}Rn/^{220}Rn$ versus precipitation (mm) at the soil-air interface, 5 cm, 50 cm and 1 m depths at Chite fault for the period of February, 2018 to July, 2018.

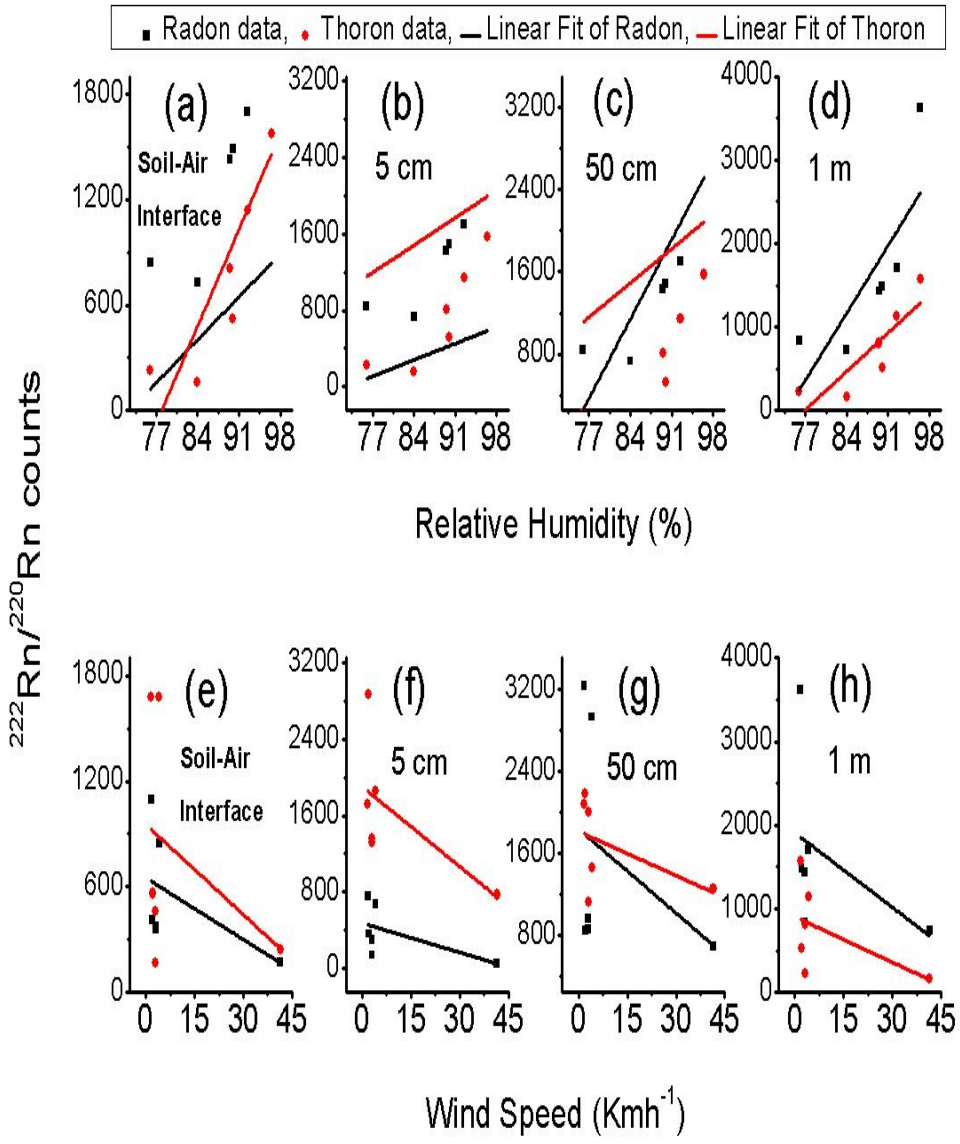

Fig. 4.12: Linear graph of (a-d) $^{222}Rn/^{220}Rn$ versus relative humidity (%) at the soil-air interface, 5 cm, 50 cm and 1 m depths (e-h) $^{222}Rn/^{220}Rn$ versus wind speed (Kmh^{-1}) at the soil-air interface, 5 cm, 50 cm and 1 m depths at Chite fault for the period of February, 2018 to July, 2018.

Table 4.11: Details of correlation between ^{222}Rn and ^{220}Rn counts with meteorological parameters (air temperature, pressure, rainfall, humidity and wind speed) at Chite fault during February, 2018-July, 2018.

Meteorological/ $^{222}Rn/^{220}Rn$ data	^{222}Rn at depth of				^{220}Rn at depth of			
	Soil-Air Interface	5 cm	50 cm	1 m	Soil-Air Interface	5 cm	50 cm	1 m
Temperature (^0C)	-0.1	-0.2	-0.2	0.2	-0.1	0.2	0.8	0.2
Pressure (mbar)	-0.7	-0.7	-0.8	-0.6	-0.7	0.2	0.2	-0.6
Rainfall (mm)	0.2	0.2	0.3	0.3	0.0	0.6	0.4	0.1
Humidity (%)	0.7	0.6	0.7	0.8	0.8	0.4	0.7	0.9
Wind speed (Kmh^{-1})	-0.5	-0.6	-0.4	-0.4	-0.4	-0.6	-0.5	-0.5

In this case, the insignificant correlation was neglected and the 50% significant correlation was accepted. Hence pressure was found to have a reverse correlation with thoron data. Again 50% significant positive correlation was observed between rainfall and thoron (0.6, 0.4) whiles a strong positive correlation was observed between humidity and thoron in all the sampling depths (0.8, 0.4, 0.7, 0.9) (Table 4.11, Fig. 4.11(i-l), Fig. 4.12(a-d)). As mentioned above these observed positive correlations was regarded as due to rainfall as humidity was masked by rainfall in the inter-correlation analysis. Hence it was assumed that a positive correlation was observed between rainfall and thoron. A moderate reverse correlation was observed between thoron and wind speed (-0.4, -0.6, -0.5, -0.5) in all the sampling depths (Table 4.11, Fig. 4.12(e-h)). However, like humidity it was found to be masked by other meteorological factors in the inter-correlation analysis and hence was neglected. Hence at Chite fault the thoron data was also found to be enhanced by precipitation and suppressed by pressure like radon. When compared the correlation analysis of the three monitoring locations pressure, rainfall and temperature seems to be the main influencing factors on the radon isotope pair data while other parameters get masked.

4.6. Determining the most influencing meteorological parameters using backwards Multiple Linear Regression (MLR) analysis

The detailed correlation analysis and significant t-test (at 95% confidence level) from the three monitoring station reveals that temperature, rainfall and pressure have significant influence on the isotope pair data. To observe the most influencing factors (the best predictor), a backward multiple linear regression was performed through different models. In the first model, the dependent variable (radon or thoron) was regressed with all the predictor variables (air temperature, pressure, rainfall, humidity, and wind speed). In the second model, the variable with the highest p-value was excluded to improve the model. The exclusion of variables in the succeeded model was completely based on the p-value being the highest in the previous model regardless of whether it is significant or not. The process keeps on repeating until no candidate predictor was available. The raw score multiple linear regression given by equation (4.2) facilitates the study of several independent variables for a given independent variable.

$$Y' = a + b_1X_1 + b_2X_2 + b_3X_3 + ... + b_nX_n \tag{4.2}$$

Where Y' is the predicted value of the dependent variable, a is the constant term, b_1, b_2, ..., b_n are the regression coefficient and X_1, X_2, ..., X_n are the independent variables. In equation (2) as the regression coefficient depends on the unit of independent variables, it was ambiguous to compare the independent variables amongst themselves for revealing the most influencing factors on the dependent variables. To fix this problem both the coefficient and variables were standardized using equation (4.3) (*Singh et al.*, 2014b) which then facilitates direct comparison among the predictors.

$$Z_Y' = \beta_1 Z_{X1} + \beta_2 Z_{X2} + ... + \beta_n Z_{Xn} \tag{4.3}$$

where β's and Z's are the standardized coefficient and Z-scores, respectively.

For identifying the most significant influencing factor on the isotope pair data, continuous data generated at Mizoram University between May, 2018-October, 2018 was selected. As mentioned in section 3.7 in the previous chapter no significant correlation was observed between thoron and meteorological factors throughout the season hence finding its most effecting factors were neglected. Now from Table 4.12, after regressing through different five models, the backward regression analysis shows that barometric pressure was the most significant influencing meteorological parameters on radon data.

Table 4.12: Different models of the backward multiple linear regressions and its output using a two tail t-test.

Model		**Unstandardized Coefficients**		**Standardiz-ed Coefficien-ts Beta**	**t-value**	**Sig. (p-value)**
		B	Std. Error			
1	(Constant)	2888.407	458.435		6.301	2.3E-09
	Temperature (0C)	-14.093	1.995	-0.504	-7.065	3.7E-11
	Humidity (%)	1.972	0.399	0.310	4.944	1.8E-06
	Rainfall (mm)	-0.464	0.171	-0.161	-2.709	0.007
	Pressure (mbar)	-2.656	0.474	-0.357	-5.599	8.2E-08
	Wind Speed (Km/h)	-8.043	1.791	-0.294	-4.492	1.3E-05
2	(Constant)	2757.398	464.064		5.942	1.5E-08
	Temperature (0C)	-12.852	1.976	-0.459	-6.503	8.0E-10
	Humidity (%)	1.887	0.405	0.296	4.661	6.2E-06
	Pressure (mbar)	-2.544	0.481	-0.342	-5.289	3.6E-07
	Wind Speed (Km/h)	-7.873	1.822	-0.287	-4.322	2.5E-05

3	(Constant)	2424.817	480.079		5.051	1.1E-06
	Temperature (0C)	-9.269	1.882	-0.331	-4.925	1.9E-06
	Humidity (%)	1.920	0.425	0.302	4.522	1.1E-05
	Pressure (mbar)	-2.301	0.501	-0.309	-4.592	8.3E-06
4	(Constant)	3286.419	464.218		7.079	3.2E-11
	Temperature (0C)	-6.367	1.864	-0.228	-3.416	0.0008
	Pressure (mbar)	-3.085	0.495	-0.415	-6.226	3.4E-09
5	(Constant)	3601.321	468.412		7.688	9.7E-13
	Pressure (mbar)	-3.561	0.490	-0.479	-7.273	1.1E-11

At the same time, it can also be seen that temperature and rainfall (humidity was the direct effect and masked by rainfall) were the second most affecting meteorological parameters on radon data. The observation was in agreement with the correlation analysis performed at three different monitoring locations where air temperature, pressure and rainfall were observed to influence the isotope pair data. Hence our observation indicates that the generated isotope pair data were affected by meteorological factors which must be identified and discarded before correlation with geophysical phenomena to avoid false prediction.

4.7. Correlation of Radon isotope pair data with Geophysical phenomena of the region

4.7.1 Determination of seismicity of the region by correlating *in-situ* radon isotope pair data at Mat fault with continuous data at Mizoram University

The geophysical properties of radon isotope pair data at Mat fault were studied during two different window periods viz. between November, 2017 to April, 2018 and May, 2018 to October, 2018. The isotope pair data were generated *in-situ* online from a rectangular grid (400 m×1000 m) of 9 spots in three different sampling depths

(5 cm, 50 cm and 1 m) with a frequency of once a month in all the measuring period (Fig. 3.2). The first period of measurements were carried out in the following dates: November 16, 2017, December 15, 2017, January 17, 2018, February 27, 2018, March 27, 2018, and April 18, 2018. These dates of measurements were represented by vertical dash-line in Fig. 4.13. The radon isotope pair data were downloaded from the monitor and categorised into anomaly (peak period) and non-anomaly (non-peak) period data. The data were grouped on the basis of the 15 min cycle continuous data at Mizoram University. As mentioned elsewhere the isotope pair data at Mizoram University were monitored under a protected environment. The correlation analysis in the previous sections (section 4.5.2) also indicates that no significant correlation was observed between the isotope pair and meteorological factors. It was also concluded that the provided shading was the reason behind the insignificant correlation. Hence it was ruled out that any observed anomaly in the isotope pair data was solely due to geophysical phenomena of the region. Such that it was utilized for differentiating the isotope pair data at Mat and Chite fault. The isotope pair data at both the faults were regarded as anomaly period data if they were generated by the time the continuous data at MZU lies above the anomaly line (peak period factors, 2σ, 1σ etc above the mean) otherwise non-anomaly period data. It must be noted that there was no definite criterion for assigning radon anomalies; hence every author defines it as appropriate to its own data. The method for selecting radon anomalies has been discussed elsewhere. For the present period, the radon anomaly was observed at 1.3σ (1SD) above the mean and was named radon peak factor (RPF) in Fig. 4.13a. As mentioned above it was used as a reference point for categorizing the field data at Mat fault. Based on this criterion radon data generated on November 16, 2017, December 15, 2017, February 27, 2017 and April 18, 2018 belongs to the anomaly period data and that of January 17, 2018 and March 27, 2018 belongs to the non-anomaly period data. On the other hand, the thoron data were categorized into five groups based on interval shifts of the thoron concentrations at MZU. Next was to cross-analyze the anomaly and non-anomaly period of the isotope pair data at MZU and Mat fault to reveal their geophysical properties.

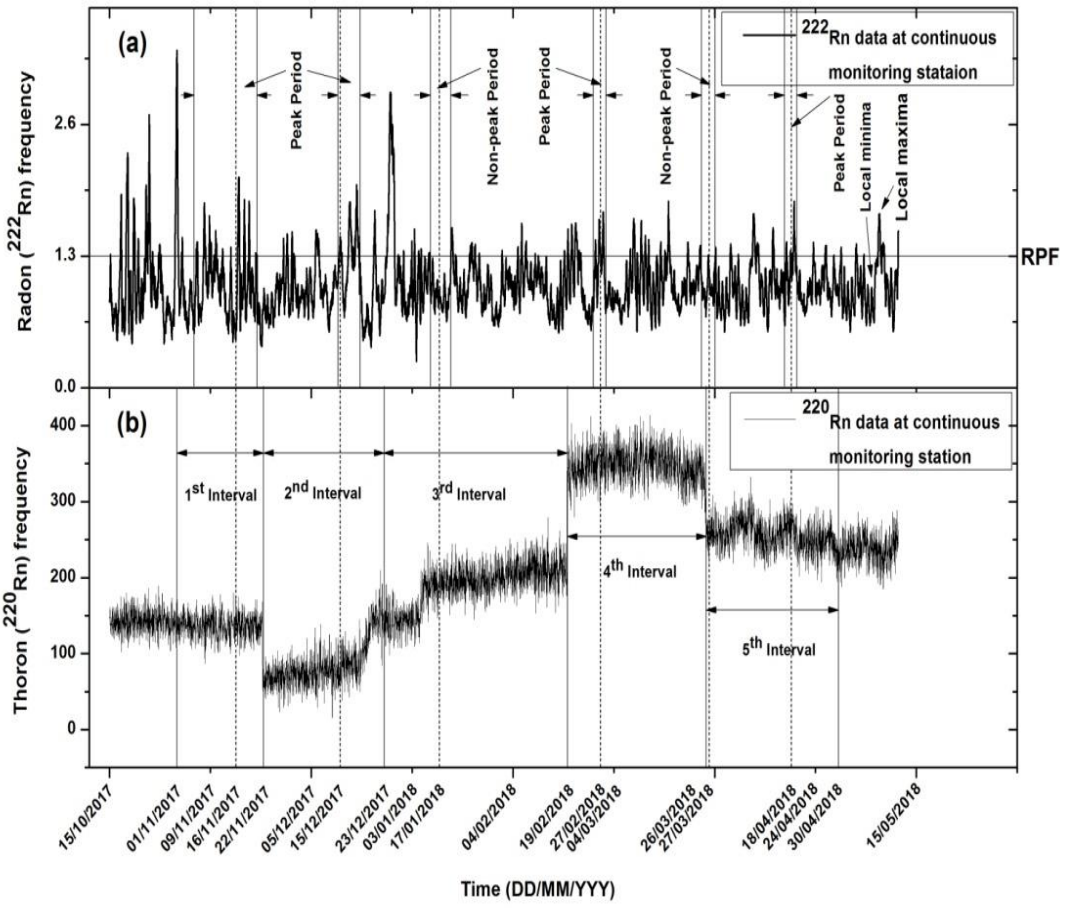

Fig. 4.13: Plot of (a) Real-time 5 cm depth ^{222}Rn data monitored at MZU showing categorisation of *in-situ* generated ^{222}Rn data at Mat fault (represented by vertical dash-line on its date of generation) into peak and non-peak period data (indicated by an interval of two vertical solid lines) between October 15, 2017 and May 15, 2018, (b) Real-time 5 cm depth ^{220}Rn data monitored at MZU between October 15, 2017 and May 15, 2018, showing categorization of *in-situ* generated Mat fault ^{220}Rn data (represented by vertical dash-line on its date of generation) into 5 different groups on the condition that their time of generation belongs to the interval.

When compared the anomaly and non-anomaly period data at Mat fault; the radon data at sampling depths of 5 cm and 50 cm shows higher radon counts during anomaly period in all the 9 sampling spots (Fig. 4.14a&4.14b). However, at 1 m depth, two sampling spots (22%) fail to show higher radon counts during anomaly

period (Fig. 4.14c). Such that, radon data of 5 cm and 50 cm depths at Mat fault fluctuates exactly as the meteorologically minimized continuous data at MZU during anomaly and non-anomaly periods. While at 1 m depth 78% (7 out of 9 spots) of the sampling spots correlated with the continuous data at MZU and 22% (2 out of 9 spots) of them fail so. But the overwhelming majority spots with higher radon counts during the anomaly period indicate that the radon data at this depth also vary in a similar manner with the continuous data at MZU with high accuracy. Hence for this study period, the *in-situ* radon data at Mat fault and the online data at MZU were in phase during geophysical and non-geophysical phenomena. The anomaly to non-anomaly period data ratio of the three successive sampling depths was 1.6, 1.9 and 1.2 respectively (Fig. 4.15). It shows that radon fluctuation due to geophysical phenomena was maximum at 50 cm depth. Hence it will serve as a suitable sample depth for monitoring radon variation due to geophysical phenomena at Mat fault.

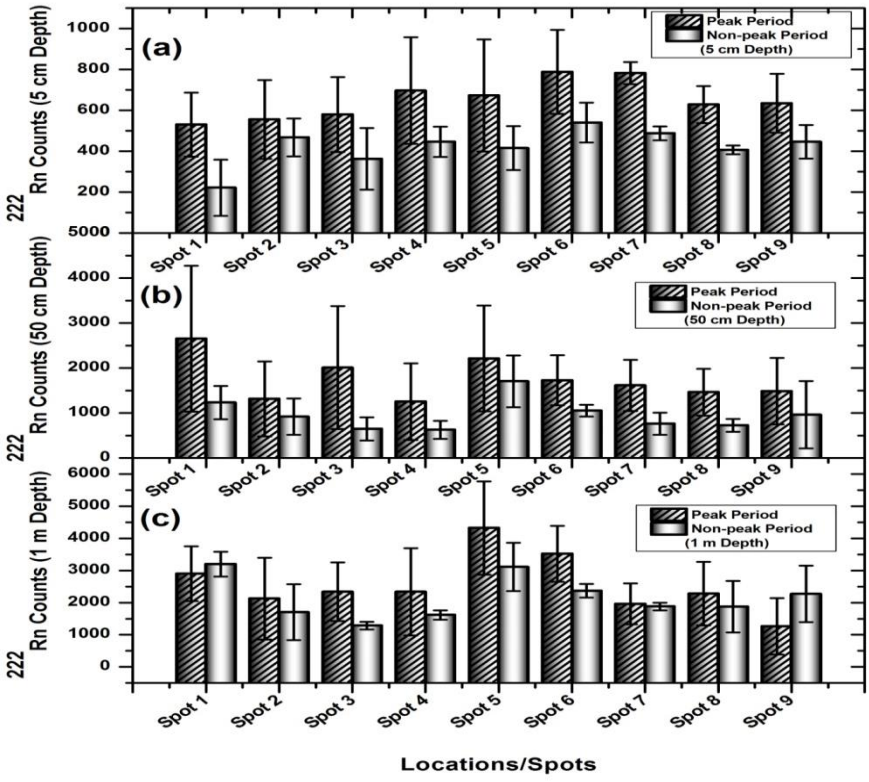

Fig. 4.14: Plot of *in-situ* online generated ^{222}Rn data for each of the 9 spots of the grid at Mat fault between November, 2017 and April, 2018 (a) average ^{222}Rn counts at depth of 5 cm during peak period and non-peak period of ^{222}Rn data at MZU (b) average ^{222}Rn counts at depth of 50 cm during peak period and non-peak period of ^{222}Rn data at MZU and (c) average ^{222}Rn counts at depth of 1 m during peak period and non-peak period of ^{222}Rn data at MZU.

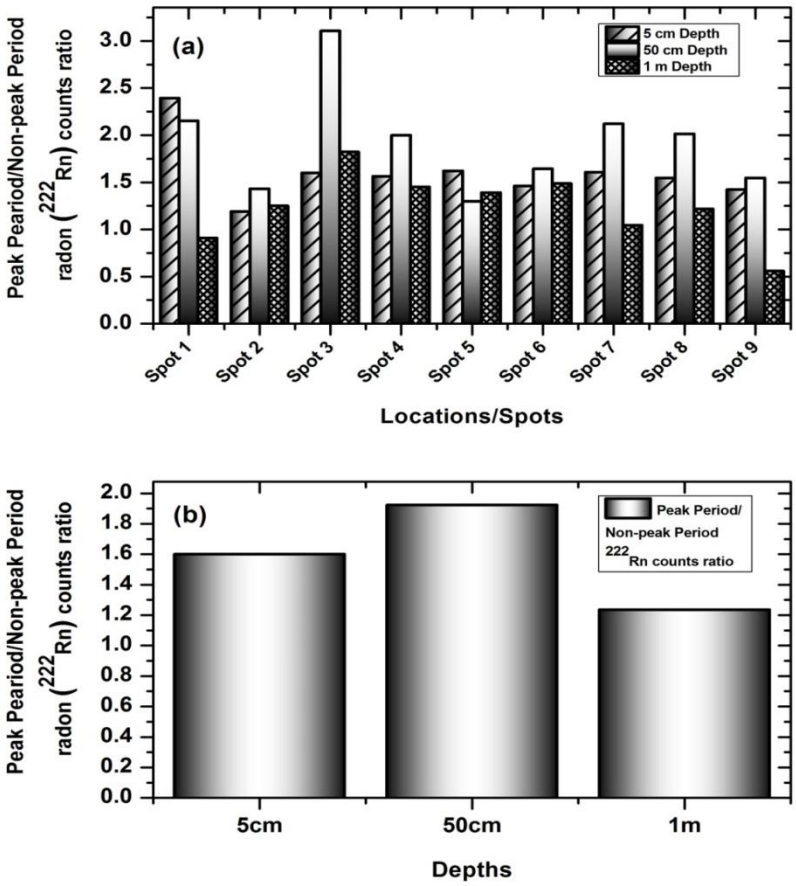

Fig. 4.15: Plot of (a) Peak period to non-peak period ^{222}Rn counts ratio at depths of 5 cm, 50 cm and 1 m below the ground surface for each of the nine spots of the grid at Mat fault (b) Average of Peak period to non-peak period ^{222}Rn counts ratio at depths of 5 cm, 50 cm and 1 m below the ground surface of Mat fault.

The thoron data at MZU doesn't show any significant peaks but varies with almost constant amplitude with high frequency. It remains equilibrium for a certain time interval and raises or falls from the previous interval and forms another equilibrium interval for a certain time period. During this investigation period five such interval of thoron count variation was observed (Fig. 4.13b, Fig. 4.16a). Such that the thoron data at Mat fault was also prepared according to that for cross-analysis. For this, the continuous MZU thoron data of each interval and thoron data of Mat fault corresponding to each interval were averaged out (Fig. 4.16). The five interval period at MZU were as follows November 1, 2017-November 23, 2017; November 23, 2017-December 25, 2017; December 25, 2017-February 19, 2018; February 19, 2018-March 27, 2018 and March 27, 2018-April 30, 2018 respectively. It was found that thoron data generated at Mat fault on November 16, 2017, December 15, 2017, January 17, 2018, February 27, 2018, belongs to the first, second, third and fourth intervals of the continuous data at MZU. And finally, those generated on March 27, 2018 and April 18, 2018 belong to the fifth interval (Fig. 4.16a). Now intervally average thoron data of the two locations were cross analyst. The thoron data at 5 cm depth in Mat fault fails to show exactly the same trend as that of the continuous data at MZU particularly at the 3^{rd} and 4^{th} intervals (Fig. 4.16b). But at 50 cm sampling depths, the thoron data at Mat fault was overwhelmingly in phase with the continuous data in all the five intervals (Fig. 4.16c). In other words, the thoron data at 50 cm varies exactly in the same manner as that of the continuous thoron data at MZU. At 1 m sampling depth in Mat fault thoron data fails to show similar variation to that of the continuous data only in one interval (5^{th} interval) while it shows the exact same variation in all the other four intervals (Fig. 4.16d). In general, we can say that during this observation period the generated thoron data at Mat fault in 50 cm depth exactly varies in the same manner with continuous data monitored at MZU. But at 5 cm and 1 m depth, it deflects from the meteorologically minimized continuous data at MZU. The correlation of thoron data with geophysical phenomena was neglected as its daily variation at the continuous monitoring station in MZU was unrecognizable instead varies in an interval fashion which was quite unreliable for studies of the geophysical process.

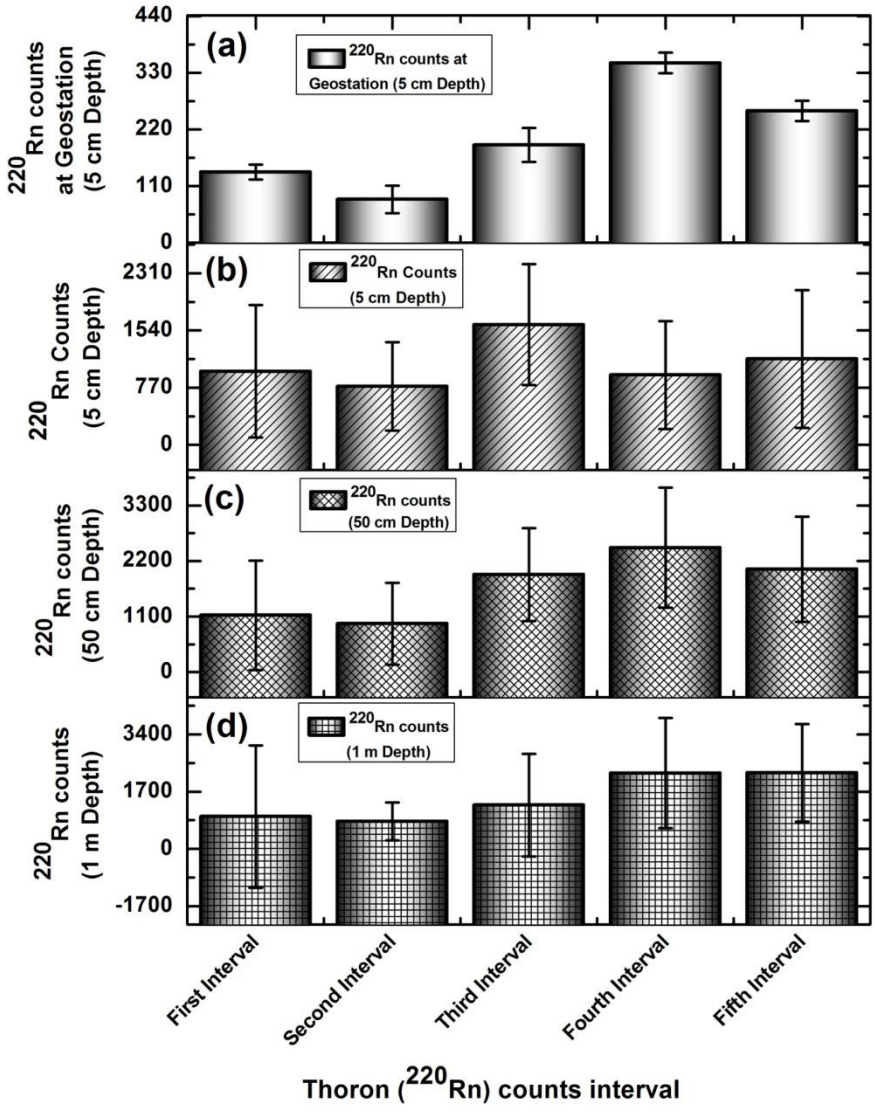

Fig. 4.16: Plot of (a) online ^{220}Rn data at MZU average out w.r.t the five different interval variations between November, 2017 and April, 2018 (b) ^{220}Rn counts at depth of 5 cm w.r.t the five different interval counts variation of ^{220}Rn data at MZU (c) ^{220}Rn counts at depth of 50 cm w.r.t the five different interval counts variation of ^{220}Rn data at MZU (d) ^{220}Rn counts at depth of 1 m w.r.t the five different interval counts variation of ^{220}Rn data at MZU.

The second study period was carried out between May, 2018 and October, 2018 comprising the rainy season of the region. The study period experiences the most turbulent weather of the season and along with the first study period forms a complete season. Like the previous study period for correlating the *in-situ* data at Mat fault firstly the anomaly period of the reference data at MZU must be defined. For this period the anomaly line or the radon peak factor (RPF) of the continuous data at MZU was observed at 1.1σ above the mean (Fig. 4.17). Hence data of June 27, 2018, July 26, 2018 and September 25, 2018 were treated as anomaly period data since the reference data at MZU lies above 1.1σ at the time of their generation at Mat fault. By the same criterion those of May 30, 2018, August 28, 2018 and October 9, 2018 were treated as non-anomaly period data as the reference data lies below 1.1σ at the time of their generation.

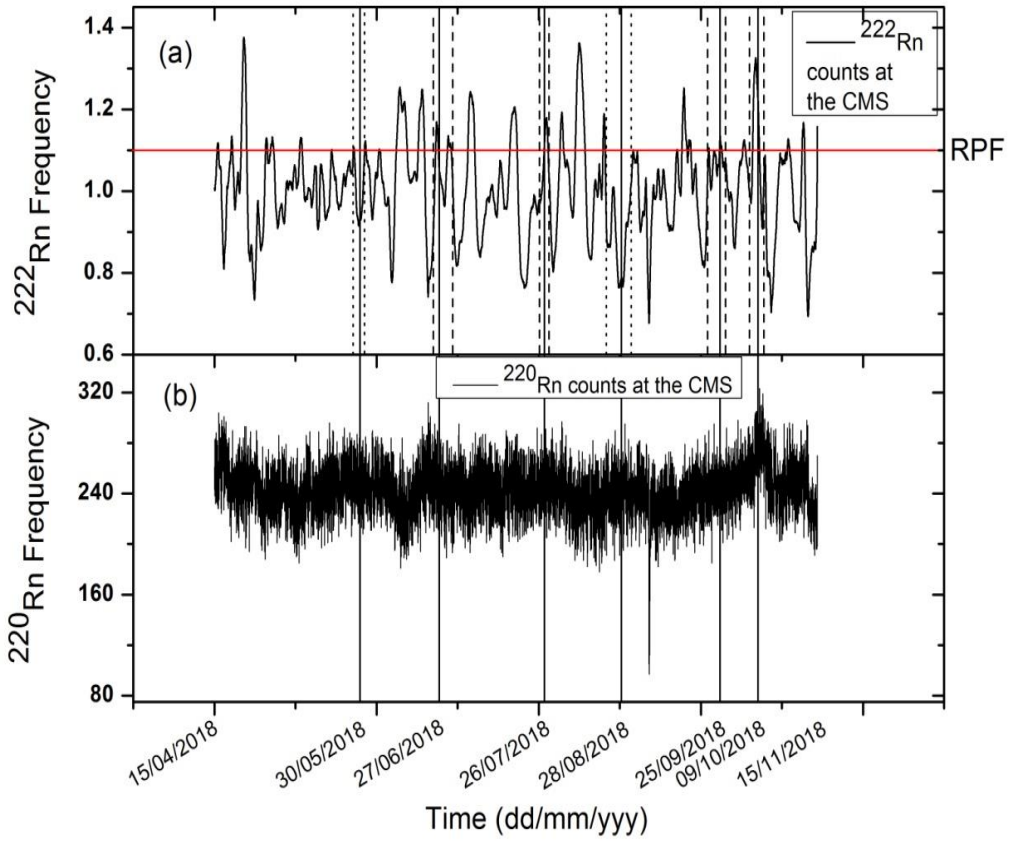

Fig. 4.17: Plot of (a) 15 minutes cycle ^{222}Rn data of the CMS versus time; showing date of ^{222}Rn measurement at Mat fault (indicated by vertical line), ^{222}Rn anomaly period (indicated by intervals of vertical dash line) and non-anomaly period (indicated by intervals of vertical dot line) and radon peak period factor (RPF) and (b) 15 minutes cycle ^{220}Rn data versus time between April 15, 2018 to November 15, 2018.

After correlating anomaly period and non-anomaly period *in-situ* data at Mat fault and continuous data at MZU, the following observation has been made for radon data of different sampling depths. At 5 cm sampling depth from the ground surface, 56% of the sampling spots (5 out of 9 spots) were found to have higher average radon exhalation during the anomalous period (geophysical phenomena) than that of the non-anomalous period (Fig. 4.18a). But in 33% (3 out of 9 spots) and 11% (1 out of 9 spots) of the spots, the average radon exhalation was lower than and equal to that of the non-anomalous period respectively (Fig. 4.18a). At 50 cm depth, it was observed that 89% of the sampling spots (8 out of 9 spots) show higher radon exhalation during anomalous period while 11% (1 out of 9 spots) of them fail it (Fig. 4.18b). Again at 1 m depth, 67% of the sampling spots show higher radon exhalation during anomaly period while 33% fail it when compared to that of the non-anomaly period (Fig. 4.18c). The anomalies to non-anomaly period data ratio of the three sampling depths were 1.1, 1.4 and 0.9 respectively (Fig. 4.19). The maximum ratio was at 50 cm depth like in case of the first study period. It confirmed that for the whole season the radon fluctuation was most pronounced and highly detectable at 50 cm depth. On the other hand, no significant correlation was observed between thoron data of the three sampling depths at Mat fault and the continuous data at MZU during this period. Hence no geophysical properties of thoron have been determined for this period which may be due to strong meteorological effects as the period falls within the most turbulence period of the weather.

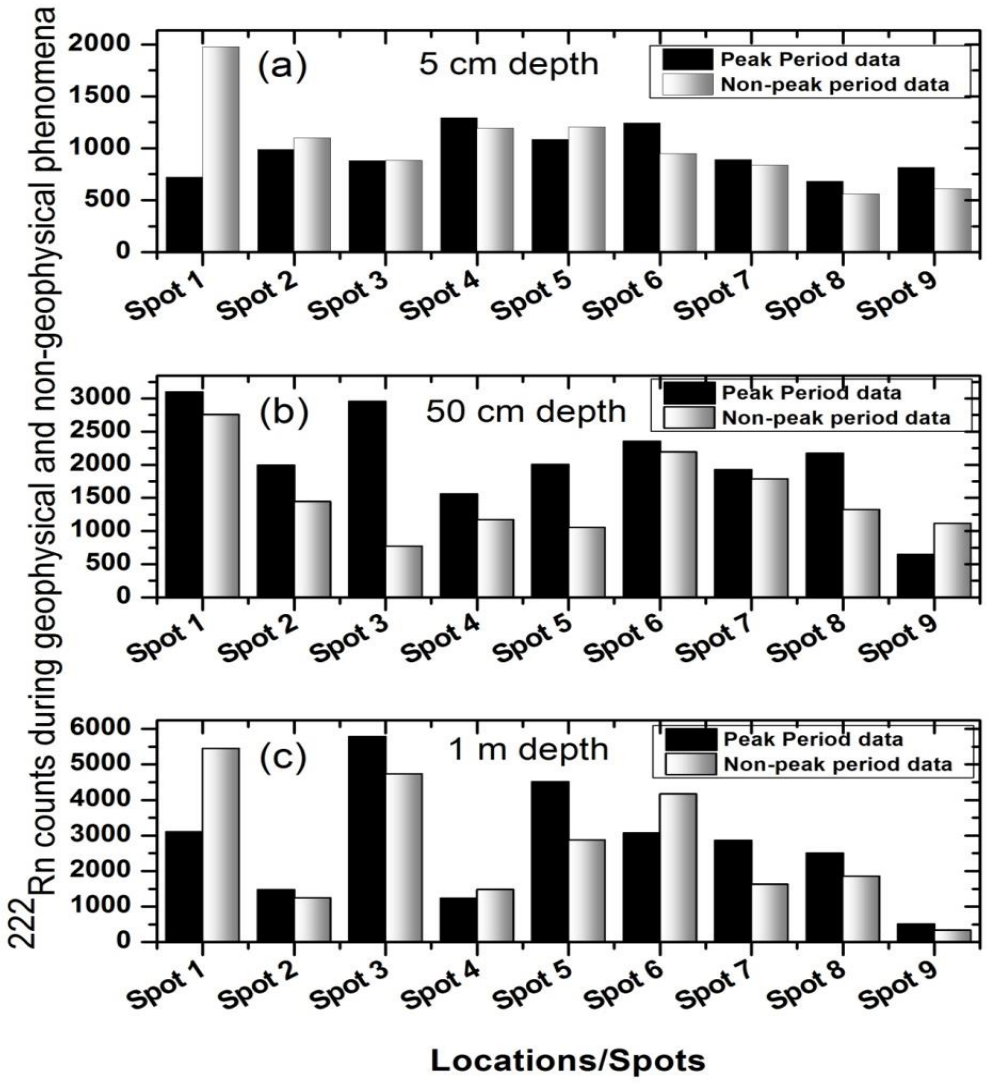

Fig. 4.18. Plot of *in-situ* online ^{222}Rn data of each sampling depth at Mat fault, during anomaly (geophysical phenomena) and non-anomaly period (non-geophysical phenomena) of ^{222}Rn data monitored at the CMS, at (a) 5 cm depth (b) 50 cm depth and (c) 1 m depth between May, 2018 and October, 2018.

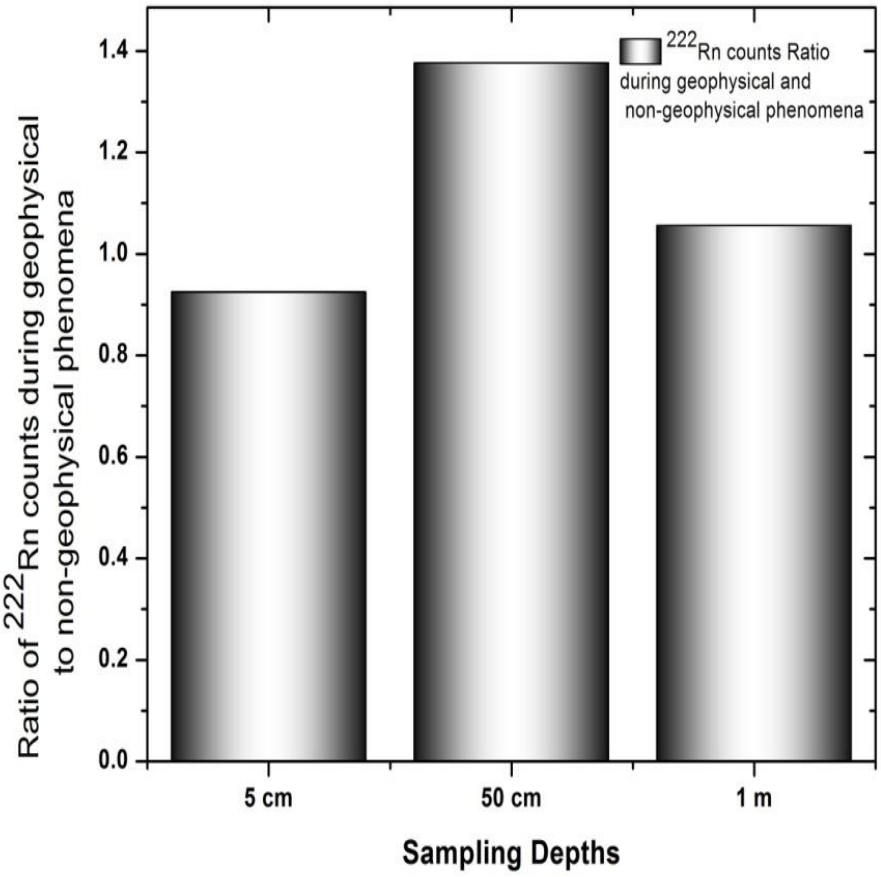

Fig. 4.19: Plot of anomaly period to non-anomaly period ^{222}Rn counts ratio of the three sampling depths at Mat fault during May, 2018-October, 2018.

When compared to that of radon data generated during the dry and calm weather (radon data of the first study period between November, 2017 and April, 2018) the number of sampling spots showing higher radon counts reduced in the second study period. As mentioned above this could be due to the meteorological effect on the isotope pair data which was expected to be maximum in this period comprising the rainy season. Despite the meteorological effect majority of the sampling spots were able to depict higher radon counts during geophysical phenomena in all the sampling depths, especially at 50 cm depth. Hence from the two observation period, the following conclusion can be made. The studies clearly show that radon data

generated at the continuous monitoring station (MZU) and Mat fault varies uniformly with high precision during geophysical phenomena even at three different sampling depths. It consequently determined that not only Mat fault was geophysically active but also the Mizoram University where the continuous monitoring station was located. Hence, upon accumulating enough online radon data at MZU it may suitably be used for forecasting seismic activity of the region. Hence, from this comparative analysis, it can be concluded that the region is seismically active and radon data of the entire season generated from the region may be utilized for future seismic-related studies.

4.7.2 Determination of seismicity of the region by correlating *in-situ* radon isotope pair data at Chite fault with continuous data at Mizoram University.

The radon isotope pair data at Chite fault were generated between February, 2018 and July, 2018. Like in Mat fault the data were *in-situ* online with one-month frequency assessed on the following dates; February 28, 2018; March 31, 2018; April 29, 2018; May 25, 2018; June 29, 2018 and July 31, 2018. In this study period, radon data at the continuous monitoring station was normalized with mean at 1 using a software name "Radon Data Processor" developed by Bhabha Atomic Research Centre, Mumbai (India). The anomaly period of this normalized continuous radon data was observed at 2σ above the mean (Fig. 4.20). Hence any radon data of Chite fault generated by the time the continuous data lies above the 2σ was considered an anomaly period data otherwise non-anomaly period data. Such that the isotope pair data of February 28, 2018 and July 31, 2018 were treated as anomaly period data while that of March 31, 2018; April 29, 2018; May 25, 2018 and June 29, 2018 were considered non-anomaly period data. Now when compared the anomaly and non-anomaly period data the following observation has been made. From Fig. 4.21(a-c) it was found that in 100% of the sampling spots the average radon count during the anomaly period was always higher than that of the non-anomaly period in all the three sampling depths (5 cm, 50cm and 1 m). The anomaly period to non-anomaly period radon counts ratio were found to be 1.9, 2.2 and 1.5 at 5 cm, 50 cm and 1 m sampling depths respectively (Fig. 4.22). The highest ratio at 50 cm depth suggests

that it is the best sampling depth for monitoring radon fluctuation due to geophysical phenomena as that of in Mat fault. Hence when compared to the two window period studies at Mat fault it suggested that the radon fluctuation was most pronounced at 50 cm depth. Finally, it can be concluded that geophysical phenomena of the region can suitably be identified by monitoring radon concentration variation at Chite fault. As Chite fault lies in the vicinity of Aizawl city (Capital of Mizoram state) the observation may serve as critical baseline data for future seismic prediction studies in the region. Correlation of thoron data with geophysical phenomena at Chite fault has been neglected as no geophysical properties have been observed for its reference data at MZU during this period.

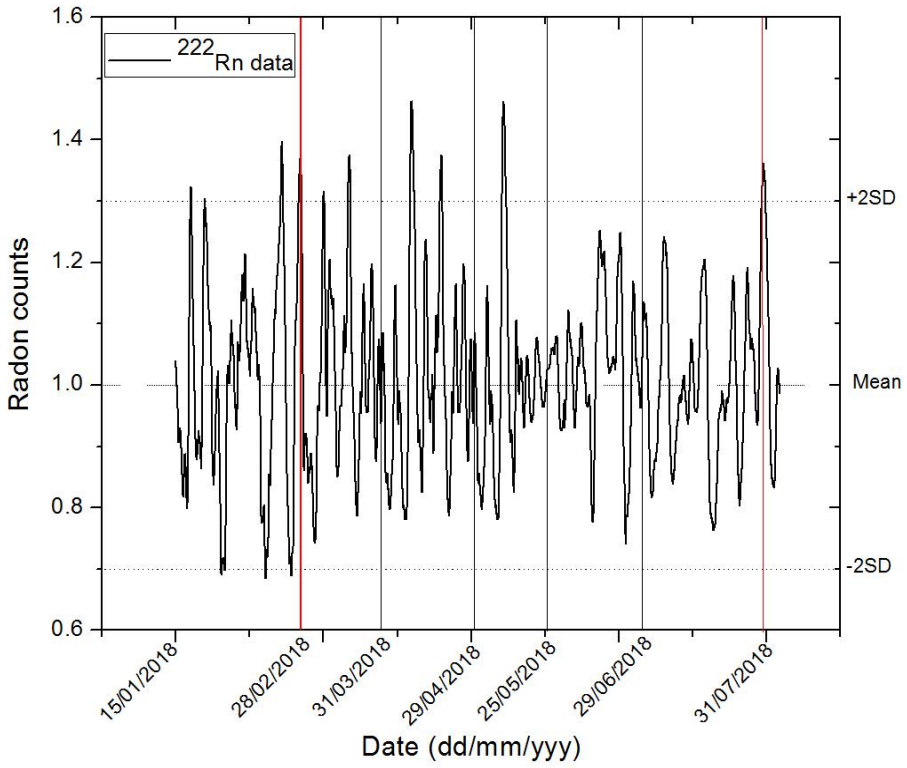

Fig. 4.20: Normalized 15 min cycle radon data of the continuous monitoring station at Mizoram University categorizing anomaly (represented by vertical red line) and non-anomaly period data (represented by vertical black line). The dates of *in-situ* measurement at Chite fault were indicated by vertical red and black lines on its date of measurement.

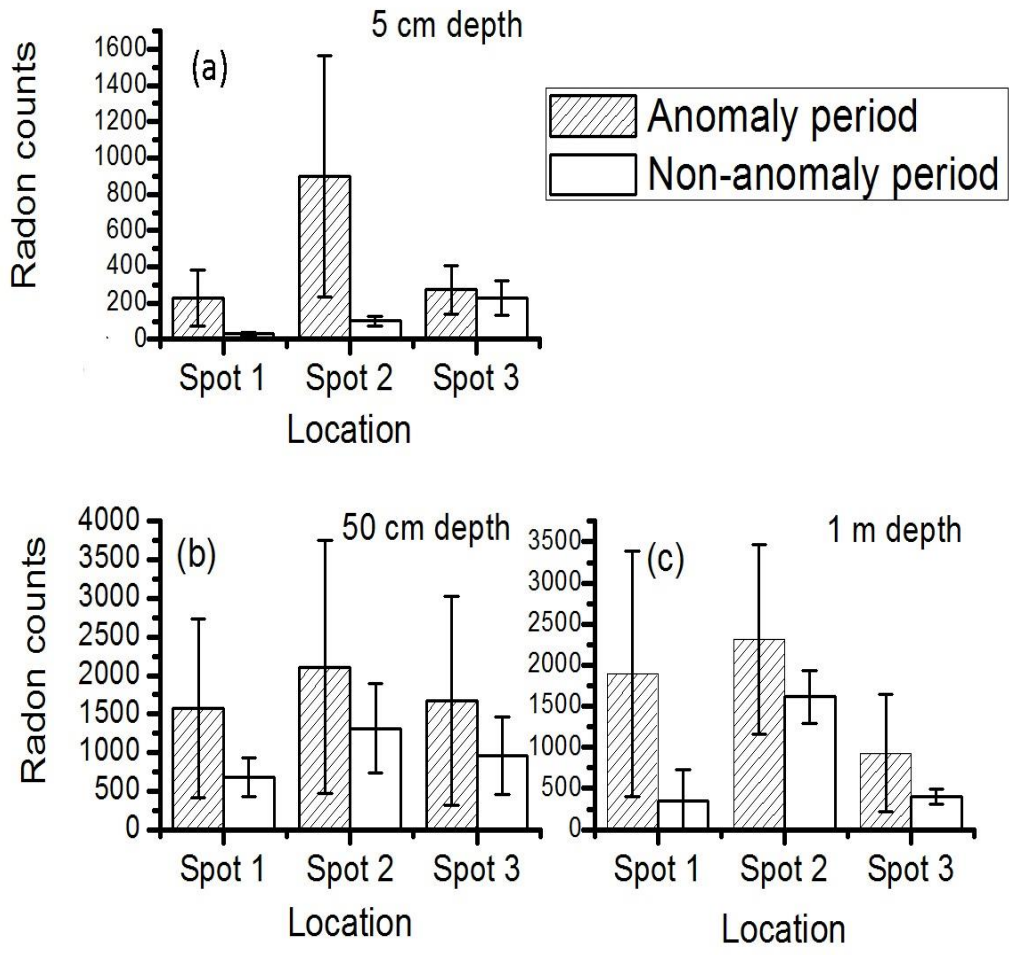

Fig. 4.21: Plot of anomaly and non-anomaly period radon data at (a) 5 cm depth, (b) 50 cm depth and (c) 1 m depth.

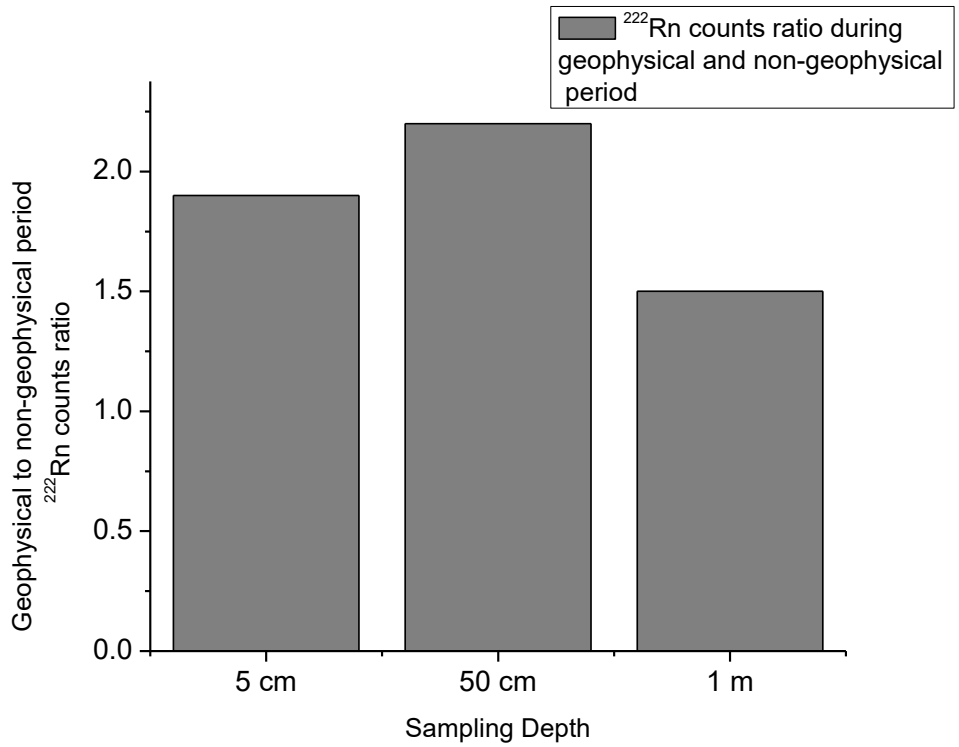

Fig. 4.22: Plot of anomaly period to non-anomaly period ^{222}Rn counts ratio of the three sampling depths at Chite fault during February, 2018-July, 2018.

4.7.3 Correlation of surface radon isotope pair data with geophysical phenomena at Mat and Chite faults.

Monitoring of soil radon isotope pair as a premonitory gas to earthquake has been done mostly in deep soil to avoid meteorological influences. Most studies (Jaishi *et al*., 2013, 2014, 2014a, 2014b, 2015; Ramola *et al*., 1990; Segovia *et al*., 1987; Singh, *et al*., 1988; Singh *et al*., 2014, 2016, 2017; Virk *et al*., 2000; Walia *et al*., 2005) except those of in air (Iwata *et al*., 2018; Muto *et al*., 2021; Omori *et al*., 2007; Yasuoka *et al*., 2009) and water (Igarashi and Wakita, 1990; Kuo *et al*., 2018) selected their sampling depths approximately 18 cm and beyond. Such that reports of radon as a premonitory gas to earthquake at the surface were hardly found. In 2016 Sahoo and Gaware, (2016) published an experimental paper which suggested that at the earth's surface the radon concentrations were low and its fluctuation, when perturbed by external factors especially by geophysical phenomena, was easily

detected. They also state that at deeper sampling depth probably from 1 m depth, the radon concentration attains its asymptotic value and identification of changes in its concentration due to external sources was hard. Adopting their method the isotope pair data has been generated at the soil-air interface both at Mat and Chite faults and at the continuous monitoring station (MZU) as well. It must also be noted that the isotope pair data were retrieved from 3 sampling spots at Chite fault and from 9 sampling spots at Mat fault. At the two faults the soil-air interface radon isotope pair data were generated during May, 2018 - October, 2018 and February, 2018 - July, 2018 respectively. But at the continuous monitoring station in MZU the soil-air interface isotope pair data has been generated since January, 2017 till date. The continuous data was monitored under a meteorologically protected environment with 15 min cycle and has been utilized for identifying geophysical properties of data at the faults by cross-analysis. For the soil-air interface data at Chite fault; since it was measured at the same time period as that of MZU data given in Fig. 4.20 (section 4.7.2above), the depicted anomaly period were as well adopted in this section for categorizing surface radon data of Chite fault. In Fig. 4.20 the reference normalized data at MZU shows anomalies at 2σ above the mean. Hence radon data of February 28, 2018 and July 31, 2018 were treated as anomaly period data as their reference data at MZU lies above 2σ at their times of measurement at Chite fault. At the same time radon data of March 31, 2018; April 29, 2018; May 25, 2018 and June 29, 2018 were considered non-anomaly period data since they were measured by the time the reference data lies below 2σ. Now when compared the anomaly and non-anomaly period data of the 3 sampling spots it was found that 100% of the spots show higher radon count during the anomaly period (Fig. 4.23). Just like that of 5 cm and 50 cm depths mentioned in the above section, the anomaly to non-anomaly period data ratio was quite high (1.7) indicating that radon fluctuation due to geophysical phenomena can be identified at this depth as well.

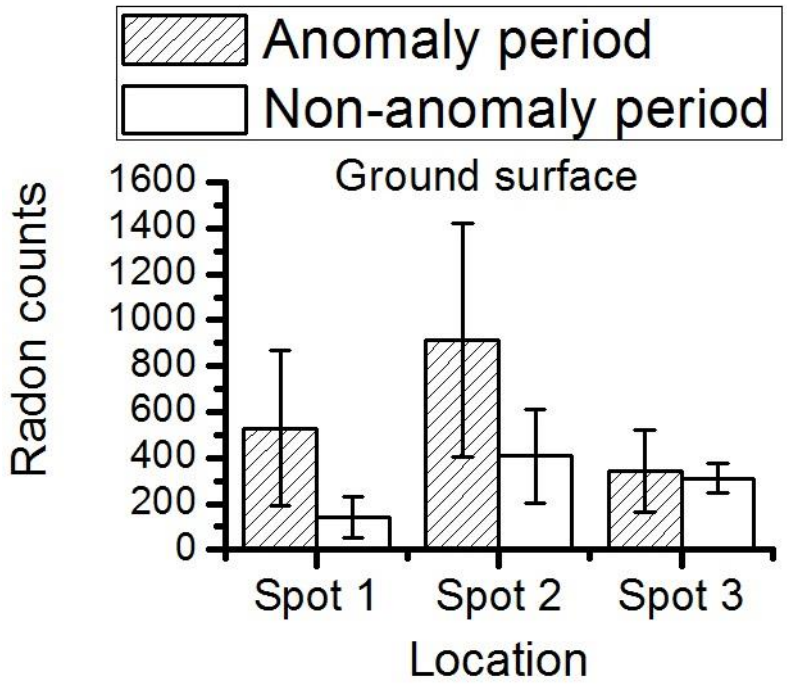

Fig. 4.23: Plot of anomaly and non-anomaly period radon data at the soil-air interface at Chite fault during February, 2018-July, 2018.

For radon data at Mat fault the reference data at MZU shows anomalies at 1σ above the mean (Fig. 4.24a). Such that data of May 30, 2018; July 26, 2018; August 28, 2018 and September 25, 2018 were considered anomaly period data while those of June 27, 2018 and October 9, 2018 were taken as non-anomaly period data. In Fig. 4.24a the 1σ line was represented by a horizontal line and the dates of the experiment by a vertical line. The vertical red and black lines represent anomaly and non-anomaly data, respectively. Thoron data of the continuous monitoring station within the said period was also given in Fig. 4.24b. Again the anomaly and non-anomaly period data were compared to reveal geophysical activeness of the sampling region. After comparison, it was found that in 78% of the spots (7 out of 9 spots), the radon counts were higher during anomaly period (Fig. 4.24c). The anomaly to non-anomaly radon data ratio was found to be 1.5 which is also quite close to that of 5 cm and 50 cm depths.

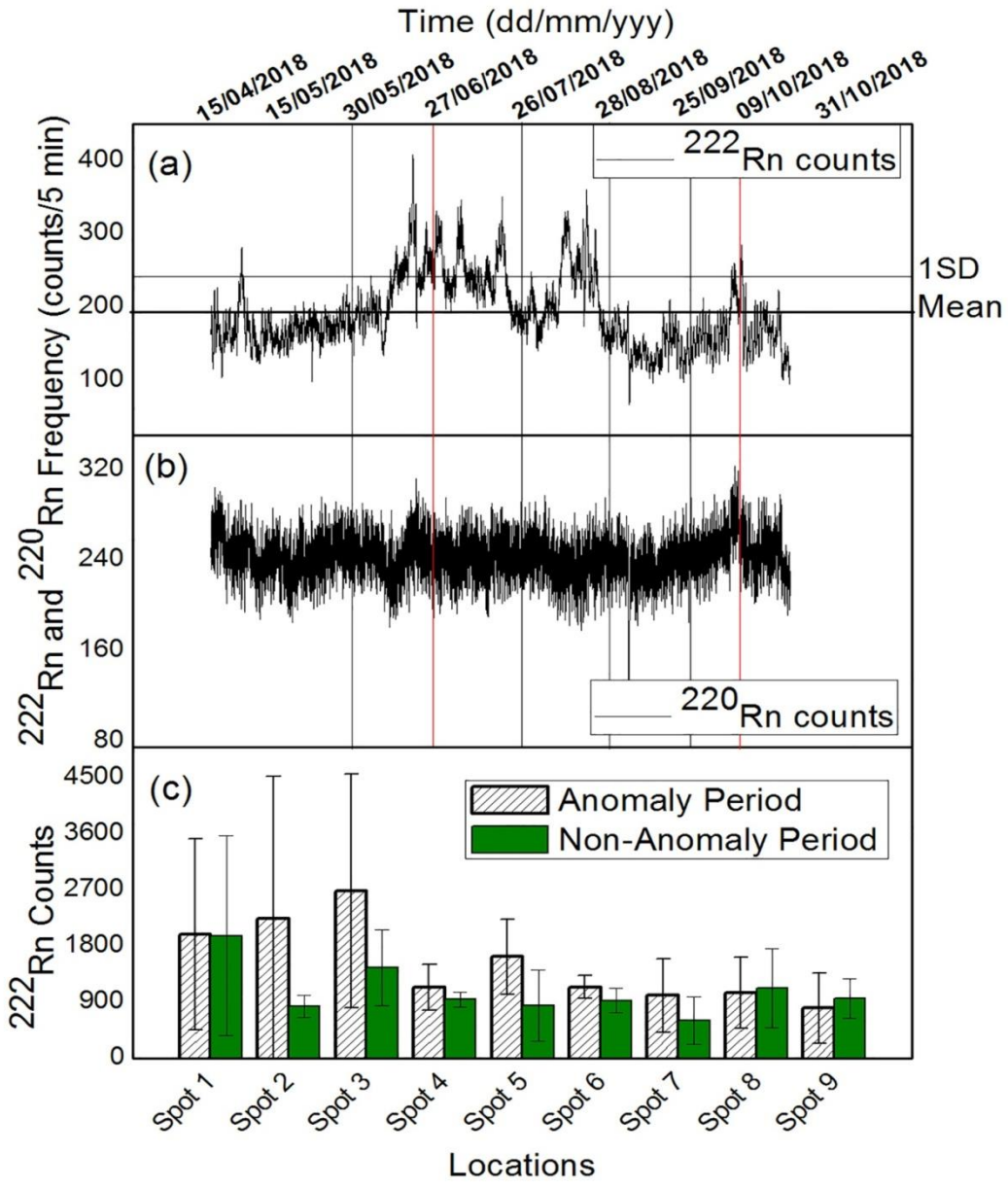

Fig. 4.24: Plot of (a) 15 minutes cycle ^{222}Rn data of MZU classifying soil-air interface *in-situ* ^{222}Rn data of Mat fault into anomaly period and non-anomaly period data generated between May, 2018 and October, 2018. The dates of the experiment were represented by vertical red and black lines, indicating anomaly period and non-anomaly period data, respectively, (b) 15 minutes cycle ^{220}Rn data at the soil-air interface of MZU between May, 2018 and October, 2018, (c) Average of anomaly period and non-anomaly period ^{222}Rn counts data for each of the nine spots from the rectangular grid at Mat fault between May, 2018 and October, 2018.

The observation reveals that majority of the sampling spot were able to show higher radon exhalation during geophysical activity which in turn indicates the fault was active. When compared the anomaly to non-anomaly radon data ratio of the other sampling depths, it was observed that in both the faults, the ratio at the sub-soil (soil-air interface, 5 cm and 50 cm depths) was noticeably high to that of deep soil (1 m depth). It shows that the radon fluctuation may be much easier to detect at the sub-soil due to its low concentration at this depth. The observation was in agreement with the experimentally demonstrated analytical model of Sahoo and Gaware (2016) mentioned above. Hence perturbation of the radon concentration was more pronounced and easier to detect than that of deep soil during stress release. Hence it may be concluded during the study period the radon data responds well to geophysical processes. Correlation of surface thoron data of both the faults with geophysical phenomena was neglected due to absence or unidentifiable geophysical properties of their reference thoron data at MZU.

4.7.4 Correlation of radon isotope pair data in water with geophysical phenomena at Mat and Chite faults

At Mat fault, the radon isotope pair data in water has been generated from 5 sampling spots at the vicinity of the 9 soil gas sampling spots as mentioned in the materials and method section. The measurement was done between May, 2018 and October, 2018 with a frequency of once a month. During this measuring period the reference data at MZU after analyzing using the mean plus "n" times standard deviation have an anomaly at 2σ above the mean (Fig. 4.25a). Such that radon data of August 29, 2018 and October 09, 2018 were treated as anomaly period data represented by vertical red line in Fig. 4.25a. At the same time data of May 30, 2018; June 28, 2018; July 27, 2018 and September 25, 2018 were considered as non-anomaly period data due to the criterion that they were generated by the time the reference data lies below 2σ. When compared the anomaly and non-anomaly period data it was found that in 100% of the sampling spots the radon counts were always higher during the anomaly period (Fig. 2.25b).

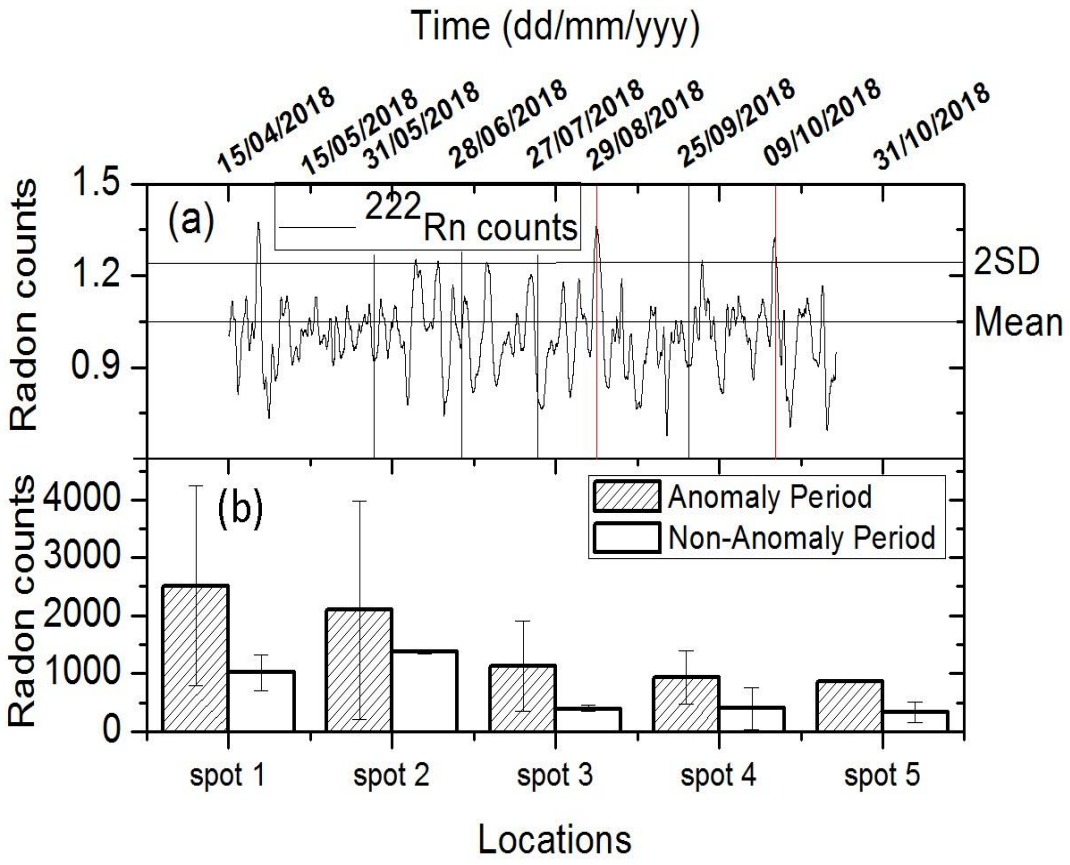

Fig. 4.25: Plot of sampling dates versus (a) continuous radon data **during May, 2018-October, 2018** at Mizoram University and (b) Average radon count in water at Mat fault during anomaly period and non-anomaly period.

At Chite fault the radon isotope pair data has been sampled from 3 designated spots with one-month frequency between February, 2018 and July, 2018. Again its time of measurement was the same as that of radon data at MZU given in Fig. 4.20 (section 4.7.2 above), the depicted anomaly period was as well adopted in this section for categorizing surface radon data. During this period the reference radon data at MZU shows an anomaly at 2σ (Fig. 4.20). Such that, based on the reference data criterion radon data of February 28, 2018 and July 31, 2018 were considered anomaly period data while that of March 31, 2018; April 29, 2018; May 25, 2018 and June 29, 2018 were considered non-anomaly period data. When compared the anomaly and non-

anomaly period data exactly like that of Mat fault 100% of the sampling spots show higher radon counts during the anomaly period (Fig. 4.26).

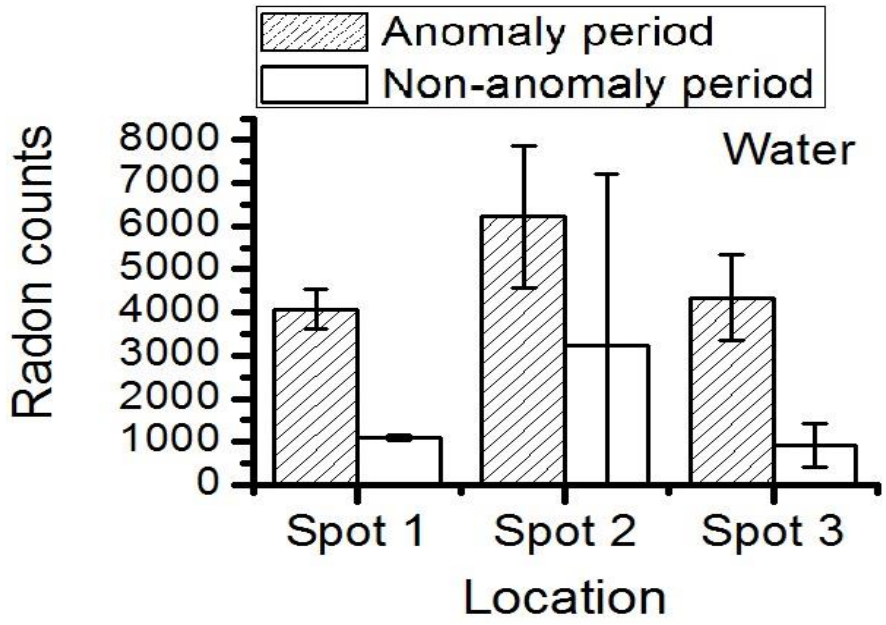

Fig. 4.26: Plot of anomaly and non-anomaly period radon data in water at Chite fault during February, 2018-July, 2018.

The anomaly to non-anomaly period data ratio was observed to be 2.2 and 2.9 at Mat fault and Chite fault respectively. When compared to that of soil radon, the observed ratios in water were in close agreement with the maximum ratios at 50 cm depths that is 1.9 at Mat fault and 2.2 at Chite fault mentioned in sections 7.1 and 7.2 respectively. Also, all the water sampling spots in both the faults show higher radon fluctuation during anomaly period while some sampling spot fails in case of soil radon. The study indicates that the radon perturbation was maximum in water and 50 cm soil depth during anomaly period, suggesting that either media is the best for monitoring radon anomaly due to geophysical phenomena of the region. In the present study as continuous monitoring can't be achieved in water, the soil media has been selected for monitoring radon data. As mentioned elsewhere the observed ratios (anomaly to non-anomaly radon data) were closely related at the sub-soil (soil-air interface, 5 cm and 50 cm depths) and lower at deep soil (1 m depth). Hence instead of 50 cm depth, the soil-air interface has been chosen for the continuous monitoring

station due to its easy access. Also, the fact that all sampling depths at the sub-soil (soil-air interface, 5 cm and 50 cm depths) having close anomaly to non-anomaly period data ratios rule out the choice in selecting any of these three sampling depths but is the same. Until now with the current analytical technique no geophysical properties of thoron have been identified in the reference data at MZU hence its correlation with geophysical phenomena at both then faults has been neglected.

4.7.5 Correlation of continuous radon data with geophysical phenomena using standard deviation method

Radon data with 15 min cycle has been continuously generated at the Department of Physics, Mizoram University, Aizawl, Mizoram (India) between January, 2017 and March, 2017. During this period a total of 7160 radon data has been recorded. The radon data were generated 47 days using a soil probe of 5 cm length and 33 days using an accumulator chamber of volume 5.0×10^{-4} m^3. As mentioned thoroughly elsewhere (materials and methods section) the monitoring station was protected from external influence by the provided shading. Such that the generated radon data was assumed to be free or highly minimized from external influence, especially meteorological factors. At the same time for this particular period, the statistical t-test analysis (95% confidence level) shows no significant correlation between the radon and meteorological data. Hence any fluctuation in radon concentrations during this period was considered solely due to geophysical phenomena of the region. For identifying anomalies in the time series radon data the mean plus "n" times standard deviation (SD) has been used (n=1, 2, 3,…….). To estimate the mean value of the time series radon data average of all the diurnal and nocturnal radon data was taken after removing the peak period data. This mean value was taken as the base count (CB) of the time series radon for the study period (Fig. 4.27c and Fig. 4.27d). It also implies that it was the count of radon data in the absence of any geophysical or meteorological perturbation. In the real-time data curve, the CB line was represented by a horizontal line passing through zero (Fig. 4.27c and Fig. 4.27d). The rise of any radon counts was a measure from this value (CB). The radon fluctuation was considered as an anomaly peak when it crosses +2.6SD or the anomaly line (AL)

(Fig. 4.27c and Fig. 4.27d). This turned out to be 1.1 times and 3 times the CB (x_{mean}) for radon data at 5 cm depth and soil-air interface respectively (Fig. 4.27c and Fig. 4.27d). Using the above method 21 radon anomaly peaks were observed during the period. Seismic data of the study period were assessed from USGS archive (United State Geological Survey, https://eartquake.usgs.gov/earthquakes/map/) and were selected using Dobrovolsky *et al*., (1979) and Fleischer, (1981) criteria given by equations (4.4) and (4.5), respectively.

$$D = 10^{0.43M}\, km \tag{4.4}$$

$$D = \frac{10^{0.813M}}{16.6}\, km \text{ for } M \leq 3$$

$$D = \frac{10^{0.48M}}{1.66}\, km \text{ for } M \geq 3 \tag{4.5}$$

Based on equations (4.4) and (4.5) 46 earthquakes qualified the criterion and were selected for correlation. It must also be noted that all of the selected earthquakes were located within 1000 km radius from the monitoring station. Details of the selected earthquakes were given in Table 4.13 and inserted as vertical lines in Fig. 4.27. Upon analysis, no post-cursory radon peak has been observed but only precursory peaks. The selected earthquakes were found to have a precursory time range of 0:39:02 min - 8 days. Details of the observed precursory time were as follows. Out of the 46 earthquakes, 23 of them (50%) occur within 1 day from the anomaly peaks. The other 50% distributes after the peaks as follows (i) 8 earthquakes within 2 days (ii) 3 earthquakes within 3 days; (iii) 5 earthquakes within 4 days; (iv) 2 earthquakes within 5 days; (v) 1 earthquake within 6 days and (vi) 2 earthquakes within 7 and 8 days from the peaks (Table 4.13). In general, most earthquakes occur close to the anomaly peaks with an average of 2.4±2.3 days after the peaks. In other words, it may be stated as 50% of the earthquakes occur within 2 days after the radon anomaly peaks; 39% of them between 3-5 days after the anomaly peaks and 11% of them after 5 days from the anomaly peaks.

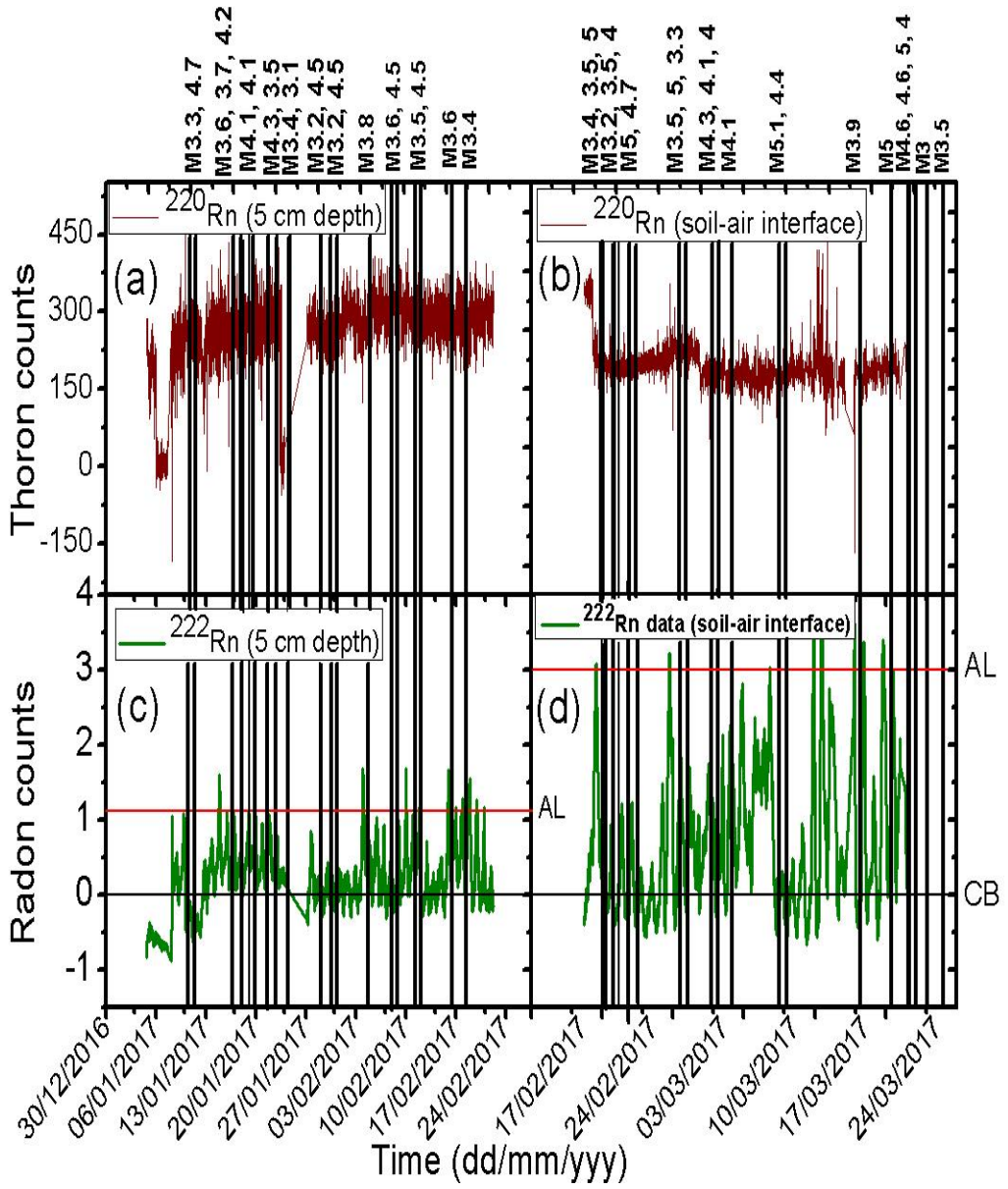

Fig. 4.27: Sampling time versus 15 minutes cycle (a) thoron data at 5 cm depth, (b) thoron data at the soil-air interface, (c) radon data at 5 cm depth and (d) radon data at soil-air interface, along with earthquakes data during the measurement period within 1000 Km radius from the monitoring station (represented by vertical lines).

Our concerns may be those earthquakes with M≥5 as they were considered fatal and destructive to mankind (Chowdhury *et al*., 2017). A total of six earthquakes with such magnitude were recorded during this three months period. They were recorded by USGS on 24/02/2017 17:32; 27/02/2017 09:07; 04/03/2017 07:41; 13/03/2017 19:49; 25/03/2017 07:35 and 26/03/2017 05:25. From Table 4.13 their precursory

times were estimated to be 1 day, 4 days, 1 day, 1 day, 3days and 1 day respectively. When compared to the estimated average precursory time (2.4±2.3 days) all of them fall within one standard deviation. Except for the earthquakes on 27/02/2017 09:07 and 25/03/2017 07:35 all of them were predicted within one day. At the same time, it must be noted that all earthquakes (including microscopic quakes) satisfying Dobrovolsky et al., (1979) and Fleischer (1981) criteria were selected irrespective of their magnitudes to improve accuracy of the prediction time. Hence the three months period study indicates that the region is seismically active and can be predicted by monitoring radon anomalies with high accuracy under controlled meteorological effects. For this particular period, all the recorded earthquakes including the fatal one (M≥5) were predicted within 2.4±2.3 days. In case of time series thoron data identification of significant anomalies peaks has been failed so far with available statistical techniques, particularly for this period. Hence correlation of thoron with seismic activity was neglected in the study. The observation supports and agrees well with the experimentally demonstrated analytical model of Sahoo and Gaware (2016) at the sub-soil. Their model suggested that due to relatively low radon concentration at the sub-soil, perturbation in its concentration due to external sources was more pronounced compared to that of the deep soil where it attains asymptotic value. The study affirmed the significance of monitoring sub-soil radon anomaly as premonitory gas to seismic activity within 1000 km radius from the monitoring site.

Table 4.13: Details of the selected earthquakes within 1000 km radius using Dobrovolsky *et al*., (1979) and Fleischer (1981) criteria represented by vertical lines in Fig. 4.27.

Dates of Radon Peak	**Dates of Earthquakes**	**Lat, Long**	**Depth (km)**	**Magnitude**	**Distance (km)**
10-01-2017 07:47:00	11-01-2017 18:51:14	28.3, 94.1	10	3.3	527
	12-01-2017 15:02:07	26.5, 95.4	75	4.7	413
15-01-2017 04:48:00	17-01-2017 20:52:16	27.6, 88.6	10	3.6	592
16-01-2017 08:03:23	18-01-2017 07:16:10	23.9, 93	27	3.7	39
17-01-2017 06:47:43	18-01-2017 08:33:17	24.5, 94.8	22	4.2	233

19-01-2017 08:47:23	19-01-2017 15:29:42	28.9, 88.2	10	4.1	729
	19-01-2017 20:48:36	28.1, 92.6	40.21	4.1	494
20-01-2017 07:31:41	21-01-2017 03:19:18	19.8, 94.7	71.98	4.3	487
22-01-2017 08:19:33	23-01-2017 15:03:05	30.8, 78.2	10	3.5	1629
	24-01-2017 17:55:38	25.6, 91.7	15	3.4	229
	24-01-2017 23:44:29	25.5, 94.6	50	3.1	277
	29-01-2017 14:39:04	24.8, 92.8	10	3.2	119
	29-01-2017 03:06:08	25.9, 96.4	41.14	4.5	457
	31-01-2017 10:58:42	26.4, 93.5	22	3.2	308
	31-01-2017 11:46:04	31.5, 94.1	32.7	4.5	885
04-02-2017 06:18:26	05-02-2017 18:24:59	27.9, 93.8	10	3.8	477
	08-02-2017 13:44:28	26.9, 92.9	15	3.6	353
	08-02-2017 02:16:16	22.5, 94.7	121	4.5	253
10-02-2017 10:04:12	11-02-2017 23:42:51	23.9, 91.8	10	3.5	90
12-02-2017 08:56:11	12-02-2017 09:35:30	25.6, 90.8	10	4.5	280
16-02-2017 08:11:00	16-02-2017 20:43:10	26.2, 92.8	20	3.6	274
	19-02-2017 00:23:42	26.6, 93	30	3.4	320
19-02-2017 04:19:45 23-02-2017 18:35:17	24-02-2017 01:46:07	23.7, 94.5	82	3.4	187
	24-02-2017 03:09:16	27.3, 88.1	150	3.5	606
	24-02-2017 17:32:49	24.1, 93.4	20	5.2	85
	25-02-2017 02:30:44	28.7, 96	36	3.2	644
	25-02-2017 05:30:44	28.7, 96	10	3.5	644
	25-02-2017 12:32:19	24.1, 92.1	33	4	70
	27-02-2017 09:07:47	27.3, 85.9	10	5	786
	27-02-2017 09:51:45	27.3, 85.9	10	4.7	786
03-03-2017 00:42:58	04-03-2017 05:08:13	24.3, 94.2	70	3.5	168
	04-03-2017 07:41:52	25.2, 94.6	70	5	255
	04-03-2017 12:20:44	25.5, 90.9	10	3.3	265
	06-03-2017 03:00:06	25.1, 95.1	89.95	4.3	294
	07-03-2017 15:29:16	26.8, 90.5	30	4.1	405
	07-03-2017 15:58:56	26.9, 89.1	10	4	503

	09-03-2017 08:25:15	25, 94.2	36	4.1	210
13-03-2017 00:14:45	13-03-2017 19:49:06	17.3, 95.9	10	5.1	785
	14-03-2017 22:09:56	27.2, 96.7	54.22	4.4	573
17-03-2017 05:24:42 18-03-2017 00:56:28 21-03-2017 07:03:31	21-03-2017 21:10:44	24.9, 92.1	37	3.9	142
22-03-2017 04:28:14 24-03-2017 02:35:17 25-03-2017 03:31:45	25-03-2017 07:35:55	25, 95.1	82	5	284
	26-03-2017 05:10:34	25.8, 99.9	33.07	4.6	769
	26-03-2017 05:25:06	25.9, 99.8	27.61	5	764
	27-03-2017 03:12:09	27.3 88.6	10	4.6	569
	27-03-2017 06:40:25	25.9, 100	10	4.1	779
	28-03-2017 15:48:49	26.5, 93.5	10	3	319

4.7.6 Correlation of continuous thoron data with geophysical phenomena using Empirical Mode Decomposition based Hilbert Huang Transform.

In the above and some previous sections, we continuously fail to identify the geophysical character in the time series thoron data. Hence correlation of thoron data with geophysical phenomena was neglected so far. In this period non-linear technique called empirical mode decomposition based (EMD) Hilbert-Huang Transform (HHT) was used. It is a two-step decomposition method capable of removing all periodic components from the raw data. Since thoron and its isotope are non-linear data influenced by periodic oscillation, especially meteorological factors, a traditional methods like standard deviation method, Fast Fourier Transform (FFT) and wavelet transform don't hold for it as they were suitable for data with uniform frequency. This is the reason why we fail to see geophysical properties of thoron in all our previous studies. It was the same problem faced by other researchers (Jaishi *et al*., 2013, 2014, 2014a, 2014b, 2015; Singh *et al*., 2014, 2016, 2017) who studies in the same region, where the removal of periodic influence from the radon isotope pair data was never accomplished. Since EMD-HHT was a non-linear method, it overcomes all the obstacles encountered in the previous study with high accuracy.

The present study also serves as the first of its kind for the region where continuous thoron data was analyzed using a non-linear method. The observation also reveals that the application of EMD-HHT for identifying anomalies in time series thoron data of the region has an optimistic outcome.

The time series thoron data was continuously generated with 15 *min* cycle between January, 2019 and December, 2019 at 1 m depth. Simultaneously the meteorological data (rainfall, temperature, pressure and humidity) were recorded by the monitor and retrieved from IMD-Regional Meteorological Centre, Guwahati, Assam (India). The recorded thoron data and meteorological data were shown in Fig. 4.28. The thoron concentration during the measurement period was found to be 2729±25 Bqm^{-3}.

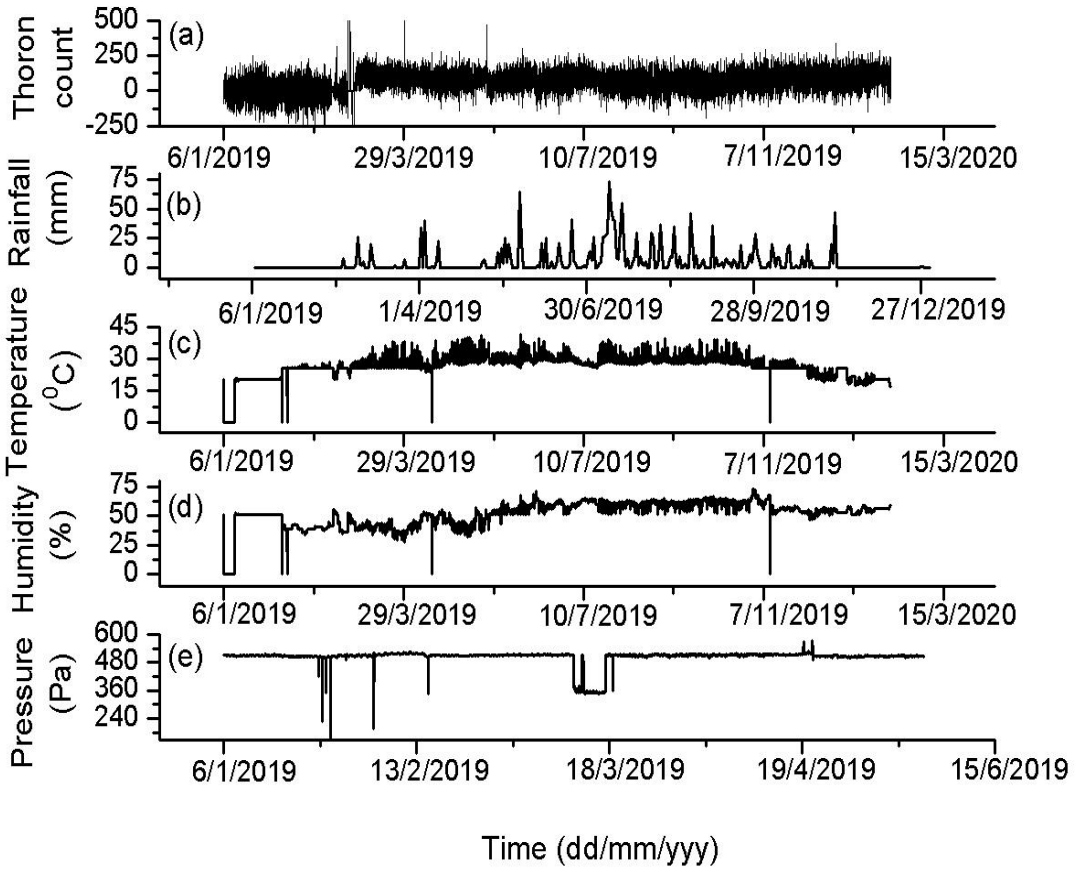

Fig. 4.28: Plot of time series (a) thoron (b) rainfall (c) temperature (d) humidity and (e) pressure data recorded at Mizoram University between January, 2019 and December, 2019.

The FFT periodogram of thoron and meteorological data were plotted to observe any oscillation mode in the thoron data possibly influence by meteorological parameters (Fig. 4.29 and Fig. 4.30). When compared the FFT periodogram of thoron data to that of the meteorological factors some common oscillation modes (7day, 4day and 2day) were observed. The common periodic oscillations were depicted in Fig. 4.29 and Fig. 4.30. Hence, it was obvious that the thoron activity was influenced by some of the meteorological factors.

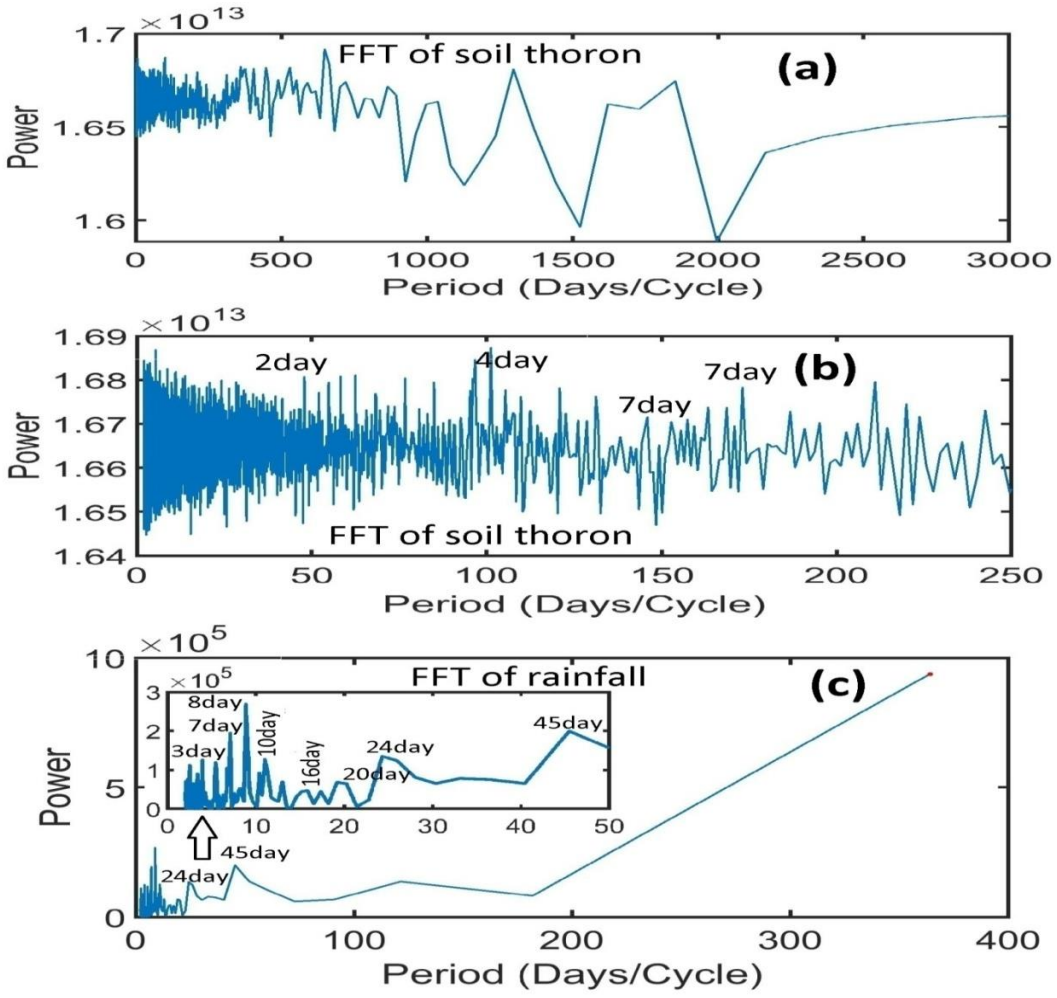

Fig. 4.29: FFT periodogram of (a) time series soil thoron data (b) enlarged section of thoron data having a period less than 250 days and (c) rainfall between January, 2019 and December, 2019.

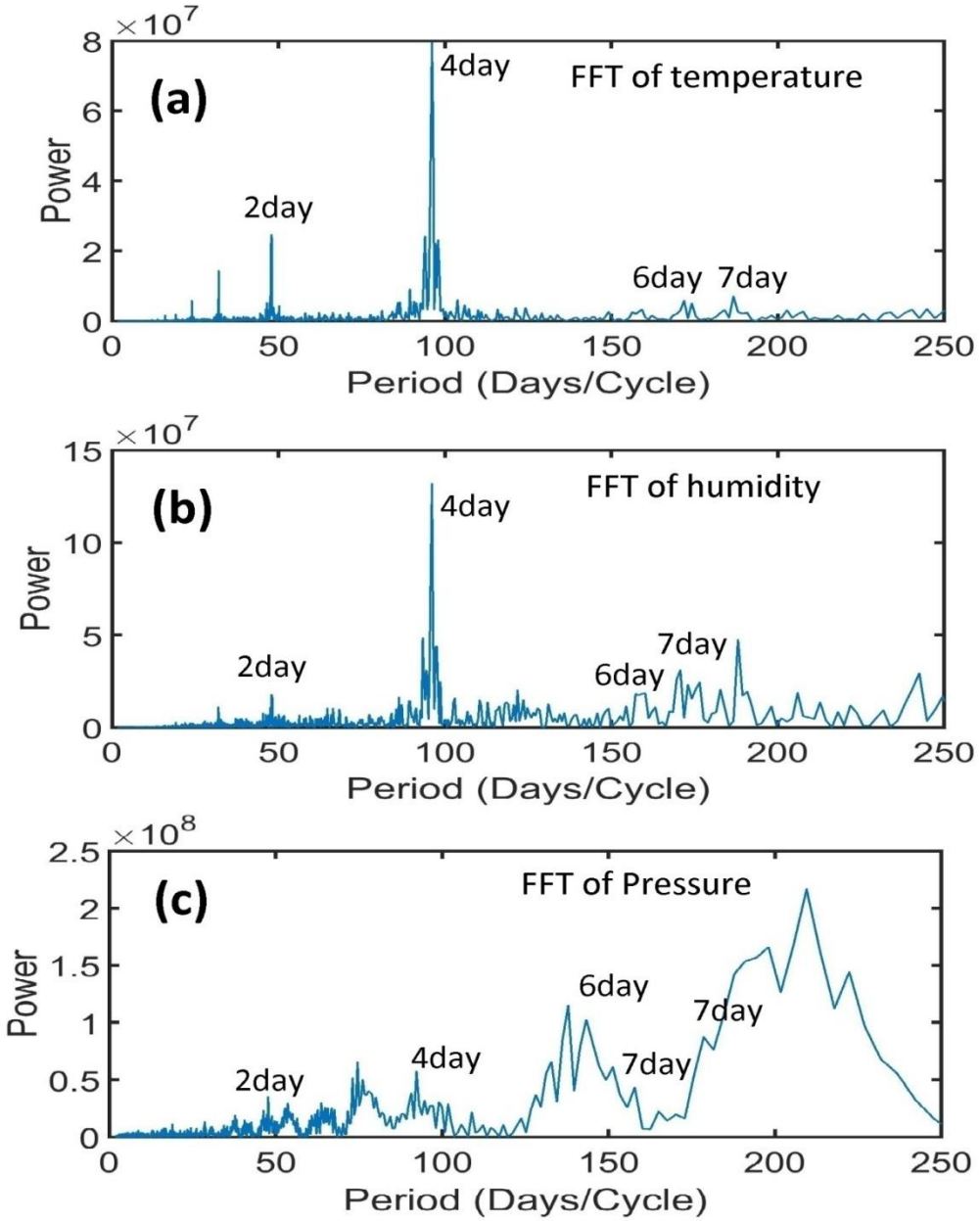

Fig. 4.30: FFT periodogram of (a) temperature (b) humidity and (c) pressure between January, 2019 and December, 2019.

To validify our observation an EMD was performed which breakdown the time series thoron data into different oscillatory modes with a unique frequency called

Intrinsic Mode Frequency (IMF) (Fig. 4.31 and Fig. 4.32). A total of 17 such IMFs were obtained from the raw thoron data as shown in Fig. 4.31 and Fig. 4.32.

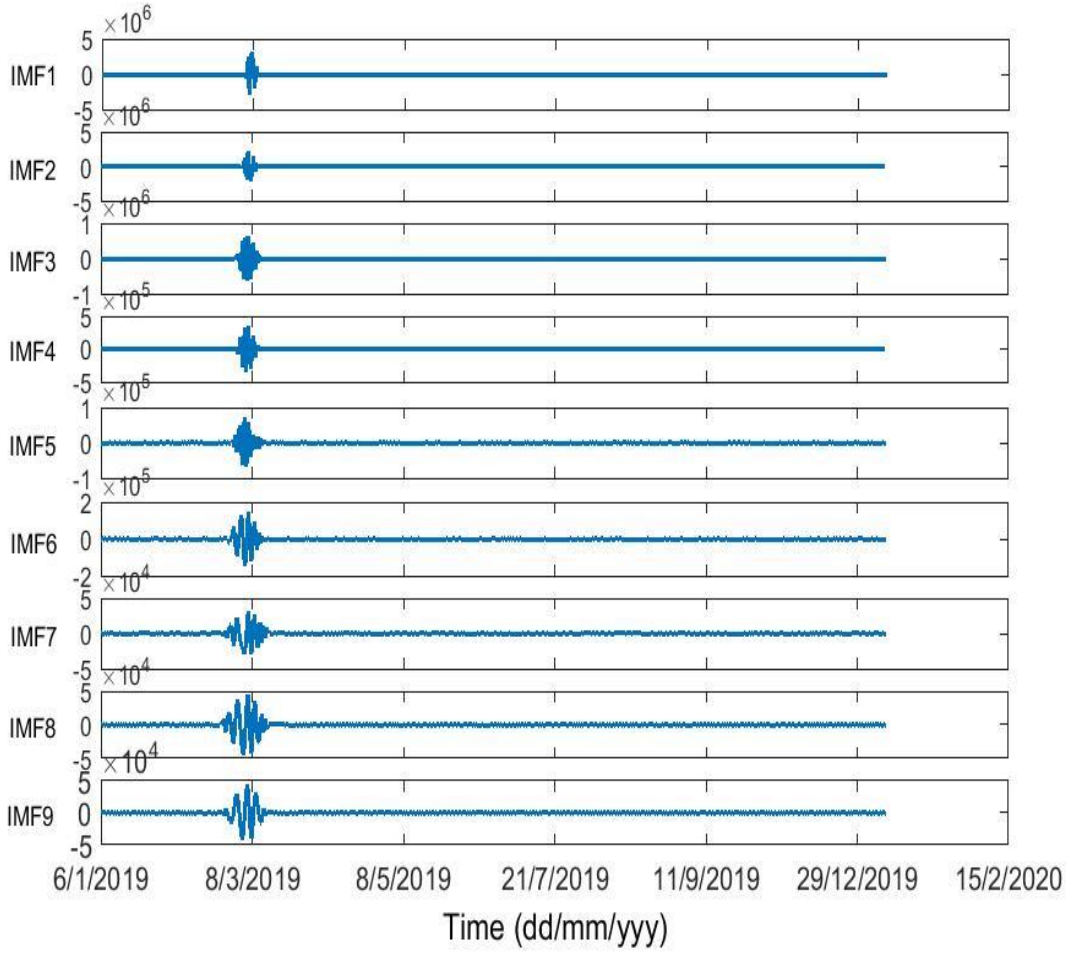

Fig. 4.31: Plot of the intrinsic mode functions (IMFs 1-9) obtained by executing empirical decomposition method (EMD) on the time series thoron data between January, 2019 and December, 2019.

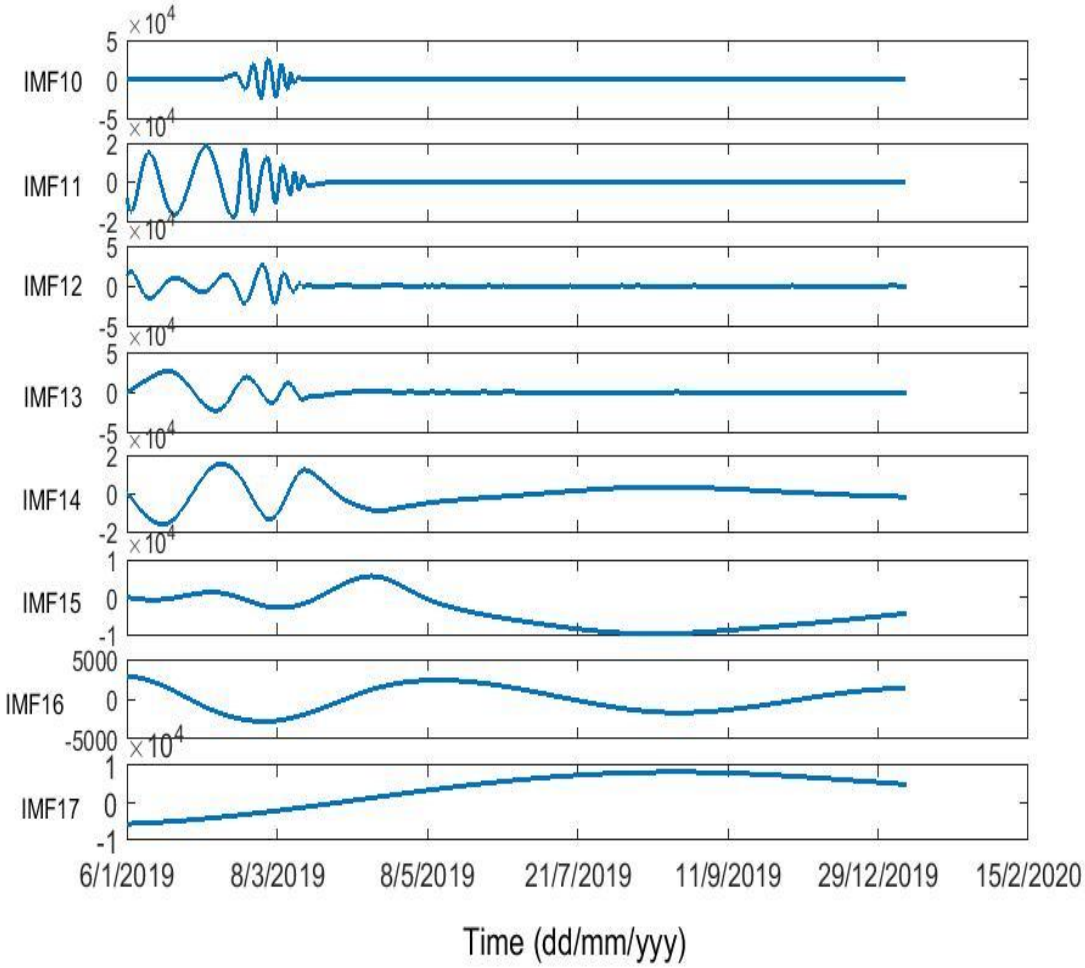

Fig. 4.32: Plot of the intrinsic mode functions (IMFs 10-17) obtained by executing empirical decomposition method (EMD) on the time series thoron data between January, 2019 and December, 2019.

To show the monofrequent nature of the IMFs, unwrapped phases of all the IMFs were performed as shown in Fig. 4.33. It also shows that lower-order IMFs carry higher unwrapped phases indicating higher frequencies and vice-versa.

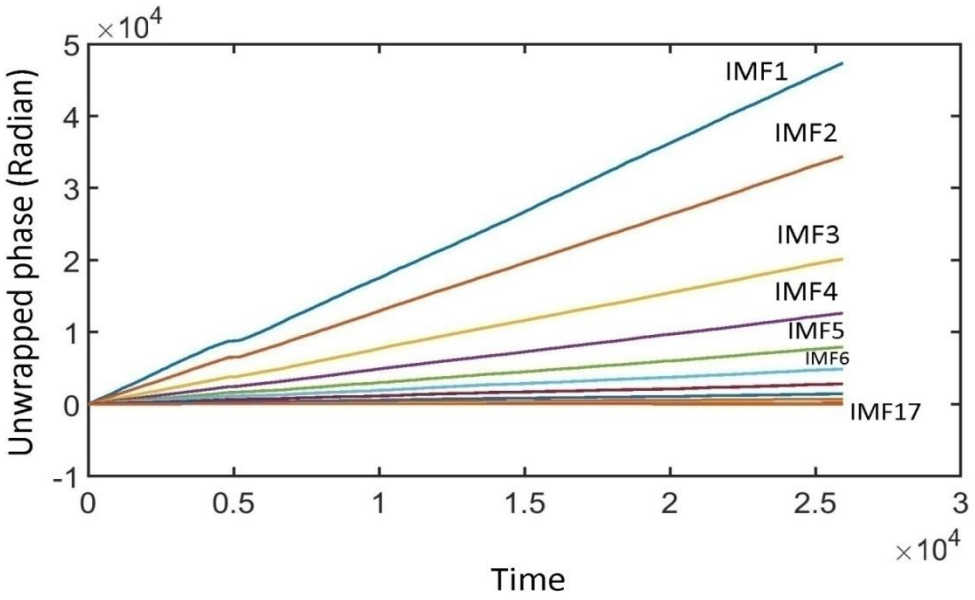

Fig. 4.33: Unwrapped phases of the obtained intrinsic mode functions (IMFs) showing that each IMF have unique frequencies (monofrequent).

For selecting the significant IMFs the following two criteria were adopted (Sahoo *et al*., 2020) (i) correlation coefficient of the IMFs with raw soil thoron was determined and (ii) comparing harmonic period of the IMFs and meteorological factors. For the first case, a Pearson correlation coefficient was obtained between each of the IMF and the raw thoron data (Table 4.14). According to *Jha et al*., (2006) and Wharton *et al*., (2013) if the correlation coefficient was greater than 10% (r=0.1) then the IMF was significant and may be considered for further analysis. Peng *et al*., (2005) also mention that the significant IMFs depict higher correlation coefficients with the raw data. From Table 4.14 it was observed that all the IMFs have correlation coefficients greater than 10% with the thoron data. Hence, no IMFs can be discarded based on the first criterion. To apply the second criterion harmonic periods of all the IMFs and meteorological factors were obtained using FFT. The calculated periodic oscillations were given in Table 4.14. When compared periods of thoron data and meteorological factors, it was observed that periods of the first six IMFs were also present in the periods of rainfall, temperature, pressure and humidity. It confirms that the first six IMFs were under the influence of periodic oscillation due to rainfall, temperature, pressure and humidity and hence they may be discarded for further analysis. Again,

the 10^{th}, 11^{th} and 12^{th} IMFs correspond to that of monthly oscillation due to tidal forces and hence they may also be excluded for further analysis. Beyond the 13^{th} IMFs may be regarded as trend of the time series thoron data as they evolve with a large period. They may also be stopped for further analysis. Finally, out of the 17 IMFs we are left with IMF7, IMF8 and IMF9 which are physically significant for analysis of thoron anomaly due to geophysical phenomena of the region.

Table 4.14: Correlation coefficient (with raw data) and harmonic periods of the intrinsic mode function (IMFs) of soil thoron data, rainfall, temperature, humidity and pressure.

IMFs No.	**Correlation coefficient with raw soil thoron data (r)**	**Harmonic Period (days) of**				
		IMFs of soil thoron data	Rainfall (mm)	Temperature (^{0}C)	Humidity (%)	Pressure (Pa)
1	0.12	7	7	7	7	7
2	0.15	7	8	7	7	7
3	0.11	7	10	7	6	6
4	0.14	6	16	6	6	8
5	0.13	6	20	6	8	
6	0.2	11	24	8	21	
7	0.23	18	45	10		
8	0.2	12		10		
9	0.25	14				
10	0.3	21				
11	0.34	77				
12	0.25	60				
13	0.31	135				
14	0.31	154				
15	0.37	1081				
16	0.36	541				
17	0.33	1081				

Now the Hilbert-Huang Transform was applied to the above three significant IMFs to obtain the Hilbert-Huang spectrum. It is a sparse matrix containing meaningful modes in the time-frequency domain. The Hilbert-Huang spectrum of the significant IMFs was shown in Fig. 4.34. From this spectrum, three important statistical characteristics of the time series thoron data were extracted viz. the marginal spectrum, degree of non-stationary and Instantaneous Energy (IE).

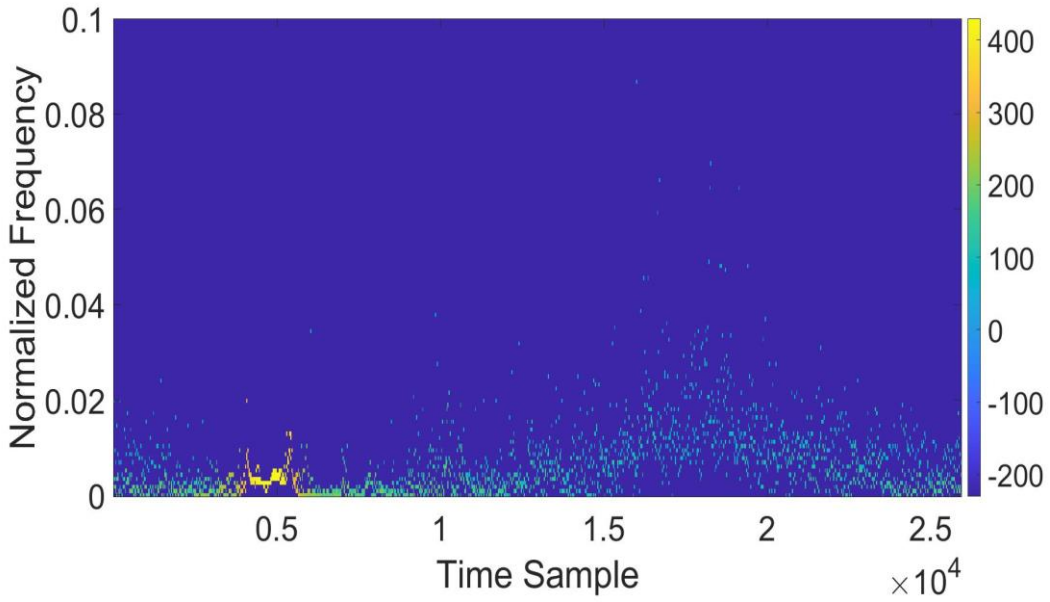

Fig. 4.34: Hilbert-Huang spectrum of the significant IMFs in a time-frequency domain.

The marginal spectrum represents the actual spectrum value which basically was a measure of the total amplitude (energy) of each frequency value. As it was obtained by empirical mode, it can detect the instantaneous change in frequency with time which was not possible in traditional analyses like fourier and wavelet transform. Fig. 4.35a shows the marginal spectrum of the thoron time series data. It was obvious from the graph that the high-frequency region possesses higher fluctuation and the low-frequency region was stable. Most importantly it shows that the thoron data was non-linear data otherwise the plot should have been parallel to the X-axis. The degree of non-stationary (DNS) on the other hand, depicts the amount by which HH-spectrum deviates from the mean marginal spectrum (Fig. 4.35b). From Fig. 4.35b it

was obvious that the high-frequency region exhibited higher order of non-stationarity compared to the low-frequency region. Above all the marginal spectrum and DNS shows the time series thoron data was a non-linear and non-stationary data where traditional analysis like FFT and wavelet transform would have failed to extract lots of its crucial information.

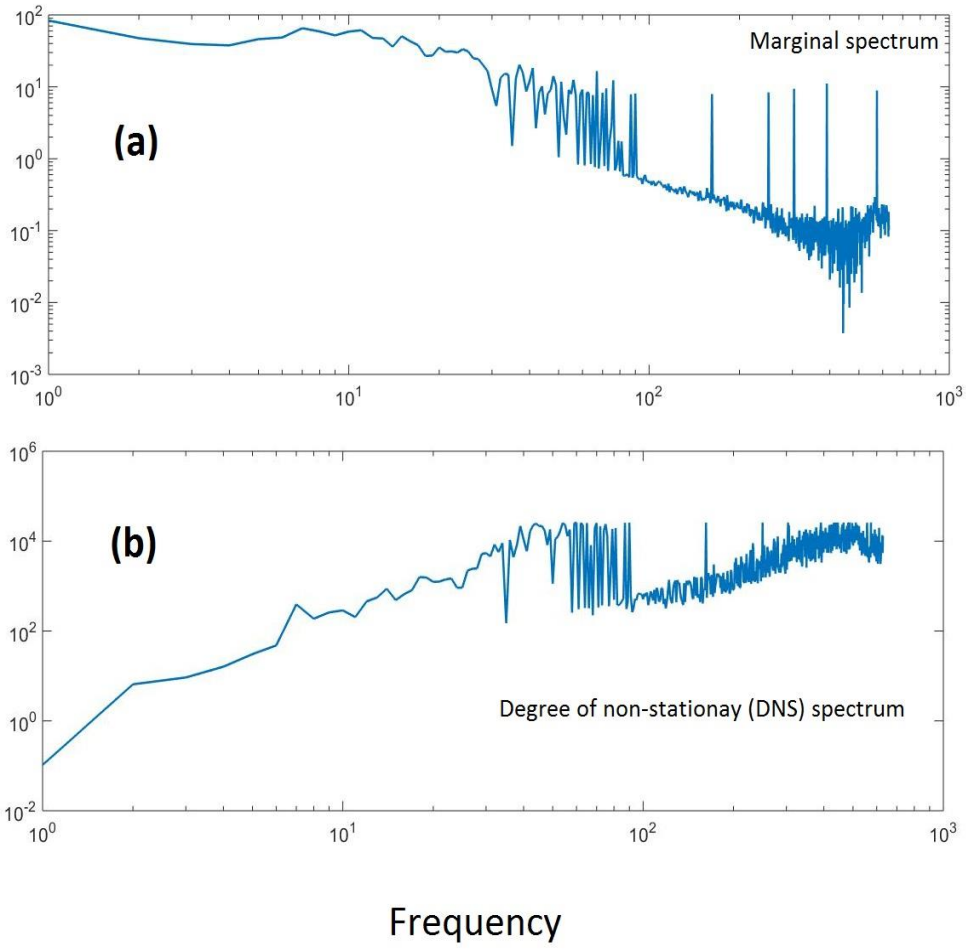

Fig. 4.35: Plot of (a) mean marginal spectrum and (b) degree of non-stationary spectrum obtained from the Hilbert-Huang spectrum.

Finally, instantaneous energy (IE) was the amplified form of the amplitude of the significant IMFs obtained from the HH-spectrum. In the IE plot (Fig. 4.36), instead of temporal variation of the raw data where identification of anomaly was complicated due to embedded noise, we are looking at the temporal variation of energy. The IE plot easily reveals the active and quiescent period of the raw data and

helps in identifying short-term seismic precursors. The IE from the entire radon data was calculated and correlated with earthquake data obtained from United State Geological Survey (USGS) archive. The earthquake data were selected in such a way that they may be in a predictable range from the monitoring station. Since thoron has such a small half-life (55.6 s) we don't expect to predict seismic activity which happens at a large epicentral distance from the monitoring station. Hence seismic activities having minimum epicentral distance around the monitoring station were selected for correlation. Seven such earthquakes with epicentral distances ranging from 113 km to 140 km from the monitoring station were selected (Table 4.15) and no earthquake occurs at an epicentral distance of less than 100 km. In addition, the prediction time range was taken as 15 days from the anomalies. To identify energy anomaly (thoron anomaly) from the IE plot the mean plus 'n' times standard deviation (SD) method was adopted.

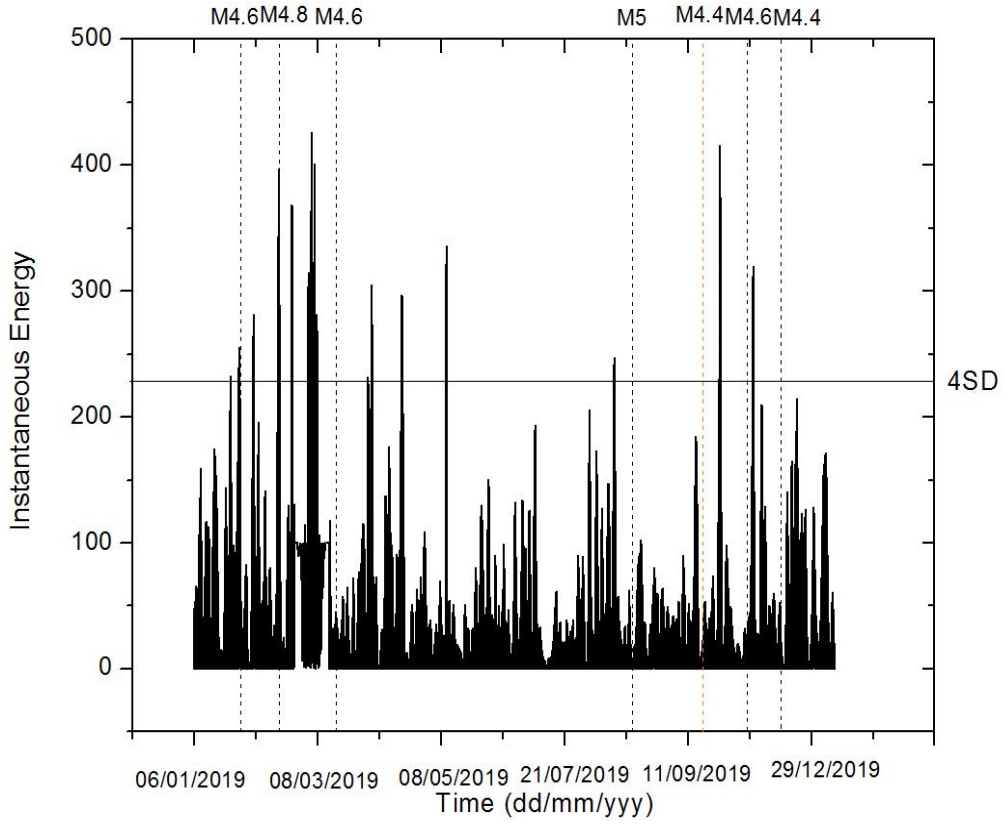

Fig. 4.36: Plot of the instantaneous energy (IE) showing thoron anomalies at 4SD and predicted earthquakes (represented by black dot lines) with epicentral distance less than 150 km from the monitoring station.

No standard value has been assigned for the factor 'n' in identifying radon anomalies but was chosen as per the convenience of the authors based on its own data as discussed elsewhere. In the present study, the thoron anomalies were observed at 4SD above the mean in the IE plot (Fig. 4.36). The anomaly level (4SD) was chosen in such a way to avoid spurious spikes but only significant anomalies due to earthquakes. It was represented by a horizontal line parallel to the X-axis in Fig. 4.36. Based on the above mention criterion 12 thoron anomalies peaks were observed from the IE plot which lies above the 4SD line as shown in Fig. 4.36. The thoron anomalies were observed on January 21, 2019; January 25, 2019; February 06, 2019; February 17, 2019; February 23, 2019; March 03, 2019; March 29, 2019; April 13, 2019; May 13, 2019; August 11, 2019; November 20, 2019 and December 05, 2019 (Table 4.15). The observed anomalies on January 21, 2019; January 25, 2019; February 06, 2019; February 17, 2019; March 29, 2019; April 13, 2019; August 11, 2019; November 20, 2019 and December 05, 2019 were succeeded by the earthquakes given in Table 4.15 except for the one on September 22, 2019 (Fig. 4.36). The earthquake of September 22, 2019 may be neglected for the present study as thoron data was absent for 20 days prior to its occurrence due to technical failure. Since it was recorded after 15 days from the last recorded data before the monitor resumed generating thoron data normally. Hence, including it for correlation will be against our criteria that the prediction time was taken as 15 days from the peak. On the other hand, thoron energy peaks of February 23, 2019; March 03, 2019 and May 13, 2019 may be regarded as false anomalies as they were not succeeded by an earthquake. Hence in total, we observed 9 positives and 3 false thoron anomalies peaks with all the earthquakes predicted (Fig. 4.36). The prediction time range for the predicted earthquakes was 9 hours-15 days with an average of 7±5 days (Table 4.15). The magnitude of the selected earthquakes ranges from 4.4-5M (Table 4.15). It signifies that the predicted earthquakes were mostly moderate ones. The spatial distribution of the selected earthquakes around the monitoring station reveals that the

thoron data specifically respond to seismic activity along the Indo-Burman Subduction line (Fig. 4.37). Hence the study concluded that by fixing the prediction time and prediction range at 15 days and 150 km from the monitoring station, respectively thoron data was able to predict all the earthquakes. And it may also be stated that its activity significantly responds even moderate seismic activity with high accuracy. Barman *et al*., (2016) mentioned that besides the prominent intermittent, one could still observe intermittencies due to sporadic nor'wester showers and increase in temperature. While Chowdhury *et al*., (2017) mentioned that smaller peaks were fluctuation due to time series evolution and should be neglected. This could also be the case for the observed three false anomaly peaks which the authors are uncertain about and unable to explain at present. When compared to their observation the present study also agrees well with them. In general, it was observed that the thoron anomaly significantly predicts nearby earthquakes despite the presence of spurious spikes.

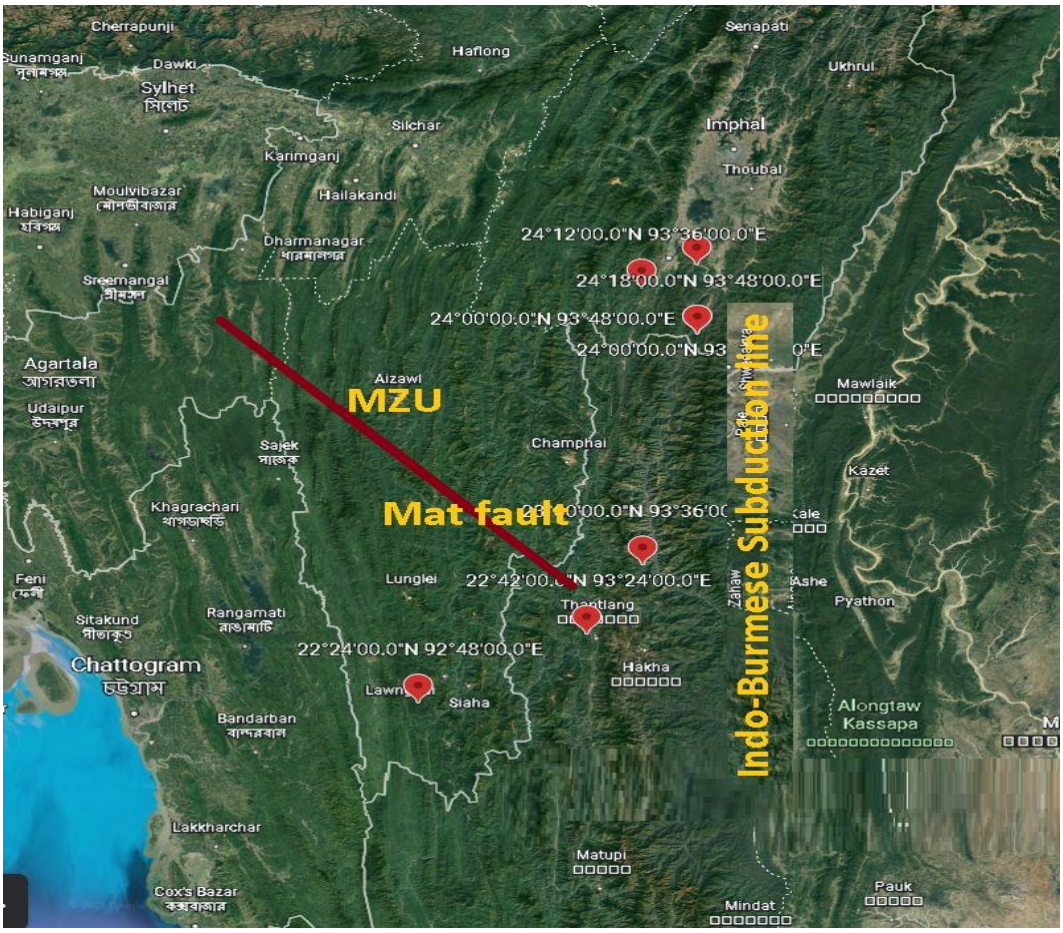

Fig. 4.37: Spatial distribution of the seven selected earthquakes (4.4M-5M) predicted by thoron data at MZU distributing along the Indo-Burmese subduction line.

Table 4.15: Details of the selected earthquakes and their precursory time.

Sl. No.	Date of Earthquake	Lat (N) Long (E)	Depth (km)	Magnitude (M)	Epicentral Distance (km)	Date and time of Precursor	Precursory Time (days)
1	26-01-2019 04:07	24.3N 93.8E	55.87	4.6	140	21-01-2019 20:32; 25-01-2019 14:47	4, 1
2	17-02-2019 13:58	22.4N 92.8E	10	4.8	148	06-02-2019 08:38; 17-02-2019 05:08	11, 9hrs
3	15-04-2019 12:39	22.7N 93.4E	56.21	4.6	134	29-03-2019 22:56; 13-04-2019 15:39	15, 2
4	18-08-2019 17:28	24.0N 93.8E	63.38	5	125	11-08-2019 06:07	7
5	22-09-2019 13:31	24.2N 93.6E	63.66	4.4	113	Unpredicted	
6	02-12-2019 12:12	23.0N 93.6E	53.48	4.6	125	20-11-2019 20:09	12
7	16-12-2019 14:10	24.0N 93.8E	55.37	4.4	129	05-12-2019 10:24	11

4.7.7 Identification of geophysical phenomena by developing a correlation between radon mass exhalation rate and *in-situ* radon data of different depths at Mat fault

To develop a correlation between the radon mass exhalation rate (radon production rate) and *in-situ* radon data of different sampling depths the radon data and soil sample were measured and collected at Mat fault once a month during May, 2018-October, 2018. The radon and thoron data of different sampling depths (soil-air interface, 5 cm, 50 cm and 1 m) and the mas exhalation rate of the collected soil

sample were assessed by the procedure mentioned in section 3.3 of the previous section. The isotope pair data and soil sample were measured and collected at Mat fault on the following dates: May 30, 2018; June 27, 2018; July 26, 2018; August 28, 2018; September 25, 2018 and October 9, 2018. Now to categorise the generated data at Mat fault into the anomaly and non-anomaly period data, the radon data at MZU of the same period was deployed as mentioned elsewhere. That is if the radon data of different sampling depths and soil samples were measured and collected by the time the radon data at MZU lies above the anomaly line they were considered anomaly period data. However, if they were generated by the time the MZU data stay below the anomaly line they were categorized as non-anomaly period data. The radon data at MZU between May, 2018 and October, 2018 categorizing the radon data at Mat fault was shown in Fig. 4.38. The dates of measurement at Mat fault were represented by vertical solid lines while the anomaly and non-anomaly periods were by intervals of the vertical dash and dot line, respectively. At the same time, the anomaly line or the radon peak period factor (RPF) was shown by the horizontal black line passing through 1 which was obtained by taking the average of all noted ^{222}Rn counts' value by the time the anomalous peaks crosses the diurnal peaks on both sides of the anomalous peak. Now based on the above criterion radon data generated (*in-situ* measured and mass exhalation rate of the collected soil sample) at Mat fault on June 27, 2018; July 26, 2018; September 25, 2018 and October 9, 2018 were categorised as anomaly period data. But those of May 30, 2018 and August 28, 2018 were categorized as non-anomaly period data (Fig. 4.38). After assessing the radon mass exhalation rate from the collected soil sample, its linear correlation with its data of the four different sampling depths during geophysical and non-geophysical phenomena was analysed. The detailed correlation analyses were shown in Fig. 4.39 and Table 4.16.

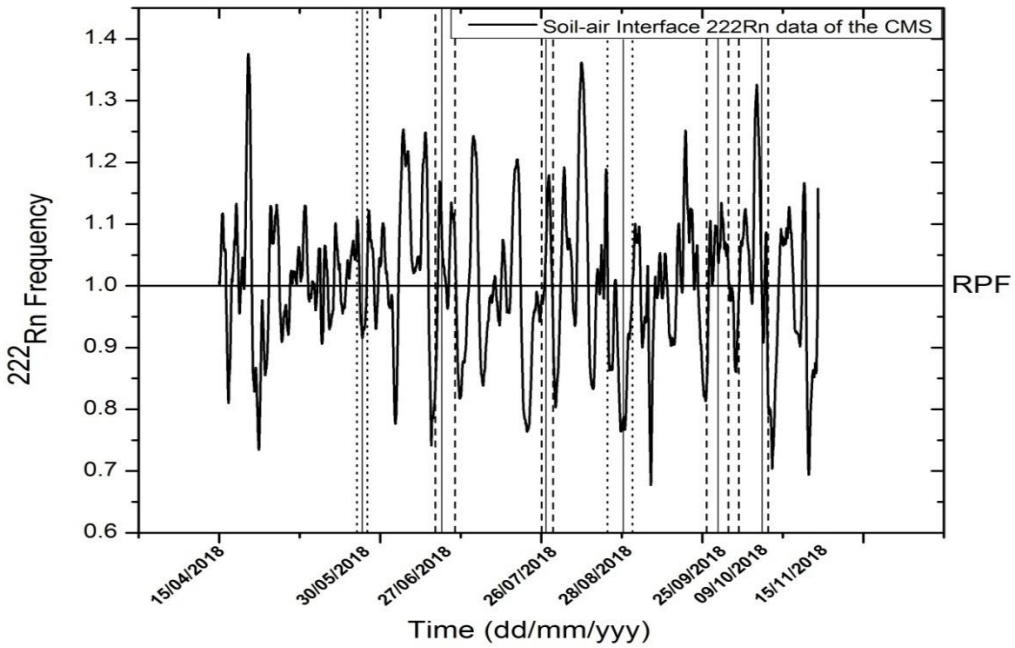

Fig. 4.38: Plot of ^{222}Rn counts versus time of the CMS between April 15, 2018 and November 15, 2018; showing dates of measurement at Mat fault by a solid vertical line and anomaly period and non-anomaly period by intervals of vertical dash and dot line, respectively.

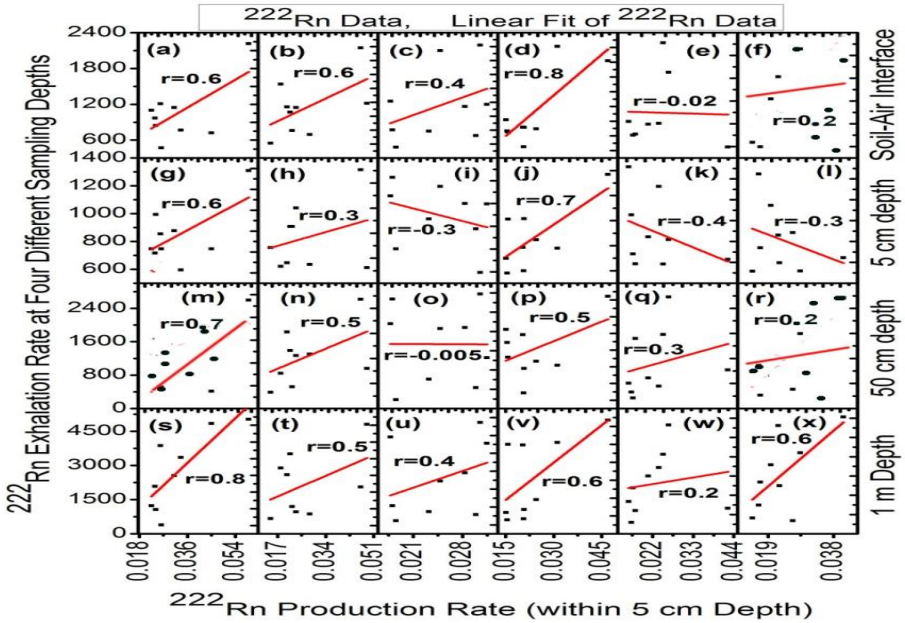

Fig. 4.39: Linear correlation plot of ^{222}Rn mass exhalation rate (assessed within 5 cm depth from the ground surface) versus its exhalation rate at (a-f) Soil-Air Interface; (g-l) 5 cm; (m-r) 50 cm and (s-x) 1 m sampling depth of May 30, 2018; June 27, 2018; July 26, 2018; August 28, 2018; September 25, 2018 and October 9, 2018, respectively.

When correlates the ^{222}Rn production rate with its flux of the soil-air interface, a correlation coefficient of 0.6, 0.6, 0.4, 0.8, -0.02 and 0.8 were observed, respectively on May 30, 2018; June 27, 2018; July 26, 2018; August 28, 2018; September 25, 2018 and October 9, 2018 (Table 4.16; Fig. 4.39(a-f)). As expected, the correlation coefficient was strong during the non-anomalous period (0.6 and 0.8 on May 30, 2018 and August 28, 2018, respectively, Table 4.16). The observation reveals that the sub-soil radon production rate and its soil-air interface flux were in proportion during the non-anomalous period. In other words, during the absence of perturbation due to geophysical phenomena the radon production rate of all the 9 sampling spots were proportional to their flux, indicating that sampling spots having high radon production rate has high radon flux at the surface and vice-versa.

Table 4.16: Details of correlation between ^{222}Rn production rate and exhalation rate of four different sampling depths and classification date of measurement into the anomaly and non-anomaly period.

Date of Measurement	**Classification Based on the CMS data**	**Correlation Coefficient between ^{222}Rn production and Exhalation rate**			
		Soil-Air Interface	5 cm	50 cm	1 m
30/05/2018	Non-Anomalous Period	0.6	0.6	0.7	0.8
27/06/2018	Anomalous Period	0.6	0.3	0.5	0.5
26/07/2018	Anomalous Period	0.4	-0.3	-0.005	0.4
28/08/2018	Non-Anomalous Period	0.8	0.7	0.5	0.6
25/09/2018	Anomalous Period	-0.02	-0.4	0.3	0.2
09/10/2018	Anomalous Period	0.2	-0.3	0.2	0.6

But during the anomalous period, both a weak and strong correlation (0.6, 0.4, -0.02 and 0.2 on June 27, 2018; July 26, 2018; September 25, 2018 and October 9, 2018 respectively) were observed between the two rates at the surface (Table 4.16). The observation indicates uncertainties or insignificant relationships between ^{222}Rn production rate and its flux during the anomalous period. This can be explained in such a way that during geophysical phenomena there is a perturbation in radon concentration due to release of trap radon gas in the pore space or abrupt upward movement of the gas, which is more pronounced and easily detected at the surface (Sahoo and Gaware, 2016). Hence radon concentration and flux of several sampling spots were perturbed and leads to an uncertain correlation with its production rate during geophysical phenomena.

Again when correlates the ^{222}Rn exhalation rate at 5 cm depth and its production rate, a clear distinct correlation during the anomalous and non-anomalous period was observed (Table 4.16, Fig. 4.39(g-l)). That is a weak and strong correlation coefficient during the anomalous period and non-anomalous period, respectively in all the measuring occasions. As mentioned above in the absence of geophysical phenomena the radon production rate of each sampling spot was proportional to its exhalation rate.

But unlike the above sampling depth, there is a sharp deviation during the anomaly period that is a weak correlation coefficient for the whole measuring period. It is evident that during the anomaly period there is no significant relationship between the radon production rate and its exhalation rate from all the 9 measuring spots. Hence examining the correlation between the radon production rate, from a soil sample collected within 5 cm depth and radon exhalation rate monitored at the soil-air interface, seems to be a suitable approach for forecasting impending geophysical phenomena especially seismic activity.

The result obtained at 50 cm and 1 m sampling depths were similar to those obtained from the soil-air interface (Table 4.16, Fig. 4.39(m-r), Fig. 4.39(s-x)). We have a strong correlation coefficient during a non-anomaly period in both the sampling but a mixture of strong and weak during the anomaly period. But when observed the

average correlation coefficient, the correlation coefficient during the non-anomaly period was strong and always higher than that of the anomaly period (Table 4.17). For example, the average correlation coefficient during the non-anomaly period at 50 cm and 1 m depths were 0.6 and 0.7 respectively while it was 0.3 and 0.4 respectively during the anomaly period (Table 4.17).

Table 4.17: Average correlation coefficient of ^{222}Rn production and exhalation rate during anomaly and non-anomaly period (May, 2018-October, 2018).

Periods	**Sampling Depth**			
	Soil-Air Interface	5 cm	50 cm	1 m
Anomaly Period	0.3	0.33	0.3	0.4
Non-Anomaly Period	0.7	0.65	0.6	0.7

From the above observation, it could be generalised that, the equilibrium state of ^{222}Rn concentrations was well depicted by a strong correlation coefficient between its exhalation rate of the four sampling depths and production rate at the sub-soil. The strong correlation coefficients indicate that the ^{222}Rn production rate and exhalation rate were strongly proportional, which might only be achieved in the absence of any geophysical phenomena or external disturbances. The presence of geophysical phenomena, on the other hand, was depicted by a weak and uncertain correlation between the ^{222}Rn production and exhalation rate at 5 cm depth and the other three depths, respectively. Indicating that, the strong proportionality between the two rates in the absence of geophysical phenomena was altered during geophysical phenomena. Hence it is obvious that monitoring of radon data with suitable statistical analysis techniques may predict geophysical phenomena of the region with high accuracy.

5

Summary and conclusion

The study was performed in an attempt to find a causal relationship between radon and thoron data of Mat fault and geophysical phenomena of the region. According to the seismic hazard zonation map of India (BIS, 2002) the region lies at seismic zone V (highest seismic level) and is one of the six most seismically active regions of the world. Mat fault is one of the most prominent and active faults in Mizoram and obliquely cuts across the state. *In-situ* online radon and thoron data were generated at Mat fault between November, 2017 and October, 2018 at four different soil depths (soil-air interface, 5 cm, 50 cm and 1m depths) and in water. The measurement was carried out through different time periods window. At the same time, 15 min cycle continuous radon and thoron data was monitored online at the Department of Physics, Mizoram University, Aizawl, Mizoram (India) from 2017 till date. It was the first of its kind where radon isotope pair data was acquired online with such high frequency and real-time in the region. Its real-time nature makes it superior to existing data generated by Jaishi *et al*., (2013, 2014, 2014a, 2014b, 2015) and Sing *et al*., (2014, 2016, 2017) whose data were passive in nature with a frequency of 15 days and 7 days respectively. An indigenously developed and calibrated ZnS(Ag) based alpha scintillation counted named SMARTRnDuo has been used for assessing the radon isotope pair data at Mat fault and Mizoram University. The standard deviation method and Empirical Mode Decomposition based Hilbert-Huang Transform (EMD-HHT) were deployed to identify anomalies in the time series radon and thoron data for correlating with geophysical phenomena of the region. In an attempt to have better results and comparison, the study has been extended to Chite fault located at the heart of the state capital from February, 2018-July, 2018. The isotope pair profile and an estimated value of their parent nuclei (Uranium and thorium) were also presented in detail.

At Mat fault, the radon and thoron concentrations were found to be 4878.8±459 Bqm^{-3} and 8483.2±592 Bqm^{-3} respectively with a ratio of 1.74. At Mizoram

University and Chite fault, the thoron and radon ratios were also observed to be 1.2 and 1.74 respectively. In all the three locations thoron concentration was found to be higher than radon. And this observation from the three locations was assumed for the region meaning that the region has a higher thoron concentration than its isotope. The isotope pair concentration falls within the global average (10^3-10^5 Bqm^{-3} in soil) given by IAEA (2013). The isotope pair depth profile also shows that radon data changes with a rate of 3.7 $Counts m^{-1} cm^{-1}$ with depths while thoron changes by 0.9 $Counts m^{-1} cm^{-1}$. The observation indicates that the isotope pair data were minimum at the surface and then increases with depth. Sahoo *et al*., (2016) suggested that this minimum region of sampling depth is an ideal depth for monitoring radon fluctuation due to geophysical phenomena as radon fluctuation is prominent and easy to identify. They also mentioned that at deeper sampling depths (~1 m and beyond) radon concentration attains asymptotic value and perturbation in its concentration is hard to identify especially when the geophysical activity is of small magnitude. Since the radon concentration at the surface is low its changes due to geophysical nudges are significant and identifiable even when the magnitude is small.

The radon and thoron fluxes at Mat fault were found to be 0.015 $Bqm^{-2}s^{-1}$ and 2.7 $Bqm^{-2}s^{-1}$, respectively while the radon mass exhalation rate was 0.030 $Bqkg^{-1}h^{-1}$. The estimated uranium and thorium content were also found to be 16.9 $Bqkg^{-1}$ and 49.7 $Bqkg^{-1}$ respectively. At Chite fault the radon and thoron fluxes were found to be 0.02 $Bqm^{-2}s^{-1}$ and 2.4 $Bqm^{-2}s^{-1}$, respectively. Also, the uranium and thorium content of Chite fault were estimated to be 32.9 $Bqkg^{-1}$ and 44.9 $Bqkg^{-1}$ respectively. When compared to global averages given by some organizations such as IAEA (2004, 2013) and UNSCEAR (1982, 2000), the radon flux and uranium content of the region was found to be within the global average. However the thoron flux and thorium content of the region estimated from the two faults surpass the global average. According to the critical value set by IAEA (2004) no radiological risk was found for the region. The higher thorium content reflects the abundant thorium concentrations in India in comparison to uranium and the importance of its 3 stages nuclear power program (https://byjus.com/free-ias-prep/indias-three-stage-nuclear-power-program/).

The comparison studies in water and soil show that the radon and thoron data in water were found to be 7557.0 and 12091.2 Bqm^{-3}, respectively. Also, the uranium and thorium content in water were estimated to be 41.6 and 124.8 $Bqkg^{-1}$, respectively. When compared to that of data acquired from soil, the isotope pair data and their parent nuclei content in water were much higher than that of soil. But when compared between the isotope pair in particular the thoron and thorium concentration was always higher than radon and uranium concentration in both the soil and water media. The radon concentration in water and soil has a ratio of 1.3 while thoron has 1.0 respectively. The uranium content in water and soil also has a ratio of 2.4 while thorium has 5.5 in the two sampling media. Finally, when compared to the global averages (IAEA, 2004, 2013; UNSCEAR, 1982, 2000) the isotope pair concentration falls within the given limit but as for their parent nuclei content, they surpass the global averages given by UNSCEAR, (2000). Also according to IAEA (2004), no radiological risk was found from the water as well.

Diurnally the radon concentration varies with temperature and was maximum in the morning (~7:47±1:40 AM) when the monitoring station received maximum sunlight and minimum in the evening (~6:20±1:39 PM) after sunset. The monitoring station received maximum sunlight in the morning because at other times it was shadowed or blocked by the Physics Department building and nearby trees. The thoron concentration remains constant with a certain limit with an average of 3648 Bqm^{-3} and its diurnal variation was not understood. The seasonal variation studies show that radon data of the region (Mat fault and Chite fault) was maximum during summer and minimum during spring. In contrast, analysis of thoron data from different sampling depths fails to converge to one season. Such that maximum thoron data was observed during spring, summer and winter and its minimum was found during summer and spring as well. Hence for this study, we are uncertain about the seasonal variation of thoron also. The maximum radon data in summer may be due to the expected precipitation and high temperature which were favourable for radon emission. Increase in the moisture content of the soil below optimum level (15-17% by weight) due to precipitation (Stranden *et al.*, 1984) was a favour for ^{222}Rn exhalation. Gases in the upper surface get expanded during raise in temperature

thereby increasing radon exhalation (Ramola *et al*., 1990; Segovia *et al*., 1987; Virk *et al*., 2000; Walia *et al*., 2005). The minimum radon concentration during spring when the temperature was expected to be highest may be due to masking effect on temperature by other parameters (Asher-Bolinder *et al*., 1991). Although no significant seasonal variation was observed for thoron one certain thing was that its seasonal variation was distinct from that of radon.

At Mat fault, the correlation analysis shows that air temperature has no significant influence on radon data but on thoron data. Barometric pressure and relative humidity were found to raise radon concentrations while they show a reverse effect on its isotope. Rainfall moderately tends to suppress radon concentration and as well thoron concentration at the surface. Wind speed strongly tries to suppress radon concentration but shows the opposite on thoron concentration. To validify this observation an inter-linear cross-analysis was performed among the meteorological parameters. The inter-correlation analysis shows that wind speed and humidity were masked by rainfall and temperature by pressure. In case of radon, during rainfall temperature was masked by the accompanying wind and then by pressure as soon as the rain ceased. But in case of thoron influence of pressure on its data was found to be masked by temperature. Hence at Mat fault temperature, pressure and rainfall were found to be the significant factors influencing radon and thoron concentrations while all others factors get masked. Rainfall and temperature tend to raise radon and thoron concentration respectively while pressure and rainfall tend to suppress them respectively. Similar to that of their seasonal variation the isotope pair data seems to respond each meteorological factor distinctly.

At Mizoram University studies of meteorological influences on the isotope pair was performed through different window period at the soil-air interface starting from dry season toward the wet season. The inter-correlation analysis shows the exact same masking effect as that of Mat fault that is wind speed and humidity were masked by rainfall and air temperature by pressure. The three window periods observation reveals that the meteorological influence on radon data slightly changes from insignificant to moderate during the rainy season. It indicates that during turbulence season radon exhalation does get affected by external factors. But the weak

correlation coefficient evinced that the isotope pair data at MZU was mildly or negligibly affected by meteorological factors. The weak correlation was attributed to the provided shading obstructing the meteorological factors inside the monitoring station. Radon and thoron data monitored under such conditions may only be perturbed by geophysical phenomena as other factors especially meteorological factors have been ruled out. Attaining such conditions was our main objective as our main focus was identifying the nature of the isotope pair data during geophysical phenomena.

The extended analysis at Chite fault also shows that rainfall tends to raise radon and thoron concentration while pressure tries to suppress the isotope pair data. In general, analysis from the three locations reveals that air temperature, pressure and precipitation were the three main factors affecting the isotope pair data. At Mat fault and Chite fault the radon data tended to enhance by rainfall while pressure tries to suppress it. In case of thoron data, it was found to enhance by temperature at Mat fault but by rainfall at Chite fault. At the same time, its exhalation was found to be suppressed by rainfall at Mat fault but by pressure at Chite fault. As mentioned above their diurnal and seasonal behaviour was distinct such that their response to each meteorological factor was also distinct. But the meteorological influence on the isotope pair data at MZU was regarded as insignificant as no strong correlation was ever observed for the whole period. Hence any observed radon and thoron anomalies at MZU may solely be regarded as due to geophysical phenomena of the region.

After regressing through different five models, the backward regression analysis shows that barometric pressure was the most significant influencing meteorological parameters on radon data. At the same time, temperature and rainfall were found to be the second most affecting meteorological parameters on radon data. The observation was in agreement with the correlation analysis performed at three different monitoring locations where air temperature, pressure and rainfall were found to be the three main effecting factors. The observation indicates that the generated isotope pair data were affected by meteorological factors which must be

identified and discarded before correlation with geophysical phenomena to avoid false prediction.

The cross-correlation analysis of radon data at Mat fault and online data at MZU shows that the radon data of Mat fault responds well to geophysical phenomena of the region despite being under meteorological influence. It was found that 100% of the sampling spots at Mat fault show higher radon counts during the anomalies period (geophysical phenomena) at 5 cm and 50 cm sampling depths during the dry periods (November, 2017-April, 2018). At 1 m depth 78% (7 out of 9 spots) of the sampling spots were able to show higher radon counts during geophysical phenomena and the anomalies to non-anomalies period data ratio was maximum at 50 cm depth. However, during the wet season (May, 2018-October, 2018) the number of sampling spots showing higher radon counts during geophysical phenomena reduces to 56% at 5 cm depth, 89% at 50 cm, and 67% at 1 m depth. The anomaly to non-anomalies period radon data ratio was also maximum at 50 cm depth as that of the dry period. The study indicates that the radon data was influenced by meteorological factors. Despite the meteorological effect majority of the sampling spots showed higher radon counts during geophysical phenomena indicating that the region is seismically active and radon data of mat fault and MZU were responding well to it. However, for thoron data, no geophysical properties were observed. Instead, it changes intervally and remains in equilibrium for quite a long time in those intervals. When compared to that of Mat fault, thoron data at 50 cm depth varies exactly in the same manner with continuous data at MZU. But at 5 cm and 1 m depth, it deflects from the meteorologically minimized continuous data at MZU.

The cross-correlation analysis study at Chite fault shows that 100% of the sampling spots were able to show higher radon counts during the anomaly period than that of the non-anomaly period in all the sampling depths. Like that of Mat fault, the highest anomaly to non-anomaly period radon data ratio was observed at 50 cm depth. It indicates that the most pronounced radon fluctuation due to geophysical phenomena was observed at 50 cm depth, hence is the best possible monitoring depth to identify geophysical phenomena in the region. As Chite fault lies in the vicinity of Aizawl city (Capital of Mizoram state) the observation may serve as critical baseline data for

future seismic prediction studies in the region. Like that of Mat fault correlation of thoron data with geophysical phenomena was neglected.

Much more emphasis were given to monitoring of radon data at the soil surface by Sahoo and Gaware (2016) as they stated that radon fluctuation was easy to identify at the surface. At Chite fault the cross-correlation analysis shows that 100% of the sampling spots were able to show higher radon counts during geophysical phenomena at the soil-air interface. At the same time, 78% of the sampling spots in Mat fault were also able to show higher radon counts during geophysical phenomena at the soil-air interface. The anomaly periods to non-anomaly period radon data ratio were 1.7 and 1.5 at Chite fault and Mat fault respectively which were close to that observed at 5 cm and 50 cm depth of both the fault. Also when compared the anomaly to non-anomaly radon data ratio of all the sampling depths, in both the faults it was observed that, the ratio at the sub-soil (soil-air interface, 5 cm and 50 cm depths) was noticeably high to that of deep soil (1 m depth). It shows that the radon fluctuation may be much easier to detect at the sub-soil due to its low concentration at this depth (Sahoo and Gaware, 2016).

The correlation analysis also shows that in 100% of the sampling spots (9 spots at Mat fault and 3 spots at Chite fault), the radon counts in water during anomaly period was higher than that of non-anomaly period. The anomaly to non-anomaly period data ratio was observed to be 2.2 and 2.9 at Mat fault and Chite fault respectively. When compared to that of soil radon, the observed ratios in water were in close agreement with the maximum ratios at 50 cm depths which is 1.9 at Mat fault and 2.2 at Chite fault. The study indicates that nudges in the radon concentration by geophysical phenomena were most pronounced and identifiable in water and 50 cm soil depth, suggesting that either media is the best for monitoring radon anomaly due to the geophysical phenomena of the region. In the present study as continuous monitoring can’t be achieved in water, the soil media has been selected for monitoring radon data. As mentioned elsewhere the observed ratios (anomaly to non-anomaly radon data) were closely related at the sub-soil (soil-air interface, 5 cm and 50 cm depths) and lower at deep soil (1 m depth). Hence instead of 50 cm depth, the soil-air interface has been chosen for the continuous monitoring station due to its

easy access. Also, the fact that all sampling depths at the sub-soil (soil-air interface, 5 cm and 50 cm depths) having close anomaly to non-anomaly period data ratios rule out the choice in selecting any of these three sampling depths but is the same.

For radon data monitored approximately for 3 months period (January, 2017-March, 2017) with 15 min cycle at the sub-soil in MZU, the standard deviation method identified the radon anomalies at 2σ. Such that, 21 radon anomalies were selected based on this method during this period. When correlated these 21 radon anomalies with earthquakes data selected by Dobrovolsky *et al*., (1979) and Fleischer, (1981) criterion, the seismic activities were found to succeed the radon anomaly peaks within 2.4±2.3 days on average and with a range of 00:39:02 min-8 days. The selected earthquakes were of during the study period within 1000 km radius from the monitoring station. A total of six earthquakes with M≥5 (hazardous) were recorded during this period. Their precursory times were also estimated to be 1 day, 4 days, 1 day, 1 day, 3days and 1 day respectively. When compared to the estimated average precursory time (2.4±2.3 days) all of them fall within one standard deviation. Also, except for two earthquakes, all of them were predicted within one day. Hence the three months period study indicates that the region is seismically active and can be predicted by monitoring radon anomalies with high accuracy under controlled meteorological effects. In case of time series thoron data identification of its significant anomalies peaks has been failed so far with the available statistical technique, particularly for this period. Hence correlation of thoron with seismic activity was neglected in the study. The observation supports and agrees well with the experimentally demonstrated analytical model of Sahoo and Gaware (2016) at the sub-soil.

Analysis of the one-year time series thoron data by EMD-HHT technique clearly depicts that the thoron data was non-linear non-stationary data and has geophysical properties which was failed to reveal continuously by other linear methods. The FFT periodogram of thoron and Meteorological parameters show some common periods, indicating that it was influenced by it. The EMD breaks down the raw data into 17 IMFs and discards those responsible for external influences other than geophysical phenomena. Three IMFs were selected to be significant and HHT was applied to

them to obtain the HH-spectrum. The marginal spectrum and the degree of non-stationary clearly indicated that the thoron data was non-linear and non-stationary data. Hence application of conventional methods such as Fourier and wavelets transform and another linear method for observing intermittencies in the thoron data is impractical and absurd. The instantaneous energy (IE) which was the amplified form of the amplitude of the significant IMFs obtained from the HH-spectrum served as a temporal variation of energy. The IE curve easily reveals the active and quiescent period of the raw data and helps in identifying short-term seismic precursors. Twelve such thoron anomalies were identified from the IE curve using the standard deviation method. The thoron anomalies were observed at 4σ and seven selected earthquakes (4.4M-5M) within 150 km radius from the monitoring were predicted. At the same time, three false radon peaks were also observed. Hence in total, we observed 9 positives and 3 false thoron anomalies peaks with all the earthquakes predicted. The earthquake prediction time was estimated to be 7±5 days on average with a range of 9 hours-15 days. It was also found that the thoron data specifically respond to seismic activity along the Indo-Burman Subduction line. The study concluded that by fixing the prediction time and prediction range at 15 days and 150 km from the monitoring station, respectively thoron data was able to predict all the earthquakes. Barman *et al*., (2016) mentioned that besides the prominent intermittent, one could still observe intermittencies due to sporadic nor'wester showers and increase in temperature. While Chowdhury *et al*., (2017) mentioned that smaller peaks were fluctuation due to time series evolution and should be neglected. This could also be the case for the observed three false anomaly peaks which the authors are uncertain about and unable to explain at present.

A causal relationship between geophysical phenomena and the correlation coefficient of ^{222}Rn exhalation rate and its production rate was observed. The nature of correlation was significantly distinctive for ^{222}Rn production rates obtained within 5 cm from the ground surface and exhalation rates at 5 cm depth. That is a distinct weak and strong correlation coefficient during anomaly and non-anomaly periods respectively. Similar to that of 5 cm depth, the ^{222}Rn production rate exhibits a strong correlation with its exhalation rate during the non-anomaly period at the soil-air

interface, 50 cm and 1 m sampling depth. However, a mixed correlation coefficient (weak and strong) was observed during the anomaly period at the above three sampling depths (soil-air interface, 50 cm and 1 m depths) which was uncertain. In general, it was concluded that in absence of geophysical phenomena (non-anomalous period) the ^{222}Rn production and exhalation rate of the four sampling depths were strongly proportional. And gets altered during geophysical phenomena due to abrupt enhancement from the bottom. The study also concluded that the method adopted in the present study was suitable for depicting the equilibrium state of ^{222}Rn concentration and the presence of geophysical phenomena to some extent.

In general, it can be concluded that except for thorium the isotope pair data and uranium content of the region was in accordance with the global average and no radiological risk was observed for the region. Diurnally radon concentration varies with temperature while their seasonal variation and relationship with meteorological factors were distinct. Meteorological influences on the isotope pair data were observed where temperature, pressure and rainfall were the main influencing factor and pressure the most. The cross-correlation analysis shows that the maximum number of the sampling spots of the region were able to sow higher radon counts during geophysical phenomena at different sampling depths and in water. The standard deviation method analysis shows that 100% of the selected earthquakes were predicted with no false radon anomalies. The EMD-HHT technique shows that 100% of the selected earthquakes were correlated but with three false thoron anomalies. When compared to that of Jaishi et al., (Jaishi *et al*., 2013, 2014, 2014a, 2014b, 2015) and Singh *et al*., (Singh et al., 2014, 2016, 2017) who studies in the same region the present success rate of more than 90% and 70% in radon and thoron respectively is quite high compared to theirs of 60%. At the same time, no attempt has been made so far in correlating thoron data with an earthquake with such a high success rate by using a non-linear technique in the region.

Future Scope of the Study:

The online and real-time (15 min cycle) nature of the present isotope pair data is quite satisfactory. Although the success rate of the study is quite high, to improve its accuracy comparison from different monitoring stations is desirable. In the present study, the isotope pair data were a comparison between one online monitoring station and *in-situ* data from two faults. Being proven to be a seismically active region, cross-correlation of the isotope pair data from at least three to four online monitoring stations may be indisputable if the result converges. Besides an additional online monitoring station, accessibility of online soil meteorological data and selection of appropriate advance non-linear statistical techniques is also desirable to improve the accuracy of the result.

Appendix: Formulae

Statistical treatment of the data has been done in SPSS version 16.0 statistical package. However, the calculations can also be performed manually by using the following formulae.

1. Correlation coefficient (r) between the two set of variables '*x*' and '*y*' can be obtained by the following relation:

$$r = \frac{\Sigma\left(\left(x-\bar{x}\right)\left(y-\bar{y}\right)\right)}{\sqrt{\left(\Sigma\left(x-\bar{x}\right)^2 \Sigma\left(y-\bar{y}\right)^2\right)}}$$

   Where $\bar{x}$ and $\bar{y}$ are the means of *x* and *y* respectively.

2. Standard deviation (SD):

$$SD = \sqrt{\frac{\Sigma\left(x-\bar{x}\right)^2}{N-1}}$$

   Where, *N* is the total number of observations.

3. Standard error of mean (SEM):

$$SEM = \frac{SD}{\sqrt{N}}$$

4. Standard error of estimates (S_e):

$$S_e = SD(y) \times \sqrt{1-r^2}$$

   Where, *SD(y)* is the standard deviation of y-scores.

5. Degrees of freedom (df) for regression (reg) and residuals (res):
   df_{reg} equals the number of variables (dependent + independent) minus 1.
   df_{res} equals number of observations minus number of variables.

6. Sum of squares (SS):

   $SS_{reg} = \Sigma\left(y'-\bar{y}\right)^2$ is the regression sum of squares.

   $SS_{res} = \Sigma\left(y-y'\right)^2$ is the residual sum of squares.

   Here, *y'* is the predicted value of *y*.

7. Mean Square (MS):

$$MS_{reg} = \frac{SS_{reg}}{df_{reg}} \text{ , and } MS_{res} = \frac{SS_{res}}{df_{res}} .$$

8. T-test (t): T-value can be obtained by dividing the value of each regression coefficient by its respective standard error. A t-test is used to find out the significance of the predictor variables.
9. F-ratio (F): F-ratio equals the ratio of MS_{reg} to that of MS_{res}. It determines the viability (significance) of the model.

$$F = \frac{MS_{reg}}{MS_{res}}$$

10. Significance (p-value):

    The significance of the t-test and F-ratio can be obtained from the t-distribution and F-distribution tables respectively.

References

Alekseev, V. A., Alekseeva, N. G., & Jchankuliev, J. (1995). On relation between fluxes of metals in waters and radon in Turkmenistan region of seismic activity. *Radiation Measurements*, *25*(1-4), 637-639.

Ambrosino, F., Thinová, L., Briestenský, M., & Sabbarese, C. (2019). Analysis of Radon time series recorded in Slovak and Czech caves for the detection of anomalies due to seismic phenomena. *Radiation Protection Dosimetry*, *186*(2-3), 428-432.

Anderson, O. L., & Grew, P. C. (1977). Stress corrosion theory of crack propagation with applications to geophysics. *Reviews of Geophysics*, *15*(1), 77-104.

Andrews, J.N., Hussain, N., Batchelor, A.S. and Kwakwa, K. (1986). ^{222}Radon solution by the circulating fluids in a hot dry rock geothermal reservoir. *Appl. Geochem.*, 1: 647-657.

Asher-Bolinder, S., Owen, D. E., & Schumann, R. R. (1991). A preliminary evaluation of environmental factors influencing day-to-day and seasonal soil-gas radon concentrations. In *Field studies of radon in rocks, soils and water* (Vol. 1971, pp. 23-31).

Aswal, S., Kandari, T., Sahoo, B. K., Bourai, A. A., & Ramola, R. C. (2016). Emission of soil gas radon concentration around main central thrust in Ukhimath (Rudraprayag) region of Garhwal Himalaya. *Radiation Protection Dosimetry*, *171*(2), 243-247.

Atkinson, B. K. (1984). Subcritical crack growth in geological materials. *Journal of Geophysical Research: Solid Earth*, *89*(B6), 4077-4114.

Auvinen, A., Mäkeläinen, I., Hakama, M., Castrén, O., Pukkala, E., Reisbacka, H., & Rytömaa, T. (1996). Indoor radon exposure and risk of lung cancer: a nested case-control study in Finland. *JNCI: Journal of the National Cancer Institute*, *88*(14), 966-972.

Ball, T. K., Cameron, D. G., Colman, T. B., & Roberts, P. D. (1991). Behaviour of radon in the geological environment: a review. *Quarterly Journal of Engineering Geology and Hydrogeology*, *24*(2), 169-182.

Barman, C., Ghose, D., Sinha, B., & Deb, A. (2016). Detection of earthquake induced radon precursors by Hilbert Huang Transform. *Journal of Applied Geophysics*, *133*, 123-131.

Baysson, H., Tirmarche, M., Tymen, G., Gouva, S., Caillaud, D., Artus, J.C., Vergnenegre, A., Ducloy, F., & Laurier, D. (2004). Indoor radon and lung cancer in France. *Epidemiology*, *15*(6), 709-716.

Bernard, P., Herrero, A., & Berge, C. (1996). Modeling directivity of heterogeneous earthquake ruptures. *Bulletin of the Seismological Society of America*, *86*(4), 1149-1160.

BIS (2002). ISI1893-2002 (Part 1): Indian Standard criteria for earthquake resistant design of structure part1-general provisions and buildings. Bureau of Indian Standards, New Delhi.

Boashash, B. (1992). Estimating and interpreting the instantaneous frequency of a signal. I. Fundamentals. *Proceedings of the IEEE*, *80*(4), 520-538.

Bossew, P. (2003). The radon emanation power of building materials, soils and rocks. *Applied Radiation and Isotopes*, *59*(5-6), 389-392.

Bossus, D. A. W. (1984). Emanating power and specific surface area. *Radiation Protection Dosimetry*, *7*(1-4), 73-76.

Brace, W. F., & Bombolakis, E. G. (1963). A note on brittle crack growth in compression. *Journal of Geophysical Research*, *68*(12), 3709-3713.

Brace, W. F., & Byerlee, J. D. (1966). Stick-slip as a mechanism for earthquakes. *Science*, *153*(3739), 990-992.

Brace, W. F., Paulding Jr, B. W., & Scholz, C. H. (1966). Dilatancy in the fracture of crystalline rocks. *Journal of Geophysical Research*, *71*(16), 3939-3953.

Briestenský, M., Thinová, L., Praksová, R., Stemberk, J., Rowberry, M. D., & Knejflová, Z. (2014). Radon, carbon dioxide and fault displacements in central Europe related to the Tōhoku earthquake. *Radiation Protection Dosimetry*, *160*(1-3), 78-82.

Burridge, R., & Knopoff, L. (1967). Model and theoretical seismicity. *Bulletin of the Seismological Society of America*, *57*(3), 341-371.

Burton, M., Neri, M., & Condarelli, D. (2004). High spatial resolution radon measurements reveal hidden active faults on Mt. Etna. *Geophysical Research Letters*, *31*(7).

Carlson, J. M., Langer, J. S., Shaw, B. E., & Tang, C. (1991). Intrinsic properties of a Burridge-Knopoff model of an earthquake fault. *Physical Review A*, *44*(2), 884.

Chaudhuri, H., Ghose, D., Bhandari, R. K., Sen, P., & Sinha, B. (2012). A geochemical approach to earthquake reconnaissance at the Baratang mud volcano, Andaman and Nicobar Islands. *Journal of Asian Earth Sciences*, *46*, 52-60.

Chowdhury, S., Deb, A., Barman, C., Nurujjaman, M., & Bora, D. K. (2022). Simultaneous monitoring of soil 222Rn in the Eastern Himalayas and the geothermal region of eastern India: an earthquake precursor. *Natural Hazards*, *112*(2), 1477-1502.

Chowdhury, S., Deb, A., Nurujjaman, M., & Barman, C. (2017). Identification of pre-seismic anomalies of soil radon-222 signal using Hilbert-Huang transform. *Natural Hazards*, *87*(3), 1587-1606.

Cohen, L. (1995). *Time-frequency analysis* (Vol. 778). Prentice hall.

Crockett, R. G. M., Gillmore, G. K., Phillips, P. S., Denman, A. R., & Groves-Kirkby, C. J. (2006). Radon anomalies preceding earthquakes which occurred in the UK, in summer and autumn 2002. *Science of the Total Environment*, *364*(1-3), 138-148.

Dahlen, F. A. (1977). The balance of energy in earthquake faulting. *Geophysical Journal International*, *48*(2), 239-261.

Deb, A., Gazi, M., Ghosh, J., Chowdhury, S., & Barman, C. (2018). Monitoring of soil radon by SSNTD in Eastern India in search of possible earthquake precursor. *Journal of Environmental Radioactivity*, *184*, 63-70.

Dewey, J. F., & Bird, J. M. (1970). Mountain belts and the new global tectonics. *Journal of Geophysical Research*, *75*(14), 2625-2647.

Dieterich, J. H. (1979). Modeling of rock friction: 1. Experimental results and constitutive equations. *Journal of Geophysical Research: Solid Earth*, *84*(B5), 2161-2168.

Dobrovolsky, I. P., Zubkov, S. I., & Miachkin, V. I. (1979). Estimation of the size of earthquake preparation zones. *Pure and Applied Geophysics*, *117*(5), 1025-1044.

Dubinchuk VT. Radon as a precursor of earthquakes. Isotopic and geochemical precursors of earthquakes and volcanic eruptions. Vienna: International Atomic Energy Agency; 1993. TECDOC-726: p. 9-22.

Duenas, C., & Fernandez, M. C. (1988). Temporal variations in soil gas radon: any possible relation to earthquakes?. *Tectonophysics*, *152*(1-2), 137-145.

Ferguson, C. D., Klein, W., Rundle, J. B., Gould, H., & Tobochnik, J. (1998). Long-range earthquake fault models. *Computers in Physics*, *12*(1), 34-40.

Finkelstein, M., Brenner, S., Eppelbaum, L., & Ne'Eman, E. (1998). Identification of anomalous radon concentrations due to geodynamic processes by elimination of Rn variations caused by other factors. *Geophysical Journal International*, *133*(2), 407-412.

Finkel V.M. (1970), Physics of fracture, *Mettalurgia*, Moscow.

Fleischer, R. L. (1981). Dislocation model for radon response to distant earthquakes. *Geophysical Research Letters*, *8*(5), 477-480.

Fleischer, R. L., & Mogro-Campero, A. (1985). Association of subsurface radon changes in Alaska and the northeastern United States with earthquakes. *Geochimica et Cosmochimica Acta*, *49*(4), 1061-1071.

Friedmann, H. (2012). Radon in earthquake prediction research. *Radiation Protection Dosimetry*, *149*(2), 177-184.

Friedmann, H., Aric, K., Gutdeutsch, R., King, C. Y., Altay, C., & Sav, H. (1988). Radon measurements for earthquake prediction along the North Anatolian Fault Zone: a progress report. *Tectonophysics*, *152*(3-4), 209-214.

Fu, C. C., Yang, T. F., Du, J., Walia, V., Chen, Y. G., Liu, T. K., & Chen, C. H. (2008). Variations of helium and radon concentrations in soil gases from an active fault zone in southern Taiwan. *Radiation Measurements*, *43*, S348-S352.

Fu, C.C., Yang, T.F., Tsai, M.C., Lee, L.C., Liu, T.K., Walia, V., Chen, C.H., Chang, W.Y., Kumar, A., & Lai, T.H. (2017). Exploring the relationship between soil degassing and seismic activity by continuous radon monitoring in the Longitudinal Valley of eastern Taiwan. *Chemical Geology*, *469*, 163-175.

Garavaglia, M., Braitenberg, C., & Zadro, M. (1998). Radon monitoring in a cave of North-Eastern Italy. *Physics and Chemistry of the Earth*, *23*(9-10), 949-952.

Gaware, J. J., Sahoo, B. K., Sapra, B. K., & Mayya, Y. S. (2011). Indigenous development and networking of online radon monitors in the underground uranium mine. *Radiation Protection and Environment*, *34*(1), 37.

Gaware, J. J., Sahoo, B. K., Sapra, B. K., & Mayya, Y. S. (2011a). Indigenous development of online radon and thoron monitors for applications in Uranium mining and Thorium processing facilities. *BARC Newsletter, DAE EA*, *30*, 149-153.

Gaware, J. J., Sahoo, B. K., Sapra, B. K., & Mayya, Y. S. (2013). Development of ZnS (Ag) detector based portable continuous radon-thoron monitors for

multiple applications. *Proceedings of, Syn in Physics and Industry held at BARC, Mumbai. January 21, pp. 80.*

Geological Survey of India (1988). Geoenvironmental appraisal of Aizawl town and its surroundings, Aizawl district, Mizoram. Unpublished Report, Field Season 1985-1986.

George, A. C. (2008, August). World history of radon research and measurement from the early 1900's to today. In *AIP Conference Proceedings* (Vol. 1034, No. 1, pp. 20-33). American Institute of Physics.

Ghosh, D., Deb, A., Sengupta, R., Patra, K. K., & Bera, S. (2007). Pronounced soil-radon anomaly-Precursor of recent earthquakes in India. *Radiation Measurements*, *42*(3), 466-471.

Gingrich, J. E. (1984). Radon as a geochemical exploration tool. *Journal of Geochemical Exploration*, *21*(1-3), 19-39.

Grammakov, A. G. (1936). On the influence of some factors in the spreading of radioactive emanations under natural conditions. *Zhur. Geofiziki*, *6*, 123-148.

Guedalia, D., Laurent, J. L., Fontan, J., Blanc, D., & Druilhet, A. (1970). A study of radon 220 emanation from soils. *Journal of Geophysical Research*, *75*(2), 357-369.

Guha Bose, A., Das, A., Chowdhury, S., & Deb, A. (2022). Studies of scintillations and TEC variations with GPS satellite links together with soil radon anomalies preceding Nepal earthquakes of April-May 2015. *Natural Hazards*, *112*(2), 1137-1163.

Gupta, R., & Sarangi, A. K. (2005). Emerging trend of uranium mining: The Indian scenario. *International Atomic Energy Agency (IAEA)(ed) Uranium production and raw materials for the nuclear fuel cycle-supply and demand, economics, the environment and energy security. ISSN*, 1563-0153.

Harley J.H. (1973), Environmental Radon, In: *Noble Gases* (Stanley R.E. and Moghissi A.A., Eds.), CONF-730915, 109-114.

Hatuda Z. (1953). Radon content and its change in soil air near the ground surface. Memoirs of the College of Science, University of Kyoto, Series B 20: 285-306.

Heaton, T. H. (1990). Evidence for and implications of self-healing pulses of slip in earthquake rupture. *Physics of the Earth and Planetary Interiors*, *64*(1), 1-20.

Hirotaka U., Moriuchi H., Takemura Y., Tsuchida H., Fujii I. and Nakamura M. (1988). Anomalously high radon discharge from the Atotsugawa fault prior to the western Nagano Prefecture earthquake (M 6.8) of September 14, 1984. *Tectonophysics*, 152, 147-152.

Huang, N.E., Shen, Z., Long, S.R., Wu, M.C., Shih, H.H., Zheng, Q., Yen, N.C., Tung, C.C. & Liu, H.H. (1998). The empirical mode decomposition and the Hilbert spectrum for nonlinear and non-stationary time series analysis. *Proceedings of the Royal Society of London. Series A: mathematical, physical and engineering sciences*, *454*(1971), 903-995.

Huang, W., Shen, Z., Huang, N. E., & Fung, Y. C. (1998a). Engineering analysis of biological variables: an example of blood pressure over 1 day. *Proceedings of the National Academy of Sciences*, *95*(9), 4816-4821.

Hwa Oh, Y., & Kim, G. (2015). A radon-thoron isotope pair as a reliable earthquake precursor. *Scientific Reports*, *5*(1), 1-6.

IAEA (2004). Safety Standards Series No. RS-G-1.7: Application of the concepts of exclusion, exemption and clearance. Safety Guide. Vienna: International Atomic Energy Agency.

IAEA (2013). Measurement and Calculation of Radon Releases from NORM Residues. Vienna: International Atomic Energy Agency. TRS 474: p. 1-74.

Igarashi, G., & Wakita, H. (1990). Groundwater radon anomalies associated with earthquakes. *Tectonophysics*, *180*(2-4), 237-254.

Imme, G., and Morelli, D. (2012). Radon as earthquake precursor, In: Earthquake Research and Analysis-Statistical Studies, Observation and Planning (Dr. Amico S.D., Ed.), ISBN: 978-953-51-0134-5, In Tech, Available from: http://www.intechopen.com/books/earthquake-research-and-analysis-statistical- studies-observations-and planning/radon-as-earthquake-precursor.

İnan, S., Akgül, T., Seyis, C., Saatçılar, R., Baykut, S., Ergintav, S., & Baş, M. (2008). Geochemical monitoring in the Marmara region (NW Turkey): A search for precursors of seismic activity. *Journal of Geophysical Research: Solid Earth*, *113*(B3).

Iwata, D., Nagahama, H., Muto, J., & Yasuoka, Y. (2018). Non-parametric detection of atmospheric radon concentration anomalies related to earthquakes. *Scientific Reports*, *8*(1), 1-9.

Jaishi, H. P., Singh, S., Tiwari, R. P., & Tiwari, R. C. (2013). Radon and thoron anomalies along Mat fault in Mizoram, India. *Journal of Earth System Science*, *122*(6), 1507-1513.

Jaishi, H. P., Singh, S., Tiwari, R. P., & Tiwari, R. C. (2014). Temporal variation of soil radon and thoron concentrations in Mizoram (India), associated with earthquakes. *Natural Hazards*, *72*(2), 443-454.

Jaishi, H. P., Singh, S., Tiwari, R. P., & Tiwari, R. C. (2014a). Correlation of radon anomalies with seismic events along Mat fault in Serchhip District, Mizoram, India. *Applied Radiation and Isotopes*, *86*, 79-84.

Jaishi, H. P., Singh, S., Tiwari, R. P., & Tiwari, R. C. (2014b). Analysis of soil radon data in earthquake precursory studies. *Annals of Geophysics*, *57*(5), S0544-S0544.

Jaishi, H. P., Singh, S., Tiwari, R. P., & Tiwari, R. C. (2015). Soil-gas thoron concentration associated with seismic activity. *Chiang Mai J Sci*, *42*(4), 972-979.

Jha, R., Raju, D., & Sen, A. (2006). Analysis of tokamak data using a novel Hilbert transform based technique. *Physics of Plasmas*, *13*(8), 082507.

Jin, X., Bu, J., Qiu, G., Ma, L., Chen, Z., Chen, T., Wu, J., Pan, B., Ji, H., Tian, J. & Wu, X. (2022). Non-normal distribution of radon and residual radon and short-term abnormal precursors of residual radon before major earthquakes. *Earth Science Informatics*, 1-17.

Kanamori, H., & Brodsky, E. E. (2001). The physics of earthquakes. *Physics Today*, *54*(6), 34-40.

Kanamori, H., & Brodsky, E. E. (2004). The physics of earthquakes. *Reports on Progress in Physics*, *67*(8), 1429.

Kanamori H. and Heaton T.H. (2000), Microscopic and macroscopic physics of earthquakes, *Geophysical Monograph Series*, 120: 147-163.

Kawada, Y., Nagahama, H., Omori, Y., Yasuoka, Y., Ishikawa, T., Tokonami, S., & Shinogi, M. (2007). Time-scale invariant changes in atmospheric radon concentration and crustal strain prior to a large earthquake. *Nonlinear Processes in Geophysics*, *14*(2), 123-130.

Kawamura, H., Hatano, T., Kato, N., Biswas, S., & Chakrabarti, B. K. (2012). Statistical physics of fracture, friction, and earthquakes. *Reviews of Modern Physics*, *84*(2), 839.

Kayal, J. R. (1996). Earthquake source process in Northeast India: a review. *Journal of Himalayan Geology*, *17*, 53-69.

Khattak, N. U., Khan, M. A., Ali, N., & Abbas, S. M. (2011). Radon monitoring for geological exploration: a review. *Journal of Himalayan Earth Sciences*, *44*(2), 91-102.

King, C. Y. (1978). Radon emanation on San Andreas fault. *Nature*, *271*(5645), 516-519.

King, C. Y. (1980). Episodic radon changes in subsurface soil gas along active faults and possible relation to earthquakes. *Journal of Geophysical Research: Solid Earth*, *85*(B6), 3065-3078.

King, C. Y. (1984). Impulsive radon emanation on a creeping segment of the San Andreas fault, California. *Pure and Applied Geophysics*, *122*(2), 340-352.

King, C. Y. (1986). Gas geochemistry applied to earthquake prediction: An overview. *Journal of Geophysical Research: Solid Earth*, *91*(B12), 12269-12281.

King, C. Y., King, B. S., Evans, W. C., & Zhang, W. (1996). Spatial radon anomalies on active faults in California. *Applied Geochemistry*, *11*(4), 497-510.

Knopoff, L. (1958). Energy release in earthquakes. *Geophysical Journal International*, *1*(1), 44-52.

Kolthoff, I.M and Philips, J. Elving., 1966. Treaties of analytical chemistry, 4, part II, 219.

Külahcı, F., İnceöz, M., Doğru, M., Aksoy, E., & Baykara, O. (2009). Artificial neural network model for earthquake prediction with radon monitoring. *Applied Radiation and Isotopes*, *67*(1), 212-219.

Kuo, T., Chen, W., & Ho, C. (2018). Anomalous decrease in groundwater radon before 2016 Mw 6.4 Meinong earthquake and its application in Taiwan. *Applied Radiation and Isotopes*, *136*, 68-72.

Malsawma, J., Lalnuntluanga, P., Badekar, A., Sangode, S. J., & Tiwari, R. P. (2010). Magnetic polarity stratigraphy of the Bhuban succession, Surma Group, Tripura-Mizoram accretionary belt. *Journal of the Geological Society of India*, *76*(2), 119-133.

Markkanen, M., & Arvela, H. (1992). Radon emanation from soils. *Radiation Protection Dosimetry*, *45*(1-4), 269-272.

Megumi, K., & Mamuro, T. (1974). Emanation and exhalation of radon and thoron gases from soil particles. *Journal of geophysical research*, *79*(23), 3357-3360.

Mjachkin, V. I., Brace, W. F., Sobolev, G. A., & Dieterich, J. H. (1975). Two models for earthquake forerunners. In: *Earthquake prediction and rock mechanics* (pp. 169-181). Birkhäuser, Basel.

Monnin, M. M., & Seidel, J. L. (1991). Radon and geophysics: recent advances. *International Journal of Radiation Applications and Instrumentation. Part D. Nuclear Tracks and Radiation Measurements*, *19*(1-4), 375-382.

Moore, W. S. (1984). Mechanism of transport of U-Th series radioisotopes from solids into ground water. *Geochimica et Cosmochimica Acta*, *48*(2), 395-399.

Morawska, L., & Jeffries, C. (1994). Distribution of radium in mineral sand grains and its potential effect on radon emanation. *Radiation Protection Dosimetry*, *56*(1-4), 199-200.

Mori, T., & Kawamura, H. (2005). Simulation study of spatiotemporal correlations of earthquakes as a stick-slip frictional instability. *Physical Review Letters*, *94*(5), 058501.

Moussa, M. M., & El Arabi, A. G. M. (2003). Soil radon survey for tracing active fault: a case study along Qena-Safaga road, Eastern Desert, Egypt. *Radiation Measurements*, *37*(3), 211-216.

Muto, J., Yasuoka, Y., Miura, N., Iwata, D., Nagahama, H., Hirano, M., Ohmomo, Y. & Mukai, T. (2021). Preseismic atmospheric radon anomaly associated with 2018 Northern Osaka earthquake. *Scientific Reports*, *11*(1), 1-8.

Nalukudiparambil, J., Gopinath, G., Ramakrishnan, R. T., & Surendran, A. K. (2021). Groundwater radon (222Rn) assessment of a coastal city in the high background radiation area (HBRA), India. *Arabian Journal of Geosciences*, *14*(8), 1-7.

Nazaroff, W.W., Nero, A. V. (1988). Radon and its decay products in indoor air, New York: John Wiley and Sons.

Nazaroff, W.W. (1992). Radon transport from soil to air, *Rewiews of Geophysics*, 30: 137-160.

Negarestani, A., Setayeshi, S., Ghannadi-Maragheh, M., & Akashe, B. (2002). Layered neural networks based analysis of radon concentration and environmental parameters in earthquake prediction. *Journal of Environmental Radioactivity*, *62*(3), 225-233.

Neri, M., Giammanco, S., Ferrera, E., Patanè, G., & Zanon, V. (2011). Spatial distribution of soil radon as a tool to recognize active faulting on an active volcano: the example of Mt. Etna (Italy). *Journal of Environmental Radioactivity*, *102*(9), 863-870.

Nevinsky, I., & Tsvetkova, T. (2005). SSNTDs in the automatic detector of radon. *Radiation Measurements*, *39*(1), 115-119.

Nur, A. (1972). Dilatancy, pore fluids, and premonitory variations of ts/tp travel times. *Bulletin of the Seismological Society of America*, *62*(5), 1217-1222.

Nur, A., & Simmons, G. (1969). The effect of saturation on velocity in low porosity rocks. *Earth and Planetary Science Letters*, *7*(2), 183-193.

Okabe S. (1956), Time variation of the atmospheric radon content near the ground surface with relation to some geophysical phenomena, *Memoirs of the College of Science,* University of Kyoto, Series A 28: 99-115.

Olami, Z., Feder, H. J. S., & Christensen, K. (1992). Self-organized criticality in a continuous, nonconservative cellular automaton modeling earthquakes. *Physical Review Letters*, *68*(8), 1244.

Omori, Y., Yasuoka, Y., Nagahama, H., Kawada, Y., Ishikawa, T., Tokonami, S., & Shinogi, M. (2007). Anomalous radon emanation linked to preseismic electromagnetic phenomena. *Natural Hazards and Earth System Sciences*, *7*(5), 629-635.

Pachuau R. (1994). Geography of Mizoram. *R. T. Enterprise Publication*, Aizawl (Mizoram).

Padilla, G.D., Hernández, P.A., Padrón, E., Barrancos, J., Pérez, N.M., Melián, G., Nolasco, D., Dionis, S., Rodríguez, F., Calvo, D. & Hernández, I. (2013). Soil gas radon emissions and volcanic activity at El Hierro (Canary Islands): The 2011-2012 submarine eruption. *Geochemistry, Geophysics, Geosystems*, *14*(2), 432-447.

Peng, Z. K., Peter, W. T., & Chu, F. L. (2005). A comparison study of improved Hilbert–Huang transform and wavelet transform: Application to fault diagnosis for rolling bearing. *Mechanical Systems and Signal Processing*, *19*(5), 974-988.

Piersanti, A., Cannelli, V., & Galli, G. (2015). Long term continuous radon monitoring in a seismically active area. Annals of Geophysics, 58, 4, 2015, S0437; doi:10.4401/ag-6735

Planinić, J., Radolić, V., & Lazanin, Ž. (2001). Temporal variations of radon in soil related to earthquakes. *Applied Radiation and Isotopes*, *55*(2), 267-272.

Ramola, R. C., Prasad, Y., Prasad, G., Kumar, S., & Choubey, V. M. (2008). Soil-gas radon as seismotectonic indicator in Garhwal Himalaya. *Applied Radiation and Isotopes*, *66*(10), 1523-1530.

Ramola, R. C., Singh, M., Sandhu, A. S., Singh, S., & Virk, H. S. (1990). The use of radon as an earthquake precursor. Int J Radiat Applic Instrum., Part E, *4*(2), 275-287.

Rastogi, B. K., Chadha, R. K., & Raju, I. P. (1986). Seismicity near Bhatsa reservoir, Maharashtra, India. *Physics of the Earth and Planetary Interiors*, *44*(2), 179-199.

Rastogi, B. K., Rao, C. R., Chadha, R. K., & Gupta, H. K. (1987). Precursory phenomena in the microearthquake sequence near the Osmansagar reservoir, Hyderabad, India. *Tectonophysics*, *138*(1), 17-24.

Reddy, D. V., Nagabhushanam, P., Sukhija, B. S., & Reddy, G. R. (2010). Continuous radon monitoring in soil gas towards earthquake precursory studies in basaltic region. *Radiation Measurements*, *45*(8), 935-942.

Richon, P., Sabroux, J. C., Halbwachs, M., Vandemeulebrouck, J., Poussielgue, N., Tabbagh, J., & Punongbayan, R. (2003). Radon anomaly in the soil of Taal volcano, the Philippines: A likely precursor of the M 7.1 Mindoro earthquake (1994). *Geophysical Research Letters*, *30*(9).

Rikitake T. (1976), Earthquake Prediction, *Elseiver*, New York.

Rundle, J.B., Turcotte, D.L., Shcherbakov, R., Klein, W. and Sammis, C. (2003). Statistical physics approach to understanding the multiscale dynamics of earthquake fault systems (invited). *Rev. Geophys. Space Phys*, *41*(4).

Sahoo, B. K., & Gaware, J. J. (2016). Radon in ground water and soil as a potential tracer for uranium exploration and earthquake precursory studies. *SRESA's Int J Life Cycle Reliab Saf Eng*, *5*(3), 21-29.

Sahoo, S. K., Katlamudi, M., Barman, C., & Lakshmi, G. U. (2020). Identification of earthquake precursors in soil radon-222 data of Kutch, Gujarat, India using empirical mode decomposition based Hilbert Huang Transform. *Journal of Environmental Radioactivity*, *222*, 106353.

Sakoda, A., Ishimori, Y., Hanamoto, K., Kataoka, T., Kawabe, A., & Yamaoka, K. (2010). Experimental and modeling studies of grain size and moisture content effects on radon emanation. *Radiation Measurements*, *45*(2), 204-210.

Sarmah, S. K. (1999). The probability of occurrence of a high magnitude earthquake in Northeast India. *Journal of Geophysics (Hyderabad)*, *20*(3), 129-135.

Sasaki, T., Gunji, Y., & Okuda, T. (2004). Radon emanation dependence on grain configuration. *Journal of Nuclear Science and Technology*, *41*(10), 993-1002.

Sasaki, T., Gunji, Y., & Okuda, T. (2005). Theoretical study of high radon emanation. *Journal of Nuclear Science and Technology*, *42*(2), 242-249.

Scholz, C. H., Sykes, L. R., & Aggarwal, Y. P. (1973). Earthquake Prediction: A Physical Basis: Rock dilatancy and water diffusion may explain a large class of phenomena precursory to earthquakes. *Science*, *181*(4102), 803-810.

Segovia N., Mena M., Seidel J.L., Monnin M., Tamez E. and Pena P. (1995). Short and long term radon in soil monitoring for geophysical purposes. *Radiation Measurements*, 25, 547-552.

Segovia N., Maciel R., Pena P., Tamez E., Rosas J. and Mena M. (1995a). Radon in soil studies in Jalisco state, Mexico. *Radiation Messurements*, 25, 617-620.

Segovia, N., Seidel, J., & Monnin, M. (1987). Variations of radon in soils induced by external factors. *Journal of Radioanalytical and Nuclear Chemistry*, *119*(3), 199-209.

Semkow, T. M. (1990). Recoil-emanation theory applied to radon release from mineral grains. *Geochimica et Cosmochimica Acta*, *54*(2), 425-440.

Semkow, T. M. (1991). Fractal model of radon emanation from solids. *Physical Review Letters*, *66*(23), 3012.

Semkow, T. M., & Parekh, P. P. (1990). The role of radium distribution and porosity in radon emanation from solids. *Geophysical Research Letters*, *17*(6), 837-840.

Shapiro, M. H., Melvin, J. D., Tombrello, T. A., Mendenhall, M. H., Larson, P. B., & Whitcomb, J. H. (1981). Relationship of the 1979 Southern California radon anomaly to a possible regional strain event. *Journal of Geophysical Research: Solid Earth*, *86*(B3), 1725-1730.

Shekel, J. (1953). Instantaneous frequency. *Proceedings of the Institute of Radio Engineers*, *41*(4), 548-548.

Singh, M., Ramola, R. C., Singh, B., Singh, S., & Virk, H. S. (1991). Subsurface soil gas radon changes associated with earthquakes. *International Journal of Radiation Applications and Instrumentation. Part D. Nuclear Tracks and Radiation Measurements*, *19*(1-4), 417-420.

Singh, M.W., Ramola, R.C., Singh, S., & Virk, H.S. (1988). The influence of meteorological parameters on soil gas radon. *Journal of Association of Exploration Geophysicists*, *9*(2), 85-90.

Singh, S., Jaishi, H. P., Tiwari, R. P., & Tiwari, R. C. (2014). Variations of soil radon concentrations along Chite Fault in Aizawl district, Mizoram, India. *Radiation Protection Dosimetry*, *162*(1-2), 73-77.

Singh, S., Jaishi, H. P., Tiwari, R. P., & Tiwari, R. C. (2016). A study of variation in soil gas concentration associated with earthquakes near Indo-Burma Subduction zone. *Geoenvironmental Disasters*, *3*(1), 1-8.

Singh, S., Jaishi, H. P., Tiwari, R. P., & Tiwari, R. C. (2017). Time series analysis of soil radon data using multiple linear regression and artificial neural network in seismic precursory studies. *Pure and Applied Geophysics*, *174*(7), 2793-2802.

Stranden, E., Kolstad, A. K., & Lind, B. (1984). The influence of moisture and temperature on radon exhalation. *Radiation Protection Dosimetry*, *7*(1-4), 55-58.

Strong, K. P., & Levins, D. M. (1982). Effect of moisture content on radon emanation from uranium ore and tailings. *Health Physics*, *42*(1), 27-32.

Sultankhodzhaev, A. N. (1984). Hydrogeoseismic precursors to earthquakes. In *Earthquake prediction. International symposium* (pp. 181-191).

Sundal, A. V., Valen, V., Soldal, O., & Strand, T. (2008). The influence of meteorological parameters on soil radon levels in permeable glacial sediments. *Science of the Total Environment*, *389*(2-3), 418-428.

Swakoń, J., Kozak, K., Paszkowski, M., Gradziński, R., Łoskiewicz, J., Mazur, J., Janik, M., Bogacz, X., Horwacik, T. and Olko, P. (2005). Radon concentration in soil gas around local disjunctive tectonic zones in the Krakow area. *Journal of Environmental Radioactivity*, *78*(2), 137-149.

Swedjemark, G. A. (2004). The history of radon from a Swedish perspective. *Radiation Protection Dosimetry*, *109*(4), 421-426.

Tanner A.B. (1959), Meterological influence on radon concentration in drill holes, *Mining Engineering*, 11: 706-708.

Tanner, A.B. (1964). Radon migration in the ground: A review, In: Symposium Proc., *Natural Radiation Environment* (Adams J.A.S. and Lowder W.M., Eds.), *University of Chicago Press,* Chicago, 161-190.

Tanner, A.B. (1980). Radon migration in the ground: A supplementary review, In: Symposium Proc., *Natural Radiation Environment III* (Gessel T.F. and Lowder W.M., Eds.), Houston, Texas, 23-28 April 1978, *US Dept. of Energy, Washington D.C.*, 5-56.

Tareen, A. D. K., Asim, K. M., Kearfott, K. J., Rafique, M., Nadeem, M. S. A., Iqbal, T., & Rahman, S. U. (2019). Automated anomalous behaviour detection in soil radon gas prior to earthquakes using computational intelligence techniques. *Journal of Environmental Radioactivity*, *203*, 48-54.

Thomas, D. (1988). Geochemical precursors to seismic activity. *Pure and Applied Geophysics*, *126*(2), 241-266.

Tiwari, R. P. (2002). Status of seismicity in the northeast India and earthquake disaster mitigation. *ENVIS Bull*, *10*(1), 15-25.

Torkar, D., Zmazek, B., Vaupotič, J., & Kobal, I. (2010). Application of artificial neural networks in simulating radon levels in soil gas. *Chemical Geology*, *270*(1-4), 1-8.

Ulomov, V. I., & Mavashev, B. Z. (1967). A precursor of a strong tectonic earthquake. In *Doklady Akademii Nauk* (Vol. 176, No. 2, pp. 319-321). Russian Academy of Sciences.

UNSCEAR, (2000). United Nation Scientific Committee on the Effect of Atomic Radiation., Sources, Effects and Risks of Ionizing Radiation., Report to the General Assembly, United Nation, New York.

UNSCAER, (1982). Ionizing Radiation: Sources and Biological Effects. Annex D: Exposures to Radon and Thoron and their decay products. United Nations.

Vaupotič, J., Riggio, A., Santulin, M., Zmazek, B., & Kobal, I. (2010). A radon anomaly in soil gas at Cazzaso, NE Italy, as a precursor of an ML= 5.1 earthquake. *Nukleonika*, *55*(4), 507-511.

Virk, H. S. (1996). A critique of empirical scaling relationship between earthquake magnitude, epicentral distance and precursor time for interpretation of radon data. *J. Earthquake Prediction. Res.*, *5*, 547-583.

Virk, H. S., & Singh, B. (1993). Radon anomalies in soil-gas and groundwater as earthquake precursor phenomena. *Tectonophysics*, *227*(1-4), 215-224.

Virk, H. S., Walia, V., & Kumar, N. (2001). Helium/radon precursory anomalies of Chamoli earthquake, Garhwal Himalaya, India. *Journal of Geodynamics*, *31*(2), 201-210.

Virk, H. S., Walia, V., Sharma, A. K., Kumar, N., & Kumar, R. (2000). Correlation of radon anomalies with microseismic events in Kangra and Chamba valleys of NW Himalaya. *Geofísica Internacional*, *39*(3), 221-227.

Wakita, H., Nakamura, Y., & Sano, Y. (1985). Groundwater radon variations reflecting changes in regional stress fields. In *Practical Approaches to Earthquake Prediction and Warning* (pp. 545-557). Springer, Dordrecht.

Walia, V., Virk, H. S., Bajwa, B. S., & Sharma, N. (2003). Relationships between radon anomalies and seismic parameters in NW Himalaya, India. *Radiation measurements*, *36*(1-6), 393-396.

Walia, V., Virk, H. S., Yang, T. F., Mahajan, S., Walia, M., & Bajwa, B. S. (2005). Earthquake prediction studies using radon as a precursor in NW Himalayas, India: a case study. *TAO: Terrestrial, Atmospheric and Oceanic Sciences*, *16*(4), 775.

Walia V., Virk H.S., Yang T.F., Mahajan S., Walia M. and Bajwa B.S. (2005a), Earthquake prediction studies using radon as a precursor in NW Himalayas, India: a case study, *Terrestrial, Atmospheric and Oceanic Sciences*, 16: 775-804.

Walia, V., Yang, T.F., Lin, S.J., Kumar, A., Fu, C.C., Chiu, J.M., Chang, H.H., Wen, K.L. & Chen, C.H. (2013). Temporal variation of soil gas compositions for earthquake surveillance in Taiwan. *Radiation Measurements*, *50*, 154-159.

Wattananikorn, K., Kanaree, M., & Wiboolsake, S. (1998). Soil gas radon as an earthquake precursor: some considerations on data improvement. *Radiation Measurements*, *29*(6), 593-598.

Wharton, A. M., Sekar Iyengar, A. N., & Janaki, M. S. (2013). Study of nonlinear oscillations in a glow discharge plasma using empirical mode decomposition and Hilbert Huang transform. *Physics of Plasmas*, *20*(2), 022301.

Whitcomb, J. H., Garmany, J. D., & Anderson, D. L. (1973). Earthquake prediction: Variation of seismic velocities before the San Francisco earthquake. *Science*, *180*(4086), 632-635.

Wood, D. M., & Belkheir, K. (1994). Strain softening and state parameter for sand modelling. *Géotechnique*, *44*(2), 335-339.

Yang, T.F., Walia, V., Chyi, L.L., Fu, C.C., Chen, C.H., Liu, T.K., Song, S.R., Lee, C.Y. & Lee, M. (2005). Variations of soil radon and thoron concentrations in a fault zone and prospective earthquakes in SW Taiwan. *Radiation Measurements*, *40*(2-6), 496-502.

Yasuoka, Y., Kawada, Y., Nagahama, H., Omori, Y., Ishikawa, T., Tokonami, S., & Shinogi, M. (2009). Preseismic changes in atmospheric radon concentration and crustal strain. *Physics and Chemistry of the Earth, Parts A/B/C*, *34*(6-7), 431-434.

Yasuoka, Y., & Shinogi, M. (1997). Anomaly in atmospheric radon concentration: a possible precursor of the 1995 Kobe, Japan, earthquake. *Health Physics*, *72*(5), 759-761.

Zhang, S., Shi, Z., Wang, G., Yan, R., & Zhang, Z. (2020). Groundwater radon precursor anomalies identification by decision tree method. *Applied Geochemistry*, *121*, 104696.

Zmazek, B., Todorovski, L., Džeroski, S., Vaupotič, J., & Kobal, I. (2003). Application of decision trees to the analysis of soil radon data for earthquake prediction. *Applied Radiation and Isotopes*, *58*(6), 697-706.

Zmazek, B., Živčić, M., Vaupotič, J., Bidovec, M., Poljak, M., & Kobal, I. (2002). Soil radon monitoring in the Krško Basin, Slovenia. *Applied Radiation and Isotopes*, *56*(4), 649-657.

Zoran, M., Savastru, R., & Savastru, D. (2012). Radon levels assessment in relation with seismic events in Vrancea region. *Journal of Radioanalytical and Nuclear Chemistry*, *293*(2), 655-663.

seismic events in Vrancea region, *J. Radioanal. Nucl. Chem.*, 293: 655-663.

Brief Bio-data of the Author

1. Name **:** T Thuamthansanga

2. Father's Name **:** T Thangmuana

3. Address **:**Kawlbem, Saitual District, Mizoram

4. Designation **:** Research Scholar (Mizoram University)

5. Date of Birth **:** 29/06/1990

6. Educational qualification:

Degree	**Year**	**University/ Board**	**Division**	**Subject taken**
High School/ HSLC	2006	MBSE	Second	English, Science,Mathematics,Social Science, Mizo
HSSLC	2009	COHSEM	First	Physics, Mathematics, Mizo Chemistry, Biology, English,
B.Sc.	2013	NEHU	First	Physics (Honors), Chemistry, Mathematics, English, EVS
M.Sc.	2015	Mizoram University	Distinction	Physics, Chemistry (optional), Mathematics (optional)

7. Research experience **:** 5 Years (JRF)

8. Area of research interest **:** Radiation and Environmental Physics

9. Publication **:** 8 (6 in peer review journals and 2 in books)

10. Conferences and workshops attended: 10

11. Working experience

- Completed training course on workshop entitled, "Measurement techniques for radon, thoron and their decay products", at Radiological Physics and Advisory Division, Bhabha Atomic Research Centre, Mumbai, during December 13-16, 2016.

12. Awards

- **Best oral presentation award** for the research paper "Study of radon concentration using soil probe and radon exhalation chamber for seismic study" during 20th national conference on solid state nuclear track detectors and their applications, 26th-28th October, 2017, Vidya Vikas Institute of Engineering and Technology, Mysuru, Karnataka, India.
- Nucleonix System Pvt. Ltd. and Indian Society for Radiation Physics conferred "**Nucleonix-ISRP Award**" for 1st best technical paper for the Research paper entitled "Identification of geophysical property for radon and thoron data for earthquake precursor in Indo-Burman subduction region" during 23rd National Symposium on Radiation Physics (NSRP-23), 19th-21st January, 2023, University of Mysore, Manasagangotri, Mysuru, Karnataka, India.

The information provided above is true to the best of my knowledge and belief.

(Signature)

List of Research Publications

Publications

Published Journals (peer reviews)

1. Thuamthansanga, T., Sahoo, B. K., Tiwari, R. C., & Sapra, B. K. (2019). A study on the anomalous behaviour of Radon in different depths of soil at a tectonic fault and its comparison with time-series data at a distant continuous monitoring station. *SN Applied Sciences*, *1*(7), 1-13.
   DOI: https://doi.org/10.1007/s42452-019-0646-6, Published by **Springer Nature. ISSN (electronic): 2523-3971. Scopus Index**

2. Thuamthansanga, T., Sahoo, B. K., Tiwari, R. C., & Tiwari, R. P. (2021). Study of meteorological influence on the count of ^{222}Rn and ^{220}Rn gases and its possibility for a forecasting gas. *Radiation Environment and Medicine*, *10*(1), 37-47.
   DOI: https://doi.org/10.51083/radiatenvironmed.10.1_37. Published by **Hirosaki University Press. ISSN :2423-9097 (PRINT), 2432-163X (ONLINE)**

3. Thuamthansanga, T., Sahoo, B. K., & Tiwari, R. C. (2021). Study of pre-seismic thoron anomaly using empirical mode decomposition based Hilbert–Huang transform at Indo-Burman subduction region. *Journal of Radioanalytical and Nuclear Chemistry*, *330*(3), 1571-1582. DOI: https://doi.org/10.1007/s10967-021-08001-6. Published by **Springer Nature. ISSN (electronic): 1588-2780, ISSN(print) 0236-5731. Scopus Index. IF=1.754**

4. Thuamthansanga, T., Sahoo, B. K., & Tiwari, R. C. (2023). Estimation of ^{238}U and ^{232}Th in soil and water of prominent fault region of Mizoram. *Environmental Engineering Research*, *28*(1).

DOI: https://doi.org/10.4491/eer.2021.106. Published by **Korean Society of Environmental Engineers. ISSN (Electronic): 2005-968X; ISSN (print): 1226-1025. Scopus Index. IF=3.932**

5. Thuamthansanga, T., & Tiwari, R. C. (2022). Correlation of *in-situ* online ^{222}Rn data at Mat fault with geophysical process. *Materials Today: Proceedings*, *65*, 2825-2831.
DOI: https://doi.org/10.1016/j.matpr.2022.06.272. Published by **Elsevier. ISSN: 2214-7853. Scopus Index**

6. Thuamthansanga, T., & Tiwari, R. C. (2022). Correlation of *in-situ* Online Generated ^{222}Rn/^{220}Rn Data with the Anomaly Period of a Distance Continuous Data as an Indirect Revelation to Geophysical Process of the Region. ***International Journal of Engineering Research & Technology*, 10(7), 35-43. DOI: 10.17577/IJERTCONV10IS07008. Published by www.ijert.org.** ISSN (Online) : 2278-0181

Published Books

1. Thuamthansanga, T., Tiwari, R.C., Sahoo, B.K., and Datta, D. (2020). Analysis of Meteorological Influence on Exhalation of ^{222}Rn and ^{220}Rn Gases at Mat Fault, *Radon: Detection, Exposure and Control.* pp. 17, (Editor: Prof. R.C. Tiwari), **Nova Science Publishers, Inc., USA. ISBN:** 978-1-53616-791-7. Scopus Index

2. Thuamthansanga, T., Sahoo, B.K., & Tiwari, R.C. (2022). Analysis of Fluctuation in Radon Concentration and its Correlation with Geophysical Phenomena of a Seismically Active Region, *Recent Developments in Using Seismic Waves as a Probe for Subsurface Investigations,* pp. 14, (Editor: Rajib Biswas), **CRC Press (Taylor & Francis Group),** eBook ISBN: 9781003177692

Others publications

1. T. Thuamthansanga, T., Sahoo, B. K., & Tiwari, R. C. (2020). Study of the influencing nature of meteorological factors air temperature and relative humidity on the exhalation process of $^{222}Rn/^{220}Rn$ gases at mat fault. *Journal of Applied and Fundamental Sciences*, *6*(1), 41. Published by **Assam Don Bosco University. ISSN 2395-5554 (Print)|ISSN 2395-5562 (Online).**

2. Thuamthansanga, T., Tiwari, R. C., Tiwari, R. P., & Sahoo, B. K. (2020). Correlation study of ^{222}Rn production rate and exhalation rate with geophysical process at mat fault in Mizoram. *J Int Acad Phys Sci*, *24*(1), 83-93. Published by **International Academy of Physical Sciences. ISSN 0974-9373.**

Papers Presented in International Conferences

1. Monitoring of soil-air interface radon flux in wet soil as a possible signal for geophysical phenomena by correlating with a distance continuous monitoring station data. In: The international conference on chemistry and environmental sustainability, 19^{th}-22^{nd} February, 2019, Mizoram University, Aizawl, Mizoram, India.
2. Study of pre-seismic radon anomaly near Indo-Burman subduction line using empirical mode decomposition based Hilbert-Huang Transform and Artificial Neural Network. In: Fifth international conference on application of radiotracers and energetic beams in sciences, 31^{st} January-5^{th} February, 2023, Sidho-Kanho-Birsha University, Purulia, West Bengal, India.
3. Study of pre-seismic radon anomaly using machine intelligent at Indo-Burman subduction region. In: First international conference on radiation awareness and detection in natural environment, 2^{nd}-4^{th} March, 2023, Dolphin (PG) Institute of Biomedical and Natural Sciences and Govt. Degree College Dehradun Shahar, Dehradun, Uttarakhand, India.

Papers Presented in National Conferences and Symposium

1. Study of radon concentration using soil probe and radon exhalation chamber for seismic study. In: 20^{th} national conference on solid state nuclear track detectors and their applications, 26^{th}-28^{th} October, 2017, Vidya Vikas Institute of Engineering and Technology, Mysuru, Karnataka, India.
2. Correlation of *in-situ* online ^{222}Rn data at Mat fault with geophysical process. In: 22^{nd} national symposium on radiation physics, 8^{th}-10^{th} November, 2019, Jawaharlal Nehru University, New Delhi, India.
3. Investigation on the responding behavior of ^{222}Rn/^{220}Rn exhalation to air temperature and relative humidity at Mat fault. In: Environmental radiation: Impact on society and its implications, 15^{th}-16^{th} November, 2019, Jadavpur University, Kolkata, India.
4. Correlation study of ^{222}Rn production rate and exhalation rate with geophysical process at Mat fault. In: National conference on functional materials and applications, 22^{nd}-23^{rd} November, 2019, National Institute of Technology, Aizawl, Mizoram, India.
5. Study of the influencing nature of meteorological factors air temperature and relative humidity on the exhalation process of ^{222}Rn/^{220}Rn gases at Mat fault. In: Trends in modern physics 2020, 24^{th}-25^{th} February, 2020, Don Bosco University, Sonapur, Assam, India.
6. Study of pre-seismic thoron anomaly using empirical mode decomposition based Hibert-Huang Transform at Indo-Burman subduction region. In: Third national conference on radiation awareness and detection in natural environment, 18^{th}-20^{th} March, 2021, Govt. P.G. College New Tehri and H.N.B Garhwal University Campus Badshahi Thaul, Tehri Garhwal, Uttarakhand, India.
7. Identification of geophysical property for radon and thoron data for earthquake precursor in Indo-Burman subduction region. In: 23^{rd} national symposium on radiation physics, 19^{th}-21^{st} January, 2023, University of Mysore, Manasagangotri, Mysuru, Karnataka, India.

Conferences and workshops attended

1. Advanced Techniques in Nano Science and Technology, held during 3rd-8th December, 2018 at Institute of Nano Science and Technology, Mohali, Punjab, India.
2. National Workshop on 'Ethics in research and preventing Plagiarism (ERPP 2019)', held on 3rd October, 2019 at Department of Physics, Mizoram University, Aizawl, Mizoram, India.

PARTICULARS OF THE CANDIDATE

Name of the candidate	:	T Thuamthansanga
Degree	:	Doctor of philosophy
Department	:	PHYSICS
Title of thesis	:	*In-situ* Online Measurement of Radon (^{222}Rn) Data and Developing its Correlation with Geophysical Phenomena in Seismically Active Regions: A case Study of Mat fault at Zawlpui, Serchhip District, Mizoram.
Date of admission	:	11th August, 2017
Approval of research proposal		
1. DRC	:	06th April, 2018
2. BOS	:	11th April, 2018
2. SCHOOL BOARD	:	24th April, 2018
3. MZU Registration No.	:	72 of 2014
4. Ph.D Registration No.	:	MZU/Ph.D./1099 of 24.04.2018
5. Extension (if any)	:	NIL

(Prof. ZAITHANZAUVA PACHUAU)

Head,

Department of Physics

ABSTRACT

IN-SITU ONLINE MEASUREMENT OF RADON (^{222}Rn) DATA AND DEVELOPING ITS CORRELATION WITH GEOPHYSICAL PHENOMENA IN SEISMICALLY ACTIVE REGIONS: A CASE STUDY OF MAT FAULT AT ZAWLPUI, SERCHHIP DISTRICT, MIZORAM

AN ABSTRACT SUBMITTED IN PARTIAL FULFILLMENT OF THE REQUIREMENTS FOR THE DEGREE OF DOCTOR OF PHILOSOPHY

T THUAMTHANSANGA

MZU REGISTRATION NO.: 72 of 2014

Ph.D. REGISTRATION NO. : MZU/Ph.D./1099 of 24.04.2018

DEPARTMENT OF PHYSICS

SCHOOL OF PHYSICAL SCIENCES

DECEMBER, 2022

IN-SITU ONLINE MEASUREMENT OF RADON (^{222}Rn) DATA AND DEVELOPING ITS CORRELATION WITH GEOPHYSICAL PHENOMENA IN SEISMICALLY ACTIVE REGIONS: A CASE STUDY OF MAT FAULT AT ZAWLPUI, SERCHHIP DISTRICT, MIZORAM

By

T Thuamthansanga

Department of Physics

Name of Supervisor: Prof. R.C. Tiwari

Name of Joint Supervisor: Prof. R.P. Tiwari

Submitted

in partial fulfillment of the requirement

of the Degree of Doctor of Philosophy in Physics of Mizoram University, Aizawl.

ABSTRACT

Radon is a radioactive noble gas discovered by German scientist Frederick Dorn in 1900. It has three naturally occurring isotopes radon (^{222}Rn: $T_{1/2}$, 3.825 d, decay series of ^{238}U), thoron (^{220}Rn: $T_{1/2}$, 55.6 s, decay series of ^{232}Th) and actinon (^{219}Rn: $T_{1/2}$, 3.6 s, decay series of ^{235}U). Due to its extremely small half-life (3.6s) and low activity concentrations in the environment relative to its two isotopes actinon has often been neglected in most practical studies as well as in this thesis. Due to its origin in the earth's crust and mobility through soil pores, radon has been extensively monitored for various purposes such as a tracer to its parent nuclei, tracer to a hidden fault, health hazard, earthquake prediction etc. Anomalies in radon concentration are known to be associated with seismic activity and creep processes on faults. Such radon concentration anomalies due to geophysical phenomena have been observed and studied in soil-gas as well as in groundwater and spring. One such officially recorded radon anomaly before an earthquake was in a Russian well before the Tashkent earthquake in 1966. The radon anomalies in soil are not only controlled by pre-seismic stress but also by external factors especially meteorological factors (soil moisture, rainfall, temperature, barometric pressure and wind velocity). These factors can change the physical characteristics of the soil and thus perturb the variation caused by geophysical processes. Hence, the influence of these parameters on the radon and thoron variation is also important and needs to be considered in seismic precursory studies.

In this thesis monitoring of radon and thoron data was performed at Mat fault in an attempt to find their causal relationship with geophysical phenomena of the region. At the same time, online radon and thoron data were continuously monitored at the Department of Physics, Mizoram University, Aizawl (India) for cross-analysis. The work has been extended to Chite fault located at the heart of Aizawl city. According to the seismic hazard zonation map of India, the region lies at seismic zone V (highest seismic level) and is one of the six most seismically active regions of the world. To worsen the situation the region had experienced phenomenal growth in

population density and development programs where mushrooming growth of unplanned urban centres has been witness in major cities and their adjoining town. Hence vulnerability and risk of the human population and physical structures of the region to impending earthquakes is at worse. A realistic approach to understanding and assessing the status of seismicity of the region is an unavoidable necessity. One such possible candidate may be monitoring radon concentration variation in a seismically active region. Keeping in view of this, we started monitoring *in-situ* and online radon isotope pair data at Mat fault, Mizoram University and Chite fault during 2017 and 2019. It was also the first study where online data with high frequency (15 min cycles) has been accomplished at one of the highest seismicity of the world i.e. at the vicinity of the Indo-Burman subduction line and at the junction of the Himalayan arc and Burmese arc.

The thesis has been documented into five chapters. Chapter 1 presents background of the radon isotope pair data, their mechanism of production in the earth's crust by emanation/recoil effect, their migration process from soil to the atmospheric air by diffusion and advection process, factors affecting radon and thoron exhalation process, the mechanism of earthquake occurrence, the isotope pair relation to earthquakes has been explained using various models, the status of seismicity of the study area, Motivation, scope and the objective of the study. Chapter 2 presents a review of the literature. It highlights a brief overview of some important studies relating soil radon variation and geophysical phenomena from the early 1950s till date. Chapter 3 presents a detailed description of the materials and the methods used in the study. Details and specifications of the ZnS(Ag) alpha-based scintillation counter have been explained, the protocol for acquiring the isotope pair data through various measurements in soil and water using the monitor has been given, a protocol for observing the relationship between the isotope pair data and meteorological parameters was discussed. The method for identifying the radon and thoron anomalies using the standard deviation method and Empirical mode decomposition (EMD) based Hilbert Huang transport (HHT) were discussed in detail. Method for estimating uranium and thorium from their respective daughter nuclei was given. Chapter 4 describes the analysis of the results obtained. The

isotope pair concentration of the region was estimated, the uranium and thorium content of the region were also estimated, the diurnal and seasonal variation of the region were presented, a detailed correlation analysis between meteorological factors and the isotope pair data was given, cross-correlation analysis of the online data at MZU and *in-situ* data of Mat and Chite fault was given in details, correlation of the online continuous data at MZU with earthquakes of the region using standard deviation method and EMD-HHT were given in detail.

In general, it was concluded that except for thorium the isotope pair data and uranium content of the region falls within the global average and no radiological risk was observed for the region. Diurnally radon concentration varies with temperature while their seasonal variation and relationship with meteorological factors were distinct. The correlation analysis shows that temperature, pressure and rainfall were the main influencing factor and pressure the most. The cross-correlation analysis shows that the maximum number of the sampling spots of the region were able to sow higher radon counts during geophysical phenomena at different sampling depths and in water. The standard deviation method analysis shows that 100% of the selected earthquakes were predicted with no false radon anomalies. The EMD-HHT technique shows that 100% of the selected earthquakes were correlated but with three uncorrelated thoron peaks. The study also highlights the necessity of additional online monitoring stations, accessibility of online soil meteorological factors and advanced non-linear statistical analysis techniques for the accuracy of the result.